Ice Nucleation by Combustion Products at Conditions Relevant to Mixed-Phase Clouds

Nsikanabasi Silas Umo

Submitted in accordance with the requirements for the degree of

Doctor of Philosophy

The University of Leeds

School of Earth and Environment

May, 2014

Intellectual Property Statement

The candidate confirms that the work submitted is his own and that appropriate credit has been given where reference has been made to the work of others.

Acknowledgements

Writing an acknowledgement for a long-term project makes me feel nervous, not because my writing skills have flown out of the windows but my fear is that the exact words that can confer my gratitude are simply non-existent. Even if I were to get appropriate words, I still fight a saggy memory not to miss out the likes of the janitors and the plumbers that kept my working environment conducive. It is on this note that I want to begin the long and never-exhaustible lists of people that rendered assistance to me during my PhD studies.

Firstly, I would like to thank my supervisors, Dr. Benjamin John Murray, Professor John M. C. Plane, and Dr. Maria T. Baeza-Romero for their unfeigned and indefatigable support throughout the course of my research programme. My particular thanks go to Ben for putting me through the tenets of research; he was never weary to discuss and to listen to every idea even when some were less of a sense. Your contributions to my academic career are invaluable and remain evergreen. My appreciation also goes to Professor Alan Williams and Professor Jenny Jones for their supports.

To all the Staff and Researchers at the School of Earth and Environment, especially Michelle Lenianski and the reception staff – I appreciate your unswerving support.

To my research colleagues: Jim Atkinson, Theo Wilson, Tom Whale, Tamsin Malkin, Danny O'Sullivan, Kelly Baustian, Hannah Price, Jo Browse, Sandy James, Ross Herbert, Amanda Lea-Langton and Thomas Mangan - thank you for the time we spent together in the lab, meetings, and seminars - debating 'science', approving and disapproving, offering constructive criticisms, sharing ideas even though some ideas were really 'crazy'. You all made it a fun-time at Howard Atmospheric Laboratory.

To my one and only wife, true friend and lover, EnoObong – thank you for being there. Your words of encouragement and support at all stages of my PhD study cannot be undermined. I salute your courage to believe in me that I will complete this project. To my son, MfonObong - thank you for allowing Daddy to stay long hours on his study desk. Your calmness and understanding was such a boost to me.

To my wonderful parents – Mr. and Mrs. Silas Udo Umo – no other parents in this world can invest in me like you do. There was hardly a week you did not call to say 'keep going'. Your prayers, financial support, and motivation will never be taken for granted in my entire life. You have taught me persistence and the *'I can'* spirit. To my lovely sisters: Idara, Itoro, and Ekuyikeno – you Gees were always available to care and support.

I would like to acknowledge the Niger Delta Development Commission (NDDC) for the financial assistance (NDDC/DEHSS/2010PGFS/AK/011) towards my PhD studies. I would like to thank the European Research Council (ERC) for the stipend support (FP7, 240449 ICE), and the School of Earth and Environment International Student Bursary (2011 – 2012). These financial supports went a long way to aid my studies.

Specially, I would like to thank the following people, who supported me in one way or the other – Profs. Etim Essien, U. J. Ekpe, K. O. Adebowale, J. U. Umo, Arch. E. I. Ette, Drs. P. C. Okafor, B. I. Olu-Owolabi, Barr & Mrs. Solomon Abai, Sir & Mrs. Joe Michael, Mrs. Mfon Mbassa, Very Rev. Okon Obot, Mr. Fidelis Uzoka, Sir (Dr.) & Lady E. U. U. Ekanem, Rev. & Deaconess J. Anago, and Mr. Sunny Umoh. May God bless you all! To all my friends: Ekemena Oseghe, Ubong Etuk, Ini Udo, Ime Akpabio, Ekpeno Udo, Monica Udoette, Esuene, and others - you were very encouraging and thank you for believing in me.

I would like to acknowledge the contributions of Lates Chief Effiong Etuk, Mrs. Cecilia O. Obot, Pastor Emmanuel Mbassa, Mrs. Ngozi Jennifer Uzoka, and Justice Edemekong Edemekong to my academic career, rather sad that you could not beat death to see this thesis. I know the joy you would have exuded in times like this. The advice and support you gave me when you were still breathing cannot be carpeted.

To my friend, Pastor & Mrs. Samuel Obafaiye and the entire congregation of Redeemed Christian Church of God – Everlasting Father's Assembly (RCCG – EFA), Leeds, UK – thank you for your support and prayers.

To the Almighty God, may all the praise and glory be to you!

...Now to the King eternal, immortal, invisible, the only wise God, be honour and glory for ever and ever. Amen (1 Timothy 1:17).

Nsikanabasi Silas Umo

Dedication

This PhD thesis is dedicated

to the Almighty God,

who through his providence and grace saw me to the end of this work

and

to my great parents – Silas Udo Umo and Atim Silas Umo,

who raised me, taught me the value of education, and believed in me.

Abstract

Quantifying the ice nucleation activity of combustion aerosols is crucial in understanding their impact on cloud properties, and consequently, on climate. This study investigates the ice nucleation abilities of soot and combustion ashes in the immersion mode at conditions relevant to mixed-phase clouds. Some physical and chemical properties of these aerosols, which aided the interpretation of their ice nucleation activities, were also explored.

Soot generated from eugenol and n-decane compounds were used as proxies for atmospheric soot from biomass and hydrocarbon combustion, respectively. Combustion ashes studied were coal fly ash (CFA), wood bottom ash, domestic bottom ash, and coal bottom ash. The ice nucleation experiments were performed with droplet freezing assay instruments; the results obtained are summarised below:

(1) Eugenol and n-decane soot particles in suspension were found to nucleate ice between -16.5 and -28 ºC. To describe the ice nucleation efficiency of these particles, a singular model of ice nucleation that yields the ice active nucleation sites density (n_s) was applied. Both soot types showed n_s in the range: 1 - ~ 10^7 cm^{-2} at a temperature range of -16 to ~ -28 °C. An estimation of potential ice nuclei (IN) number based on the ice nucleation efficiency of these soot types indicated that soot substantially contributes to primary ice formation in mixed-phase clouds from temperatures below -22 ºC. At ~ - 25 ºC, soot showed a competition with mineral dust IN. This study suggests that soot is an important IN in mixed-phase clouds especially in regions where mineral dust is not a dominant IN.

(2) The freezing temperatures for combustion ashes were between -15 to -36 °C. The fraction of droplets frozen showed that the freezing temperatures were in this order of significance: CFA>>wood ash>domestic ash>coal ash. The n_s values estimated for all ashes were between 10^{-2} and 10^7 cm^{-2} for freezing temperatures between -15 and -36 °C. The best estimate suggests that combustion ashes can account for global primary ice nuclei number up to 1 cm^{-3}, and this could impact on primary ice formation budget in mixed-phase clouds.

Table of Contents

Intellectual Property Statement ..... **iii**

Acknowledgements ..... **v**

Dedication ..... **vii**

Abstract ..... **ix**

Table of Contents ..... **xi**

List of Tables ..... **xv**

List of Figures ..... **xvii**

List of Abbreviations and Acronyms ..... **xxi**

Chapter 1 Aerosols, clouds, and climate **25**

1.1 Atmospheric aerosols 25

1.2 Clouds and aerosols 30

1.3 Statement of problem – why are combustion aerosols important? 32

1.4 Objectives of this study 37

1.5 Project location and approach 38

1.6 Summary of the thesis layout/presentation 38

1.7 Chapter summary 39

Chapter 2 Ice nucleation and carbonaceous aerosols **41**

2.1 Introduction 41

2.2 The theory of ice nucleation and modes of ice nucleation process 41

2.3 Models associated with ice nucleation 42

2.4 Ice nucleation by carbonaceous aerosols - soot and other biomass particles. Literature review 47

2.5 Uncertainties associated with ice nucleation measurements of soot 51

2.6 Chapter summary 52

Chapter 3 Experimental methodology for ice nucleation studies 53

3.1 Introduction 53

3.2 Materials and samples preparation for the freezing experiments 54

3.2.1 Ultra-pure water 54

3.2.2 Solvents 54

3.2.3 Soot suspensions 54

3.2.4 Ash suspensions 55

3.2.5 Droplet generation 56

3.3 Instrumental set-ups and freezing experiments 58

3.3.1 Microlitre drop freezing instrument and experiments (µL-NIPI) 59

3.3.2 Effects of pipette tips on the freezing behaviour of droplets generated for µL-NIPI experiments 62

3.3.3 Nanolitre and picolitre drop freezing instruments and experiments (nL- and pL-NIPI) 63

3.3.3.1 Modifications to the cold-stage for nanolitre drop freezing experiments 66

3.3.3.2 Validation of the modified nL-NIPI set-up by homogeneous experiments 67

3.4 Artefacts associated with µL-NIPI, nL-NIPI, and pL-NIPI experiments 70

3.5 Data analyses 73

3.5.1 Video analyses 73

3.5.2 Data processing 74

3.6 Chapter summary 76

Chapter 4 Generation and characterisation of soot and ash particles 77

4.1 Introduction 77

4.2 Soot and combustion ash aerosols 77

4.2.1 Formation mechanisms of soot and ashes during combustion 77

4.2.2 Generation of soot and combustion ash particles from fuels for ice nucleation work in this thesis 80

4.3 Characterisation of eugenol and n-decane soot 84

4.3.1 Soot charaterisation by Raman spectroscopy 84

4.3.2 Surface morphology and particle size analyses 90

4.3.3 Surface area analyses 92

4.3.4 Chemical composition of eugenol and n-decane soot – organic carbon (OC) versus elemental carbon (EC) 97

4.4 Characterisation of combustion ashes 97

4.4.1 Mineralogy of ash particle by X-ray diffractometry (XRD) 97

4.4.2 Surface morphology of combustion ashes 100

4.4.3 Elemental analysis of ashes by energy-dispersive X-ray spectrometry (EDS) 108

4.4.4 Particle size analysis of combustion ashes – laser diffraction method and BET 113

4.5 Effect of dispersant on particles size distribution of CFA 115

4.6 Concentration of dissolved ions in ash suspensions 116

4.7 Variation in the pH of ash suspensions 119

4.8 Chapter summary 119

Chapter 5 Ice nucleation by eugenol and n-decane soot 121

5.1 Freezing by eugenol and n-decane soot 121

5.1.1 Results from freezing experiments by eugenol and n-decane soot in the µL-NIPI 121

5.1.2 Results from freezing experiments by eugenol and n-decane soot in the nL-NIPI 123

5.2 Description of the ice nucleation efficiency of soot 124

5.3 Evidence of aggregation of soot particles in suspensions 127

5.4 Effect of soot-water interaction time on their ice nucleation activity 130

5.5 Comparison with other soot types studied in literature 135

5.6 Estimation of ice nuclei from soot ice nucleation efficiency 141

5.7 Atmospheric relevance of this study 143

5.8 Conclusion 143

5.9 Chapter Summary 144

Chapter 6 Combustion ashes as potential ice nuclei 145

6.1 Combustion ashes in the atmosphere 145

6.2 Global emissions of combustion ashes 145

6.3 Combustion ashes as aerosol particles and motivation for the study 146

6.4 Ice nucleation studies on ashes (literature) 148

6.5 Results and discussion 149

6.5.1 Freezing of ashes in the immersion mode – CFA, wood, domestic, and coal bottom ashes 150

6.5.2 Distribution of ice nucleation sites of combustion ashes 155

6.6 Comparison of ice nucleation activities of combustion ashes to IN of varied mineralogies 158

6.7 Study on the possible relationship between soluble ions concentration and pH on the ice nucleation activity of combustion ashes 161

6.8 Study on the possible relationship between ice nucleation properties of ashes and dissolved chemical components 162

6.9 Impacts of combustion ash aerosols on mixed-phase clouds 162

6.10 Conclusion 166

6.11 Chapter summary 167

Chapter 7 Summary, conclusions, and future research directions 169

7.1 Summary of the major outcomes 169

7.2 Major conclusions 170

7.3 Recommendations for future research 171

Appendix 173

References 187

List of Tables

Table 1.1: Proportion of soot (black carbon) in ice crystal residues.....36

Table 2.1: A summary of ice nucleation studies of different soot types in the immersion mode from 1990 to 2013.....50

Table 4.1: Specific surface areas (SSA) obtained from BET measurements of eugenol soot, n-decane soot and combustion ashes.....94

Table 4.2: BET specific surface areas (m^2/g) of different soot types. 95

Table 4.3: Mineral compositions of CFA, wood, domestic and coal bottom ashes (%) were obtained from XRD.....99

Table 4.4: Concentrations (ppm) of dissolved ions in combustion ash solutions.....118

List of Figures

Figure 1.1: A schematic showing the emission sources of black carbon. 26

Figure 1.2: Global wild fire hot spots indicating possible carbonaceous aerosol emission, especially, soot and other combustion by-products.. 28

Figure 1.3: A chart showing the radiative forcing (W m^{-2}) estimates. 31

Figure 1.4: Correlation of ice number concentration and refractory black carbon as observed from analyses of ice crystal residues. 34

Figure 2.1: Homogeneous and heterogeneous freezing mechanisms ……..…. 42

Figure 3.1: A set-up for sieving ash samples into ≤ 40 μm size. 55

Figure 3.2: A distribution of droplets sizes formed by nebulizing ultra-pure water 57

Figure 3.3: Droplets containing soot particles 58

Figure 3.4: A schematic showing a cross-section of droplets distributed in silicon oil to prevent mass transfer 58

Figure 3.5: A schematic of a μL-NIPI set-up 59

Figure 3.6: Images of different droplets sizes for NIPI drop freezing experiments. 60

Figure 3.7: Fraction of frozen droplets of ultra-pure water. 62

Figure 3.8: Fraction of droplets frozen and the distribution of ice nucleation active sites for 0.1 wt% suspension of coal fly ash particles. 63

Figure 3.9: A cold-stage coupled to an optical microscope 65

Figure 3.10: Various parts of the cold stage coupled to an optical microscope 65

Figure 3.11: C-mounts and brass washer combinations used for pL-NIPI (**A**) and nL-NIPI (**B**) experiments. 67

Figure 3.12: Homogeneous freezing of ultra-pure water using a cold-stage coupled to an optical microscope for nL-NIPI. 68

Figure 3.13: Nucleation rates J_{hom} (cm^{-3} s^{-1}) of ultra-pure water 69

Figure 3.14: Some experimental artefacts associated with the µL-NIPI setup for drop freezing assay experiments. 71

Figure 3.15: Images showing condensation and bubble trapping during nL-NIPI or pL-NIPI freezing experiments. T. 72

Figure 3.16: A 0.01 mm micrometre length to computer screen size at 150% 73

Figure 3.17: Schematic of droplets on hydrophobic surface 74

Figure 4.1: Combustion route of biomass showing possible emitted species. 78

Figure 4.2: A diagram showing a possible formation mechanism of combustion ashes as illustrated by Williams et al. (2012). 79

Figure 4.3: Chemical structures and formulae of eugenol and n-decane 80

Figure 4.4: A set-up for generating eugenol and n-decane soot in the laboratory. 82

Figure 4.5: A schematic of the solid fuel stove (boiler stove model) that was used for the generation of wood (biomass) and coal bottom ash samples. 84

Figure 4.6: A schematic illustrating the Raman scattering. 85

Figure 4.7: A schematic of a Raman measurement set-up. 86

Figure 4.8: Raman spectra (λ_0 = 514 nm) of (1) eugenol soot and (2) n-decane soot 88

Figure 4.9: Raman spectrum of airborne soot showing the experimental spectrum and the 5-band deconvolution model. 89

Figure 4.10: Transmission Electron Microscopy (TEM) images of eugenol and n-decane soot 91

Figure 4.11: Mineral compositions by weight (%) of the bulk sample of coal fly ash (CFA) 100

Figure 4.12: Scanning electron microscopy (SEM) images of CFA particles 102

Figure 4.13: Scanning electron microscopy (SEM) images of wood (biomass) bottom ash particles 104

Figure 4.14: Scanning electron microscopy (SEM) images of domestic bottom ash sample 105

Figure 4.15: Scanning electron microscopy (SEM) images of coal bottom ash sample 107

Figure 4.16: Elemental composition of coal fly ash obtained from energy dispersive X-ray spectroscopy coupled to SEM. 109

Figure 4.17: Elemental composition of wood bottom ash 110

Figure 4.18: Elemental composition of domestic bottom ash 111

Figure 4.19: Elemental composition of coal bottom ash o 112

Figure 4.20: Particle size distribution of combustion ashes - coal fly ash, wood, domestic, and coal bottom ashes. 114

Figure 4.21: Effect of dispersant on the particle size distribution of coal fly ash..... 116

Figure 5.1: Freezing behaviour of eugenol soot particles from the µL-NIPI experiments. 122

Figure 5.2: Fractions of droplets frozen for eugenol and n-decane soot obtained from the nL-NIPI set-up..... 124

Figure 5.3: The cumulative number of ice nucleation active sites (n_s) for eugenol and n-decane soot particles..... 126

Figure 5.4: Possible forms that soot particles can restructure in water suspension. 128

Figure 5.5: Particle size distribution obtained from a dynamic light scattering (DLS) instrument. 129

Figure 5.6: Freezing behaviour of eugenol soot particles in suspension over time from a µL-NIPI. 131

Figure 5.7: Freezing behaviour of n-decane soot particles in suspension over time from a µL-NIPI. 132

Figure 5.8: n_s plot of eugenol soot suspensions that were left stirring for 24 hours (d1), 144 hours (d6), and 504 hours (d21). 133

Figure 5.9: n_s plot of n-decane soot suspensions that were left stirring for 24 hours (d1), 144 hours (d6), and 504 hours (d21). 134

Figure 5.10: Nucleation sites density (n_s) for both eugenol and n-decane soot from both µL-NIPI and nL-NIPI experimental set-ups 136

Figure 5.11: Nucleation sites density (n_s) plot for eugenol soot and n-decane soot 139

Figure 5.12: Estimation of IN from soot ice nucleation efficiency..... 142

Figure 6.1: Annual emissions of coal fly ash (Tg) from different countries and continents.. 146

Figure 6.2: IN concentrations observed from Millipore filters exposed to a background air and a plume from a coal fired power plant.. 149

Figure 6.3: Fraction of droplets frozen from freezing experiments in the µL-NIPI. 151

Figure 6.4: Fraction of droplets frozen from freezing experiment in the nL-NIPI. 153

Figure 6.5: Fraction of droplets frozen for different freezing experiments of 0.1 wt% of CFA, coal, wood and domestic bottom ash suspensions using the µL-NIPI. 154

Figure 6.6: Ice nucleation active sites distribution for various weight percentages (wt%) of CFA, wood (biomass) bottom ash, domestic bottom ash, and coal bottom ash suspensions, ... 156

Figure 6.7: Comparison of ice nucleation sites distribution for combustion ashes and other mineral ice nuclei 159

Figure 6.8: An estimation of ice nuclei number (N_{ice}) cm^{-3} that would result based on the ice nucleation activity of combustion ashes from this study. 165

List of Abbreviations and Acronyms

Abbreviations		Full meaning
“	-	inches
°C	-	degree **C**elsius
µL-NIPI	-	micro**l**itre - **N**ucleation by **I**mmersed **P**articles **I**nstruments
µm	-	micro**m**etres
AZTD	-	**A**ri**z**ona **T**est **D**ust
BB	-	**B**iomass **B**urning
BC	-	**B**lack **C**arbon, also referred to as ‘**E**lemental **C**arbon’
BET	-	**B**runauer-**E**mmet-**T**eller method
CCD	-	**C**harge **C**ouple **D**evice
CCN	-	**C**loud **C**ondensation **N**uclei
CCPs	-	**C**oal **C**ombustion **P**roducts
CFA	-	**C**oal **f**ly **a**sh
CFDC	-	**C**ontinuous Flow Diffusion Chamber
cm	-	**c**enti**m**etres
CNT	-	**C**lassical **N**ucleation **T**heory
CO	-	**C**arbon mon**o**xide
CO_2	-	**C**arbon di**o**xide
EC	-	**E**lemental **C**arbon
EDX	-	**E**nergy **D**ispersive **X**-ray
FGD	-	**F**lue **G**as **D**esulfurization
Fig. / Figs.	-	**Fig**ure / **Fig**ure**s**

FoV	-	**F**ield **o**f **V**iew
GLOMAP	-	**Glo**bal **M**odel of **A**erosol **P**rocesses
HAL	-	**H**oward **A**tmospheric **L**aboratory
hPa	-	**h**ecto**pa**scal
HPLC	-	**H**igh **P**erformance **L**iquid **C**hromatography
IN	-	**I**ce **N**uclei
INAS	-	**I**ce **N**ucleation **A**ctive **S**ites
IPCC	-	**I**ntergovernmental **P**anel on **C**limate **C**hange
lpm	-	**L**itres **p**er **M**inute
mm	-	**m**illi**m**etre
MODIS	-	**Mod**erate Resolution **I**maging **S**pectroradiometer
Mt	-	**M**etric **t**onnes
MΩ.cm	-	**m**egaohms centimetres
NASA	-	**N**ational **A**eronautics and **S**pace **A**dministration
N_{ice}	-	**Ice N**umber concentrations
nL-NIPI	-	nano**l**itre - **N**ucleation by **I**mmersed **P**articles **I**nstruments
NO_x	-	**N**itrogen **O**xides species
NWP	-	**N**umerical **W**eather **P**rediction
OC	-	**O**rganic **C**arbon
OM	-	**O**rganic **M**atter
PAHs	-	**P**olycyclic **A**romatic **H**ydrocarbon**s**
POCs	-	**P**olymeric **O**rganic **C**ompound**s**
ppb	-	**p**arts **p**er **b**illion
PRT Probe	-	**P**latinum **R**esistance **T**emperature **P**robe
RH	-	**R**elative **H**umidity
rpm	-	**r**ate **p**er **m**inute
RSG	-	**R**esearch **S**upport **G**roup

SEM	-	**S**canning **E**lectron **M**icroscopy
SO_2	-	Sulfur di**o**xide
SOA	-	**S**econdary **O**rganic **A**erosols
Tg / Tg y^{-1}	-	**T**eragram / **T**eragram per year
TOC	-	**T**otal **O**rganic **C**arbon
VIs	-	**V**irtual **I**nstrument**s**
VOCs	-	**V**olatile **O**rganic **C**ompound**s**
W m^{-2}	-	**W**atts per square **m**etre
wt%	-	**w**eight percent
XRD	-	**X**-ray **D**iffractometry

Chapter 1

Aerosols, clouds, and climate

1.1 Atmospheric aerosols

Aerosol is a system of suspended solid or liquid particles in the air or gas. In the atmosphere, which comprises mainly gases and water vapour, particles are also dispersed in it - these dispersed particles in the atmosphere are generally referred to as 'aerosol' particles. In an atmospheric context, these particles can sometimes be referred to directly as aerosols. Some of the particles present in the atmosphere are mineral, organic or biogenic in nature. Mineral particles include natural dusts, volcanic ashes, combustion ashes, sea salts; organic particles are soot, black carbon, secondary organic materials; and the biogenic compositions are pollen, fungi, bacteria (Wallace and Hobbs, 2006; Seinfeld and Pandis, 2006).

Atmospheric aerosol particles can be grouped into different genres based on their emission sources, type of materials, and sizes; and sometimes, based on their atmospheric processing. Based on aerosol sources, two major categories can be identified – natural and anthropogenic (man-made) sources. For example, sea salts and volcanic-related aerosol particles such as volcanic ashes/sulphates have natural sources while a significant proportion of soot aerosols are emitted from anthropogenic sources (Pruppacher and Klett, 2010). Although, emission of soot particles can come from both sources - for instance, wild fires can result from either a natural or a man-made cause, they are mainly classified as anthropogenic.

As earlier indicated aerosol particles can either be mineral based (inorganic), organic or biological. In terms of sizes, aerosol particles can fall into the following categories: nucleation, Aitken, accumulation and coarse modes. Measurements of aerosol particles in the atmosphere show an overlap between the various modes (Seinfeld and Pandis, 2006). Finally, aerosol particles can be grouped as either primary or secondary particles, depending on how they are created and their aging processes. The abundance of these aerosol particles in the atmosphere varies with respect to their altitude and locations;

also, weather and climatic conditions can affect their global distribution (Seinfeld and Pandis, 2006; Monteith and Unsworth, 2013; Gill, 1982).

Combustion processes serve as one of the major sources of carbonaceous aerosol particles emission (Cao et al., 2013; Zheng et al., 2006). These carbonaceous aerosol particles are soot (black carbon), tar balls, furans, dioxins, fly ashes, bottom ashes and any other emissions from biomass burning (Petters et al., 2009; Posfai et al., 2004; Fitzpatrick et al., 2008). This study is focused on soot (black carbon) and combustion ashes. Sources of black carbon aerosols to the atmosphere and their fates are summarised in Figure 1.1.

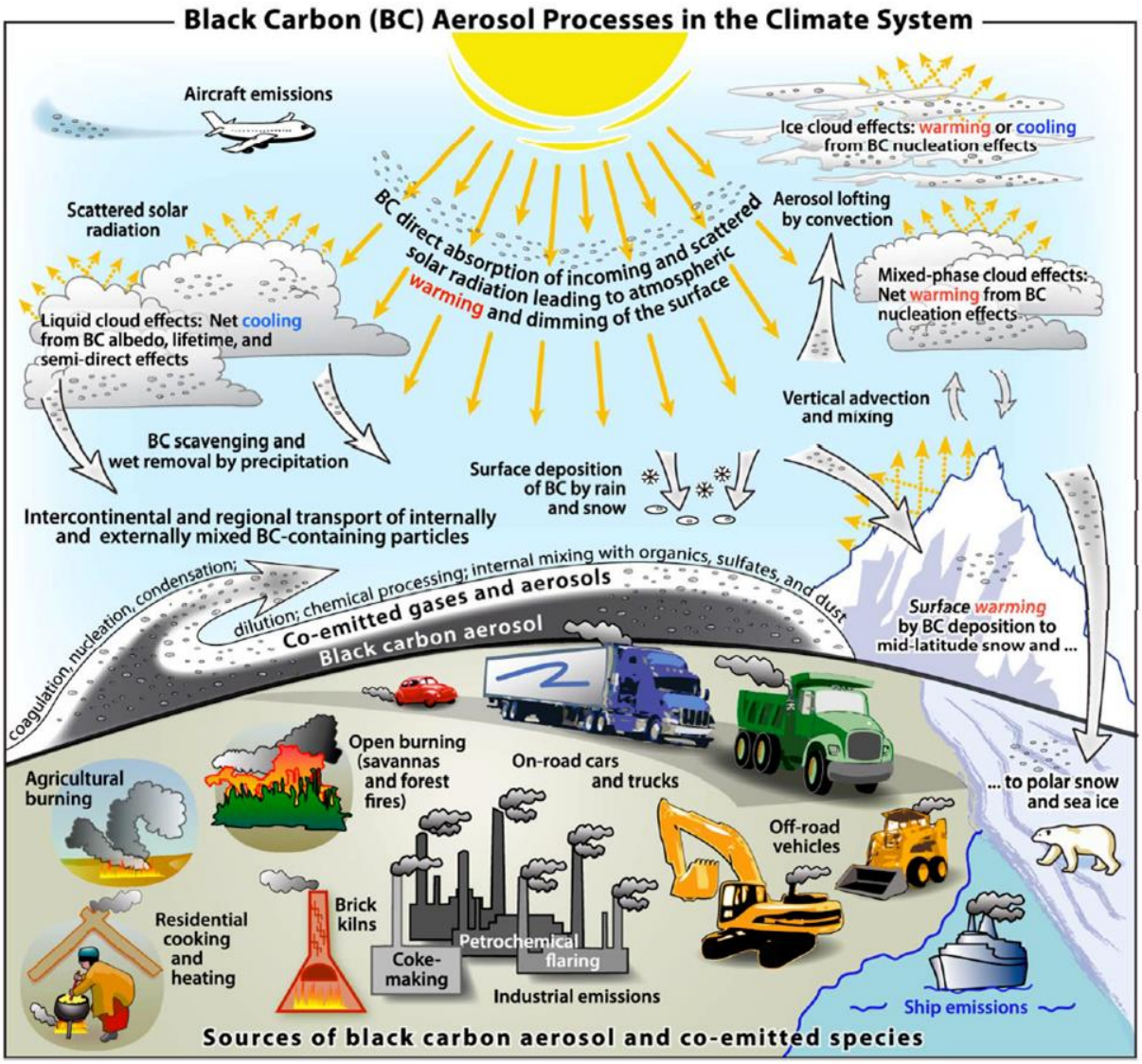

Figure 1.1: A schematic showing the emission sources of black carbon aerosol and other co-emitted species into the atmosphere, their interactions, fate, and impacts on the climate system as depicted by Bond et al. (2013).

For the purpose of this research, soot is described as black or brown particles released during the combustion of biomass or fossil fuels; it comprises mainly a carbon core and may or may not be associated with organics such as polycyclic aromatic hydrocarbons (PAHs). Many attempts have been made to define soot or establish clear distinction between soot and black carbon (Andreae and Gelencsér, 2006; Posfai et al., 2004; Buseck et al., 2012; Petzold et al., 2013) and references therein. In this work, the definition of soot by Charlson and Heintzenberg (1995) is adopted, which soot is described as 'particles formed during the quenching of gases at the outer edge of flames of organic vapours, consisting predominantly of carbon, with lesser amount of oxygen and hydrogen present as carboxyl and phenolic group and exhibiting an imperfect graphitic structure'. The soot definition above can be contrasted with that of black carbon as presented by the latest the Intergovernmental Panel on Climate Change (IPCC) report (Boucher, 2013); which defines black carbon (BC) as 'a distinct type of carbonaceous material formed from the incomplete combustion of fossil and biomass based fuels under certain conditions'. Going by this definition, there is no clear distinction between both types of carbonaceous particles. However, it can be directly inferred that soot are commonly generated in oxygen-sufficient conditions during combustion processes while black carbon results in an insufficient oxidant conditions or BC is a product of incomplete combustion of a carbon material. In the atmospheric science community, BC measurements and aerosol groupings include soot but they are quite distinct by their optical properties and measurement methods (Buseck et al., 2014). Despite these attempts, there is still an ongoing debate on the exact nomenclature and definition of soot.

The major sources of soot in the atmosphere are biomass burning and combustion of fossil fuels (Bond et al., 2013; Ramanathan and Carmichael, 2008; Simoneit, 2002). A fire detection algorithm MODIS developed by Giglio et al. (2003) and Davies et al. (2004) for NASA indicates global emission spots for wild fires as shown in Figure 1.2.

Globally, an average of ~ 7.5 Tg of soot is released into the atmosphere via different sources (Bond et al., 2013) and Figure 1.1 gave an illustration on the diverse sources of black carbon and their pathways in the atmosphere. Soot is classed by their different properties ranging from the refractive index, morphology, size distribution to their optical properties (Tumolva et al., 2010).

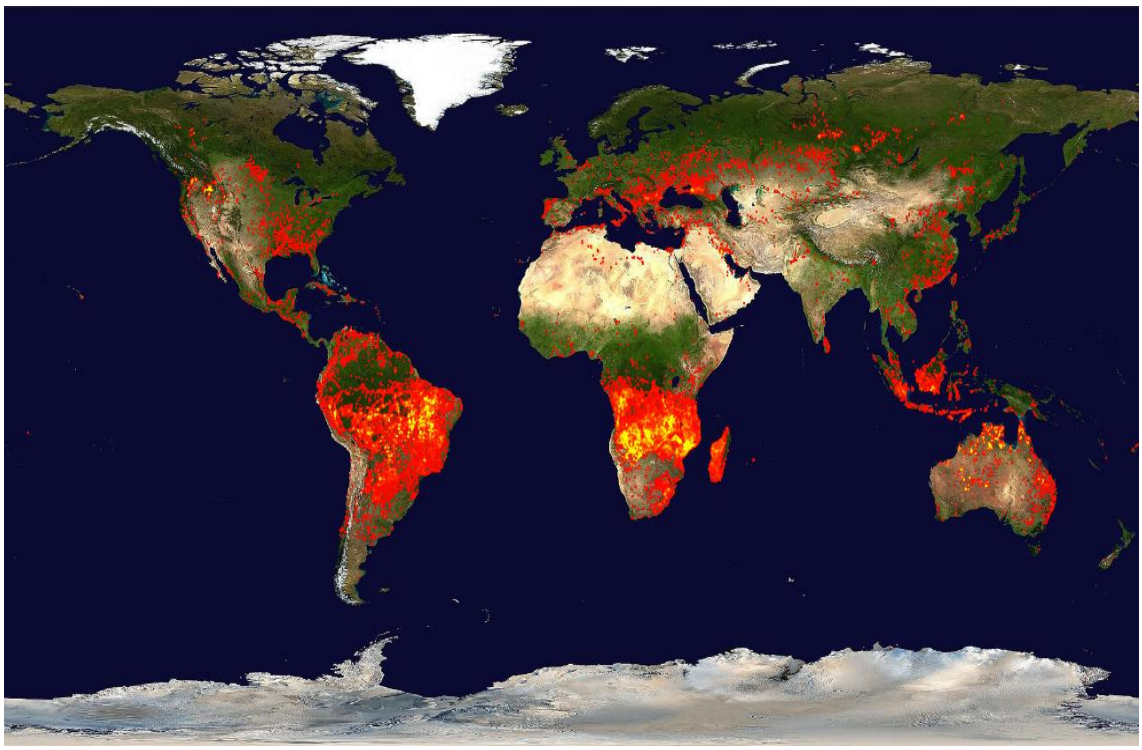

Figure 1.2: Global wild fire hot spots indicating possible carbonaceous aerosol emission, especially, soot and other combustion by-products. Each of these fire maps accumulates the locations of the fires detected by MODIS on board the Terra and Aqua satellites over a 10-day period. Each coloured dot indicates a location where MODIS detected at least one fire during the compositing period (10 days). Colour ranges from red where the fire count is low to yellow where number of fires is large. This figure and its description was extracted from the MODIS NASA website (Davies et al., 2004; Giglio et al., 2003).

They can undergo both physical and chemical processing in the atmosphere usually referred to as aging. Physically, the fractal number of soot can change and the size of its spherules can be altered due to abrasion mechanism. The chemical properties of soot can be altered via oxidation by substances such as ozone, coating by sulphates, PAHs, VOCs, and others. Soot can also get externally and internally mixed with other atmospheric particles like metals and see salts (Seinfeld and Pandis, 2006; Liu et al., 2013; Han et al., 2012b). Notwithstanding, the total impact of soot in the atmosphere depends on its residence time, particles size, scavenging processes, mixing states and reactivity in the troposphere (Johnson et al., 2005; McMeeking et al., 2011a; Browse et al., 2012; McMeeking et al., 2011b; Cape et al., 2012). Soot interacts with various components of the troposphere and with radiation; this can influence the climatic properties of the Earth.

Another major group of combustion by-products released into the atmosphere is ash, which can come from combustion of fossil and biomass fuels used for energy production (Schauer et al., 2001; Nussbaumer, 2003). Their emissions vary throughout

the globe depending on the emission sources e.g. power plants, which are distributed all over the world; and these power plants produce significant amount of these aerosol particles in metric tonnes (ACCA, 2013; WCA, 2013). Interestingly, due to small sizes of these particles and low density, they are capable of long-range transportation; therefore, their impact could be felt in regions far away from their emission source (Perry et al., 1999; Mandrioli et al., 1984). Combustion ashes are emitted either as fly or bottom ashes, depending on the combustion system. For this particular study, combustion ashes are referred to mineral particles - the burnt-out components of a solid fuel that are released during the combustion process or left behind after combustion. It is majorly the non-soot combustion by-product.

Combustion aerosols have significant impacts on health, visibility, built environment, clouds, and others. A certain range of particle diameter is important in quantifying aerosols impact on health, usually below 2.5 μm, and soot falls into this size range. The amount of particulate matter $\leq$ 2.5 μm is used in establishing clean air index for the environment (Forster, 2007; Ruuskanen et al., 2001; Anenberg et al., 2011). Particles resulting from biomass burning can have robust impact on air quality directly or indirectly by reacting with other aerosol particles to form smog that impairs visibility (Claeys et al., 2004; Singh et al., 2008).

Most importantly for the present study, combustion aerosols have a known impact on cloud formation systems by acting as cloud condensation nuclei (CCN) (Spracklen et al., 2011; Koehler et al., 2009; Engelhart et al., 2012; Friedman et al., 2013), and as ice nuclei (IN) (Dymarska et al., 2006; Koehler et al., 2009; Corbin et al., 2012). Biomass burning and fossil fuel combustion pollutants have been reported to modify weather (Ding et al., 2013; Lu and Sokolik, 2013; Rosenfeld et al., 2011). A study carried out in Nanjing, China showed that fossil fuel combustion pollution resulted in a decrease in the solar radiation intensity by more than 70%, a decrease in the sensible heat by more than 85%, a temperature drop by almost 10K. Also, a change in rainfall during both daytime and night-time has been observed (Ding et al., 2013).

In summary, the behaviour of combustion aerosol particles as CCN and IN can impact on the Earth's climatic conditions at both regional and global scale (Forster, 2007; Ramanathan et al., 2007; Lu and Sokolik, 2013; Ding et al., 2013; Bond et al., 2013).

1.2 Clouds and aerosols

Clouds occur in various forms, extent and attitudes. They can be grouped into many categories based on their altitudes, extent and temperatures (Pruppacher and Klett, 2010). The temperature regime and conditions from which clouds form are crucial, which give rise to various cloud types and classification; mainly, into three families – high clouds, medium clouds, and low level clouds. There are also clouds with vertical development and special types of clouds such as the lenticulars (Barry and Chorley, 2009; Murray et al., 2012; Mason, 1962). In relation to the cloud composition, clouds can have its water content mainly in an ice phase; liquid state, or in both liquid phase and ice particles. The latter cloud type is referred to as 'mixed-phase' cloud (Mason, 1962; Platt, 1977). Mixed-phase clouds have been observed over a temperature range of 0 °C to ~ -38 °C and it has been established that they can trigger precipitation when the ice particles grow to a critical size big enough to fall out from the clouds. (Rosenfeld and Woodley, 2000; Murray et al., 2012; Pruppacher and Klett, 2010). The growth of these ice crystals at the expense of the supercooled water droplets in the clouds is referred to as Bergeron-Findeisen process (Pruppacher and Klett, 2010). With the occurrence of this phenomenon, this makes mixed-phase cloud an important cloud type in modifying weather and, consequently, climate.

Usually, water droplets containing particles form ice at near 0 °C but in a pristine atmosphere (air with no particles); water droplets can be supercooled up to ~ -37 °C before forming ice. This is due to the high energy of germ formation and the molar activation energy required for the formation of the ice embryo. These energies depends on temperature, so the supercooling temperature increases the energy reduces making it possible for the water molecules to overcome the water-water bonds and form a water-ice bonds (Pruppacher and Klett, 2010). However, in the presence of an appropriate aerosol particle, ice formation can take place at much warmer temperatures, these particles are referred to *'ice nuclei'* (IN) (Pruppacher and Klett, 2010; Murray et al., 2012; Hoose and Möhler, 2012; Seinfeld and Pandis, 2006). Partly, this can explain why many ice-containing clouds have warmer temperatures than would be expected by only 'pure' water freezing mechanism. In mixed-phase clouds, the ice formation process can take place via two pathways – primary or secondary ice formation, or the former process followed by the latter (Pruppacher and Klett, 2010; Mossop, 1985). The primary ice formation process is mainly via a freezing process which in this case is

heterogeneous ice nucleation, while processes such as riming, ice multiplication (Hallett-Mossop process), ice splintering, ice fragmentation and others are the major secondary ice formation processes (Phillips et al., 2008; Phillips et al., 2012; Cui et al., 2011; Young, 1993; Phillips et al., 2003).

Understanding the ice formation process is important in quantifying the indirect effects of aerosol-cloud interactions in mixed-phase clouds, which currently, is limited. The latest Intergovernmental Panel on Climate Change (IPCC) report showed that there is still a significant uncertainty associated with cloud adjustments due to aerosols as presented in Figure 1.3. Because of this, the level of scientific understanding and confidence in estimating the radiative forcing due to cloud adjustments by aerosols is low (IPCC, 2013; Carslaw et al., 2010).

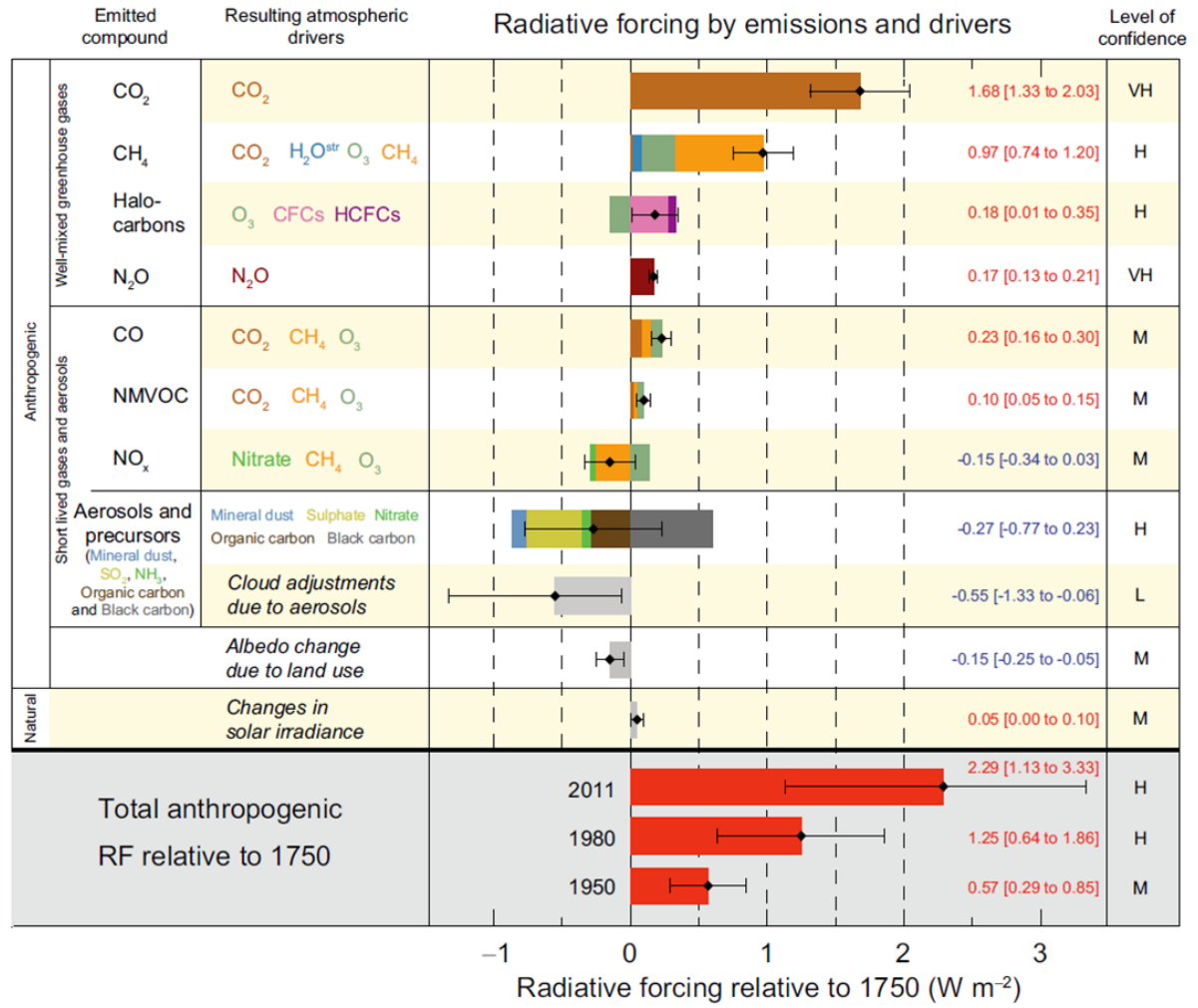

Figure 1.3: A chart showing the radiative forcing (W m^{-2}) estimates for different atmospheric components between 1750 and 2011. There is a low confidence label on the radiative forcing estimate by cloud adjustments due to aerosols probably because of the level of uncertainty associated with the contribution of aerosols to the cloud adjustments. This high level of uncertainty is tied to the low level of scientific understanding of aerosol-cloud interactions. The chart was taken from IPCC (2013).

To improve on the understanding of ice formation processes, especially, in mixed-phase cloud systems, it is important for the impact of aerosols on cloud properties to be properly quantified; this means the microphysics of cloud formation by these aerosols needs to be constrained (Bond et al., 2013; Graf, 2004; Gettelman et al., 2013).

Soot and combustion ashes are ubiquitous aerosols and they are capable of influencing the ice cloud microphysics as earlier stated. Therefore, to fully constrain the impact of aerosols on climate, it is important to evaluate the contributions of combustion aerosols such as soot and ashes to cloud adjustments.

1.3 Statement of problem – why are combustion aerosols important?

Combustion aerosols have direct, semi-direct and indirect impacts on the Earth's energy budget. This involves the energy balancing of the incoming solar radiation taking into accounts the incoming, outgoing, absorbed and part of the radiation that have interacted the other components of the Earth (Forster, 2007). Types of indirect aerosol effects which can contribute to the global energy budget include the following: (1) the cloud albedo or Twomey effect which explains why smaller cloud particles reflect more radiation (Warner and Twomey, 1967). (2) the cloud life time effect that describes the efficiency of smaller cloud particles in inhibiting precipitation, hence, increasing the cloud lifetime. (3) semi-direct effect explains the evaporation of cloud particles by the absorptive abilities of aerosol particles e.g. soot. (4) the thermodynamic effect which explains that smaller cloud droplets delay the onset freezing. (5) glaciation indirect effect which suggests that more ice nuclei increase the precipitation efficiency. (6) riming effect which has to do with the decrease in the riming efficiency by smaller cloud droplets, and finally, (7) the surface energy budget effect, which predicts that the increase in the optical thickness of clouds and aerosol can decrease the net surface solar radiation (Lohmann and Feichter, 2005; Forster, 2007). Of these indirect effects, thermodynamic, glaciation and riming are the most dominant effects in mixed-phase clouds. In addition, of the seven effects listed here, only glaciation effect is very crucial to soot INPs components of the cloud/aerosols (Lohmann and Diehl, 2006; Lohmann, 2002).

For an overall assessment of the Earth's radiative budget, the total contributions by direct, semi-direct and all the indirect effect must be considered. Some scientific studies and reports have focused on the warming effect of soot in the atmosphere (direct effect)

because of its high absorbing properties e.g. Jacobson (2001); Ramanathan and Carmichael (2008); Yu et al. (2006); Saleh et al. (2013); Jacobson (2012). In addition to the direct aerosol effect, there is also the semi-direct effect (Hansen et al., 1997). Black carbon has been reported to cause a warming in the boundary layer which leads to overall reduction in the liquid-water path (LWP), hence, causing a positive semi-direct radiative forcing (Hill and Dobbie, 2008). However, less attention has been given to its indirect contributions. Hence, the understanding of indirect effects caused by combustion aerosols on clouds is limited due to ageing of these materials in the atmosphere. This aging process can involve their interactions with other atmospheric species such as ozone, SO_2, nitrates, organics and other particles, which can alter their initial chemistry and behaviour. This forms part of the indirect aerosol chemistry effect. This has resulted in significant uncertainties associated with the assessment of total radiative properties of clouds (Bond et al., 2013; Ervens and Feingold, 2013; Forster, 2007; Boucher, 2013; Graf, 2004; Tao et al., 2012). More so, attempts by aerosol-climate models to represent the role of combustion aerosols are handicapped by limited parameterizations (Phillips et al., 2008; Phillips et al., 2012).

Recently, data from analyses of ice crystals residues from in-situ observations showed that there is a very strong correlation (R^2 = 0.996) between the number of ice particles and the concentration of black carbon (BC) measured in the same region as depicted in in Figure 1.4 (Twohy et al., 2010). This study was conducted over the Rocky Mountains, USA, to investigate the ice concentrations in orographic wave clouds at temperatures -24 to -29 °C (see Table 1.1). A variety of techniques was used to measure the ice nuclei compositions as listed on Table 1.1. Electron microscopy images of the various particles collected during the flights showed soot, sulphates and other biomass components. Although a strong correlation is established with black carbon, the work also suggested internal mixing of soot with soluble materials like sulphate or other salts (Twohy et al., 2010). It should be noted in Figure 1.4 that the data is not forced through the origin hence; the data should not be extrapolated beyond what is reported.

Other field measurements also indicate that soot, combustion ashes, and other combustion particles are seen in ice crystal residues to varying degrees (Pratt et al., 2009; Pratt et al., 2010; Twohy et al., 2010; Kamphus et al., 2010; Stith et al., 2011; Cozic et al., 2008).

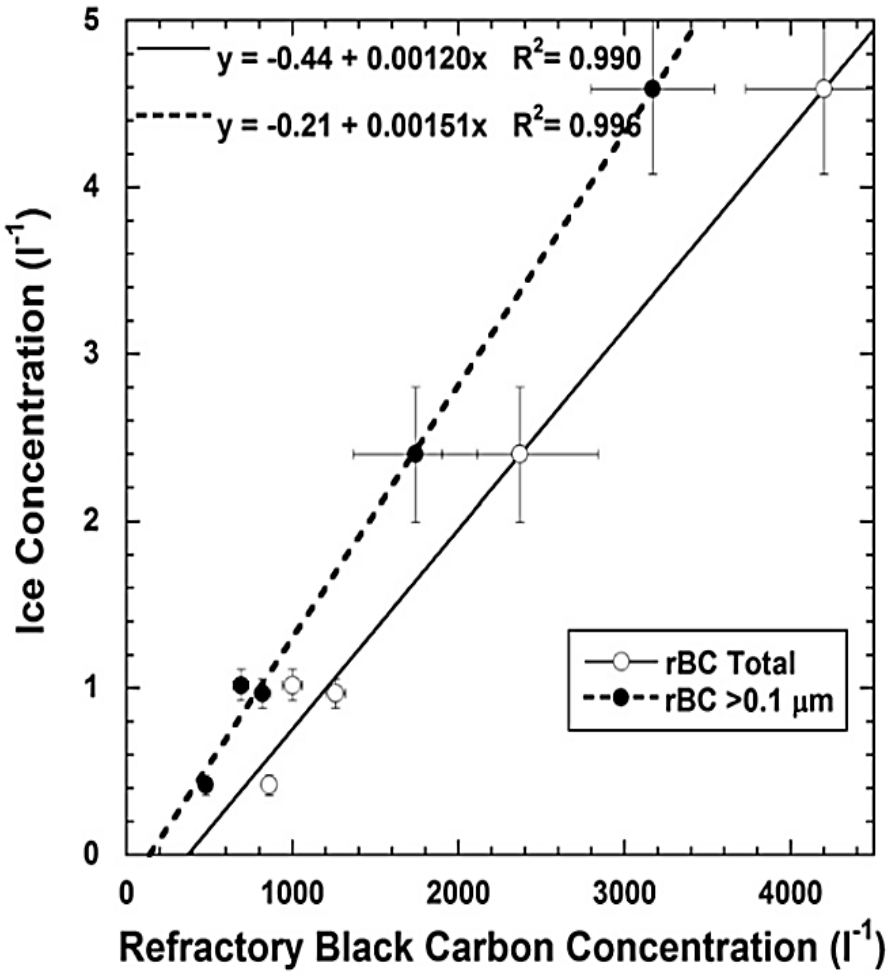

Figure 1.4: Correlation of ice number concentration and refractory black carbon as observed from analyses of ice crystal residues. The plot is from Twohy et al. (2010).

A summary of these data are shown in Table 1.1. High concentrations of ice particles have been measured in both primary and secondary wakes of aircrafts and this observation is attributed to ice nucleation induced by soot particles (Schumann et al., 2013). Again, this provides another piece of evidence that soot may be playing an important role in modifying cloud properties.

However, the data from these observations seems to contradict some experimental data which considers soot (black carbon) as relatively poor ice nuclei. Although, some studies observed soot to nucleate ice, the overall picture of soot's ice nucleation activity is mixed (Dymarska et al., 2006; Petters et al., 2009; Crawford et al., 2011; DeMott et al., 1999; Gorbunov et al., 2001; Sakaeda et al., 2011; Murray et al., 2012; Hoose and Möhler, 2012). Also, aged soot particles by organics and sulphates are reported to only improve its hygroscopic property and not necessarily its ice nucleation efficiency (Mohler et al., 2005a; Pant et al., 2006; Friedman et al., 2011). This is because the materials such as sulphates and organics are coated on the surface of the soot and do not

necessarily alter the surface chemical structure of the soot. For example, in the immersion mode where these coated soot particles are fully immersed, the coatings may dissolve into the bulk solution leaving behind bare soot surface. However, a strong oxidizing substance such as ozone may modify the chemical surface of soot (Disselkamp et al., 2000) which may change its ice nucleation behaviour.

Aside from soot, investigations on the interactions of combustion ashes particles with clouds are rare. Only three studies, that the author is aware of, reported the potential of combustion ash as IN and it was shown that no significant ice-forming abilities were observed (Schnell et al., 1976; Parungo et al., 1978; Langer et al., 1967); although ice residue analyses of cirrus clouds have suggested mineral/fly ash to be one of the dominant components (DeMott et al., 2003). In addition, many reports usually grouped combustion ashes with mineral dust particles (DeMott et al., 2003; Kamphus et al., 2010; Chen et al., 1998). DeMott et al. (2003) observed that about 33 % of the ice residues from cirrus clouds were from mineral dust/fly ash and Chen et al. (1998), 65 %. These data sets give a clue that combustion ashes may contribute significantly to the primary ice formation in other cloud types such as mixed-phase clouds; however, data is lacking.

Paucity of data and limited understanding of the behaviour of combustion aerosols as IN in mixed-phase clouds, can limit the robustness of ice parameterization schemes e.g. Phillips et al. (2008). Clearly, there is need to improve the current understanding of the behaviour of soot and combustion ashes as IN which will help in reducing the level of uncertainty (IPCC, 2013) associated with cloud adjustments by aerosols, especially, in ice clouds.

Table 1.1: Proportion of soot (black carbon) in ice crystal residues sampled in a temperature regime of mixed-phase clouds. The percentage of ice composition due to soot ranges from 2 % to ~ 27%.

S/No.	Locations	Time	Project	Proportion of the residue due to soot	Temperature range measured (°C)	Cloud Temperature (°C)	Instrumentation	Reference
1.	Wyoming (43° N, 107° - 108° W) at 7.9 - 8.3 km above mean sea level (m.s.l.)	7 Nov, 2007	Ice in Clouds Experiment – Layer Clouds (ICE-L)	4 %	-31 to -34	-31	2D-C probe, CVI, CFDC, and A-ATOFMS	Pratt et al. (2009)
2.	Wyoming (43.1 - 44.5° N, 106.0° - 107.3° W) at 4.7 - 7.3 km above m.s.l.	16 Dec, 2007	*Same as above*	12 ± 2 % (A-ATOFMS) ~ 4 ± 3% Soot + sulphate = 22 ± 6 % (STEM-EDX) ~ 5 % (C-ToF-AMS+SP2	-24.1 to -25.2	-24.1 to -25.2	2D-C probe, CVI, CFDC, A-ATOFMS, SP2, C-ToF-AMS, STEM-EDX,CDP, FSSP-100, TDL, CCN spectrometer, UHSAS, and CPC	Pratt et al. (2010)
3.	Rock Mountains, Colorado, USA	7 Nov to 16 Dec, 2007	*Same as above*	-	-24 to -25	-	*Same as above*	Twohy et al. (2010)
4.	Jungfraujoch (Swiss Alps at 7° 59' 2" E, 46° 32' 53" N) 3580 m a.s.l.	Feb and Mar, 2007	Cloud and Aerosol Characterisation Experiment (CLACE 6)	2 % Mineral + black carbon 2% Total ~ 4 %		-6 to -16	Ice-CVI, SPLAT, ATOFMS, OPC, and CFDC	Kamphus et al. (2010)
5.	East Asia, Western Pacific Ocean	April to May, 2007	Pacific Dust Experiment (PACDEX)	Not specific. It was reported that higher number of rBC were found.	-30 to -33	-24 to -29	2D-C probe, CVI, CFDC, SP2, STEM-EDX, CDP, FSSP-100, and UHSAS	Stith et al. (2011)
6.	Jungfraujoch (3580 m asl, Switzerland).	Winter 2004 and 2005	Cloud and Aerosol Characterization Experiment (CLACE 3 and 4)	~27 %	-5 to -28	-	Ice-CVI, SPLAT, ATOFMS	Cozic et al. (2008)

2-Dimensional-Cloud Probe (2D-C probe), Counterflow Virtual Impactor (CVI), Continuous Flow Diffusion Chamber (CFDC), Aircraft-Aerosol Time-of-Flight Mass Spectrometer (A-ATOFMS), Single Particle Soot Photometer (SP2), Optical Particle Counter (OPC), Aerodyne Compact Time-of-Flight Aerosol Mass Spectrometer (C-ToF-AMS), Scanning Transmission Electron Microscopes-Energy-Dispersive X-ray (STEM-EDX), Cloud Droplet Probe (CDP), Forward Scattering Spectrometer Probe – 100 (FSSP-100), Tunable Diode Laser (TDL), Cloud Condensation Nuclei spectrometer (CCN spectrometer), Ultra-High Sensitivity Aerosol Spectrometer (UHSAS), Condensation Particle Counter (CPC), Single Particle Laser Ablation Time-of-flight mass spectrometer (SPLAT).

36

1.4 Objectives of this study

The study aims to quantify the ice nucleation efficiency of combustion products – soot from eugenol and n-decane soot, and combustion ashes - for conditions relevant to mixed-phase clouds. Eugenol and n-decane soot are used as proxies for atmospheric soot obtained from biomass burning and hydrocarbon fuel, respectively (details in chapter 5). In the past, different soot types obtained from different sources have been used to study the ice nucleation activities and some of the soot may be contaminated with other particles, e.g. (Diehl and Mitra, 1998), and this may show unrealistic ice nucleation activity of soot. Secondly, no proxy has been used for biomass soot.

Eugenol (4-Allyl-2-methoxyphenol) is a major compound released as an intermediate during the combustion process of lignin in most biomass fuels. Eugenol also has a potential of being used as a biofuel or a bio-additive to existing fuels (Kadarohman et al., 2010; Fitzpatrick et al., 2007). As a main component pyrolysis product from lignin - one of the three major components of biomass: cellulose, hemicellulose, and lignin - this compound undergoes combustion during the biomass combustion process to produce soot (Baeza-Romero et al., 2010; Wilson et al., 2013). Its chemical structure is shown in Figure 4.3A. Since eugenol can be obtained in a pure form, it serves as a proxy for fuel which generates soot produced from one of the essential components for biomass burning.

To compare eugenol soot with a typical hydrocarbon soot source, a compound with the same number of carbons atoms (10) as eugenol was choosen, n-decane (the chemical structure/formula is shown in Figure 4.3B). Since the combustion by-product of the fuels (soot) is composed of mainly carbon, it was important to choose an ydrocarbon fuel with similar carbon atoms. Both compounds exhibit analogous combustion mechanisms, but their soot production mechanisms are slightly different, hence, they present variability in their final soot compositions (Wilson et al., 2013).

The ice nucleation activities of both eugenol and n-decane have not been studied before; hence, this study is designed to systematically study their ice nucleation activity in a well controlled experiments – from the genration of the soot to the freezing experiments. In addition, this work will also investigate the ice nucleation activities of combustion ashes as non-soot by-products of a combustion process, which has never been done. The understanding gained and data obtained would potentially provide improved ice nucleation parameterizations for aerosol-cloud microphysics models,

which in future can lead to reduction in the present uncertainties associated with aerosol-cloud interactions (IPCC, 2013).

This study has the following specific objectives:

i. To generate soot from eugenol and n-decane compounds and characterise some of the soot properties that may be useful in interpreting results from the ice nucleation study.
ii. To quantify the ice nucleation efficiency of eugenol and n-decane soot at mixed-phase cloud conditions (in the immersion mode).
iii. To compare the ice nucleation efficiencies of other soot types previously studied in similar cloud conditions.
iv. To characterize atmospherically relevant properties of coal fly ash, coal bottom ash, wood (biomass) bottom ash, and domestic bottom ash.
v. To measure the ice nucleation abilities of combustion ashes listed above and attempt to quantify their relevance to mixed-phase clouds.

1.5 Project location and approach

This work was planned, designed, and carried out in Howard Atmospheric Laboratory (HAL) located in the School of Earth and Environment, University of Leeds, United Kingdom. Some measurements were performed at Facilities located in the School of Engineering, University of Leeds. All soot samples used in the study were generated in HAL from starter materials that were sourced commercially. Combustion ashes were generated mainly from a combustion Facility at the School of Engineering, University of Leeds. Details of the material sources, study and the research approach are stated in the methodology/results chapters (3, 4, 5, and 6).

1.6 Summary of the thesis layout/presentation

This thesis is presented in chapters; each chapter has an introduction, the results/discussions, followed by the chapter summary and the conclusion. All references are pulled together at the end of this thesis as well as some relevant materials at the Appendix.

Chapter 1 gives the introduction to carbonaceous (combustion) aerosols, clouds and climate and the main objectives of this research.

Chapter 2 examines the theory of ice nucleation and its associated models from the classical nucleation theory (CNT) to the singularity hypothesis. A literature review of ice nucleation studies of soot is also given.

Chapter 3 introduces the experimental methodologies/approach and instrumental set-ups used for the study. Existing set-ups were briefly described and some modifications that were made to them.

Chapter 4 has the characterisation results of both soot and combustion ashes. Detailed results of the atmospherically relevant properties are shown in this chapter. Other plots are shown in the Appendix (1st result chapter).

Chapter 5 presents the results from the ice nucleation experiments on eugenol and n-decane soot. This chapter also discusses the freezing curves of these soot types, their ice nucleation abilities and the potential impact on mixed-phase clouds (2nd result chapter).

Chapter 6 discusses the results from the ice nucleation studies on combustion ashes – coal fly ash, coal, wood (biomass) and domestic bottom ashes. Their relevance to mixed-phase clouds is underlined in this chapter (3rd result chapter).

Chapter 7 highlights the major findings from the study (summary and conclusions) as well as future directions for ice nucleation studies on soot and combustion ashes.

1.7 Chapter summary

This chapter opened with a general overview of the Earth's atmosphere. The relevance of atmospheric components and how these components, specifically aerosols, affect the weather and climate systems was highlighted. The major atmospheric components focused on were aerosol particles and their impacts were briefly discussed. Lastly, a general synopsis of carbonaceous aerosols was given with specific mention to soot (black carbon) and combustion ashes, which ice nucleation abilities, were later investigated as the main thrust of this work.

Chapter 2

Ice nucleation and carbonaceous aerosols

2.1 Introduction

Ice nucleation is one of the principal cloud microphysical processes that influences cloud properties. This chapter introduces the theory of ice nucleation, some proposed mechanisms, and its relevance in understanding aerosol-cloud interactions. A review of the relevant literature on ice nucleation studies by carbonaceous aerosols is discussed, with specific focus on the immersion mode ice nucleation by soot aerosols. In addition, the uncertainties associated with ice nucleation experiments involving soot particles are also listed.

2.2 The theory of ice nucleation and modes of ice nucleation process

Ice formation in the atmosphere takes place via two major processes – homogeneous and heterogeneous ice formation (Pruppacher and Klett, 2010). While homogeneous process involves the formation of ice particles without any foreign material, usually referred to as *'ice nuclei'* (see chapter 1), heterogeneous ice formation requires a particle for ice to nucleate on which leads to freezing as illustrated in Figure 2.1. The latter process can occur via different nucleation or freezing mechanisms referred to as modes of heterogeneous ice formation: deposition nucleation, contact, condensation and immersion freezing (Pruppacher and Klett, 2010; Vali, 1999; Murray et al., 2011; Hoose and Möhler, 2012; O'Sullivan et al., 2014; Vali, 1985).

Deposition nucleation mechanism entails a direct formation of ice from the water vapour phase on a dry particle; this process usually requires high water vapour super-saturation with respect to ice.

Contact freezing mechanism is generally described as an ice formation mechanism that occurs when a particle comes in contact with a supercooled water droplet. The contact by a particle can either be from the outside or the inside of the droplet. However, the extent to which the particle must make contact with the interface of the supercooled

water droplet before ice formation takes place is not clearly understood (Fornea et al., 2009; Hoffmann et al., 2013).

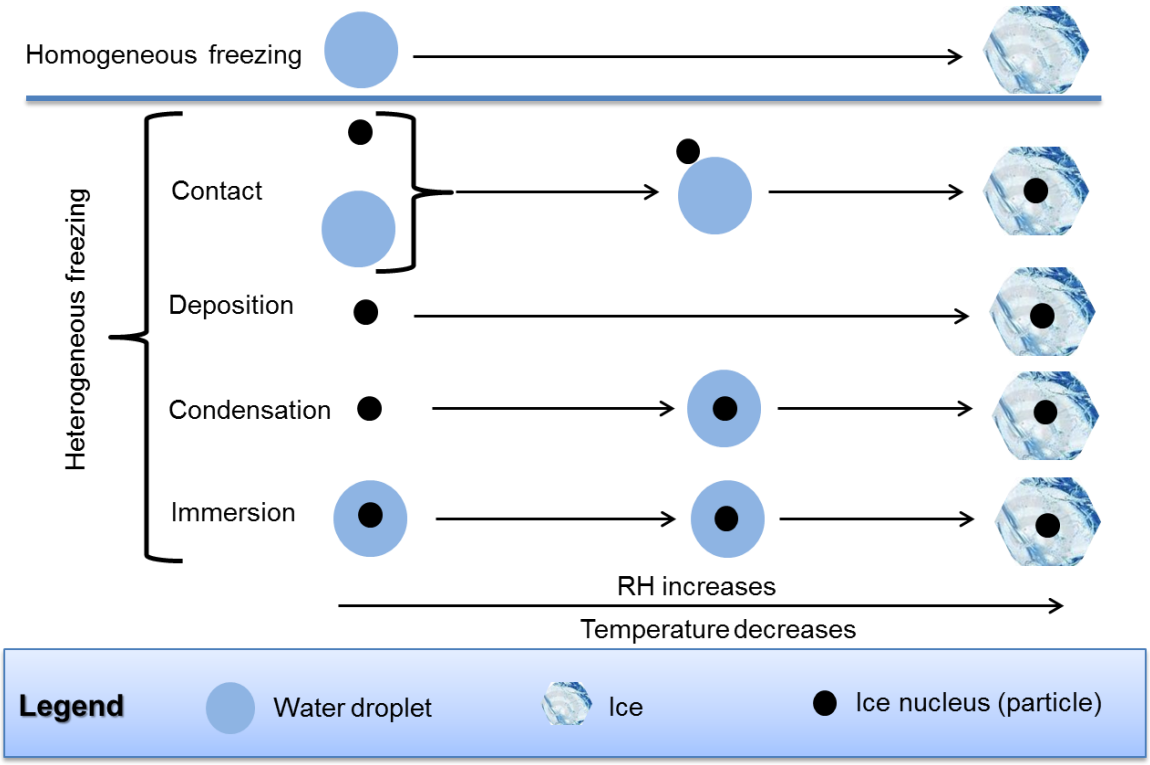

Figure 2.1: A summary of both homogeneous and heterogeneous freezing mechanisms. The focus of this study is on the immersion freezing mechanism.

On the other hand, condensation freezing is defined to be a mechanism whereby water condenses on a particle followed by ice formation.

Lastly, the immersion ice nucleation occurs when a particle is completely immersed in a water droplet and cooled before ice nucleation takes place (Murray et al., 2012; Vali, 1985). Looking at the interaction of aerosol particles and water in the atmosphere, it is unclear how the last two mechanisms - condensation and immersion freezing, can be distinguished in the atmosphere. If the specific definition of condensation freezing involves the condensation of supercooled water on the particle then a clear distinction can be made between the two processes. Also, the timescale between the condensation process and freezing of water needs to be clearly defined. The model shown in Figure 2.1 summarized the different heterogeneous freezing pathways.

2.3 Models associated with ice nucleation

Understanding the process of ice nucleation is important not only in describing ice nucleation properties of aerosols in the atmosphere but also in predicting the ice

nucleation behaviour of new materials. Classical nucleation theory (CNT) describes the formation of new phases from a parent phase which is usually a metastable phase (Vali, 1999; Pruppacher and Klett, 2010; Mullin, 2001).

By adapting the works of Gibbs (1948) as illustrated by Mullin (2001): In the process of homogeneous nucleation, the overall free energy (G_i) is dependent on the free energy of the unit volume (ΔG_v) and free energy associated with the transformation in the interfacial surface tension (ΔG_s) that depends on the surface area (σ).

$$\Delta G_i = (\mu_l - \mu_v)i + 4\pi\sigma r^2 \tag{2.1}$$

Where μ_v - μ_l is the chemical potential between a molecule in the vapour and liquid phase, r is the radius, and when the vapour pressure exceeds that of the same substance at the same temperature over a flat surface, then

$$\mu_v - \mu_l = kTlnS = \frac{2\sigma v}{r} \tag{2.2}$$

Where *S* is the ratio of vapour pressures of liquid water and ice (P_l/P_{ice}), which can be obtained as previously defined by Murphy and Koop (2005). *k* is the Boltzmann constant, *T* is the temperature. By combining equation 2.1 and 2.2, it results in the equation 2.3

$$\Delta G_i = 4\pi\sigma r^2 - \frac{4\pi kTlnS}{3v} r^3 \tag{2.3}$$

The first term explains the energy of the interface between the new phase and the parent phase; while the second term is the energy associated with the molecular volume of the new phase. The free energy of a subsaturated vapour (S > 1) is known to increase as the radius (r) increase. Hence, at a certain radius, the overall free energy will reach a maximum and this is equivalent to the amount of energy needed to overcome the barrier for a cluster of new phase to form. The CNT suggests that for a new phase to form there is a critical radius (r*) that a cluster of molecules must reach.

$$r^* = \frac{2\sigma v}{kTlnS} \tag{2.4}$$

The Gibb's energy of formation (*G**) needed to overcome the barrier for a critical radius (r*) can then be obtained by substituting equation 2.4 into 2.3:

$$\Delta G^* = \frac{16\pi\sigma^3 v^2}{3(kTlnS)^2} \tag{2.5}$$

From the expression above, the nucleation rate of the new phase (ice) can be obtained from an Arrhenius form equation:

$$J = Aexp(-\frac{\Delta G^*}{kT}) \quad (2.6)$$

where *J* is the nucleation rate usually reported as nucleation events per volume per unit time, and *A* is the pre-exponential factor, which depends on viscosity and other parameters (Murray et al., 2010a). Substituting equation 2.5 in 2.6 will result in:

$$ln\, J = ln\, A - \frac{16\pi\sigma^3 v^2}{3k^3T^3(lnS)^2} \quad (2.7)$$

Which a plot of ln *J* versus *T*^-3 (ln *S*)^-2 can allow the calculation of *A* from the intercept.

For heterogeneous ice nucleation where a particle is involved, equation 2.6 can be modified to accommodate the particle properties that are responsible for the reduction in the Gibb's energy as shown below:

$$J = Aexp(-\frac{\Delta G^* \partial}{kT}) \quad (2.8)$$

where ∂ represents the factor that accounts for the surface properties of the particle involved in the nucleation process (i.e. in the formation of the new phase).

To describe an atmospherically relevant ice nucleation mechanism by different particles, various models have been adopted (Vali and Stansbury, 1966; Vali, 1994; Vali, 2008; Broadley et al., 2012; Murray et al., 2012; Marcolli et al., 2007; Niedermeier et al., 2011; Herbert et al., 2014). It is known that the behaviour of IN particles in the immersion mode can depend on several factors such as the cooling rate, the temperature, the nature of particle, dispersion of the particles in droplets, and others (Hoose and Möhler, 2012; Murray et al., 2012; Kireeva et al., 2009).

The two main models of interest are – (1) the time-dependent model or stochastic, and (2) the time-independent model that is called 'singular' or 'deterministic' model. The stochastic model describes the probability of a critical cluster forming as being time-dependent – meaning that the tendency of ice forming is higher for a longer timescale cooling. In a time-dependent freezing model, the freezing temperature is higher at a slower cooling rate and vice versa.

In the homogeneous case, the rate at which droplets freeze is defined by:

$$R = \frac{dN}{dt} = -J_{hom} VN \quad (2.9)$$

where J_{hom} is the homogeneous nucleation rate, V is the volume of the droplet which freezes at time t, and N is the number of liquid droplets. When the above equation is integrated within the integral limits of N_1 to N_2 and a corresponding time change of t_1 to t_2, the resultant equation is stated below:

$$N_2 = N_1 \exp(-J_{hom} V \Delta t) \tag{2.10}$$

where N_1 is the number of droplets at t = 0, and N_2 is the number of droplets at t = t. When $N_2 = N_1$, the probability of all droplets frozen is 1.

However, when a particle is present in a droplet, the volume parameter is substituted with an approximate parameter (σ), which describes the surface area of the particle immersed in the droplet, as illustrated in equation 2.11. There is also a corresponding change in the units from J_{hom} ($cm^{-3}s^{-1}$) to J_{het} ($cm^{-2}s^{-1}$).

$$N_2 = N_1 \exp(-J_{het} \sigma \Delta t) \tag{2.11}$$

Here, J_{het} represents the heterogeneous nucleation rate defined as nucleation events per unit surface area (σ) of the particle per droplet per unit time. The assumption here is that there is a particle-to-particle uniformity for every droplets studied; and this model is described as the single-component stochastic model (Murray et al., 2012).

In a situation where there is particle-to-particle variability, the observed distribution of freezing temperatures is a product of both the stochastic nature of nucleation and the variability of individual nucleation sites present in the droplet. This can be described using a multiple-component stochastic model (Murray et al., 2012; Herbert et al., 2014). However, for this study, time-dependent model will not be applied, because in an atmospheric timescale of cloud formation in the mixed-phase cloud, time-dependency is less important (Vali, 1994). For instance, in a deep convective cloud system with an assumed updraft of 10 m s^{-1} with a lapse rate of 6.8 K km^{-1}, then the rate will be ~ 4 K min^{-1}. From laboratory experiments, it is shown that an order of magnitude difference in the cooling rate does not introduce any significant change (Wright et al., 2013). In atmospheric modelling studies, the error from neglecting time dependence is negligible compared to the exact thermodynamics conditions of the cloud (Wright and Petters, 2013).

More so, Vali (2008) and Ervens and Feingold (2013) suggested that particle-to-particle variability is more important than the time-dependency of IN. The latter study showed

that sensitivity of CNT for immersion freezing established that ice nucleation has by far a lowest sensitivity to time as compared to temperature, INP diameter, and the contact angle. Although a recent study on soot ice nucleation in the immersion mode showed that there is a weak dependence of soot on the cooling rate (Wright et al., 2013); the adoption of a modified singular approximation is found valid for all range of times and temperatures encountered in mixed phase clouds.

For a singular or a deterministic model, ice nucleation is assumed to occur at a characteristic temperature irrespective of the cooling rate at which the particle is subjected to (Murray et al., 2011; Broadley et al., 2012). Here, a particle is assumed to have sites on its surface, and each site has a predetermined temperature at which it can trigger freezing. Assuming a droplet contains only one particle with different sites, the overall freezing temperature of the droplet will depend on the site with the highest characteristic temperature. To estimate the active sites distribution on particles, the stochastic model shown in equation 2.11 is directly modified to define the active sites density as shown in equation 2.13:

$$N_2 = N_1 \exp(-n_s(T)\sigma) \tag{2.12}$$

where n_s (T) is the density of nucleation sites that become active at a particular temperature (T) per unit surface area, and σ is the surface area per unit volume (in this study, a unit volume is represented by a droplet). Usually, the freezing occurs over a range of temperatures, therefore, it is useful to represent the fraction of frozen droplets at temperature T (Vali, 1971):

$$f_{\mathrm{ice}}(T) = \frac{n_{\mathrm{ice}}(T)}{N_{\mathrm{tot}}} = 1 - \exp(-n_{\mathrm{s}}(T)\sigma) \tag{2.13}$$

where f_{ice} (T) is the cumulative number of frozen droplets at temperature T and n_s (T) is the cumulative number of nucleation sites per unit surface area that are active between 0 °C and temperature T °C. This was adopted for the calculation of n_s throughout this study. Calculations of ice nucleation active sites density allowed a comparison of ice nucleation activities of other aerosol particles in separate studies to be evaluated as reported in chapters 5 and 6 and Table 2.1.

2.4 Ice nucleation by carbonaceous aerosols - soot and other biomass particles. Literature review

Carbonaceous particles are ubiquitous in the atmosphere, and they have a potential of acting as CCN or IN (Zaveri et al., 2012; Ramanathan et al., 2001). Ice nucleation properties of some carbonaceous particles from biomass have been studied, for example Petters et al. (2009); Chou et al. (2013); however, some of these particles have not been well-characterised or defined, except a few such as tar balls (Posfai et al., 2004). Soot is a distinct class of carbonaceous aerosols, and it is an important aerosol in the atmosphere. Some studies have looked at the CCN activities of soot in the atmosphere (Koehler et al., 2009; Popovicheva et al., 2004; Starik et al., 2006). The IN activities of soot have also been investigated in the various modes of ice nucleation mechanism described in section 2.2 above: contact nucleation (Fornea et al., 2009; Diehl and Mitra, 1998), deposition mode (Dymarska et al., 2006; Tishkova et al., 2011; Kanji and Abbatt, 2006; Chou et al., 2013; Crawford et al., 2011; Suzanne et al., 2003; Mohler et al., 2005a; Mohler et al., 2005b; Koehler et al., 2009; Kanji et al., 2011; Friedman et al., 2011; DeMott et al., 1999; Demirdjian et al., 2009), condensation mode (Chou et al., 2013; Koehler et al., 2009; Kanji et al., 2011; Friedman et al., 2011; Dymarska et al., 2006), and the immersion mode (DeMott, 1990; Popovicheva et al., 2008a; Kireeva et al., 2009; Diehl and Mitra, 1998; Wright et al., 2013). For some studies, the mode of nucleation is not clearly defined e.g. Gorbunov et al. (2001). This section focuses on studies carried out in the immersion mode.

Study of ice nucleation by soot in the immersion mode had spanned over 20 years; yet, only a relatively small number of studies have been done in comparison to other aerosols such as mineral dust e.g. see Murray et al. (2012) and Hoose and Möhler (2012).

DeMott (1990) explored the ice nucleation efficiency of acetylene soot in the immersion mode by using a continuous flow expansion cloud chamber. Acetylene soot particles of approximately 0.08 µm and 0.12 µm sizes were found to nucleate ice from ~ -24 °C to ~ -34 °C. Variation in the cooling rate of the 0.08 µm particles from 1 K min^{-1} to 2 K min^{-1} did not alter the freezing temperatures. In a more recent by Wright et al. (2013), it is reported that there is a weak cooling rate or time-dependence of black carbon. The cooling rate in Wright et al experiment was varied up to 2 orders of magnitude

compared to the study with acetylene. Although, a variation of cooling from 1 to 2 K min^{-1} is not large enough, the two results does not show any disagreement. Nucleation sites density (n_s) for the acetylene soot studied by DeMott (1990) was estimated in the range of ~ 10^6 cm^{-2} to 10^8 cm^{-2} for the temperature range of -24 °C to ~ -34 °C (Murray et al., 2012; Hoose and Möhler, 2012).

In another study, Diehl and Mitra (1998) investigated the ice nucleation properties of kerosene soot. The freezing temperatures reported for five different droplet sizes between 172 µm and 409 µm, contaminated by kerosene soot were between -18 °C to -28 °C. Murray et al. (2012) attempted to calculate the n_s of this soot and reported values between 10^5 cm^{-2} and 10^7 cm^{-2} for the temperature range of -18 °C to -28 °C. However, in a bid to recalculate the n_s, it was observed that based on the information provided by the study, the concentrations of soot particles in those droplets were highly unrealistic because the expected number of particles in the droplets was << 1 as described in section 5.5. Although, the freezing temperatures were within the same range as observed by DeMott (1990), it was difficult to compare the activities of the two soot types because of the reasons stated earlier.

In addition, the two studies mentioned above looked at two different soot types, which were also generated differently. While acetylene soot was generated by combusting acetylene in a burner set at a sooting boundary with a limited oxygen supply (DeMott, 1990), the kerosene soot was obtained from an exhaust of a burner simulated to the exhaust characteristics of a jet engine (Diehl and Mitra, 1998). Analyses performed on the plume from the kerosene burner showed that some pollutants such as SO_2, CO_2, NO_x, CO, and other hydrocarbons were detected. It is established that the combustion properties of soot affect its physical and chemical properties (Han et al., 2012a), and this variability in their properties could influence their ice nucleating abilities as discussed in section 5.5.

Gorbunov et al. (2001) conducted a study on the ice nucleation of benzene and toluene soot obtained from two different soot aerosol generators - a thermal decomposition aerosol generator and an aerosol combustion generator. Benzene and toluene were used as fuel for the two soot generators. The nucleation mode that the ice-forming abilities of these soot types were examined, were not clearly defined in their report. However, the study reported that the freezing temperatures were from -5 °C to -20 °C. The hydrophobic soot particles which were generated by the thermal decomposition aerosol

generator had a lower ice-forming ability than soot with surface chemical groups that can form bond with water molecules, which were obtained from the combustion generator (Gorbunov et al., 2001). This observation contradicts a recent model results that an atomically flat carbon surfaces will promote heterogeneous ice nucleation because of an enhanced interfacial water layering (Lupi et al., 2014; Lupi and Molinero, 2014). However, it is not clear how hydrophilic ends on a carbon surface might aid this interfacial water layering. For this study, because the ice nucleation mechanism considered in this study was not clearly defined, it was difficult to compare the ice nucleation activity of benzene and toluene soot to other soot types. A summary of these immersion mode ice nucleation studies from 1990 to 2013 are shown in Table 2.1.

The effect of other soot types in the immersion mode was reported by Popovicheva et al. (2008a) and Kireeva et al. (2009). The studies looked at the freezing abilities of different soot types: lamb black, furnace black, channel black, acetylene soot, thermal soot (T-900), aircraft engine combustor soot, soot from TC1 kerosene flame, TC1 oxidized soot (TC1-O), and soot from combustor remote.

Freezing temperatures reported for these soot types were between ~ -6.8 °C to ~ -11.9 °C. The ice nucleation efficiencies for these soot types were found to correlate with the stability and the degree of dispersion of these soot particles in the suspensions studied (Kireeva et al., 2009). Freezing efficiency of soot particles left in the suspension was also observed to increase over time probably due to the kinetics of wetting (Popovicheva et al., 2008a). This involves the interaction of water and soot particles. Hydrophilic soot has a higher tendency to interact with water than a hydrophobic soot sample. This can depend on the porosity and the polarity of the soot particles (Popovicheva et al., 2008b).

The ice nucleation activities were between 10^{-5} cm^{-2} to ~ 10^{-2} cm^{-2} for the temperature range of -1.9 °C to -15 °C as shown on Table 2.1. Comparing these soot activities to that of acetylene soot studied by DeMott (1990), it was about 10 orders of magnitude different. Although studies by Popovicheva et al. (2008a) and Kireeva et al. (2009) looked at freezing abilities of soot at higher temperatures, a study by DeMott (1990) was comparatively at a lower temperature regime. This leaves out a reasonable temperature gap that both studies did not cover, hence, it is difficult to parameterise ice-forming abilities of soot to cover 0 °C to -36 °C based on these two results.

Table 2.1: A summary of ice nucleation studies of different soot types in the immersion mode from 1990 to 2013. In the table below, LIA means ***l**imited **i**nformation **a**vailable* and NA stands for ***n**ot **a**vailable*. Freezing temperatures cover a regime of -1.9 °C to -36 °C, and the n_s covers 10^{-5} cm^{-2} to 10^{8} cm^{-2} for that temperature range. A further description of some parameters represented on this table is available on the table footnotes.

Soot type investigated	**Surface Area (m^2/g)**	**Range of freezing temperatures (°C)**	**n_s density (cm^{-2})**	**Instrumentation**	**Reference**
Acetylene soot (0.08 µm and 0.12 µm sizes)	NA	-24 to -34	10^{6} - ~ 10^{8}	expansion cloud chamber	DeMott (1990)
Kerosene soot	NA	-18 to -28	LIA	drops in a wind tunnel	Diehl and Mitra (1998)
Benzene soot	NA	-5 to -20	LIA	cloud chamber	Gorbonov et al (2001)ǂ
Toluene soot	NA	-5 to -20	LIA	cloud chamber	Gorbonov et al (2001)ǂ
Lamb black (LB) (produced in the furnace flame by burning liquid oil)	22	-6.6 to -14.3*	10^{-4} - ~ 10^{-2}	cold-stage	Popovicheva et al (2008) Kireeva et al (2009)
Furnace black (FB) (produced in the furnace flame by burning natural gas)	100	-5.4 to -10.9*§	10^{-5} - ~ 10^{-2}	cold-stage	"
Channel black (FW2) (obtained from gaseous hydrocarbons in the channel-type process)	420	-5.3 to -12.0*	10^{-5} - ~ 10^{-4}	cold-stage	"
Acetylene soot (AS)	86	-1.9 to -10.1*	10^{-5} - ~ 10^{-2}	cold-stage	"
Thermal soot (T-900) (obtained from pyrolysis of natural gas)	10	-8.2 to -14.7*	10^{-4} - ~ 10^{-3}	cold-stage	"
Aircraft engine combustor soot (AEC)	12.6	-7.1 to -15.0*§	10^{-4} - ~ 10^{-2}	cold-stage	"
Ethylene soot	NA	-11 to -24	LIA	cold stage	Wright et al (2013)

ǂ For this particular study, the mode of ice nucleation was not clearly defined.

* The baseline above which heterogeneous freezing was considered for these experiments is taken as -10 °C. Although the freezing temperatures range covered all the observed temperatures, only temperature values above -10 °C were used in the calculation of n_s.

§ Direct data on the freezing temperatures were not available. Therefore, the freezing temperatures were reconstructed from the available information on the assumption that the freezing temperatures were normally distributed. Information provided included median temperatures, standard deviation, and total number of droplets used in the experiments. The same method was applied to 'FW2' and 'T_900' soot data, and n_s values obtained were similar to the ones obtained from calculations using the original data that was supplied by the researchers.

In a recent soot study, Wright et al. (2013) studied the effect of cooling rate on the IN activity of ethylene soot in the immersion mode. The study observed that there is a weak dependence of cooling rate on the ice nucleating ability of the ethylene soot. This

was similar to what was observed by DeMott (1990) that changing the cooling rate did not alter the freezing temperatures of acetylene soot. Nonetheless, the data shown by Wright et al. (2013) could not be used to compare with the previous studies because no detailed information was provided on neither the soot concentration in their droplets nor the exact droplet sizes used.

2.5 Uncertainties associated with ice nucleation measurements of soot

There is variability in the ice nucleation behaviour of different soot types. This variation could be explained away either by the intrinsic ice nucleation properties of the different soot types or as a result of uncertainties associated with the ice nucleation measurements of soot. Obviously, these uncertainties could be passed on in the process of generating a unified soot parameterisation for use in an aerosol-cloud microphysics model.

Some of the factors that can affect the ice nucleation measurements of soot include:

(1) Variability in *soot sources or origin* - the nature of fuel from which the soot is generated can affect its ice nucleation properties (Dymarska et al., 2006; Gorbunov et al., 2001).

(2) *Combustion processes and conditions* – the ice nucleation properties of the various soot types discussed in section 2.4 were generated in different conditions, for example, low or high temperatures, a limited or an excess oxidant supply, varied oxidant to fuel ratio, different aerosol generators/burners, at different burner settings, and others. These differences may directly or indirectly affect their ice nucleation abilities (these factors are discussed in more detail in chapter 5).

(3) *Ice nucleation measurement conditions and instrumental set-ups* – these are other major sources of variability between the literature results discussed in section 2.4. Some studies were performed in a cloud chamber and some on different cold-stages. This could potentially affect the ice nucleation results due to experimental validation problems associated with some set-ups. In the cloud chamber such as Continuous Flow Diffusion Chamber (CFDC), the pressure and high relative humidity can limit the INP activity range that can be assessed. For example, CSU-CFDC results is corrected to a factor of 3 to measurements in a large cloud chamber such as Aerosol Interactions and Dynamics in the Atmosphere (AIDA) cloud chamber (DeMott et al., 2014),whereas in

the drop freezing assay all temperature range in mixed-phase cloud regime (0 to -37 °C)can be accessed. However, the temperature uncertainties between different cold stages may vary and all these need to be taken into consideration when comparing results ice nucleation results. CFDC can easily be deployed for field campaigns and ice nucleation can be activated at a particular temperature or regime. Also, it can be used in tandem with other instruments and it is more automated than a typical drop freezing assay set-up. These differences may contribute to the uncertainties associated with the ice nucleation quantification by soot in the literature.

2.6 Chapter summary

This chapter introduced the theory of ice nucleation and the various modes of ice nucleation – contact, deposition, condensation, and immersion. Classical nucleation framework was also highlighted alongside the different models adopted in describing the results from experimental ice nucleation by aerosol particles. A brief review of the ice nucleation studies by soot was discussed. The activity of some soot types could not be compared due to the limited information provided or the uncertainty in the method used in the studies. However, ice nucleation activities reported by DeMott (1990), Popovicheva et al. (2008a) and Kireeva et al. (2009) showed that there is a freezing temperature gap that needs to be filled in order to generate an efficient ice nucleation parameterisation by soot. This chapter concluded by highlighting the uncertainties associated with ice nucleation measurements of soot.

Chapter 3

Experimental methodology for ice nucleation studies

3.1 Introduction

This chapter discusses the experimental methodology used in this study for quantifying the ice nucleation behaviour of soot and combustion ash particles. It provides a detailed description of the freezing experiments and other analytical methods adopted for this study. The chapter concludes with a section on the data analyses approach used for the treatment of the various data sets obtained during the experiments.

Contributions to instrument development

The µL-NIPI instrumentation described in this chapter was developed mainly by Thomas Whale (A PhD student, School of Earth and Environment, University of Leeds, UK); with contributions from Murray, B. J., O'Sullivan, D., **Umo, N. S.**, Baustian, K. J., Atkinson, J. D., and Morris, G. J.: The concept, design and the full description of the instrument is currently written up as 'A technique for quantifying rare ice nucleation events' for publication in the 'Atmospheric Measurement Techniques Discussion' journal.

The pL-NIPI instrumentation was initially developed and set-up by Ben Murray research group at Leeds before 2010 (Murray et al., 2010a). Then, it was further developed and modified by Dr. James Atkinson to improve its temperature sensitivity (Atkinson, 2013). A prototype of the set-up was built by Dr. Daniel O'Sullivan; I developed this prototype further by making modifications to the washer used on the instrument's cold-stage and the optics to allow larger droplets (nanolitre range) to be studied. Details of the modifications that I did are discussed in section 3.3.3.1.

One of the homogeneous results shown in Figure 3.12 & 3.13 (ultra-pure water 3) was performed by Dr. Daniel O'Sullivan and it is included here with his permission.

3.2 Materials and samples preparation for the freezing experiments

This section reports the materials for the experiments and how the soot and ashes suspensions were prepared for the freezing experiments.

3.2.1 Ultra-pure water

For the purpose of establishing a baseline and for validating the two instrumental set-ups used in this study, ultra-pure water was used. The ultra-pure water (Type 1 Milli-Q water) was obtained from a Milli-Q Integral System (Millipore Water Purifier, USA) with the following properties: 18.2 MΩ.cm at 25 °C resistivity, TOC < 10 ppb, and filtered through a 0.22 µm. All suspensions of soot and ash particles were prepared with this water source and the water was collected from the Milli-Q Integral System dispenser just before use. All pre-cleaning procedures were also carried out with the same water source.

3.2.2 Solvents

Chloroform (anhydrous ≥ 99 %, containing 0.5 – 1.0 % ethanol stabiliser), methanol (chromasolv for HPLC ≥ 99.9 %), and silicon oil (CAS 63148-62-9) were all obtained from the Sigma-Aldrich Corporation.

3.2.3 Soot suspensions

A known amount of eugenol and n-decane soot particles was weighed in a glass vial using a Fisher Brand PS-60 digital weighing balance (uncertainty = ± 0.1 mg, max = 60 g, 4 d.p). The weighed soot particles were transferred into a glass volumetric flask by using glass funnel and stainless steel spatula to avoid the particles sticking on the walls of the transferring apparatus. The weighing containers were repeatedly rinsed with ultra-pure water to avoid losing the soot material. Then a known volume of ultra-pure water was added to the volumetric flask to make the suspension. The suspension was placed in an ultra-sonication bath for about 10 minutes to disperse the soot particles or fractals into individual particles. This method was used in previous studies to break soot aggregates and for a uniform dispersion of the particles (Samson et al., 1987; Rigg et al., 2013). Banús et al. (2009) reported that the process of sonication is an effective way of redistributing soot particles in a solvent but it is unclear if this process can denature the surface of the soot particles. This means that the structural morphology of the soot

surface can be altered which can influence its chemical and physical behaviour. The soot suspension was later stirred for a set-time - depending upon the experiment design – on a magnetic stirrer at about 1200 – 1500 rpm. This was done in order to obtain a uniform distribution of the soot particles in the suspension before freezing experiments were carried out. To obtain lower concentrations of the soot suspension such as 2.0 x 10^{-3} wt% and 2.0 x 10^{-4} wt%, a dilution principle was applied to the 0.1 wt% soot suspension in order to limit uncertainties that could be introduced by the weighing process. All dilutions were done with a calibrated Eppendorf® pipettes (10 µL, 100 µL, and 1000 µL).

3.2.4 Ash suspensions

Ash particles were size-segregated to ≤ 40 µm by using Endecotts test sieves and a sieve shaker (Endecotts M100, UK; ISO 9001 certified) as shown in Figure 3.1. Four 100 mm diameter test sieves (71 µm, 63 µm, 55 µm, 50 µm) were stacked before the 40 µm test sieve.

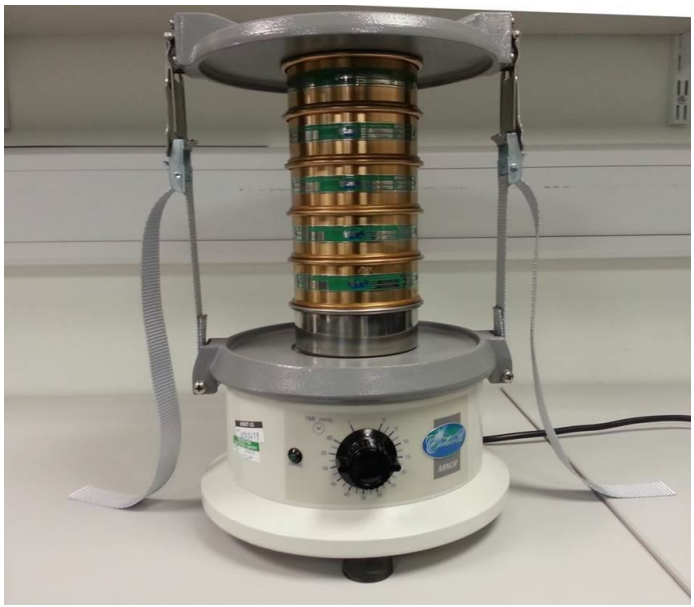

Figure 3.1: A set-up for sieving ash samples into ≤ 40 µm size. A sieve shaker - Endecotts M100, UK; ISO 9001 certified was used with a stack of test sieves - 100 mm diameter test sieves (71 µm, 63 µm, 55 µm, 50 µm, and 40 µm). The bottom sample collector is made up stainless steel; this limits the possibilities of contamination from the container.

The ash particles passed through the 40 µm test sieve with ease indicating that two dimensions of the particles were smaller than the mesh sizes, details of this process is described in section 4.4.1. However, it could be that the shapes of the ash particles were oriented to favour their passage through the mesh holes. The ash samples obtained were made into suspensions in a similar way as described in section 3.2.3.

3.2.5 Droplet generation

From the well-dispersed soot or ash suspension, various sizes of soot- or ash-containing droplets were generated onto a hydrophobic glass surface. The hydrophobic glass surface is made from a high purity glass finished with a siliconised surface (Hampton Research, USA). Two types of these siliconised glass circle cover slides (hereafter referred to as glass slide) were used – a 12 mm (HR3-277) and a 22 mm (HR3-231) - for experiments on microliter-Nucleation by Immersed Particles Instrument (µL-NIPI) and nanolitre-Nucleation by Immersed Particles Instrument (nL-NIPI) set-ups, respectively. The glass slide was used to support the droplets for freezing experiments because this surface allows the droplets to maintain a maximum contact angle, thereby reducing its surface wettability (Murray et al., 2010a). Other studies have reportedly used similar surfaces (Fornea et al., 2009; O'Sullivan et al., 2014).

All factory-supplied glass slides were pre-cleaned before use – first, with ultra-pure water to remove any possible water-soluble particles on the glass slide surface, then with HPLC grade methanol to remove other dirt not soluble in water but soluble in a mild organic solvent, and finally, with chloroform to remove all possible organic-soluble particles. The progressive use of ultra-pure water-methanol-chloroform was to create a solubility interface between the solvents to prevent solvent layering that could occur due to immiscibility of solvents. During the cleaning process, each of the solvents used was air-dried with an air-jet of a zero-grade compressed nitrogen gas, 99.998% (BOC gases, UK). The cleaning was done to ensure that glass slide surfaces are particles-free.

Droplets were generated onto the glass slide in two ways depending on the experimental set-up to be used. For a µL-NIPI, the required volumes (0.5 µL, 1.0 µL and 5.0 µL) of ultra-pure water, soot- or ash-containing droplets were placed directly onto a pre-cleaned glass slide (22 mm diameter) with the use of a Picus BIOHIT electronic automated pipette set (Satorius Ltd, UK); which has a volume delivery range of 0.2 µL - 10 µL with an increment of 0.02 µL and an inaccuracy (%) of 0.90, 1.00, and 2.50 for test volumes (µL) of 10, 5, and 1, respectively. The pipetting process was carried out as fast as possible to limit evaporation of the droplets by the preceding droplets (mass transfer effect). This could result in mass concentration variation for each droplet thereby introducing bias in the measurements. Details of experiments with the µL-NIPI are described in section 3.3.1.

In the case of experiments with a pL-NIPI or a nL-NIPI: the pre-cleaned glass slide was supported with a cleaned microscope slide and placed in a glass chamber ready for the nebulization of ultra-pure water, soot or ash dispersions on it. To produce ultra-pure water droplets, soot- or ash-containing droplets, a bespoke nebulizing set, fabricated from glass pipettes and a few pieces of Swagelok joints was used, as well as a commercially available concentric glass nebulizing set (Meinhard Nebulizer, TR-30-C1, USA). These nebulizers generated fine aerosol of water or suspensions (while stirring) into the glass chamber, which was maintained at approximately 100 % relative humidity with respect to water (RH_w) with humidified zero-grade nitrogen gas. The relative humidity was achieved by constantly passing nitrogen gas humidified with warm water to the glass chamber until water was left at the bottom of the chamber. This was continued until the nebulization process was over. The relative humidity was measured with a GE Optica Hygrometer (Model: OPA10AN100). These fine mists settled onto the pre-cleaned glass sides with varied droplet sizes as shown in Figure 3.2.

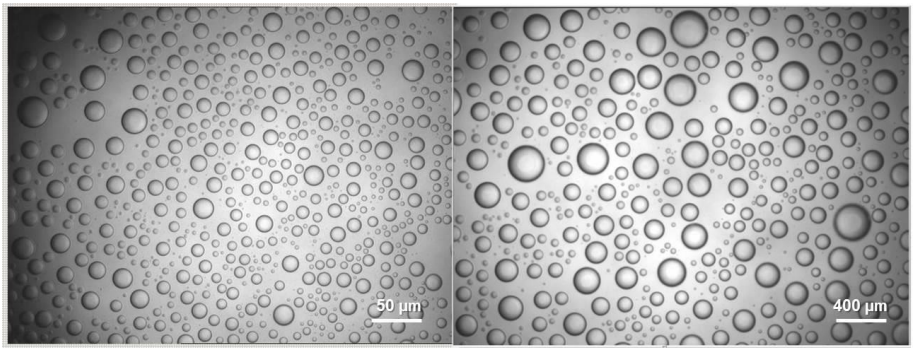

Figure 3.2: A distribution of droplets sizes formed by nebulizing ultra-pure water into a chamber maintained at ~ 100 % RH_w. The droplets were formed by deposition onto the hydrophobic glass slides and some droplets may grow bigger by a coalescence process.

For suspensions containing soot or ash particles, the droplets formed contained an equivalent mass to volume of particles depending on the concentration of the suspension as shown in Figure 3.3.

After making the droplets, silicon oil (CAS 63148-62-9) was immediately placed over the droplets array while in the chamber to prevent an evaporation (mass transfer), which could alter the mass concentration of the droplet (Murray et al., 2011). Care was taken to ensure that the silicon oil filled every available space to avoid air entrapment.

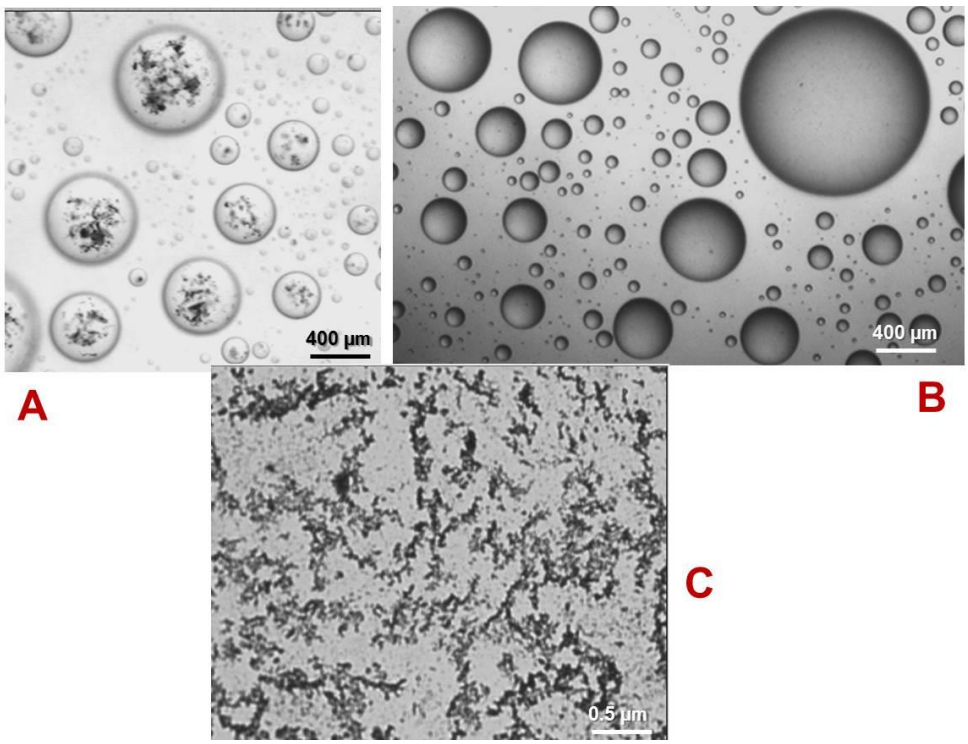

Figure 3.3: Droplets containing soot particles, which were generated with a nebulizing set in a humidified chamber. Panel (**A)** shows droplets formed from a suspension with a high concentration of soot particles, and panel (**B)** shows droplets obtained from a suspension with a lower soot concentration. When a droplet obtained from a suspension of high soot concentration is left to dry out, the soot particles in the droplets can settle on the glass slide as indicated in panel (**C)**. These images were taken for illustration purposes; the suspensions shown here were left for over 3 hours.

A schematic of the droplets covered with silicon oil is shown in Figure 3.4. The droplets sealed with the silicon oil were then introduced into pL-NIPI or nL-NIPI set-ups for freezing experiments as described in the sections following.

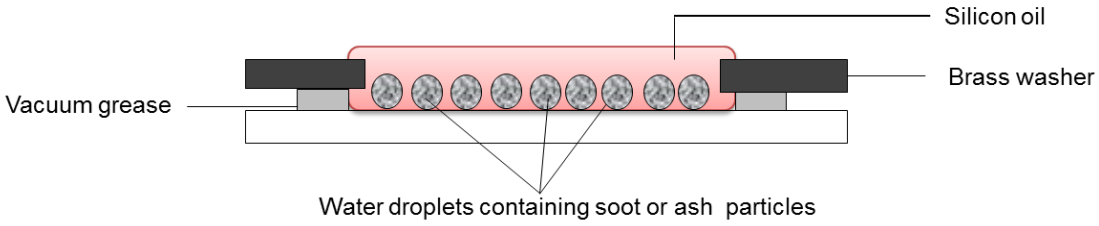

Figure 3.4: A schematic showing a cross-section of droplets distributed in silicon oil to prevent mass transfer before freezing experiments are performed on a ρL-NIPI or a nL-NIPI set-ups. High-vacuum grease obtained from Dow Corning ® Corporation, USA was used for the sealing.

3.3 Instrumental set-ups and freezing experiments

Drop freezing assay is a long established method and is widely applied in studying the ice nucleating abilities of particles in cloud conditions (Murray et al., 2011; Kireeva et al., 2009; Lüönd et al., 2010; Fornea et al., 2009; Murray et al., 2010a) and others. This

technique involves a simultaneous cooling of droplets of equal volumes - here, in cloud-relevant conditions, while the freezing temperatures are observed and recorded (Vali, 1971).

In this study, two major set-ups were used for drop freezing assay experiments. The two set-ups are generically called Nucleation by Immersed Particles Instrument (NIPI). NIPIs are further categorised based on a range of the volume of droplets that can be studied in them – a microlitre (µL-NIPI), a nanolitre (nL-NIPI), and a picolitre (pL-NIPI). The µL-NIPI is distinguished from the nL-NIPI and pL-NIPI set-ups. The sections following describe the differences and their experimental protocols.

3.3.1 Microlitre drop freezing instrument and experiments (µL-NIPI)

Microlitre drop freezing assay set-up (µL-NIPI) was developed to investigate droplet volume of ~ 10^{-6} L, and all the droplets were approximately the same volume. Although the volume can be adjusted depending on the experiment design, a uniform droplet volume was used for a particular experiment. The µL-NIPI set-up comprised a Stirling engine with a cold plate (cold-stage) at the top - a Grant-Asymptote EF600 instrument, a humidity-controlled cell made of Perspex, a CCD camera, and a gas flow meter as shown in the schematics in Figure 3.5. Real pictures of the set-up are shown in Appendix A1.

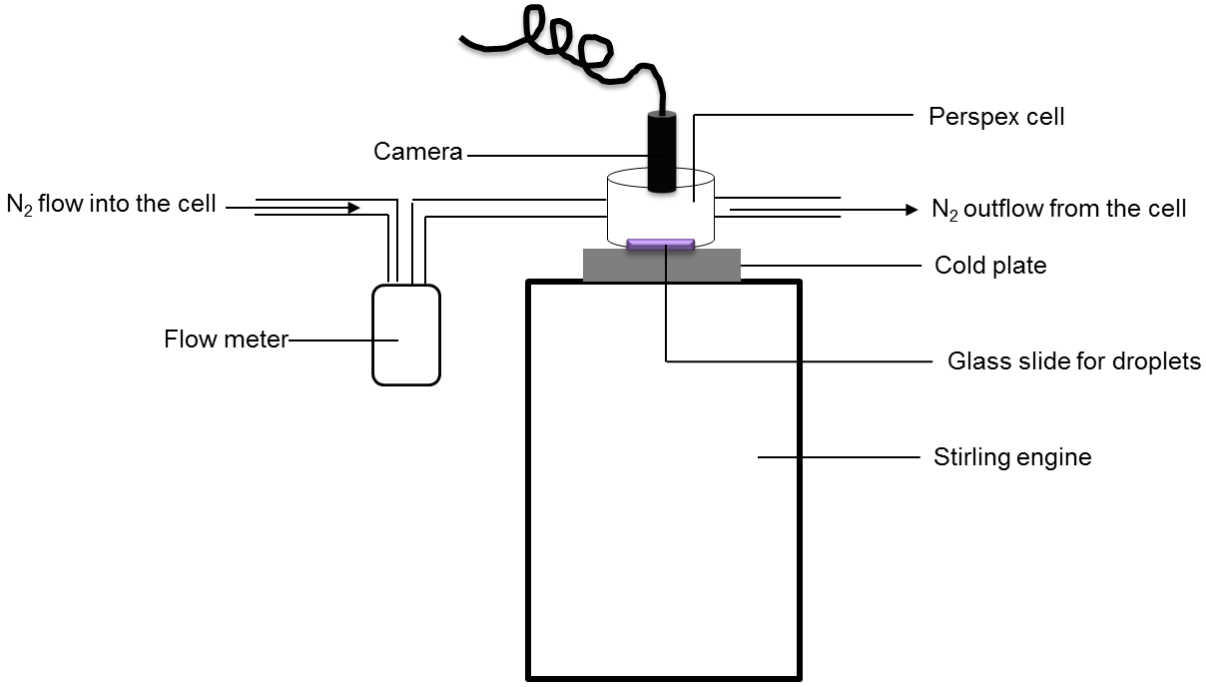

Figure 3.5: A schematic of a µL-NIPI set-up. The main Stirling engine is a Grant-Asymptote EF600® instrument. Other components were sourced and coupled for the purpose of the experiment. The camera is a CCD camera that was fed to a computer-controlled LabVIEW VI.

All the temperature and video data generated during the experiments were acquired with a built-in default *human embryo 1* program and LabVIEW VIs, respectively. For the freezing experiment, a pre-cleaned glass slide (22 mm diameter) was placed on the centre of the cold plate; droplets of a required suspension or ultra-pure water were printed, and then enclosed with a Perspex cell that was constantly flushed with a zero-grade nitrogen gas. The nitrogen flow prevented frost growth on the plate, which could set-off a freezing event when in contact with an independent droplet (see section 3.4 for details on experimental artefacts). A µL-NIPI set-up, as the name implies, has an advantage of allowing larger droplet sizes in the microlitre regime to be studied as illustrated in Figure 3.6C.

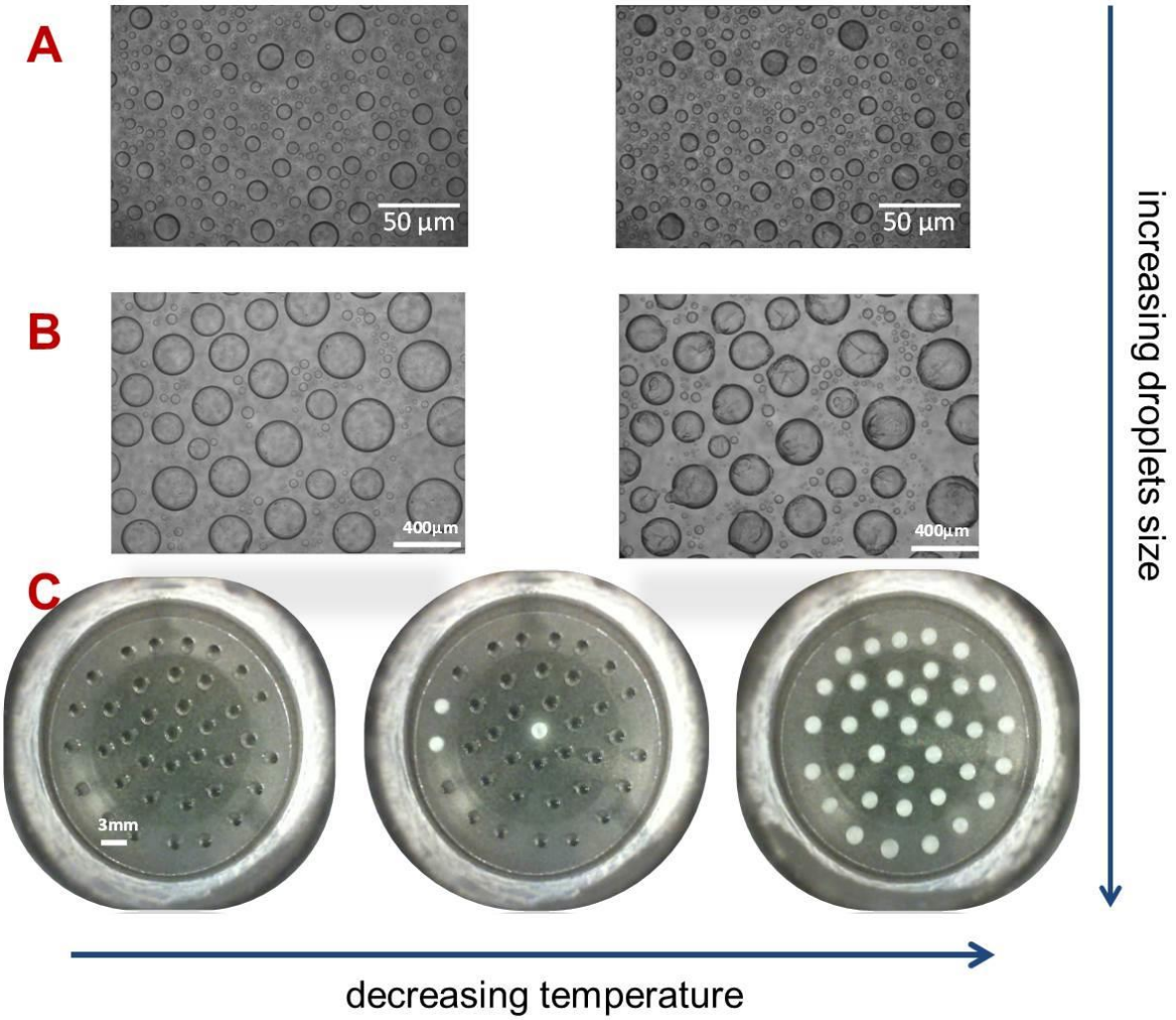

Figure 3.6: Images of different droplets sizes for NIPI drop freezing assay experiments. (**A**) represents a typical ρL-NIPI experiment (~ 10^{-12} L), (**B**) represents the nL-NIPI experiments (~ 10^{-9} L), while (**C**) is for a typical µL-NIPI experiments (~ 10^{-6} L). For (**A**) and (**B**), a darkening of a droplet or cracks indicates a freezing event whereas in (**C**) a change in the brightness of a droplet indicates a freezing event. During the experiment, time/temperature data are logged for further analyses.

For experiment on a µL-NIPI set-up, the Stirling engine was programmed such that freezing events from 20 °C to -35 °C at a cooling rate of 1 K min^{-1} could be monitored for all the experiments. The set-point and cold plate temperatures were automatically logged to correspond with the freezing events recorded with a static CCD camera as frame times. The CCD camera was attached to the Perspex cell (humidity-controlled cell) and sealed with high-vacuum grease. All experimental data acquired were later analysed as discussed in section 3.5 to obtain the freezing temperatures of the droplets and time.

Before carrying out experiments with soot- or ash-containing droplets, it was necessary to establish a baseline for the instrument/experiment. The freezing of ultra-pure water was used to check the performance and sensitivity of the µL-NIPI set-up, as well as to establish a baseline for the drop freezing experiment for this particular set-up. The baseline here is defined as the cut-off temperature that allows a distinction to be made between freezing caused by particles immersed in droplets and freezing that is due to ultra-pure water alone or the supporting surface (substrate). For each baseline test, ultra-pure water was obtained from a Milli-Q machine daily and used for the experiment. A summary of the fraction of droplets frozen for the ultra-pure water on the µL-NIPI is shown in Figure 3.7.

Droplets of ultra-pure water (~ 1.0 µL) froze within ~ 18 °C range, which is unusual for the freezing of ultra-pure water. This wide range of freezing temperatures could be due to a surface dependent nucleation mechanism. From the plot, it is shown that more than 90% of the droplets froze at temperatures below -23 °C. Following this observation, -23 °C was chosen as a reasonable baseline for the µL-NIPI set-up. The sporadic freezing events of droplets population observed above -23 °C could be due to impurities in the water or irregularities on the surface used for supporting the droplets. Further filtering of the water with a 0.02 µm did not improve the freezing curve which indicates that the sporadic freezing could be caused more by the irregularities on the surface. This could not be tested because of limited instrumentation.

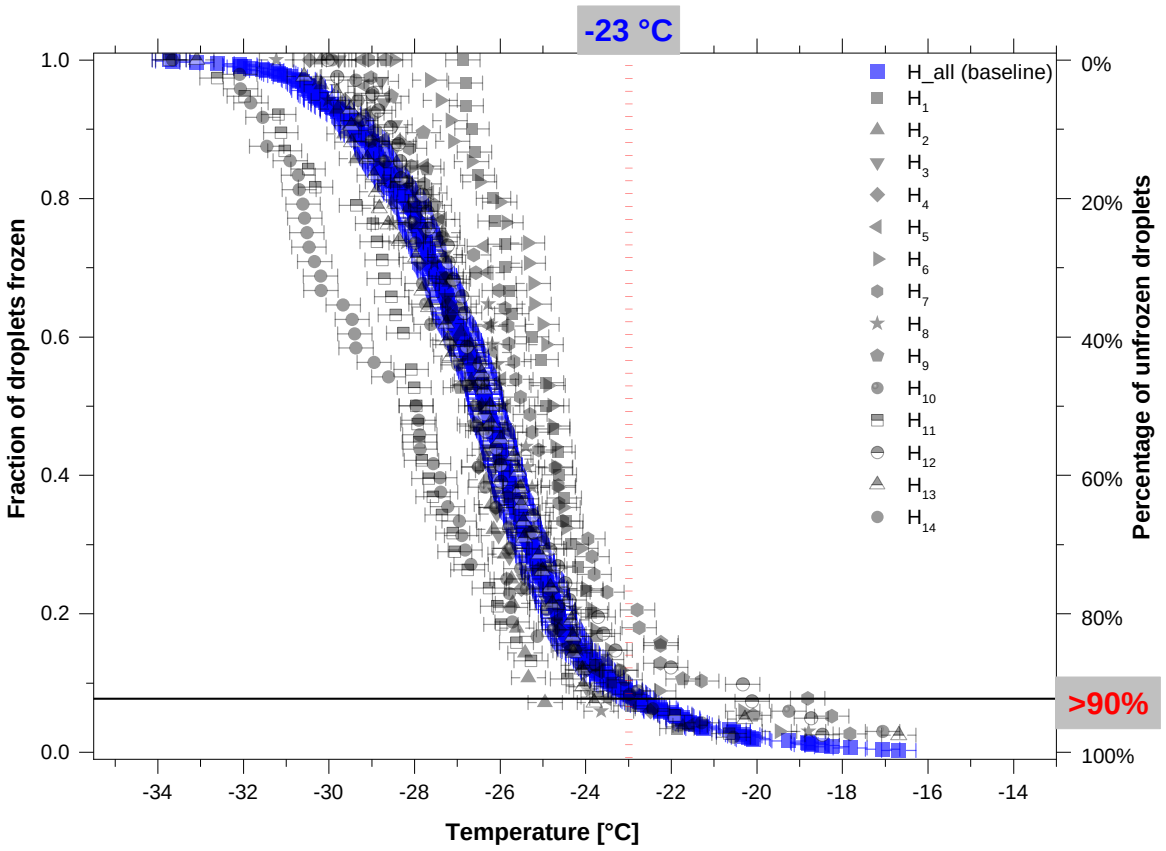

Figure 3.7: Fraction of frozen droplets of ultra-pure water (18.2 MΩ.cm resistivity @ 25 °C), and the percentage of unfrozen droplets used in establishing a freezing baseline or a threshold for the µL-NIPI experiment. The uncertainty in the temperature is quoted as ± 0.4 °C. The grey data points indicate fourteen (14) different experiments with ultra-pure water while the blue sigmodal fit is the cumulative fraction of all frozen droplets (~ 500 droplets). The vertical red dotted line indicates where the baseline is taken.

3.3.2 Effects of pipette tips on the freezing behaviour of droplets generated for µL-NIPI experiments

Firstly, an independent test was carried out to ensure that particles were not retained in the pipette tips used in printing the droplets. Two types of pipette tips were studied – normal pipette tips and a low retention pipette tips (certified RN_{ASE} /DN_{ASE} and pyrogen safe). A suspension of coal fly ash particles (0.1 wt%) was used in the study. The fraction of droplets frozen and the distribution of ice nucleation active sites for coal fly ash particles are shown in Figure 3.8 (main) and the inserted plot, respectively.

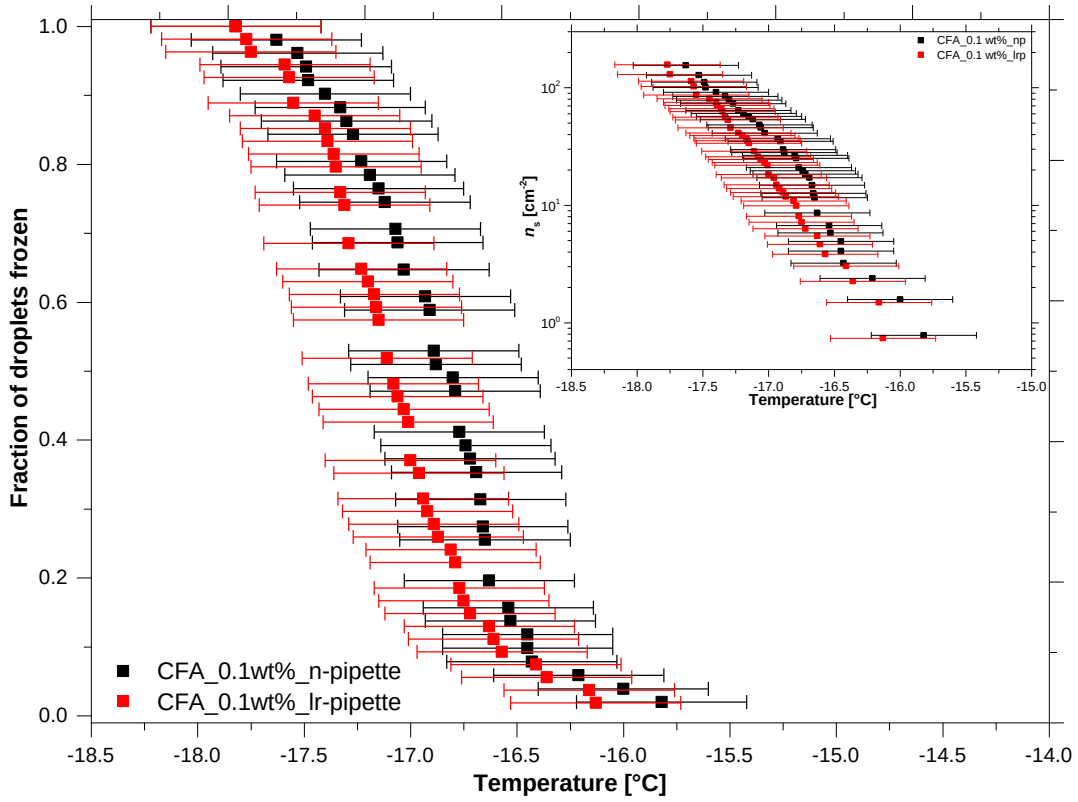

Figure 3.8: Fraction of droplets frozen and the distribution of ice nucleation active sites for 0.1 wt% suspension of coal fly ash particles. The normal pipette (n-pipette) and the low retention pipette (lr-pipette). The temperature uncertainty is ± 0.4 °C for both plots. The calculated error on the ordinate of the inserted figure is significantly small such that it is masked by the black and red data points.

The results indicate that within the temperature uncertainty of µL-NIPI experiments, no significant difference was observed between the two types of pipette tips. However, it seemed that the low retention pipette tips showed a lower freezing temperature range than the normal pipette tips but within the temperature uncertainty quoted ± 0.4 °C, they are the same. Settling effects by the same pipette was earlier tested and showed that it has insignificant effect on the experimental results obtained (O'Sullivan et al., 2013). In this study, normal pipette tips were used for all µL-NIPI experiments.

3.3.3 Nanolitre and picolitre drop freezing instruments and experiments (nL- and pL-NIPI)

As earlier mentioned, the naming of a NIPI set-up makes reference to the droplet volume that the instrument can be used to study. A nL-NIPI and a pL-NIPI are used for ~ 10^{-9} L and ~ 10^{-12} L droplets, respectively. However, in contrast to Vali (1971) definition of a drop assay technique, the array of droplet sizes varied from a few to 100s of microns radii solely because of the method used in generating the droplets (section

3.2.5). The variability in droplet sizes was taken into consideration during the analysis of the data as discussed in details in section 3.5.2. Both nL-NIPI and pL-NIPI were carried out on a cold-stage coupled to an optical microscope as previously described in Murray et al. (2010a). A schematic showing the various components of the nL-NIPI or pL-NIPI set-up is shown in Figure 3.9.

A brief overview of the set-up is given in the paragraph following; in addition, some modifications were made to it to accommodate experiments with soot particles as will be discussed in section 3.3.3.1.

Hydrophobic glass slide with the generated droplets and sealed with silicon oil, as illustrated in Figure 3.4, was placed on the cold-stage. The cold-stage is made of an aluminium block and a set of hollow copper wire embedded in the aluminium block for pumping liquid nitrogen through the block as shown in the pictures (see Figure 3.10).

The stage was cooled by pumping the liquid nitrogen around the aluminium block. A set of heaters (2 x 35 W) controlled by a Eurotherm (Eurotherm 2416) were fitted into the aluminium block to maintain the temperature at a set ramp rate or a fixed temperature. Two Platinum Resistance Thermometers (PRT) probes (resistance 100 Ω) were fitted into the aluminium block with thermal grease for temperature measurements during the experiments.

Before the droplets were placed on the cold stage, the stage was cooled and maintained at ~ 8 ^{o}C to avoid frost or condensation on the diamond chip which was placed on the cold stage to limit the effect of temperature gradient across the glass slide with droplets during the cooling process. Temperature of the droplets were monitored with the PRT probes, and the uncertainty is ± 0.2 K (Atkinson et al., 2013).

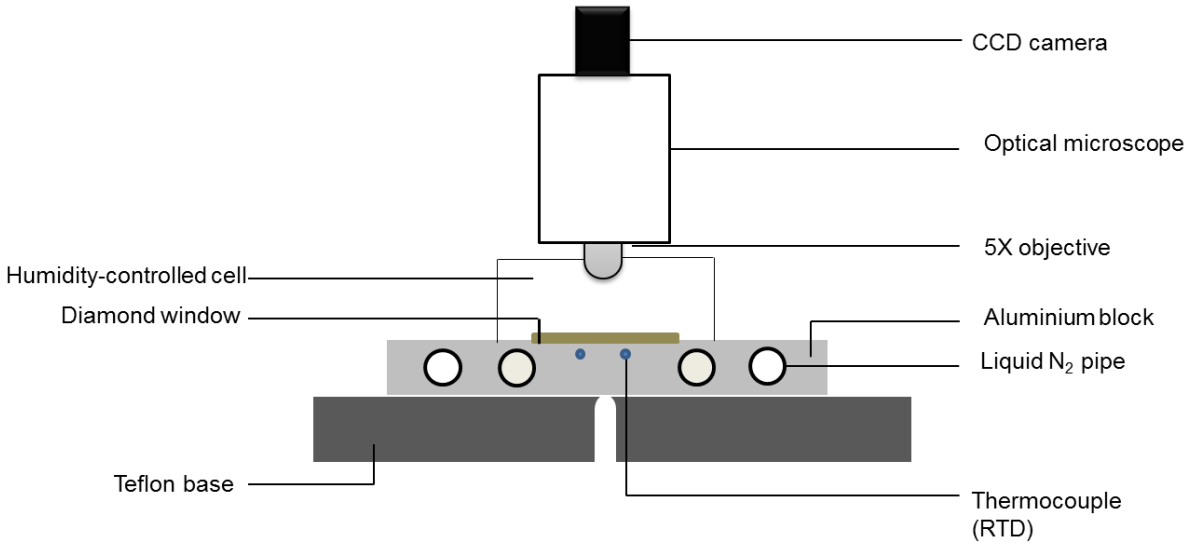

Figure 3.9: A cold-stage coupled to an optical microscope (Olympus BX53), with a 5X objective (Olympus 5X/0.25, ∞/-/FN22 – U-CMAD3, Japan) for soot and ash freezing experiments in the immersion mode. The 5X optical lens was coupled to a BSDC67OU 0.67x direct C-mount adapter (Best Scientific, UK) for a 2/3'' chip camera giving a larger field of view (FoV - 11mm diagonal) for the nL-NIPI experiments. This schematic was adapted and modified from Murray et al. (2010a).

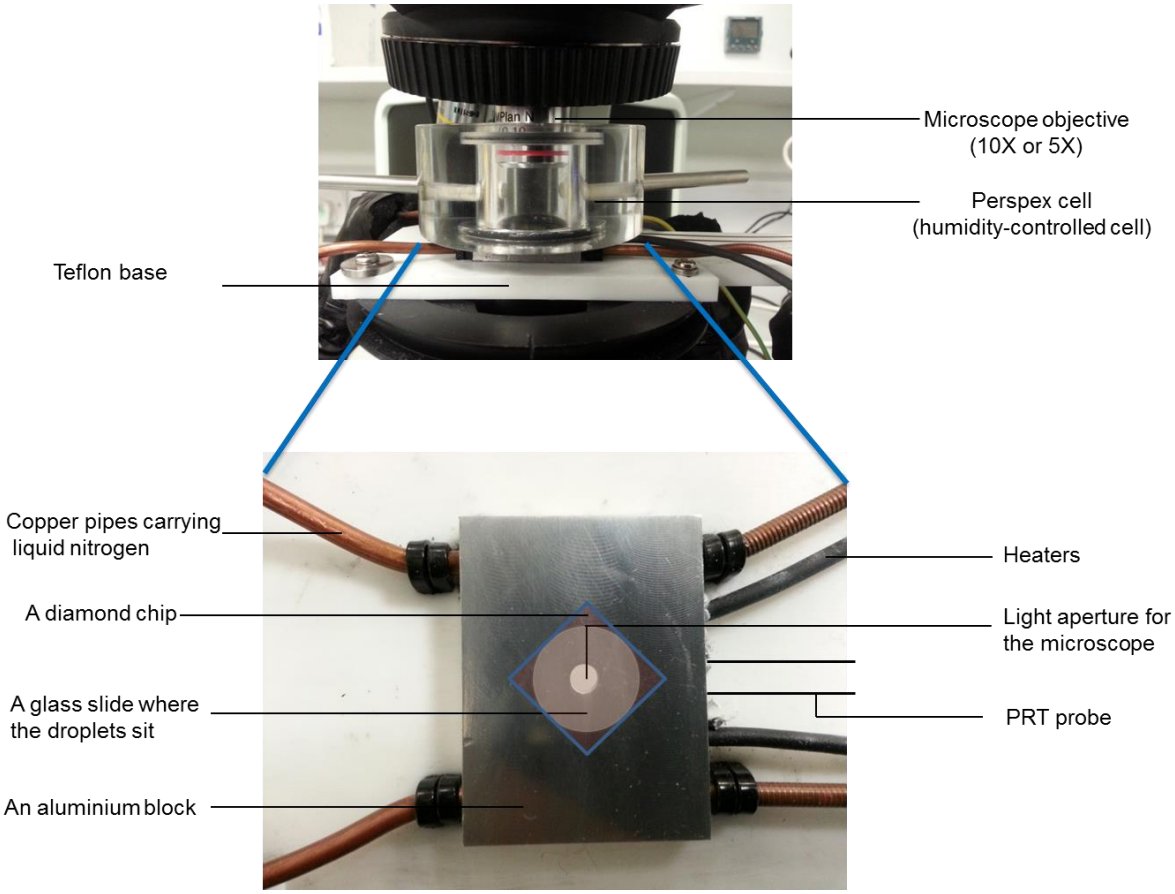

Figure 3.10: Various parts of the cold stage coupled to an optical microscope (Olympus BX53) for nL- or ρL-NIPI experiments. The picture is not scaled to the actual size.

All temperature readings were logged using a temperature-control system (Eurotherm 2416) and a temperature logger - 1524 Reference thermometer (RS 232, 12 V DC from Fluke Hart Scientific USA). The entire temperature, time and video settings were controlled by a customized National Instrument (NI) LabVIEW software. The LabVIEW VI allowed the cooling rate (or ramp rate in K min^{-1}) to be changed depending on the experiment design. Videos of the droplet freezing events were also recorded with NI LabVIEW VIs via a 2/3'' chip camera connected to a 5X objective. After the freezing process, videos were analysed to obtain the time of the freezing events with their corresponding temperatures as described in section 3.5.

3.3.3.1 Modifications to the cold-stage for nanolitre drop freezing experiments

In the initial experiments with soot, only a few droplets nucleated ice and these were mainly droplets in the nanolitre scale. The results from the initial experiments suggested that soot could possess rare nucleation sites that can be detected with larger droplets. However, the challenge was to design an experiment in such a way that more of these nanolitre droplets could be accommodated in a statistically significant numbers. To do this, the instrumentation needed to be modified to suit the purpose of the experiment. The cold-stage was initially designed to look at the picolitre (pL) volume droplets but this was limited because it could not allow access to rare ice nucleation sites that can be accessed with a larger particle surface area such as soot particles. To resolve this issue, I took up the responsibility of modifying the existing set-up and to validate the modified instrumentation for use in freezing experiments. Three major changes were made that aimed at obtaining a larger field of view (FoV); this means many larger micron-sized droplets could be viewed in a particular experiment. These major changes were:

(1) The aperture in the aluminium block was expanded from 1.5 mm to 3.2 mm to allow more light through the condenser of the microscope.

(2) The first modification automatically called for a modification to the brass washer. The brass plate served as a good temperature conductor for the stage and was used mainly for the sealing of the glass slides, droplets and the silicon oil. Therefore, the aperture of the brass washer was expanded from 1.94 mm to 3.15 mm, as shown in Figure 3.11.

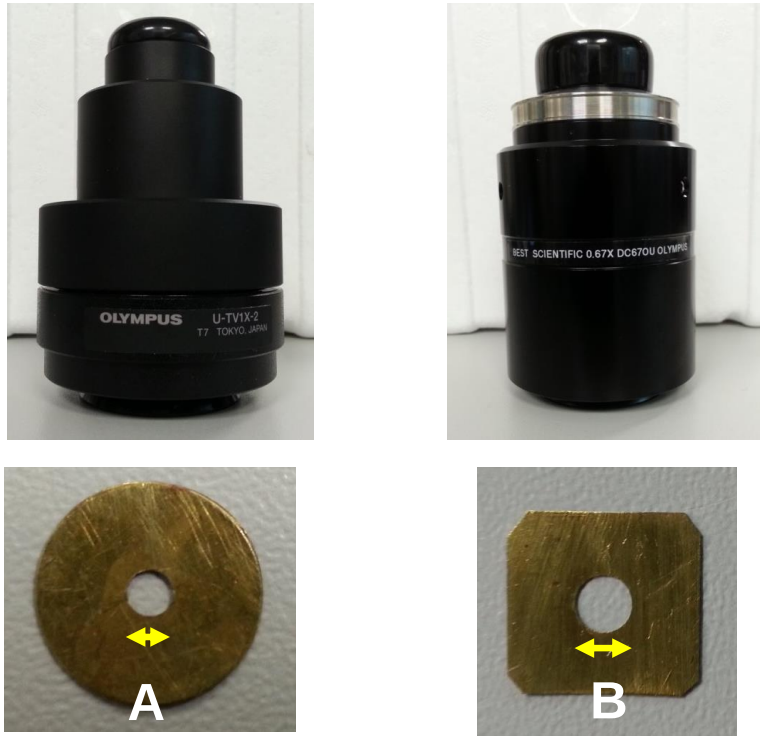

Figure 3.11: C-mounts and brass washer combinations used for pL-NIPI (**A**) and nL-NIPI (**B**) experiments. The yellow arrow shows the modification that was done to the brass washer based on calculations to obtain a larger field of view.

(3) To obtain a larger field of view, a set of combination of a C-mount adapter of the optical microscope and an objective lens need to result in a wider field of view (FoV) to accommodate the planned sizes of droplets for the experiment. After series of calculations and tests of different objectives/adapter, I came up with an accurate combination that was suitable for the experiment. Hence, the previous C-mount adapter (Olympus U-TV1X-2, Japan) was replaced with a BSDC67OU 0.67x direct (Best Scientific, UK) that enabled the 2/3'' chip camera (KP-MIAP) to cover a wider FoV, about 11 mm diagonal length (see Figure 3.11). In addition, a 5X Olympus objective lens (5X / 0.10 ∞ / - / FN22 Mplan N) was used with the new C-mount adapter to accommodate more droplets per FoV. These changes increased the sensitivity and allowed measurement of smaller values of IN active sites on particles.

3.3.3.2 Validation of the modified nL-NIPI set-up by homogeneous experiments

As previously discussed for µL-NIPI set-up, a quality control experiment was performed to validate the set-up. Previously, homogeneous experiments had been reported for the pL-NIPI set-up and re-checked before ice nucleation studies (Murray et

al., 2010a; Murray et al., 2011; Broadley et al., 2012; Atkinson et al., 2013). After the set-up was modified about five homogeneous experiments have been performed to validate the nL-NIPI. Three of these experiments were performed in the range of droplets sizes of ~ 30 µm to 260 µm, which are shown in Figure 3.12. The other two experiments were performed with smaller droplets in the picolitre range (Dr. Daniel O'Sullivan, unpublished results). For this study, freezing of ultra-pure water was carried out in the range of droplets sizes chosen for the soot or ash particles ice nucleation studies. The fractions of droplets frozen curves are shown in Figure 3.12.

The plot shows that more than 97 % of the droplets froze between -35 °C and –38 °C. The few sporadic freezing events observed for the three runs could be caused by surface irregularities or impurities in the water. It is not entirely clear what causes these sporadic freezing events at higher temperatures.

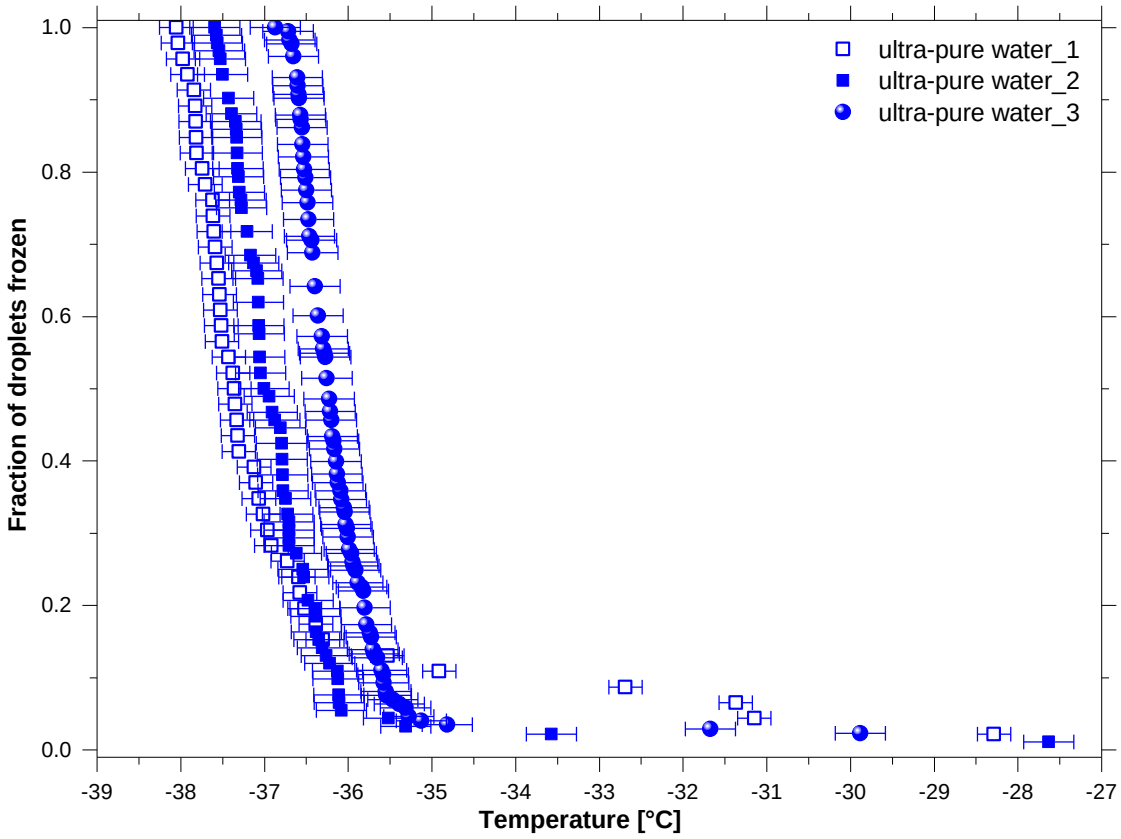

Figure 3.12: Homogeneous freezing of ultra-pure water using a cold-stage coupled to an optical microscope for nL-NIPI. The temperature uncertainty is ± 0.2 °C for ultra-pure water 1, and ± 0.3 °C for ultra-pure water 2 & 3 results following a recent calibration of the PRT probes. The filled square data points were obtained at a ramp rate of 5 K min^{-1}, the open square data points were obtained at 1 K min^{-1} while the filled circle data points were obtained at 10 K min^{-1}.

To compare the data obtained here with some homogeneous data in the literature, the nucleation rate which represents the formation rate of the critical ice nucleus of water molecules for ice to form was calculated from equation 3.1:

$$n_i = n(1 - \exp(-J_{hom}Vt)) \quad (3.1)$$

where n_i is the number of droplets that froze homogeneously, and n is the total number of droplets at t = 0, V is the volume the droplets at time (t). Results from similar calculation had been reported by other researchers. e.g. (Murray et al., 2010a; Benz et al., 2005; Pruppacher, 1995; Riechers et al., 2013). The nucleation rates due to homogeneous ice formation by the ultra-pure water (J_{hom} values) are presented in Figure 3.13.

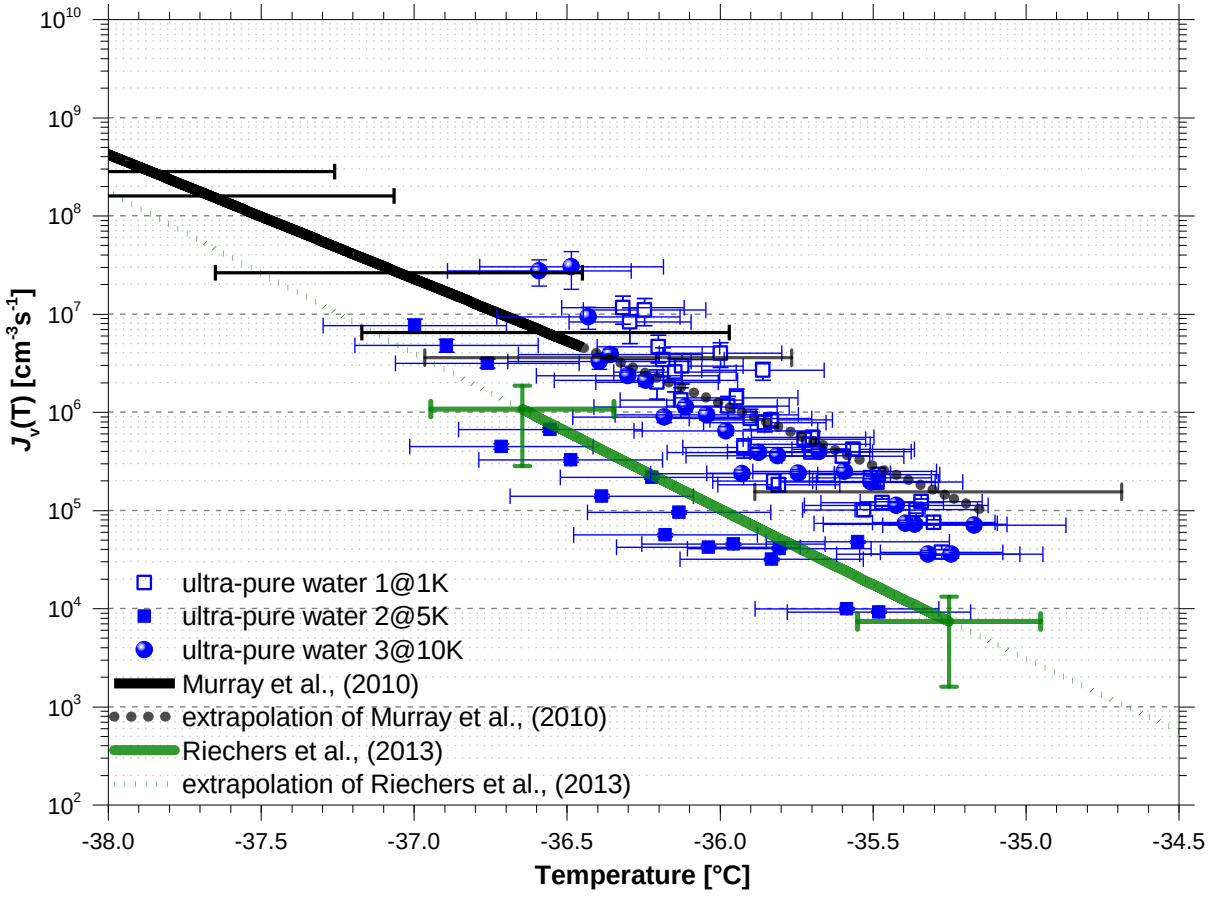

Figure 3.13: Nucleation rates J_{hom} (cm^{-3} s^{-1}) of ultra-pure water obtained from nL-NIPI. The nucleation rate was calculated from a volume-dependent homogeneous ice nucleation equation 3.1. The green and black lines show fits to nucleation rates data reported by Riechers et al. (2013) and Murray et al. (2010a), respectively, while the corresponding green and black dotted lines are extrapolation of the nucleation rate fits. The open square cells data points were obtained at 1 K min^{-1}, the filled square cells were obtained at 5 K min^{-1}, while the filled circle data points represent 10 K min^{-1} experiment (performed by Dr. Daniel O'Sullivan). The uncertainty in temperature is quoted as ± 0.2 °C.

The J_{hom} values (cm^{-3} s^{-1}) obtained from experiments at 1 K min^{-1} and 10 K min^{-1} show agreement with Murray et al. (2010a) homogeneous line while the 5 K min^{-1} was closer

to the Riechers et al. (2013) fit. The fits to the three experimental results followed similar gradient. However, there seem to be a temperature off-set of about ~0.3 K between the 5 K min^{-1} and 1 or 10 K min^{-1}. This temperature off-set which caused the variation may be due to slight variation observed in the droplet sizes distribution and a noise in temperature readings. Temperature uncertainty can have a significant effect on the homogeneous nucleation rate (Riechers et al., 2013). The two fits were chosen because Murray et al. (2010a) which reported a temperature uncertainty of ~ 0.6 K (as shown in Figure 3.13), performed their experiment with the same basic set-up although some modifications have been made to it. And Riechers et al. (2013) which temperature uncertainty was quoted as ± 0.3 K was chosen because detailed temperature calibration and uncertainty analyses were reported in their work. The experimental results showed in Figure 3.13 were well within the temperature uncertainty quoted for both Murray et al. (2010a) and Riechers et al. (2013) homogeneous fits. In summary, the results show that homogeneous freezing of ultra-pure water is observed on the nL-NIPI cold-stage for droplet sizes of 10s to a few 100s of microns radii. This result established a good quality control for the soot and ash ice nucleation study using the same set-up.

3.4 Artefacts associated with µL-NIPI, nL-NIPI, and pL-NIPI experiments

Experimental artefacts and uncertainties are common problems in most laboratory measurements; and, an experimental procedure is always aimed at keeping the possible error sources as minimal as possible (Brereton, 2003). For the freezing experiments described in sections 3.3.1 and 3.3.3, some experimental artefacts were observed and the knowledge gained enabled the experimental methods to be optimized to ensure accurate results. Some artefacts observed during the µL-NIPI, nL-NIPI and pL-NIPI experiments are highlighted below:

(1) µL-NIPI set-up: A humidity-controlled cell was used to limit the effect of mass transfer by the droplets (i.e. evaporation of droplets). In order to achieve, nitrogen gas was flushed through the cell constantly during the experiment. The flow rate of nitrogen gas that was passed through the humidity-controlled cell was optimized to ~ 1.8 x 10^{-3} lpm. This was measured with a Gilibrator 2 flow meter (Sensidyne, USA). A flow rate that is non-optimal could cause evaporation of the droplets, around the area directly in the path of the flow or where the flow directed towards as shown in Figure 3.14A. However, if the nitrogen flow is not sufficient to create and maintain the required balance in the

humidity-controlled cell, it can result in a frost formation or condensation on or around the droplets (see Figure 3.14B).

This frost formation could trigger the freezing of nearby droplets, thereby setting-off a freezing chain. This will ultimately lead to incorrect measurement of the actual freezing temperatures. The flow rate optimisation can depend on some external factors such as the dew point of the experimental conditions as well as the general arrangement of the flow tubes to the humidity-controlled cell.

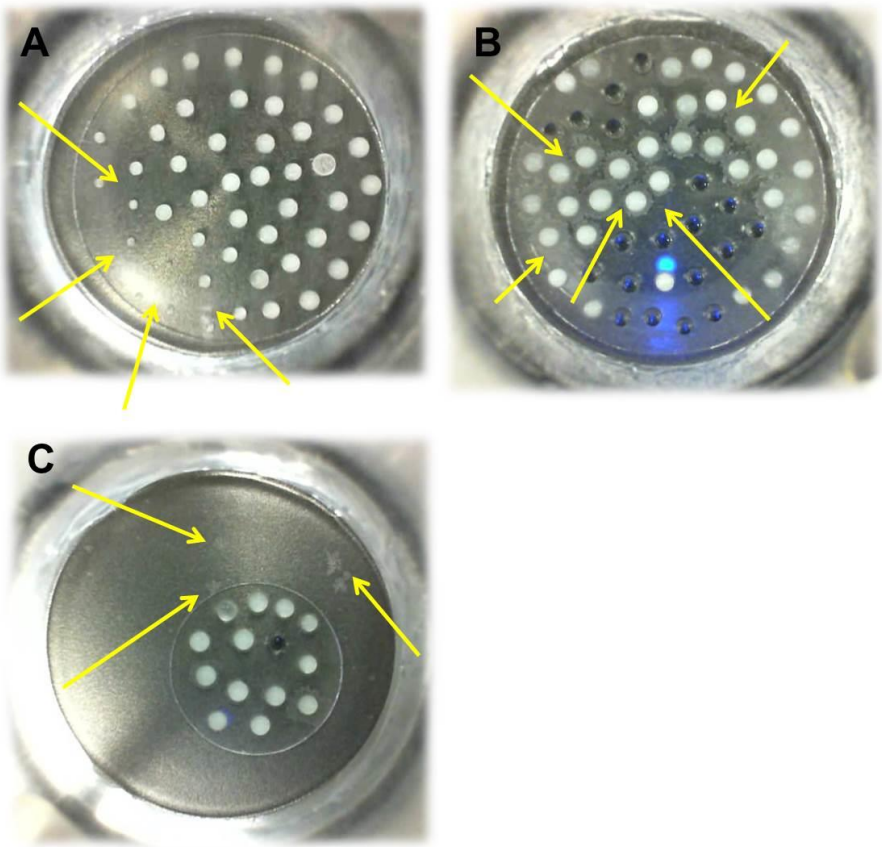

Figure 3.14: Some experimental artefacts associated with the µL-NIPI setup for drop freezing assay experiments. These artefacts can range from droplets evaporation (**A**), condensation and frost growth around the droplets (**B**), and frost formation on the cold plate (**C**).

Another effect observed was a frost formation on the cold plate as shown in Figure 3.14**C**. This happens as a result of deposition nucleation on the cold plate which may have formed from saturation vapour in the humidity-controlled cell.

(2) In nL-NIPI or pL-NIPI set-up, two common artefacts were associated with these experiments - condensation and trapping of air bubbles. Sometimes, condensation was observed in the silicon oil when humidified air was trapped within the layers of the oil during the sealing process. A picture of this

phenomenon is shown on the top panels of Figure 3.15. During nL-NIPI or pL-NIPI experiments, this artefact should be avoided although it is unclear what sort of effect this may have on the freezing process.

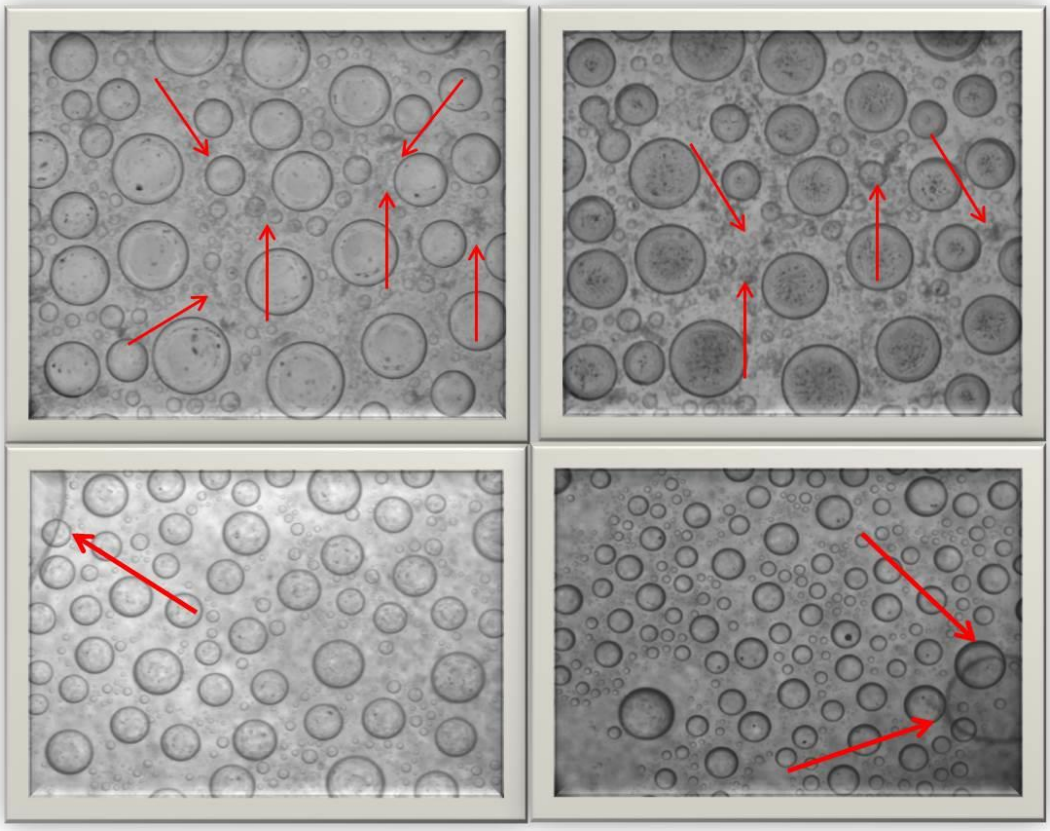

Figure 3.15: Images showing condensation and bubble trapping during nL-NIPI or pL-NIPI freezing experiments. The two top panels show the condensation effect which looks like a dark spot in between droplets, while the two bottom panels show air bubble trapped in the silicon oil used in sealing the droplets array.

Another experimental artefact associated with the nL-NIPI or pL-NIPI experiments was a case whereby air bubble is trapped in the silicon oil as shown in the bottom panels of Figure 3.15. During the freezing process if bubbles moves and disturb the droplets this can set-off a freezing event that could introduce bias into the results.

All possible experimental artefacts observed here were avoided throughout the experiments.

3.5 Data analyses

This section highlights the major steps taken in the processing of data obtained from the freezing experiments that are described in sections 3.3.1 and 3.3.3. Only significant parts of the calculations are mentioned.

3.5.1 Video analyses

All video recordings that have the freezing events and their corresponding temperatures were analysed manually. The video was replayed on a computer screen and the sizes of the droplets were measured by a pre-calibrated 30 cm ruler. The computer screen was calibrated against an equivalent size of a 0.01 mm length micrometre by generating a micrometre to screen size ratio (see Figure 3.16). This was done for each combination of the optics and all video analyses.

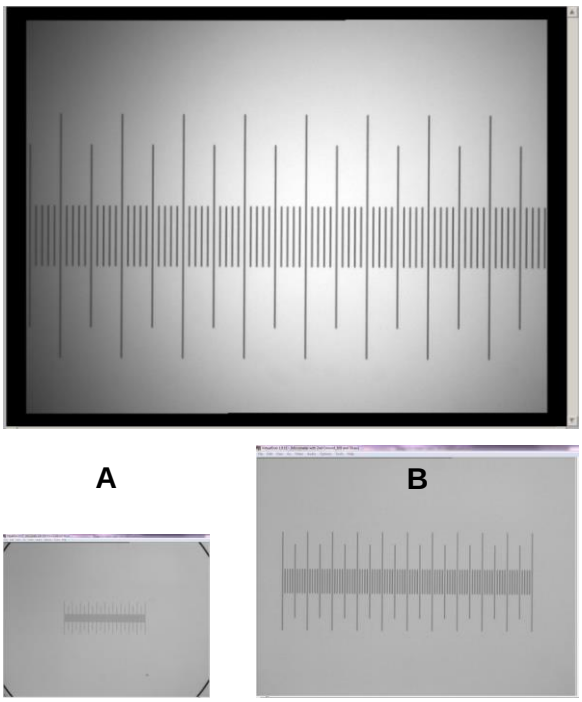

Figure 3.16: A 0.01 mm micrometre length to computer screen size at 150% zoom for both nL-NIPI (A) and pL-NIPI experiments (B). Images not scaled to size.

The size of the droplets were converted to the actual size and used for further data processing. For each droplet both the size measurement and the frame times were recorded. The frame times were later matched with data from both the 1524 Reference thermometer and the Eurotherm 2416 to derive the time and the freezing temperatures that the events occurred. Similar approach had been previously used for data reported in (Atkinson et al., 2013; O'Sullivan et al., 2014; Broadley et al., 2012).

3.5.2 Data processing

After the freezing experiments and acquisition of data, processing the acquired data was a priority. The steps taken in processing the data are summarised below:

a. All temperature, time, and video data that were automatically logged during the experiments were acquired and all necessary corrections were made to the computer time and temperatures (based on the temperature calibration).

b. Calculation of the droplets volume used: For droplets used in the µL-NIPI experiment, the droplets volume were uniform (1.00 ± 0.03 µL); therefore, the same volume was used in the data analyses. In contrast, the droplet sizes generated for both nL-NIPI and pL-NIPI freezing experiments varied from 10's to 100's µm diameter. In addition to the varied droplets sizes, the droplets sit on a glass slide which gives it a contact angle of about 100°. Therefore, to obtain the volume of the droplets, an indirect approach was used to calculate the volume of a spherical cap as illustrated in Figure 3.17. This is not the exact volume but a best estimate for the volume assuming there is no further distortion. In Figure 3.17, the part below the hydrophobic surface is to show how the height (h) is obtained by assuming '2r' is equivalent to 'h' or it is a bit less by 'a'.

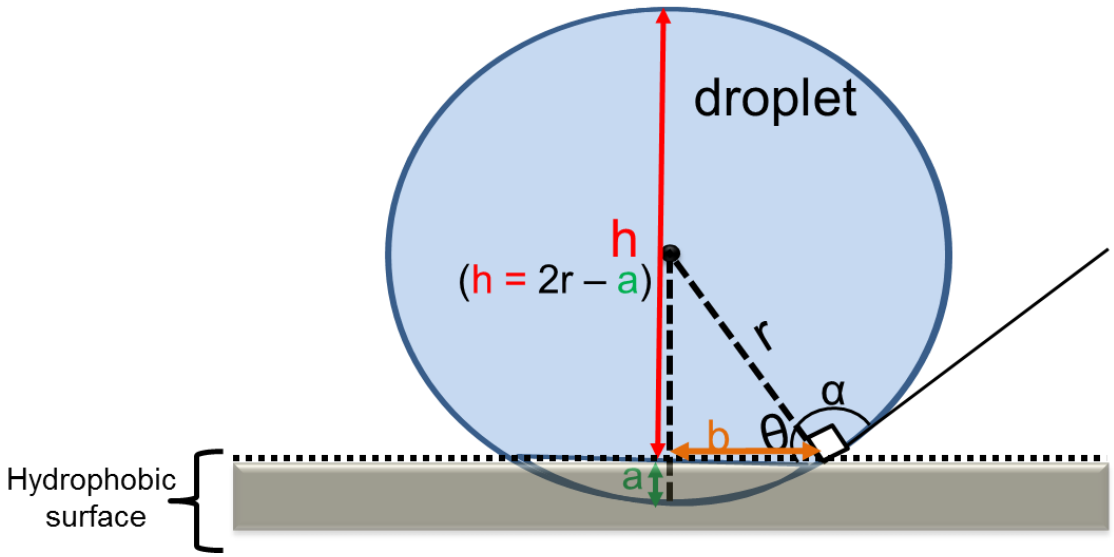

Figure 3.17: Schematic of droplets on hydrophobic surface similar to what is obtained after nebulizing droplets onto a clean glass slide for µL – or nL-NIPI experiments. The illustrations show how the volume of the spherical cap is used in calculating the volume of the droplets when the contact angle and the radius are known.

The volume of the droplets was calculated from the formula of a spherical cap as represented in equation 3.2 (Harris and Stöcker, 1998):

$$V = \frac{\pi h^2}{3}(3r - h) \tag{3.2}$$

Where V is the volume of the spherical cap (shaded blue), h is the height of the spherical cap and r is the radius of the sphere. Using the Pythagorean Theorem, the volume can be expressed as a function of a radius of the sphere and the contact angle with the normal of the sphere as shown in equation 3.3:

$$V = \frac{\pi r^3}{3}(2 + 3\sin\theta - \sin^3\theta) \tag{3.3}$$

Where V is the volume of the droplet, r is the radius of the droplets measured from the video analysis (section 3.5.1) and θ is the contact angle of the droplets with the hydrophobic surface which in this case is the glass slide. The basic assumption here is that there is no evaporation of droplets sealed with the silicon oil. Due to the wide range of droplets sizes used for the experiment, droplets were put in designated bins with less bias and treated together in order to obtain a symmetric value for further calculations.

Aside the method of size-binning the droplets, another method was adopted if droplets size distribution was highly skewed called 'rolling averaging'. In rolling averaging method, the rolled-over average of the droplet volumes was used in lieu of the median volume used in the binning method. This approach prevented the bias that could have been introduced by median volume in the data analyses.

c. Fraction of droplets frozen: From the video analysis, the total number of droplets at time t = 0 and also the freezing events with their corresponding temperatures were obtained. The fraction of droplets frozen (f_{ice}) per nucleation event were calculated by the equation represented in equation 3.3 (Murray et al., 2011):

$$f_{\text{ice}} = \frac{N(\text{T})}{N_{\text{o}}} \tag{3.3}$$

Where N (T) is the number of droplets frozen at temperature T, and N_{o} is the initial number of liquid droplets at t = 0 of the experiment.

d. The nucleation rate: For each experiment, the homogeneous nucleation rate coefficient or the nucleation rate coefficient of the nucleation species (soot and

ashes) were calculated by solving the nucleation rate equation (equation 2.11) within the experimental boundaries of the initial time, $t = t_1 = 0$, $n = N_o = N_1$ and at $t = t_2$, $n = N_2$. For homogeneous equation, the equation is shown earlier in equation 2.10 and 3.1, while heterogeneous nucleation rate equation is represented in equation 2.11.

e. Lastly, the nucleation sites density (n_s) following the ice nucleation singular model approach was calculated from equation 2.12. For the n_s calculations, the surface area was obtained from the BET measurements (section 4.3.3). Uncertainty analyses were also performed by propagating the error through the calculations using the uncertainty values quoted for each measurement. The error bars are shown in the results plots except in a case whereby the error bar is too small to be visible, for example in micro-litre experiments.

3.6 Chapter summary

This chapter presented the ice nucleation experimental approach adopted in the study of the ice nucleating efficiencies of soot and ash particles. The baseline temperature for heterogeneous freezing for all µL-NIPI experiments was taken as -23 °C, below this temperature means that the freezing is influenced by the background freezing (freezing of pure water). This was determined following a series of experiments performed with ultra-pure water. Although, the pL-NIPI set-up was modified to accommodate experiments in the nanolitre scale (nL-NIPI), homogeneous freezing of pure water was observed, which their nucleation rates showed an agreement with earlier studies by Murray et al. (2010a), and Riechers et al. (2013) within the temperature uncertainties quoted. Most of the experiments performed were repeated to ensure reproducibility (precision). All results obtained from the ice nucleation study of soot and ash particles are presented in chapters 5 and 6, respectively.

Chapter 4

Generation and characterisation of soot and ash particles

4.1 Introduction

Soot and ash particles used for the ice nucleation study in this project were generated or obtained from a controlled and a well-defined system. This chapter deals with the generation of these soot and ash particles, their proposed mechanism of formation, and the results from the characterisation of their physical and chemical properties. The method with which these particles were produced or obtained allowed a certain degree of confidence on the source, conditions, and compositional analyses of these particles before any ice nucleation experiments were carried out. The information acquired from this investigation will be useful later in this study, in discussing the ice nucleation behaviour of these particles.

The x-ray powder diffractometer machine was operated by Dr. Tamsin Malkin, who also took the x-ray diffraction patterns for the combustion ashes. I assisted in identifying the possible mineral compositions in the combustion ashes. The soot TEM images were taken by the Research Group of Professor Alan Williams and Professor Jenny Jones.

4.2 Soot and combustion ash aerosols

Combustion of materials releases soot, VOCs, ashes, tars, and other substances as mentioned in Chapter 1. These by-products are released into the atmosphere via different routes depending on their formation mechanisms and the way they are generated. The following sub-sections give an overview of the possible formation mechanisms of soot and ashes, and how the samples used in this study were generated.

4.2.1 Formation mechanisms of soot and ashes during combustion

Aerosol particles can get into the atmosphere via different pathways and mechanisms, which can be either natural or anthropogenic. For example, mineral dust is known to get

into the atmosphere mostly by convection systems e.g. dust storms (Sassen et al., 2003) or during agricultural practices such as tilling, (Tegen and Fung, 1995). In most combustion processes, soot and ash particles form a major part of the combustion aerosol particles mass (Williams et al., 2012); and they can be injected directly into the atmosphere during biomass burning or during an industrial process e.g. power plants that utilize coal or biomass fuel.

Soot formation arises from an incomplete combustion of materials whereas ashes ('fly ash' and 'bottom ash', a definition of both types of ashes is given in 4.2.2) are emitted either during a combustion process or after combustion, but they are mainly by-products of a complete combustion process.

Generally, soot is made up of elemental carbon and sometimes has coatings of PAHs whereas combustion ashes are mainly a characteristic of the source material although there are similarities among different types of ashes (Fernandes and Costa, 2013). A proposed mechanism for soot formation/release during a combustion process is schematically shown in Figure 4.1. However, this may differ slightly from case to case depending on the meteorological conditions at the time of emission.

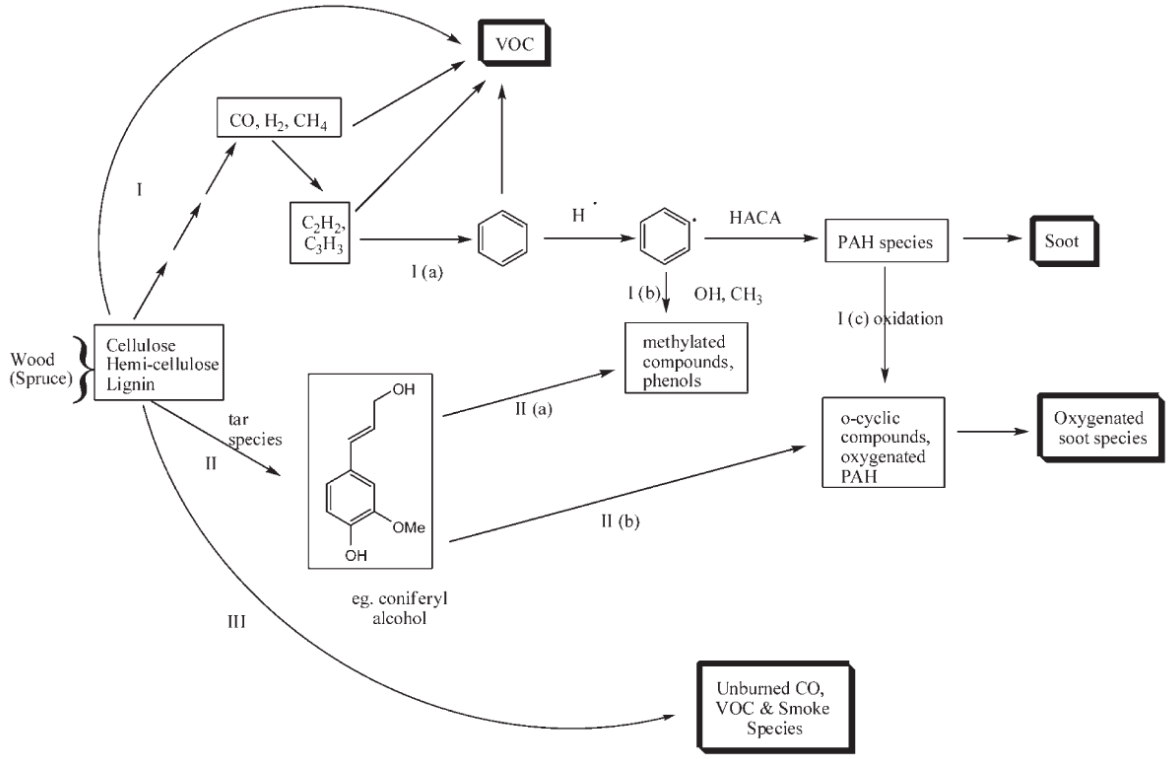

Figure 4.1: Combustion route of biomass showing possible emitted species. The products depend on the route of chemical species, oxygen availability, and combustion time/temperatures. PAH = Polycyclic Aromatic Hydrocarbons, VOC = Volatile Organic

Compounds, HACA = ‘‘H-abstraction-C_2H_2-addition - see Frenklach (2002). This illustration is from Fitzpatrick et al. (2007).

For combustion ashes, a possible pathway for their formation is illustrated in Figure 4.2. The schematic shown in Figure 4.2 illustrates how these materials are formed in an industrial scale; there may be a slight difference in the pathway with which they are formed during domestic combustion processes. Both soot and ash formation mechanisms showed emissions of volatile compounds, which can condense on the soot or ash particles; hence, their compositions and chemistries can be subsequently affected (Williams et al., 2012). It is also important to note that the crucial factors in the formation of these materials are: (1) the oxidant supply, (2) the fuel source, and (3) the temperature of the combustion process - a factor that depends on the oxidant supply and the combustion device. For instance, biomass that has excessive oxidant supply is likely to produce less soot and a maximum ash content or high ash factor (Misra et al., 1993). Without proper containment, these materials make into the atmosphere and constitute part of the aerosol particles in the troposphere.

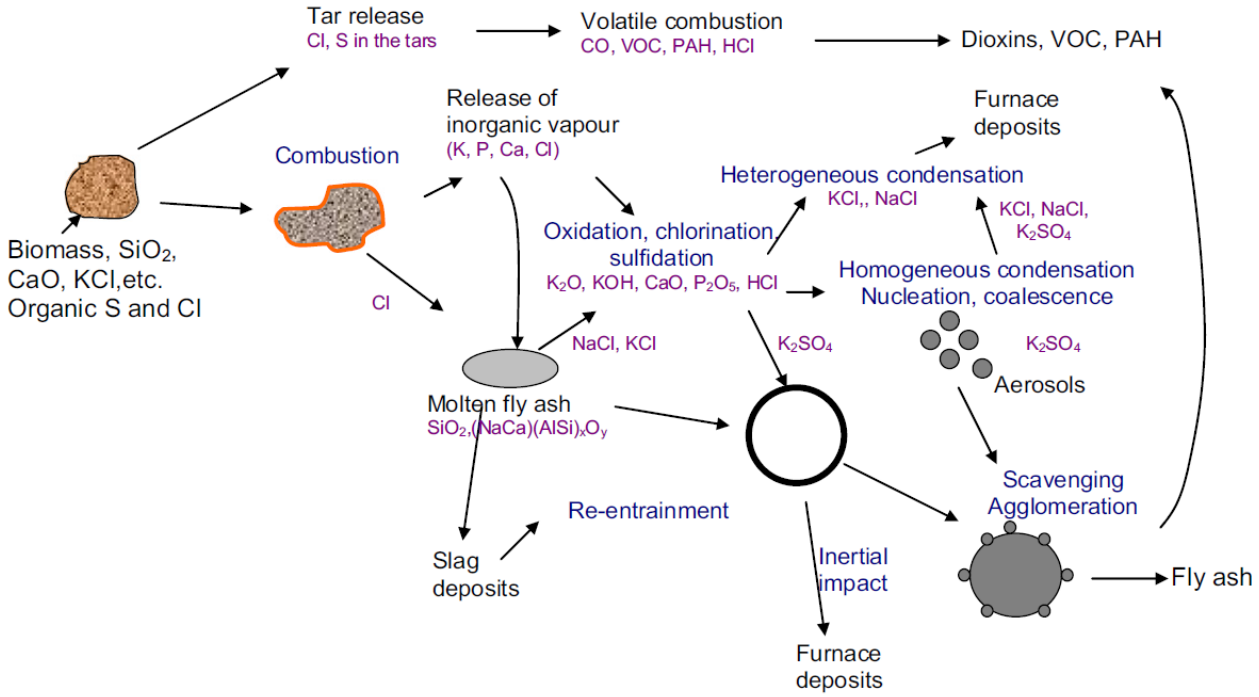

Figure 4.2: A diagram showing a possible formation mechanism of combustion ashes as illustrated by Williams et al. (2012). PAH = Polycyclic Aromatic Hydrocarbons, VOC = Volatile Organic Compounds.

4.2.2 Generation of soot and combustion ash particles from fuels for ice nucleation work in this thesis

Eugenol and n-decane soot used for this study were produced from eugenol ($C_{10}H_{12}O_2$ - 99%) and n-decane ($C_{10}H_{22}$ - 99%) fuels, obtained from Alfa Aesar, Lancs, United Kingdom. The high purity forms of these compounds were needed to ensure that the soot generated from them where mainly a combustion by-product of each specific fuel. In addition, this gives confidence that the starter fuels were not contaminated with other compounds. The chemical structures/formulae of these compounds are shown in Figure 4.3.

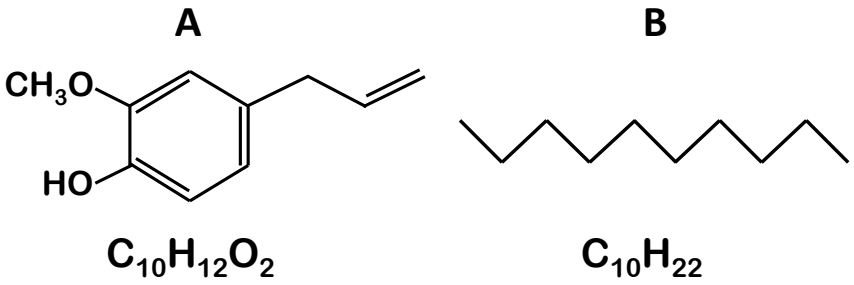

Figure 4.3: Chemical structures and formulae of 4-Allyl-2-methoxyphenol (eugenol) (**A**) and n-decane (**B**) used as proxies for soot from biomass burning and hydrocarbon sources respectively. Both soot types are used in this ice nucleation study.

The two soot types were generated in the laboratory with a set-up comprising a fabricated quartz-glass chimney, a diffusive flame burner (this is a type of flame produced when the oxidant combines with the fuel through diffusion), and a collector as depicted in Figure 4.4. A similar set-up had been used to generate soot for laboratory studies in the past (Baeza-Romero et al., 2010; Samson et al., 1987; DeMott et al., 2009), but with a slight modification to fit the purpose and the design of ice nucleation experiments (Chapter 5). A brief description of the set-up is given below.

A diffusive flame burner containing the required fuel (eugenol or n-decane liquid compound), was ignited with a butane torch in a fume hood, and covered with a quartz-glass chimney. Clean air was supplied as oxidant to the burner via the quartz-glass chimney using a zero air generator (Nitrox pure air generator AG 20-IR) at about 15 lpm. Here, the clean air prevents contaminants from getting into the combustion process. The oxidant supply was at a constant rate, but at sufficient level to ensure a reproducible combustion emission as described by Wilson et al. (2013). In each experiment, the soot produced was collected into a clean borosilicate glass bottle and

capped immediately, to avoid the soot sample being exposed to air. The soot particles generated formed aggregates, which is typical of soot particles (Köylü et al., 1995). The Transmission Electron Microscopy (TEM) images of the eugenol and n-decane soot particles obtained from this set-up are shown in Figure 4.10, which revealed its fractal nature. These images were later used in estimating the particle sizes of the soot.

The two types of combustion ashes used in this study were: fly ashes and bottom ashes. Combustion ashes of interest were made from combusting coal, wood (biomass) and a composite source that was mainly wood with some pieces of newsprint. Both fly ash and bottom ash were obtained from coal fuel whereas only bottom ash was generated from the other fuel sources. Fly ash particles were not generated from other fuel sources because there was no set-up designed for fly ash collection in HAL as at the time of this study, and also due to limited time and resources, collection of fly ashes from other fuel sources was not explored.

There are three ways that the ashes were obtained for the study:

(1) Coal fly ash (hereafter refer to as CFA) was fly ash released during coal combustion process in a typical coal-fired power plant - specifically, from a large coal-fired power station located in the United Kingdom. CFA was collected from an electrostatic precipitator used to trap these particles to avoid their direct emission - which usually consists mainly of coal fly ashes and flue gases (ACCA, 2013; Zhao et al., 2008; Fisher et al., 1976). It should be pointed out that, it is this part of the emission (fly ash trapped by the electrostatic precipitator) that escapes into the atmosphere if not trapped effectively or by inefficient handling methods during storage or disposal (see section 6.2). This CFA was freshly collected and was not atmospherically processed before its use in this study.

(2) Wood (biomass) and coal bottom ashes were obtained from the solid fuel stove as end-products of wood (biomass) and coal fuel combustion, respectively. The schematic for the solid fuel stove used is shown in Figure 4.5. This stove is a laboratory facility at the University of Leeds Engineering Faculty; it is similar to a multi-fuel domestic stove (http://www.euroheat.co.uk/Wood-Burning-Stove/1555/Harmony-23-Evo-Green.html). It was developed to be consistent with the standard model (BS EN 13240:2001 + A2:2004) *(Projects notes of University of Leeds Solid Fuel Stove Project)*. The fire was ignited by a clean and smokeless standard firelighter. This method of igniting the solid

fuels did not introduce contaminants as the initial ash collected was disposed, and the same standard firelighter was used for all the ashes generated.

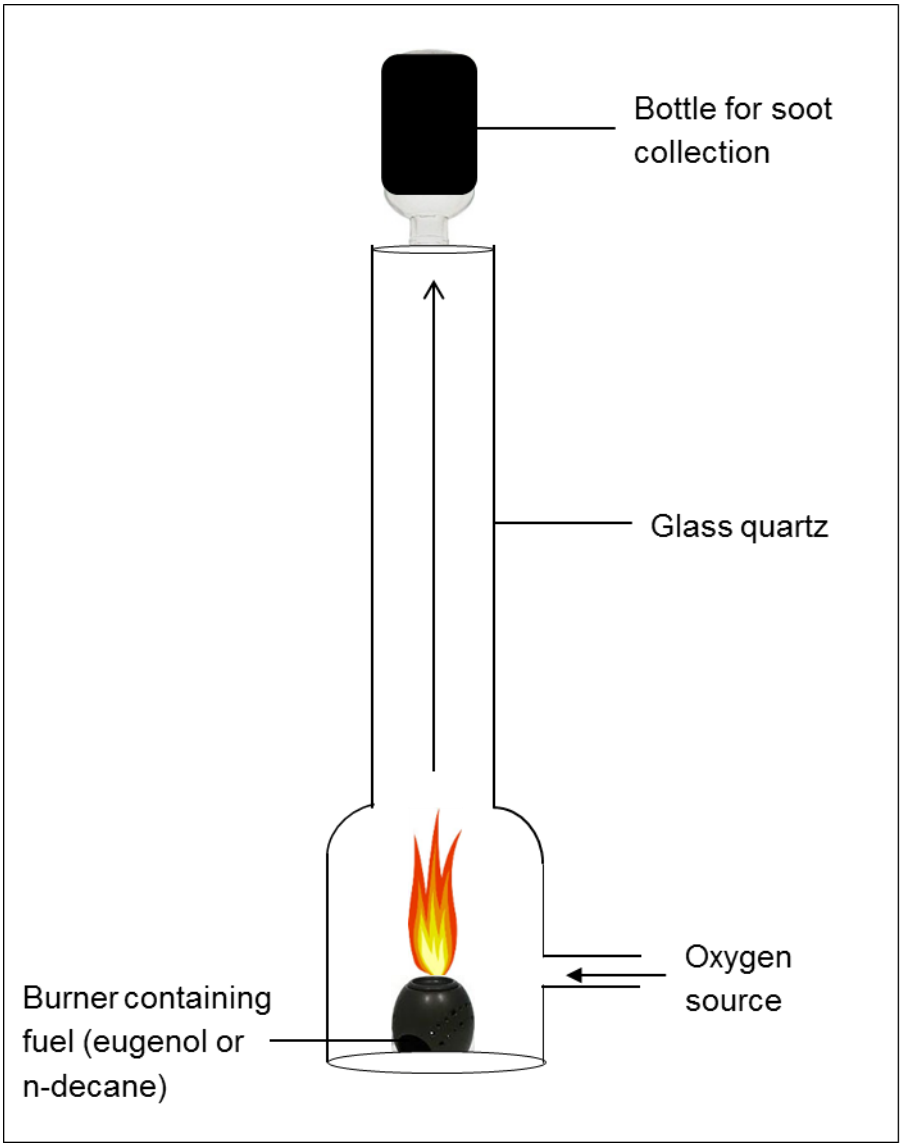

Figure 4.4: A set-up for generating eugenol and n-decane soot in the laboratory. It comprises a diffusion flame burner (containing the fuel – eugenol or n-decane), a quartz glass chimney, and a borosilicate glass bottle. The quartz glass tube has a diameter of 3.4 cm at the top and 21.0 cm high. The quartz glass was connected to a sufficient oxidant supply system from a clean air generator.

Both fuels were separately burned in the stove to generate ashes and then collected in a tray placed underneath the combustion chamber of the stove. The tray is made of stainless steel to avoid introducing any metal contamination during the collection process. All unburnt pieces of the solid fuels and charcoal were completely removed from the ash samples with the help of a gauze wire separator that was placed between the sieve and the combustion chamber. The combustion temperature of the solid fuels in the stove was ~ 300 °C, which is lower than what a typical high-temperature

combustion system would be. For instance, the combustion temperatures in a power plant can reach a threshold temperature of up to 1200 °C – 1600 °C (Cheng et al., 2003).

(3) Domestic bottom ashes were obtained in a similar way to wood and coal bottom ashes. It was generated and collected from a commercially available multi-fuel stove used for an efficient burning of varied solid fuels similar to the type described earlier. The difference between this particular stove and the one at the Engineering Faculty is that, this one was Dr. Ben Murray's personal stove in his house. The materials burned to obtain the domestic ash were mainly unspecified wood fuel – both soft and hard woods - with a few pieces of newsprint sheets used to start the fire.

Before the fire was set up, all previous fire debris was carefully cleaned out from the fireplace to avoid contamination. The domestic ash obtained is a representative of bottom ashes usually generated in residential homes across Europe. Sometimes, solid fuels burned in residential fireplaces, barbecues fires or bon fires can be a composite of things such as pieces of coal, wood, and paper. Because of this composite nature of fuel sources, it is important to characterise the ash obtained before any freezing experiment is performed. Details of these characterisation and results are highlighted in subsequent sections.

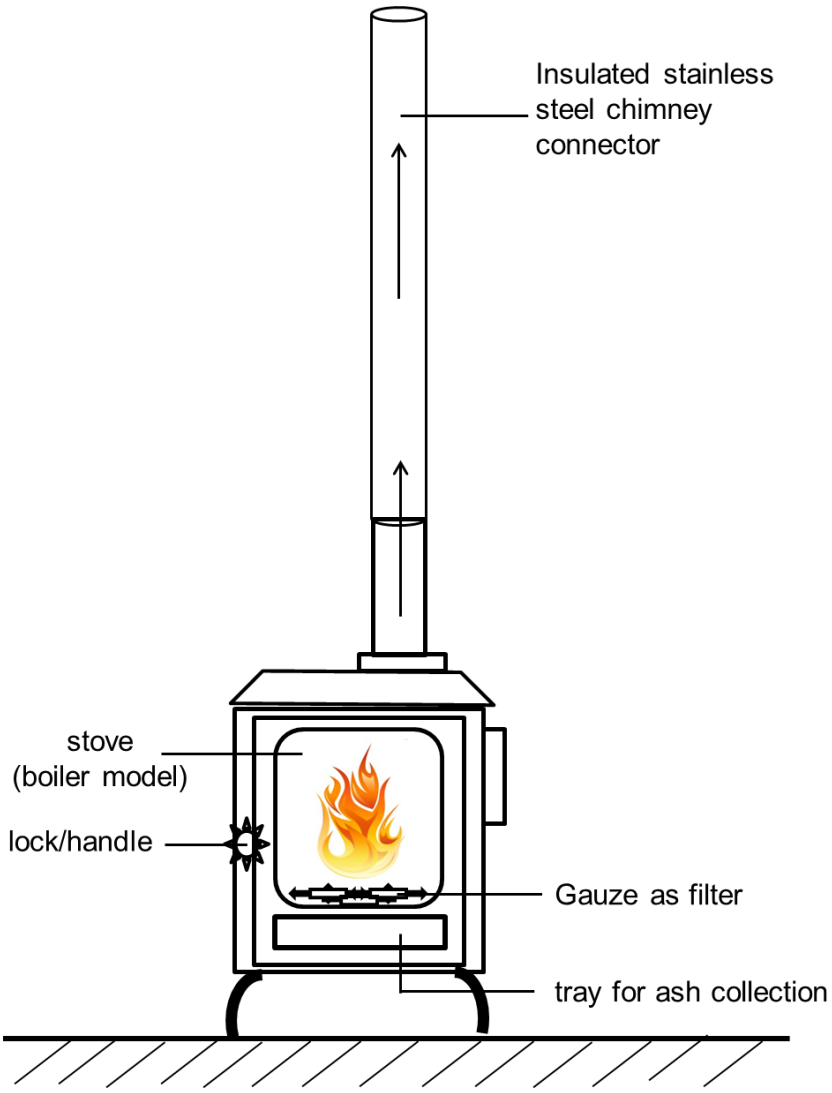

Figure 4.5: A schematic of the solid fuel stove (boiler stove model) that was used for the generation of wood (biomass) and coal bottom ash samples. The ash samples were collected in a tray placed beneath the combustion chamber. Stainless steel gauze was placed between the combustion chamber and the tray to separate unburnt particles from the ash. The combustion temperature was ~ 300°C to mimic a combustion temperature of biomass burning, household combustion systems such as fireplaces and domestic cooking.

4.3 Characterisation of eugenol and n-decane soot

All the soot samples that were generated for this study were systematically characterised to ascertain their material composition, structure, and sizes. The methods applied in the characterisation of these aerosol properties are described in the following sub-sections. Relevant results from the methods are also shown and concurrently discussed.

4.3.1 Soot charaterisation by Raman spectroscopy

The use of spectroscopic analysis technique such as Raman spectroscopy in elucidating the structure and composition of substances have been applied in material sciences and

in the characterisation of atmospheric aerosols (Price et al., 2014; Salzmann et al., 2007; Sadezky et al., 2005). Raman characterisation involves the use of a monochromatic light source (laser) to radiate on a material of interest; the sample scatters most of the incident radiation in the same wavelength as the incident radiation (Rayleigh scattering); however, a proportion is also scattered at a wavelength shifted from the incident laser wavelength called Raman scattering. The Raman scattered light is directed to a multichannel (CCD) detector, which generates a plot of the intensity of the incident radiation to the frequency difference from the incident frequency. This difference is referred to as the Raman shift (usually reported in cm^{-1}). The schematics in Figures 4.5 and 4.6 illustrate a Raman scattering (inelastic) versus the Rayleigh scattering (elastic), and a brief set-up of a Raman measurement system, respectively.

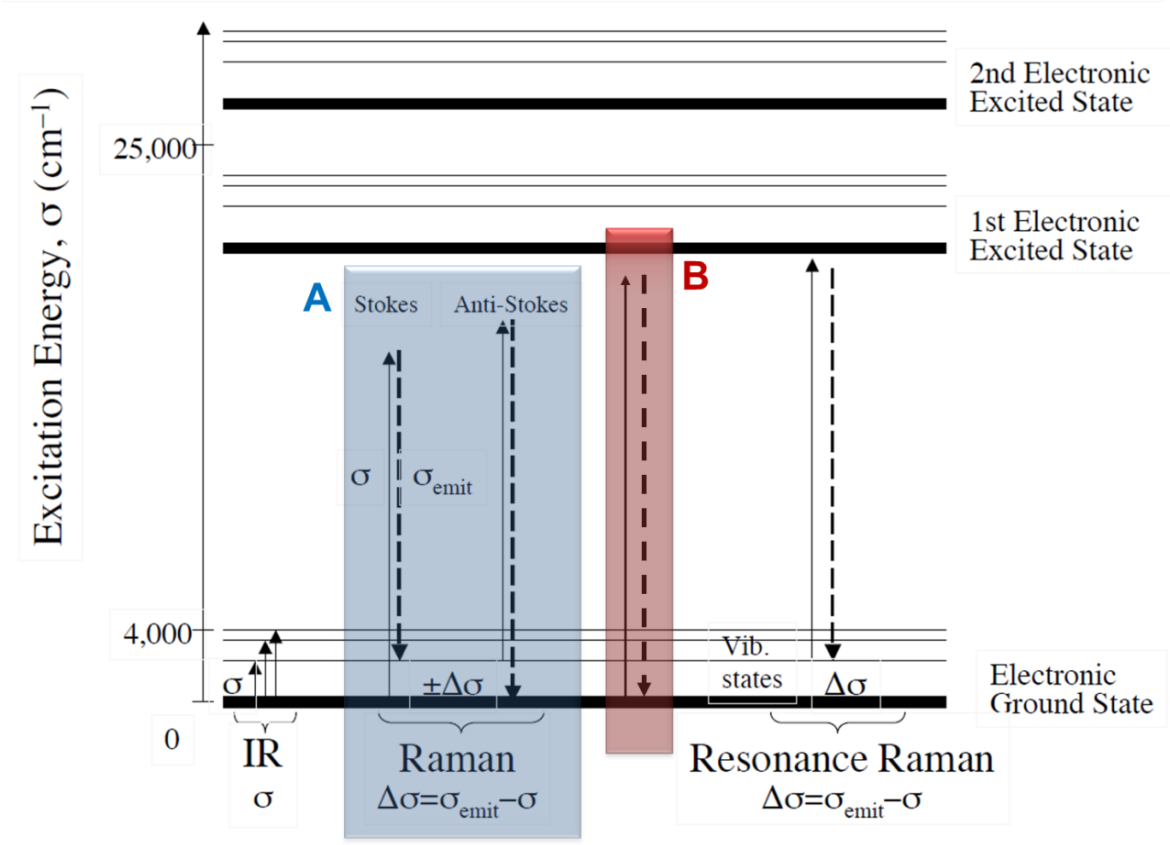

Figure 4.6: A schematic illustrating the Raman scattering. The Stokes scattering involves an emission of higher wavelength while the Anti-Stokes scattering shows emission of a smaller wavelength due to an existing vibrational excitation of the molecule (A - blue). On the other hand, (B - red) shows the elastic scattering of radiation on molecule representing Rayleigh scattering. (This diagram was adapted and modified from a presentation by Kit Umbach, Cornell Centre for Material Research (CCMR), Cornell University).

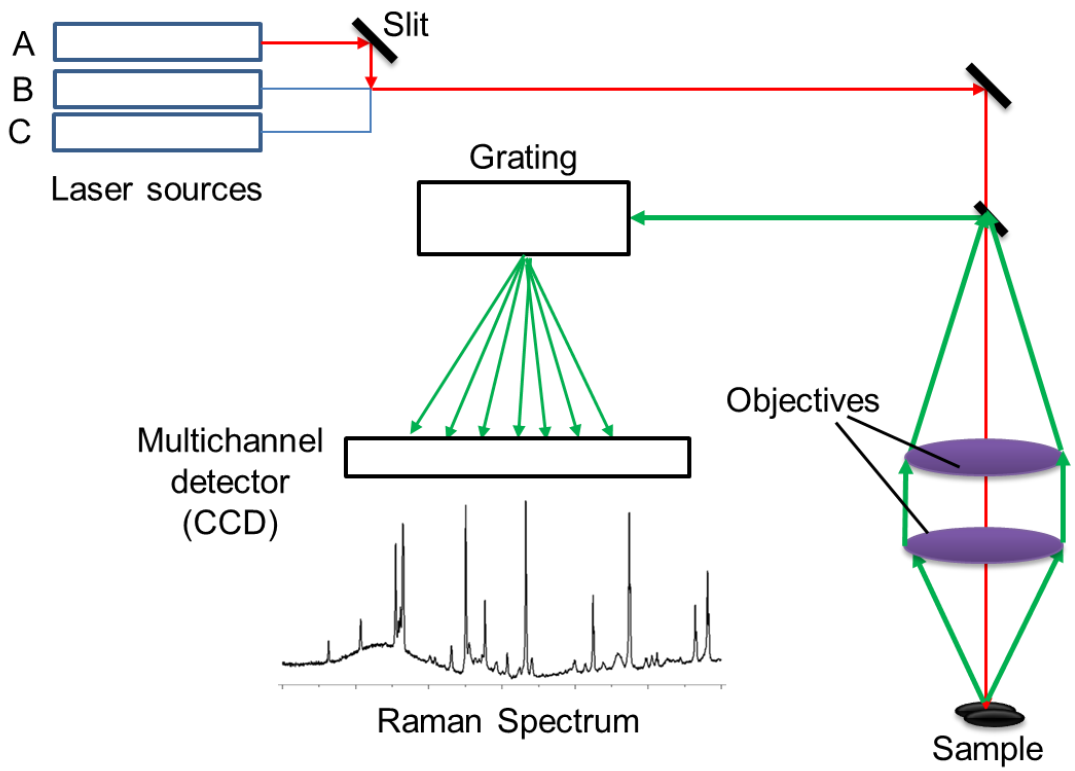

Figure 4.7: A schematic of a Raman measurement set-up. A, B, and C are different laser sources which only one is used as shown by the red line.

The measurement of these Raman shifts is used to observe the vibrational state of the molecules in the material. These vibrational modes give information that is a characteristic of the material (Lin-Vien et al., 1991; Williams and Fleming, 1980; Nakamoto, 1978; Banwell and McCash, 1994). The Raman intensity is inversely proportional to the wavelength as:

$$I_R \propto \frac{1}{\lambda^4} \tag{4.1}$$

where I_R is the Raman intensity and λ is the laser excitation wavelength.

For this investigation, a Renishaw InVia Raman Spectrometer (UK) coupled to a light microscope equipped with a 50X objective lens was used to look at the Raman spectra of eugenol and n-decane soot. The main purpose was to confirm that the material obtained from the combustion process in the laboratory was soot and that they have a similar Raman spectrum to what had been previously reported. Fresh eugenol and n-decane soot were generated for the Raman spectral analyses. All Raman spectra were taken at the excitation wavelength (λ_0) of 514 nm and at the same timescale (i.e. number of accumulations). Spectral analyses were carried out with the default software of

Renishaw (WiRE 3.2). Eugenol and n-decane soot spectra obtained are shown in Figure 4.8.

Generally, Raman shifts for soot are usually observed between 1150 cm^{-1} and 1650 cm^{-1} (Sadezky et al., 2005). The centre of bands of interest are 1350 cm^{-1} and 1580 cm^{-1}, which represents the C-C and C=C stretch bands.

From past work, a 5-band mathematical curve fitting model had been developed and used to look at the excitation bands of soot. This sort of fitting was first proposed by Sadezky et al. (2005), and since then, this had been successfully applied to various soot types such as Printex U, diesel soot, industrial carbon black, spark discharge soot, and others (Liu et al., 2010; Catelani et al., 2013; Sadezky et al., 2005; Knauer et al., 2009). The bands and their respective Raman shifts are: G (~1580 cm^{-1}), D1 (~1350 cm^{-1}), D2 (~1620 cm^{-1}), D3 (~1500 cm^{-1}) and D4 (~1200 cm^{-1}). The G band represents an undisturbed Graphitic lattice and is exhibited only in one first-order band whereas the D bands represent 'Defect' graphitic bar that exhibits additional first-order bands and the numbers 1, 2, 3, and 4 signifies their intensities with D1 being the most intensive of them (Sadezky et al., 2005). Sadezky et al. (2005) recommended that a better combination of fitting shapes is: Lorentzian-shaped bands for G, D1, D2, D4 and a Gaussian-shaped band for D3. These line shapes give the best results for goodness-of-fit for the Raman spectra.

Here, the fit generated by the combination of the bands (G, D1, D2, D3 and D4) from the mathematical model was compared to the experimental spectra of eugenol and n-decane soot. A good fit by the 5-band combination to the experimental spectra signifies that the combustion product obtained is soot. The goodness-of-fit for the experimental spectra was quantified by the Chi-Square (χ^2) of the residuals as reported in Figure 4.8. To make the comparison, the Raman spectra for eugenol and n-decane soot was performed by initializing the 5-band wavenumbers for G, D1, D2, D3 and D4 to 1580 cm^{-1}, 1350 cm^{-1}, 1620 cm^{-1}, 1500 cm^{-1} and D4, 1180 cm^{-1} at a full intensity range, respectively. All first-order spectral comparison results are plotted alongside with the raw experimental spectrum in Figure 4.8.

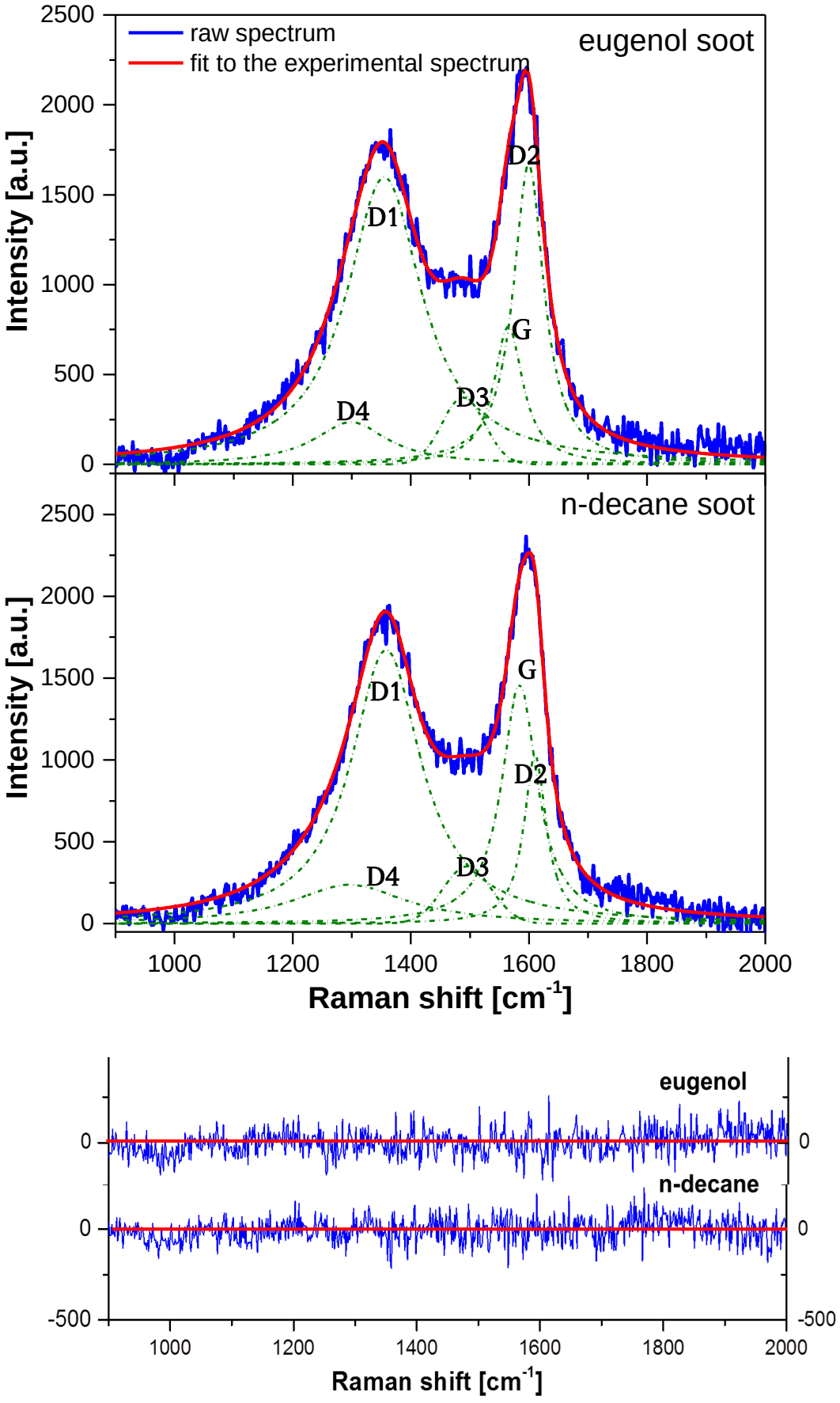

Figure 4.8: Raman spectra (λ_0 = 514 nm) of (1) eugenol soot and (2) n-decane soot after background removal. A first order 5-band convolutions model (G, D1, D2, D3, and D4) are plotted for each soot type in dotted green lines while observed spectra lines and modelled curve

fit lines are shown with blue and red lines, respectively. The fit to the experimental spectra was not significantly different from what would be expected, χ^2 _eu (4, N = 340) = 0.87379, $p \leq 0.05$ and χ^2_ndec (4, N = 9000) = 1.19758, $p \leq 0.05$. The bottom plot shows the residuals for both eugenol and n-decane soot fits to the experimental spectra

Both eugenol and n-decane soot experimental spectra showed major bands at approximately 1350 cm^{-1} and 1580 cm^{-1}, these were similar to what was seen for Printex U model soot (Liu et al., 2010) and airborne soot (Catelani et al., 2013). However, looking at the curve fittings, D1 and D2 showed better fits for eugenol while n-decane soot had D1 and G bands as high peaks of the cure fits. The D1 bands can give information about the molecular and the reactivity of soot (Knauer et al., 2009). However, the focus of this structural analysis was to confirm that the material generated from the combustion process is similar to airborne soot type and agrees with Raman spectra of various soot types previously reported. Hence, eugenol and n-decane soot obtained from this set-up had similar structure. The 5-band deconvolution model of airborne soot by Catelani et al. (2013) as shown in Figure 4.9; by comparing the peaks of the Raman spectra of eugenol and n-decane to that of the airborne soot, it shows that the soot generated for this study is a good representative of soot sample observed in the atmosphere.

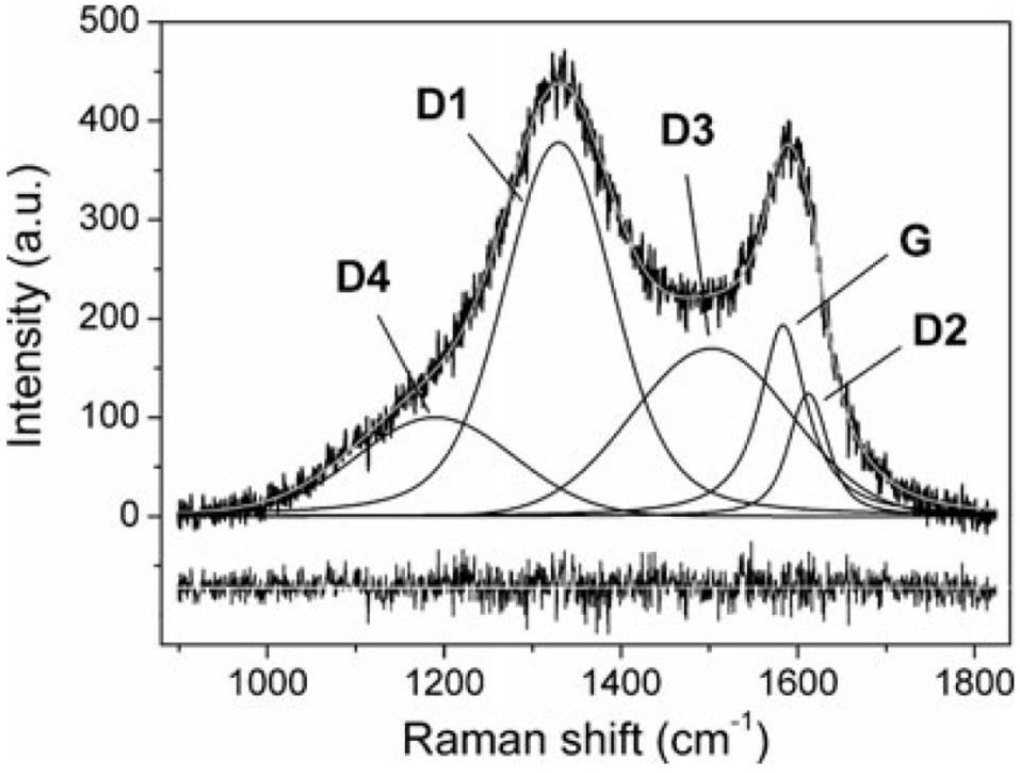

Figure 4.9: Raman spectrum of airborne soot showing the experimental spectrum and the 5-band deconvolution model. The Raman spectrum was taken at the excitation wavelength (λ_0) of 632.8 nm. The plot is from Catelani et al. (2013).

4.3.2 Surface morphology and particle size analyses

Surface imaging of aerosol particles can give more information about the behaviour of particles, for example, its adsorption abilities. In ice nucleation studies, characterising the surface morphologies of IN is useful in understanding the nature of the material that may be important in its ice nucleation activity (Hiranuma et al., 2014). To look at the morphology of soot, a Transmission Electron Microscopy (TEM) method was used to look at eugenol and n-decane soot samples generated from the set-up described in section 4.2.2.

This technique involves accelerating a beam of high energy electrons (up to 100 – 400 kV) through an ultra-thin sample (here, soot), then these electrons interact with the sample and eventually they are transmitted in different ways. These transmitted electrons are re-focused into an imaging device such as a fluorescent screen by electromagnetic lenses to be detected by a sensor such as a CCD camera. Also, the transmitted electrons can be focused onto a device that can create a diffraction pattern. The image obtained reveals the micro or nanostructure of the material investigated. (Fultz and Howe, 2012; Williams et al., 1998). If the transmitted electrons are passed through a nano-analytical spectrum e.g. EDS detector, information on the elemental composition of the sample can be obtained. The images of eugenol and n-decane soot taken by the research group of Professor Alan Williams and Professor Jenny Jones' are shown in Figure 4.10.

Firstly, fractal formations of the soot particles were seen for both eugenol and n-decane soot [Figure 4.10 (a) and (c)]; this agrees with the general structural appearance of atmospheric soot particles (Köylü et al., 1995; Cai et al., 1993; Samson et al., 1987). Particle to particle attraction is thought to be the reason for this fractal formation.

Secondly, looking closely at the individual particles [Figure 4.10 (b) and (d)]; well-aligned structures are observed which is a characteristic of a graphitic core found for most black carbon. These are similar to what Rissler et al. (2013) observed with a high resolution TEM for heavy-duty diesel soot types and candle soot. Many soot particles generated during combustion process adsorb organic compounds, e.g. PAHs, on them leading to a coating on the outer layer of the soot, while the graphitic core is mainly carbon; and this may affect their morphology and other properties (Ghazi and Olfert, 2012; Adachi and Buseck, 2013). However, this phenomenon was not physically

observed in the morphology of these soot particles but from chemical studies by using an Aerosol Time Of Flight Mass Spectrometer (ATOFMS), PAHs contents of both eugenol and n-decane soot were reported (Wilson et al., 2013). These soot types were generated in a similar way to the soot particles in this present study.

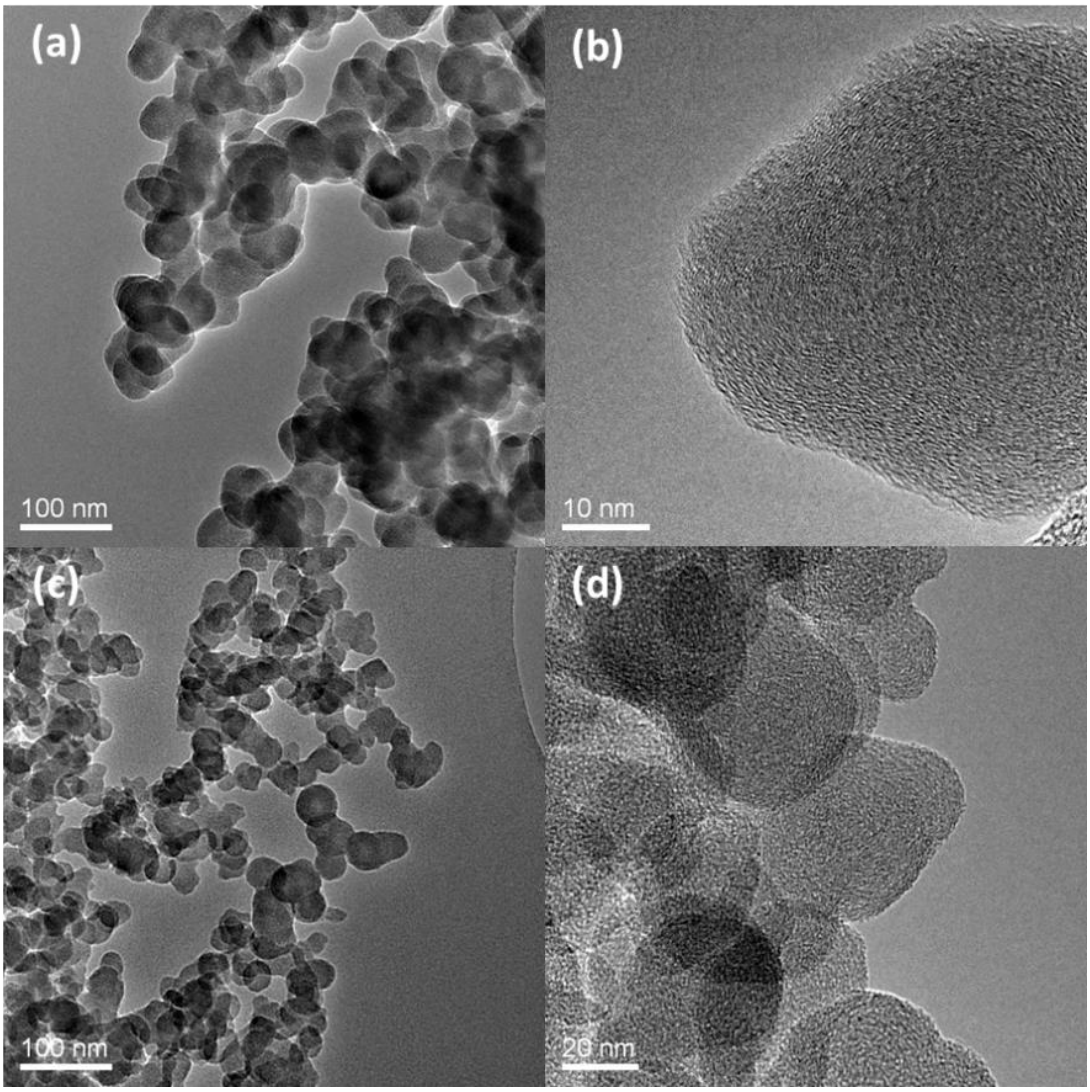

Figure 4.10: Transmission Electron Microscopy (TEM) images of eugenol and n-decane soot that were generated from the set-up described in section 4.2.2. Eugenol soot images are shown on the top plates [(a) and (b)] while the plates below [(c) and (d)] are n-decane soot images. The magnification of each image is labelled at the bottom left hand corner of the image (These pictures were taken by Professor J. Jones and Professor A. Williams research group at Faculty of Engineering, University of Leeds, UK).

Thirdly, some particles are observed to have an oblong or amoebic shape against the expected spherical shapes for soot particles as widely reported (Mikhailov et al., 2006). When two spherical particles merge, this sort of globule shape can result and this phenomenon is called ‘accretion’. Some studies on the structure of soot in water, and on the effect of coating mass on soot have reported a collapse of an initial soot structure

which has a similar effect as an accretion phenomenon (Ghazi and Olfert, 2012; Mikhailov et al., 2006; Prado et al., 1983). However, some soot types are reported to exhibit weaker restructuring effect e.g. diesel soot (Weingartner et al., 1997), which is due to an existing more compact structure.

Processing these images, particle sizes of soot can be obtained by a direct measurement of the diameter of the particles shown in these TEM images. This was done by measuring 30 images of individual spherical soot particles: the average individual particle sizes of eugenol and n-decane soot measured were 49 ± 4 nm and 35 ± 6 nm, respectively. These sizes were smaller than the average sizes reported by an aerodynamic diameter measurement that was found to be 175 nm and 125 nm for eugenol and n-decane, respectively (Wilson, 2011). The aerodynamic sizes reported by Wilson (2011) are likely to be diameter for soot aggregates rather than individual soot particles; however, the sizes were within the range of particle sizes of soot obtained from controlled flames (Slowik et al., 2007). The overall size range (~35 nm – 175 nm) reported for both soot types were within the range of various soot types generated by different methods (Tumolva et al., 2010).

It should be stated here that estimating the particle size by direct measurement of TEM/SEM individual soot images method should be treated with caution because it may not give a realistic size distribution observed for soot particles sizes in the atmosphere. However, this estimate can give a rough approximation of the particle sizing for the ice nucleation study (details in Chapter 5). Another limitation is that accretion, as earlier mentioned, may also introduce uncertainty in particle size measurements because of irregularities in shapes especially for instruments that relies on comparing particles shapes to an equivalent sphere-volume model e.g. Mastersizer and differential mobility analyser (aerodynamic sizer).

4.3.3 Surface area analyses

A number of methods can be engaged in measuring the surface area of particles such as direct geometric calculations from particle size, light scattering methods, aerodynamic comparisons, gas adsorption isotherms and others. For each of these methods there are comparative advantages and disadvantages or limitations.

In this study, the specific surface areas (SSA; unit surface area per unit mass) of eugenol and n-decane soot samples were obtained by Brunauer-Emmet-Teller (BET) nitrogen

gas adsorption method, which has been described previously in Brunauer et al. (1938), Smekens et al. (2005), and Sing and Gregg (1982). Briefly, the principle involves the adsorption of a monolayer of gas molecules (nitrogen) on the surface of particles. Knowing the number of gas molecules adsorbed and the individual area that each molecule occupied in a monolayer can allow a calculation of the surface area of the particle. The number of molecules (n_m) can be estimated from the gradient of the BET equation (Sing and Gregg, 1982):

$$\frac{P/P^\circ}{n(1-P/P^\circ)} = \frac{1}{n_m c} + \frac{c-1}{n_m c}\left(\frac{P}{P^\circ}\right) \qquad 4.2$$

Where P is the pressure at which an amount of gas (n) is adsorbed and P° is the saturation vapour pressure and c is the BET constant. A plot of $(P/P^\circ)/n(1 - P/P^\circ)$ against P/P° gives a straight line equation y = mx + c; therefore, the gradient of the line ($c - 1 / n_m c$) or the intercept ($1/ n_m c$) can be used to calculate the n_m.

In addition to the standard procedure, an accelerated surface area and porosimetry system (Micromeritics ASAP 2020 Analyser, UK) was used for the measurement. About 120 mg of the samples (soot or combustion ash) was weighed and put into a flask with a predefined internal surface and volume. The samples were degassed at about 120 °C for 3 hours to prevent denaturing the soot particles. Then this was cooled with liquid nitrogen before a stream of nitrogen gas was added to adsorb on the particles. The Micromeritics auto system recorded the differences between the gas adsorbed by the samples and that expected to be adsorbed by the reference flask. All calculations were performed by the default software of the Micromeritics ASAP 2020 Analyser. The SSAs obtained by this technique for eugenol and n-decane soot are shown in Table 4.1. SSA results for combustion ashes are also shown here but will be discussed later.

Table 4.1: Specific surface areas (SSA) obtained from BET measurements of eugenol soot, n-decane soot and combustion ashes. All coal fly ash, wood (biomass), domestic, and coal bottom ashes were sieved to ≤ 40 μm before the measurement. Coal fly ash (bulk) denotes a raw coal fly ash sample as obtained from the electrostatic precipitator of a coal-fired power plant. All measurements were obtained from a five-point adsorption isotherm with correlation coefficient of ≥ 0.9975. The respective uncertainties in the measurements are indicated on a separate column.

Samples	**BET (m^2/g)**	**Uncertainty (m^2/g)**
eugenol soot	49.43	0.89
n-decane soot	65.47	0.81
coal fly ash (bulk)	1.85	0.04
coal fly ash (sieved to ≤ 40 μm)	2.54	0.04
wood ash	6.98	0.30
coal ash	8.86	0.38
domestic ash	3.87	0.20

Eugenol and n-decane soot SSA was found to be 49.43 ± 0.89 m^2/g and 65.47 ± 0.81 m^2/g, respectively. The BET surface area of eugenol and n-decane soot can be compared with other soot types that their SSA have been previously reported in the literature as shown in Table 4.2. Variation in the surface area of different soot types could be due to the difference in fuel sources that the soot particles were produced from, combustion conditions, and the fractal factor of the soot.

Table 4.2: BET specific surface areas (m^2/g) of different soot types as reported in the literature, including results from this study.

Soot types	**diameter (nm)**	**Surface Area (m^2/g)**	**References**
Lamb black (LB)	95	22	Popovicheva et al. (2008a)
Furnace black (FB)	35	100	
FW2 (Channel Black)	13	420	
Acetylene (AS)	50	86	
Thermal (T-900)	246	10	
Aircraft engine combustor (AEC)	48	12	
TC1 kerosene flame (TC1)	30 - 50	87	
TC1 oxidized soot (TC1-O)	57	49	
Combustor remote (CRS)	30 - 50	104	
Wood black carbon (WB)	NR	1.5	Kireeva et al. (2009)
Carbon black Cabot 1999	30	94	Smekens et al. (2005)
Diesel soot	30	45	
Biodiesel soot	26	53	
Domestic heating soot	24	14	
Aircraft exhaust soot	31	31	
Fresh diesel soot	NR	71	Chughtai et al. (1999)*
Aged diesel soot	NR	65	Chughtai et al. (1999)*
Diesel soot	NR	20	Pott (1991)*
Diesel soot	NR	52	Ishiguro et al. (1991)*
Extracted diesel soot	NR	34	Pott (1991)*
Diesel soot	NR	250 - 300	Covitch (1989)*
Oil-fired electric power station	NR	5.8	De Santis and Allegrini (1992)*
Urban boiler	NR	6.5	De Santis and Allegrini (1992)*
Aviation fuel	NR	65	Chughtai et al. (1999)*

Aircraft soot (calculated)	NR	75	Karcher et al. (1996)*
Pines needles burning	NR	80	Chughtai et al. (1999)*
Coal combustion	NR	84	Chughtai et al. (1999)*
N-hexane soot: diffusion flame	NR	89	Dymarska et al. (2006)
N-hexane soot: air/fuel = 0.53	NR	100	
N-hexane soot: air/fuel = 2.4	NR	156	
Lamp black 101	NR	20	
Degussa FW2 (channel black)	NR	460	
Printex 40 (Furnace black)	NR	90	
Palas	6.6	308	Popovicheva et al. (2008c)
CAST-4	300	46	
CAST-27	32, 90, 140	21	
AEC	NR	6	
Combustor	30 - 50	54	
Eugenol	*50*	*49.43*	*this study*
n-decane	*35*	*65.47*	*this study*
Average	**40.6 ± 22**ł	**85 ± 104**	

* these datasets were extracted from Smekens et al. (2005)
ł sizes bigger that 100 nm were removed because there is a higher probability that those sizes are diameters of soot aggregates rather than individual particles.
NR Not Reported

Surface areas of combustion ash particles were also measured using the BET method as described in this section. The results obtained are shown in Table 4.1. The order of SSA of the ashes is: CFA (bulk) < CFA (sieved) < domestic bottom ash < wood bottom ash < coal bottom ash. The increase in the SSA favours ashes with smaller particles as is later shown by the SEM images and the laser diffraction particle size distribution (see sections 4.4.2 and 4.4.4).

In this work, the BET surface areas obtained were used for the ice nucleation calculations; similar approach have been adopted for other ice nucleation works (Broadley et al., 2012; Rigg et al., 2013; Hiranuma et al., 2013).

4.3.4 Chemical composition of eugenol and n-decane soot – organic carbon (OC) versus elemental carbon (EC)

Chemical compositions of eugenol and n-decane soot have been previously studied by Baeza-Romero et al. (2010) and Wilson et al. (2013). The compositional analyses were done on soot generated from the same system as described in section 4.2.2. Soot is known to contain both organic and elemental carbon and the relative ratio of these components can determine their chemical behaviours.

However, to quantify the ratio of OC, a relative proportion of the total carbon (TC) content needs to be determined (Ferge et al., 2006). Following the method of determining the relative elemental and organic carbon content of aerosol samples by an online ATOFMS by Ferge et al. (2006), the EC/TC ratio of eugenol and n-decane were measured as 52 ± 6 % and 88 ± 5 %, respectively (Wilson et al., 2013; Baeza-Romero et al., 2010). This indicates that the EC content of n-decane was higher than that of eugenol soot; this could be attributed to the chemical structure of n-decane ($C_{10}H_{12}$) which is likely to generate lesser amount of organics than eugenol ($C_{10}H_{12}O_2$) and lower temperature of eugenol flame. Eugenol soot was found to comprise PAHs and oxygenated organics in higher amounts than n-decane soot based on the mass spectroscopy analyses, (Baeza-Romero et al., 2010; Wilson et al., 2013).

4.4 Characterisation of combustion ashes

All combustion ashes investigated here were obtained or generated as described in section 4.2.2, although some were sieved before characterisation to remove the largest particles and charcoal. This section presents the mineralogy assay, surface morphology, particle size analyses, and surface area determination of these ashes. A short summary of the principle of each analytical method used is given on each subsection.

4.4.1 Mineralogy of ash particle by X-ray diffractometry (XRD)

The mineral composition of the ashes was investigated using the X-ray diffractometry (XRD) method. The XRD technique involves the use of X-ray beams on samples, and then the diffracted rays are recorded with respect to the incident rays. X-ray diffraction obtained is a characteristic of the crystal structure of the material examined. This

characteristic diffraction is described by the Bragg's Law (Dinnebier and Billinge, 2008):

$$n\lambda = 2dsin\theta \tag{4.3}$$

where n is an integer of the X-ray wavelength λ, d is the distance between interfering atoms, and 2θ is the diffraction angle, i.e. the angle between the incident (incoming) and outgoing (emitted) X-ray beams.

The information from the analysis of the diffraction patterns can be used to identify the crystal phases present in the material (Dinnebier and Billinge, 2008; Duckett and Gilbert, 2000).

This work was carried out using an X-ray diffractometer (Bruker D8 Advance). Before the mineralogy characterisation, raw ash samples from CFA, wood (biomass), domestic and coal bottom ashes were first fractionated to obtain atmospheric relevant particle sizes by sieving to ≤ 40 μm sized particles. This was achieved by using Endecotts test sieves and a sieve shaker (Endecotts M100, UK; ISO 9001 certified). Four 100 mm diameter test sieves (71 μm, 63 μm, 55 μm, 50 μm) were stacked, before the 40 μm test sieve. This was the smallest aperture test sieve that was accessible as at the time of the experiment; nevertheless, ash particles passed through it with ease suggesting that at least two dimensions of the ash particles were smaller than 40 μm. This assumption was confirmed from the particle size estimation by the Scanning Electron Microscopy (SEM) images of CFA.

For the XRD investigation, an internal standard method was used which involved the addition of a known quantity of a corundum (Aluminium Oxide) before taking the diffraction pattern. Here, a specified amount of corundum obtained from Logitech, UK, was added to each ash sample as internal standard. The diffraction peaks of the ash samples were identified by matching the sample peaks to the reference peaks provided by the machine's database. Similar method had been applied in characterising the mineral composition of mineral dust (Atkinson et al., 2013), soil and agricultural dust samples (O'Sullivan et al., 2014). Table 4.3 shows the relative mineral compositions of the ashes in percentages of the total volume of the sample used. The diffraction patterns obtained are shown in Appendix B (B1, B2, B3, B4, and B5).

Table 4.3: Mineral compositions of CFA, wood, domestic and coal bottom ashes (%) were obtained from XRD. All samples were sieved to ≤ 40 μm except indicated such as the bulk CFA, which the mineral composition analysis was done on the raw sample as obtained from the power plant. Larger part of the samples consisted of amorphous materials.

Minerals	**Possible chemical formula of the minerals**	**Ash samples (%)**						
		CFA (Bulk)	CFA (≤40 μm) (1)	CFA (≤40 μm) (2)	CFA (≤40 μm) (Ave)	wood ash	domestic ash	coal ash
quartz	SiO_2	13.1	5.2	5.0	5.1	14.4	15.1	7.5
mullite	$Al_6Si_2O_{13}$	13.5	12.4	11.6	12	0.0	0.0	10.4
pyrite	FeS_2	7.2	4.5	4.1	4.3	0.0	0.0	4.9
calcite/ gypsum	$CaCO_3$ / $CaSO_4$	0.4	0.5	0.0	0.25	23.6	54.0	7.7
haematite	Fe_2O_3	1.9	2.8	2.8	2.8	6.2	7.3	3.3
magnetite	Fe^{2+} / $Fe^{3+}{}_2O_4$	0.8	1.6	1.6	1.6	0.0	0.0	3.4
amorphous components	-	63.1	73.0	74.9	74.0	55.8	23.7	62.8

Minerals found in the combustion ashes - CFA, wood, domestic, and coal bottom ashes varied from sample to sample but largely, the major minerals found are similar to the type of minerals found in natural dust samples although some minerals such as clay and feldspar were absent. Also, one other difference with desert dust is that the XRD results showed that all the ash samples had amorphous materials in them: CFA_bulk (63.1%), CFA_sieved (74.0%), wood (biomass) ash (55.8%), domestic ash (23.7%), and coal ash (62.8%). The amorphous materials were identified by broad diffraction peaks in the X-ray diffraction spectrum against crystalline peaks that are spikes and sharp. These amorphous materials could be amorphous silica or carbon because the diffraction peaks were similar to what are obtained for these materials. Crystalline and amorphous form of the same material may have different optical properties (Dimitrov et al., 1999). The amorphous compositions of CFA determined by XRD have been previously reported for a bulk CFA and carbonated fly ash obtained from Mpumalanga province of South Africa as 64.99% and 59.46%, respectively (Nyambura et al., 2011). Major minerals found in our combustion ashes include: quartz, mullite, pyrite, calcite/gypsum, haematite, and magnetite (Table 4.3).

Mullite ($Al_6Si_2O_{13}$) was observed to be present in CFA and coal bottom ash but not in other ashes studied. This compound is a characteristic of coal formations. Mullite

composition decreased by 12% between the bulk sample and the sieved sample as shown in Figure 4.11. This suggests that the compound was associated more with larger particles of the bulk than smaller particles.

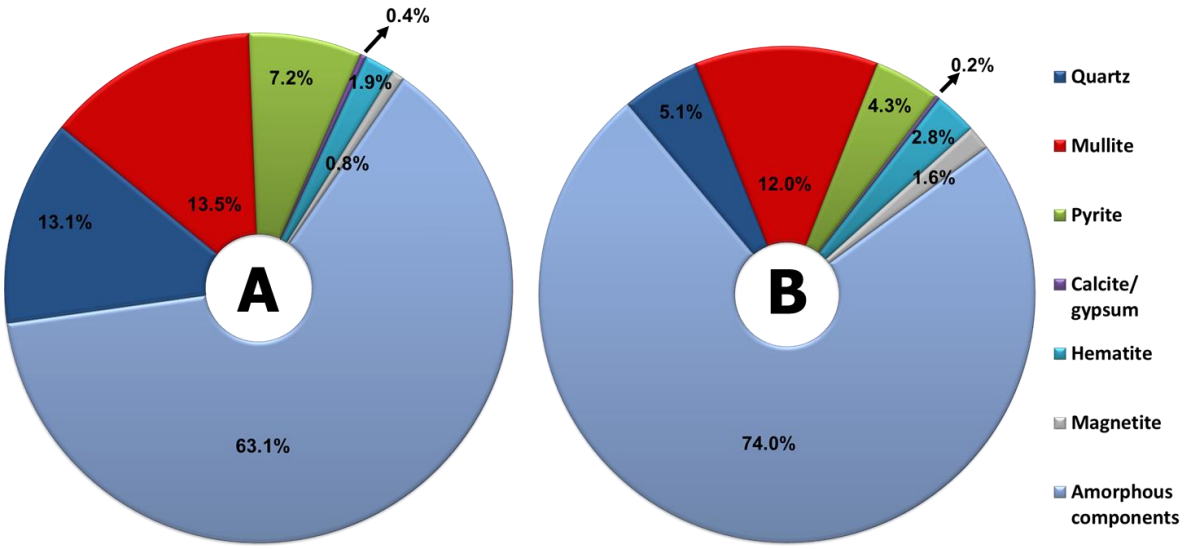

Figure 4.11: Mineral compositions by weight (%) of the bulk sample of coal fly ash (CFA) (**A**) and its sieved sample (≤ 40 µm) (**B**). Aside quartz, pyrite dominated the sieved sample by weight while no significant difference was observed for calcite.

However, all minerals found in the bulk sample were all present in the sieved CFA sample, although the amount of quartz decreased indicating that quartz may have been associated more with the bigger particles. Higher calcite weight percentages were found in bottom ashes compared to the high temperature generated fly ash: CFA (0.25%), wood bottom ash (23.6%), domestic bottom ash (54.0%) and coal bottom ash (7.7%). Some of these minerals in Table 4.3 are found in natural dusts (Atkinson et al., 2013) and model studies showed that some elemental composition of smaller particles of coal fly ash (< 1 µm - 2 µm) are similar to that of Arizona test dust (AZTD) (< 0.5 µm - 1 µm) (Chen et al., 2012); this could also be applicable to other combustion ashes mentioned here. Due to difficulty in differentiating the origin or source of these elemental compositions in the atmosphere most of the online aerosol analyses identified as mineral dust could be contributed by combustion ashes; hence, most particles measurements are grouped as mineral/fly ash e.g. Cziczo et al. (2013).

4.4.2 Surface morphology of combustion ashes

Scanning electron microscopy (SEM) technique was used to examine the surface morphology of the combustion ashes. The basic principle of SEM had previously been

described in section 4.3.2. However, in SEM, the electrons that bounced off the surface of the material were measured contrary to the transmitted electrons in the case of TEM. Particles of the combustion ash samples were placed on customized carbon nano surface and later coated with platinum (80% platinum and 20% palladium) before it was introduced into the SEM machine. This platinum coating serves as an earthing medium to conduct charges away from the sample surface. This prevents the sample from charging which can lower the emitted radiated and lead to poor imaging.

The images obtained are presented in Figures 4.12, 4.13, 4.14, and 4.15 for CFA, wood, domestic and coal bottom ashes, respectively.

For all the ashes, only CFA showed spherical shape particles (Figure 4.12), others had irregular shapes and tended to form aggregates.

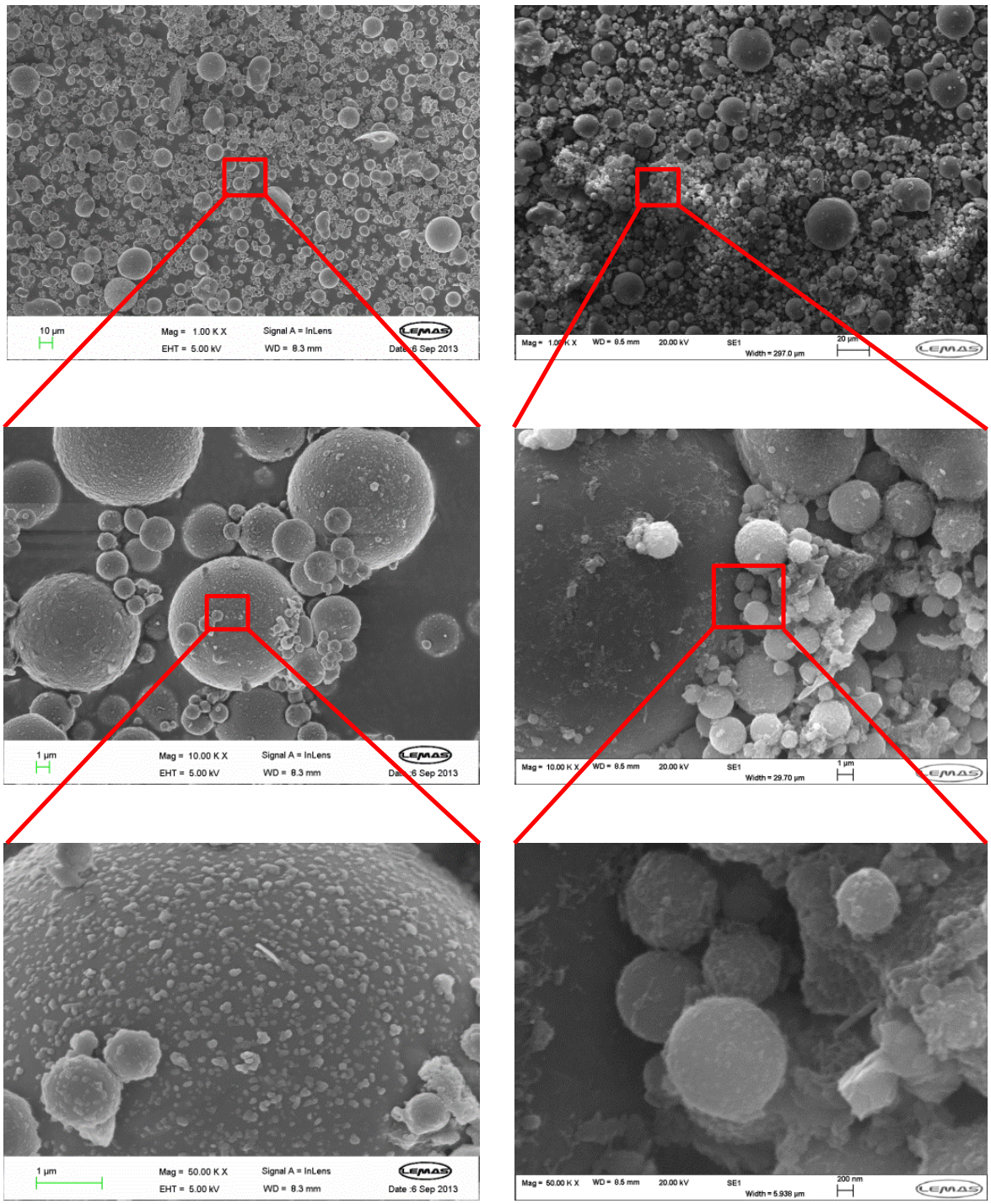

Figure 4.12: Scanning electron microscopy (SEM) images of CFA particles used for the ice nucleation studies. The left-hand side are SEM images from CFA samples sieved to ≤ 40 µm sizes, while the right-hand side panels represents images of the same sample but recovered from 0.1 wt% CFA suspension. The magnification and scale are indicated at the base of each SEM image panel.

The spherical shape of CFA is attributed to the formation mechanism of these particles (Fenelonov et al., 2010). Some CFA particles are spheres with empty space inside (hollow particles); these types of particles are referred to as ‘cenospheres’. Some of these cenospheres may be filled up by smaller sized particles of CFA and are referred to

as ‘plerospheres’. The details of the mechanism of their formation is discussed in Fenelonov et al. (2010). High temperatures and expansion of gas pockets are required for the formation of these cenospheres. The average particle size of CFA was estimated by using Image J® software as approximately 5 µm. Spherical shape of CFA is reported by many researchers (Del Monte and Sabbioni, 1984; Nyambura et al., 2011; Flanders, 1999; Li and Shao, 2009). There was no significant difference between the SEM images of CFA particles recovered from its suspensions (right panel of Figure 4.12) and the unsuspended particles. Notwithstanding, some deposits of crystallised salts or minerals could be seen on the surface of the particles that were recovered from suspensions as shown in Figure 4.12 (right). Mahlaba et al. (2012) reported that SEM images of CFA particle recovered from deionized water-based CFA slurry remained similar to unreacted (fresh) CFA. In addition, it could be observed that there were more tiny particles in the first panel (right-hand), which suggest that a couple of the plerospheres may have smashed to release these smaller particles with sonication. Some plates-like shapes could also be seen which may be broken hollow spheres (cenospheres) (see Figure 4.12 (right)).

Wood bottom ash particles showed irregular shapes and aggregated particles as shown in Figure 4.13, although smaller compared to the CFA particles. Wood ash particles recovered from the suspension (right-hand panel) were slightly separated but not enough to distinguish each particle shape. The 50,000X magnification panel of the recovered wood ash showed spiky formations, which could be the recrystallized minerals that dissolved into the suspension. Owing to the irregularity in particle shapes; it was difficult to estimate the particle sizes from the SEM images. The generation and formation mechanism of wood bottom ash are completely different from CFA as earlier described in section 4.2.2; therefore, the shape of the particles could be related to the formation mechanisms of these particles. Domestic bottom ash particles were highly agglomerated and asymmetrical shaped as shown in Figure 4.14, but smaller than CFA, although they are within the same size range as wood ash particles. Domestic and wood bottom ashes were generated from similar fuel source and in comparable combustion conditions; hence, the particles may likely show analogous morphology.

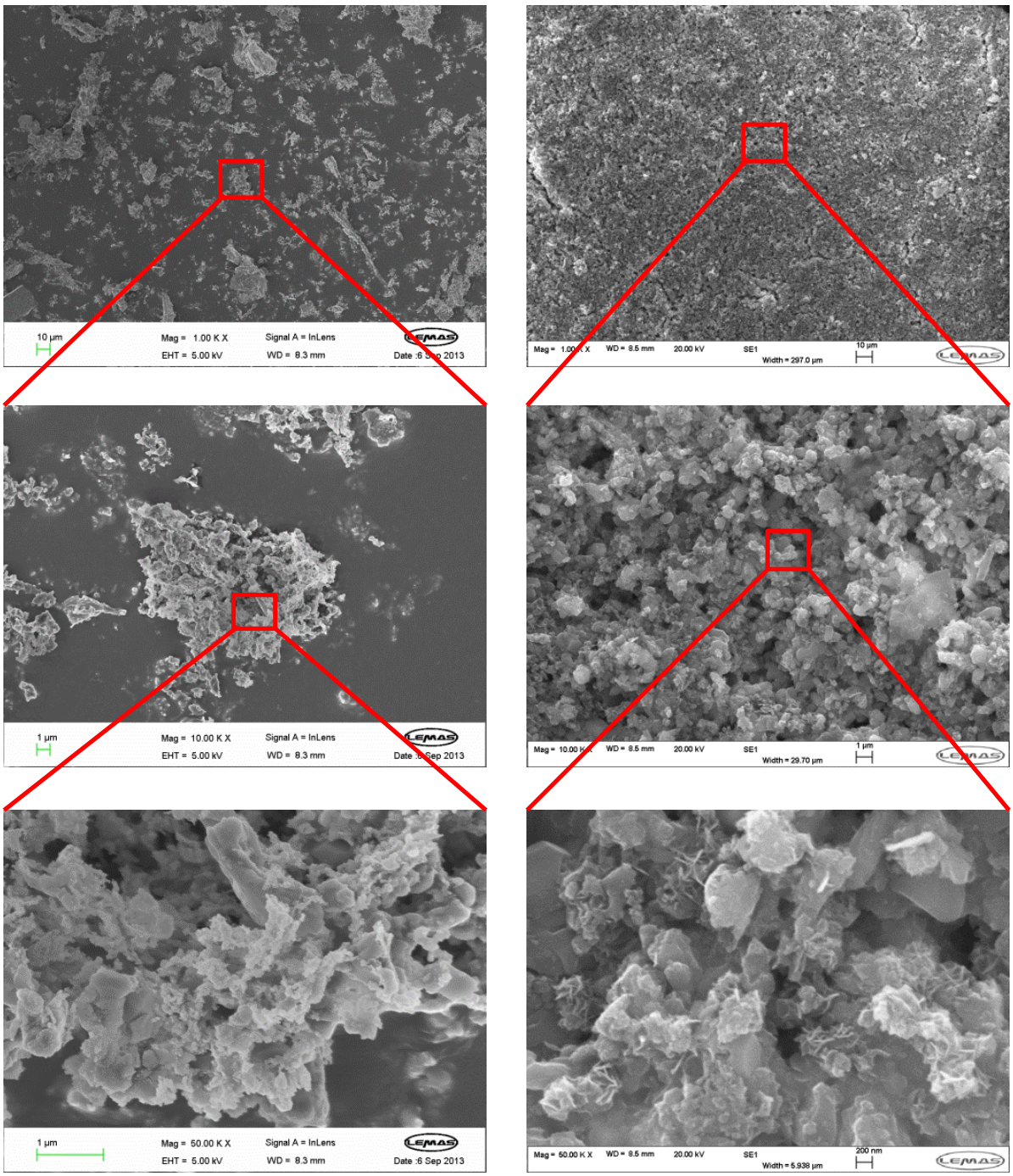

Figure 4.13: Scanning electron microscopy (SEM) images of wood (biomass) bottom ash particles used for the ice nucleation studies. The left-hand side are SEM images from wood ash sample sieved to ≤ 40 µm, while the right-hand side panels represents images of the same sample but recovered from 0.1 wt% wood bottom ash suspension. The magnification and scales are indicated at the base of each SEM image panel.

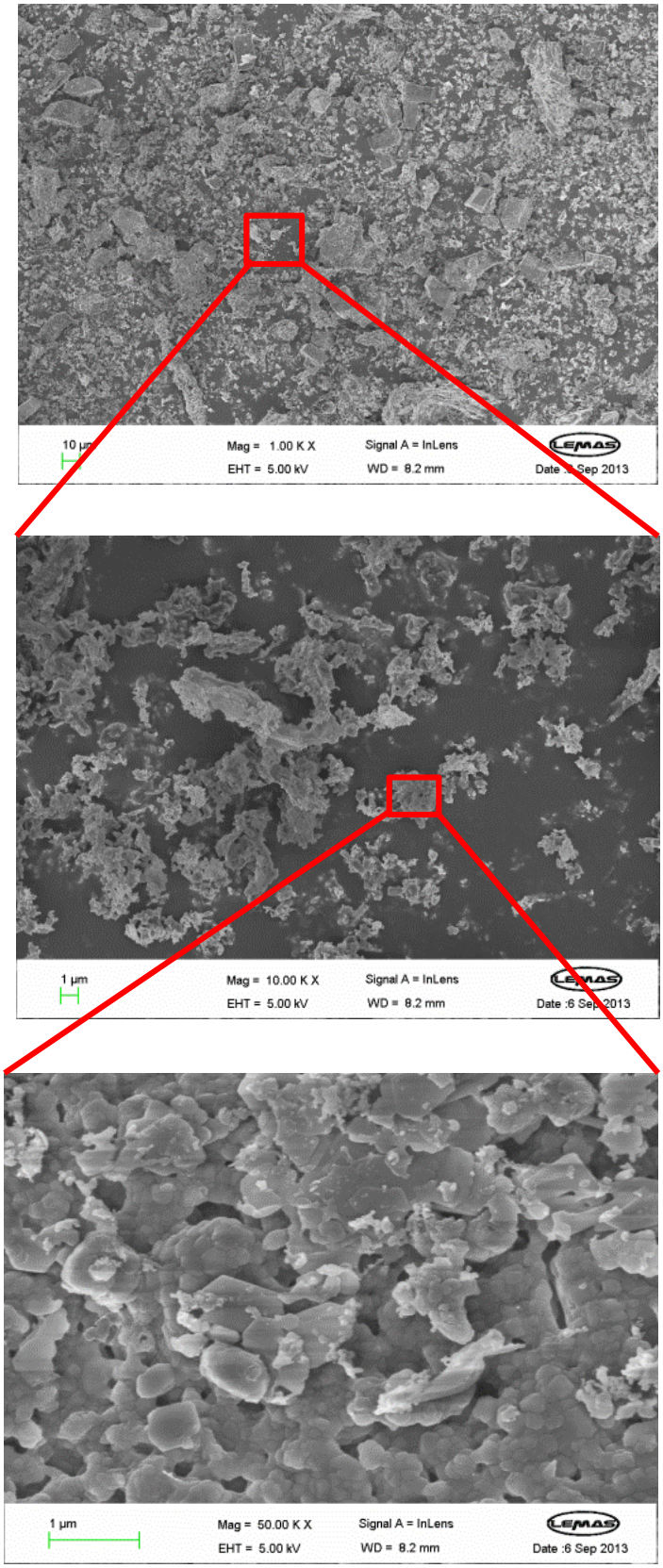

Figure 4.14: Scanning electron microscopy (SEM) images of domestic bottom ash sample used for the ice nucleation studies. The three panels are SEM images of domestic ash particles sieved to ≤ 40 µm sized particles. The magnification and scales are indicated at the base of each SEM image panel.

The SEM images of coal bottom ash particles are shown in Figure 4.15. The particles were highly agglomerated and comprised smaller particles compared to CFA. The bottom ash particles generally showed smaller particles but fused. This was confirmed by the laser diffraction particle size distribution results which showed that an average particle size for the bottom ashes were smaller than that of the CFA particles.

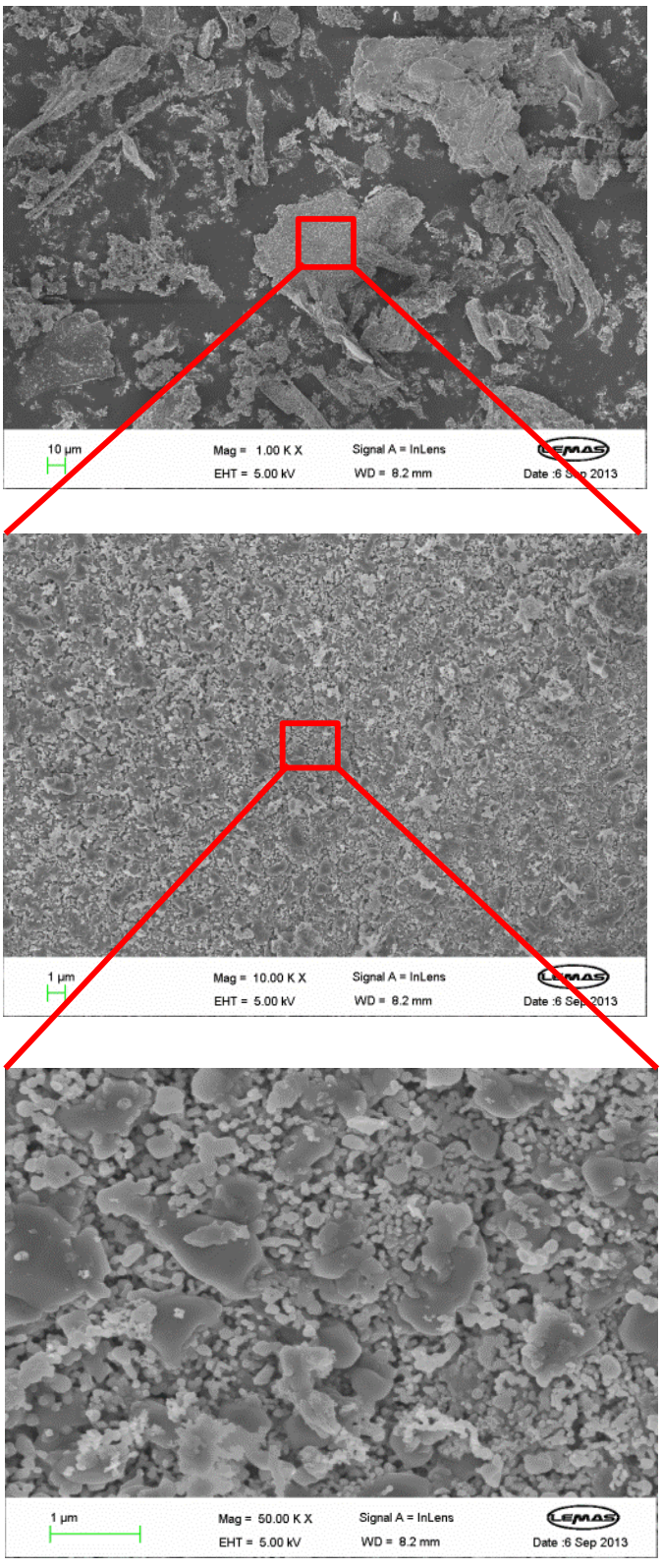

Figure 4.15: Scanning electron microscopy (SEM) images of coal bottom ash sample used for the ice nucleation studies. The three panels are SEM images of coal ash particles sieved to ≤ 40 µm sized particles. The magnification and scales are indicated at the base of each SEM image panel.

4.4.3 Elemental analysis of ashes by energy-dispersive X-ray spectrometry (EDS)

Another spectroscopic method was explored to confirm the mineral compositions of combustion ashes in this study. The method, energy-dispersive X-ray Spectrometry (EDS), elucidates the elemental composition of materials. From the elemental composition, possible combinations for the actual mineral identified with other techniques can be checked. EDS uses beam of electrons to knock off an electron at the surface of material, then, during a relaxation process, the energy emitted by the excited electron is measured as a characteristic of that element (Newbury et al., 1987; Goldstein et al., 1997).

The EDS machine used for this study was coupled to the scanning electron microscopy (SEM) instrument, during analysis some particles were isolated and studied. The same sample prepared for the SEM imaging was used for the EDS analysis. The EDS results for CFA, wood, domestic, and coal bottom ashes are shown in Figures - 4.16, 4.17, 4.18, and 4.19, respectively.

The elements platinum (Pt) and palladium (Pd) showed in the EDS spectra are artefacts, which come from the coating layer used on the sample before the measurements; hence, they should be ignored in interpreting the results. The height of the peaks in counts per second per energy unit (cps/eV) (ordinate) indicates the intensity of the signal for that particular element while the abscissa indicates the X-ray energy (KeV) which is a characteristic of each element at each excitation level. The background spectra were removed in all the plots shown. The spectra labels (spec_1, spec_2, …, spec_n) on the SEM images are the locations from which the EDS scanned.

The EDS results are highly dependent on the location of the scan; therefore, in a case where a sample is not uniform or ineffectively homogenised (for example, by grinding), then elemental results obtained may just be the composition of that location. Here, the EDS results were only used to confirmed the XRD mineral assay and were not used to report the relative amount of each element present.

The key elements found in the CFA EDS spectra as shown in Figure 4.16 are: Al, Si, O, Ca, Fe, Mg, Na, C, and K. Based on the locations analysed, dominant elements were Al, Si, Fe, O, and C. These dominant elements are components of the minerals with higher percentage, from the XRD results shown: SiO_2 (13.1%), $Al_6Si_2O_{13}$ (13.5%), and FeS_2 (7.2%). This result agrees with EDS spectra of ultra-fine ash particles, which is reported

to comprise high levels Ca, Si, and Fe (Chen et al., 2005). However, carbon (C) showed a high count in the EDS spectra but is not part of the minerals highlighted; this suggests that C may be a major composition of the amorphous components of the CFA.

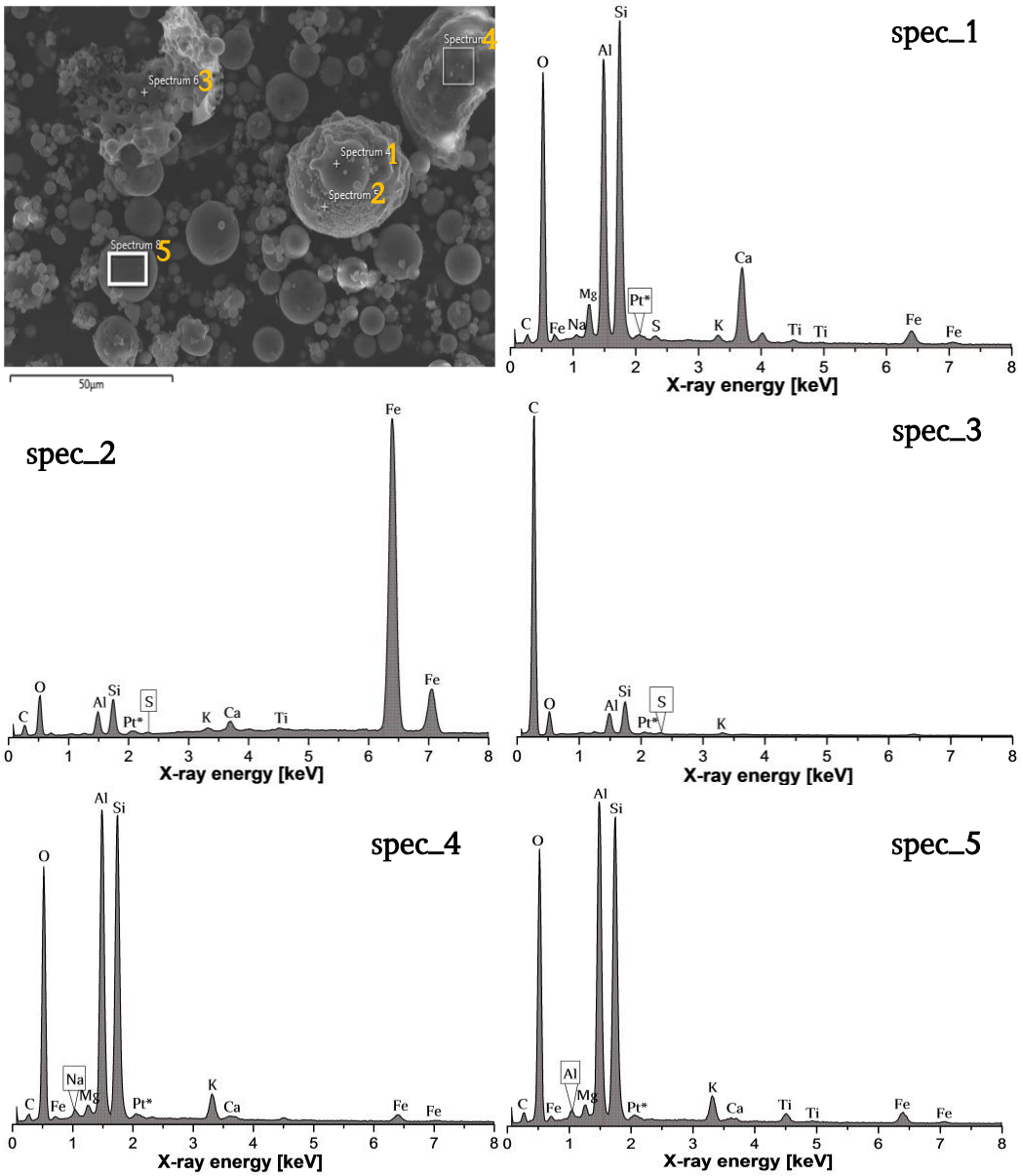

Figure 4.16: Elemental composition of coal fly ash obtained from energy dispersive X-ray spectroscopy coupled to SEM. Platinum (Pt) was used to coat the ashes before SEM/EDS was obtained; hence, it is asterisked on the spectra. The backgrounds of the spectra were subtracted before plotting. The ordinate indicating count per second per energy unit (cps/eV) is not shown in the plots.

The EDS spectra of wood bottom ash are shown in Figure 4.17. Elements identified include: C, O, Ca, Si, Mn, Fe, Mg, S, Na, C, and K. High counts were observed for C, Ca, O, Mg, and Ca. From the XRD, wood bottom ash mineralogy showed that $CaCO_3$ / $CaSO_4$ (23.6%) and SiO_2 (14.4%) are the major components. Therefore, high elemental contents of Ca and O are from the calcite/gypsum mineral found in the ash. Although

SiO_2 is a major mineral also found in the ash but the amount of Si is substantially lower. It could be that the location where the EDS was focused on did not contain quartz in a significant proportion. This is one disadvantage of this method since not all the particles are assayed. However, the elements identified are consistent with the mineralogy assay by the XRD method.

Similarly, domestic ash EDS spectra (Figure 4.18) showed similar elements as wood bottom ash in a relative proportion to the mineral compositions as shown in Figure 4.17.

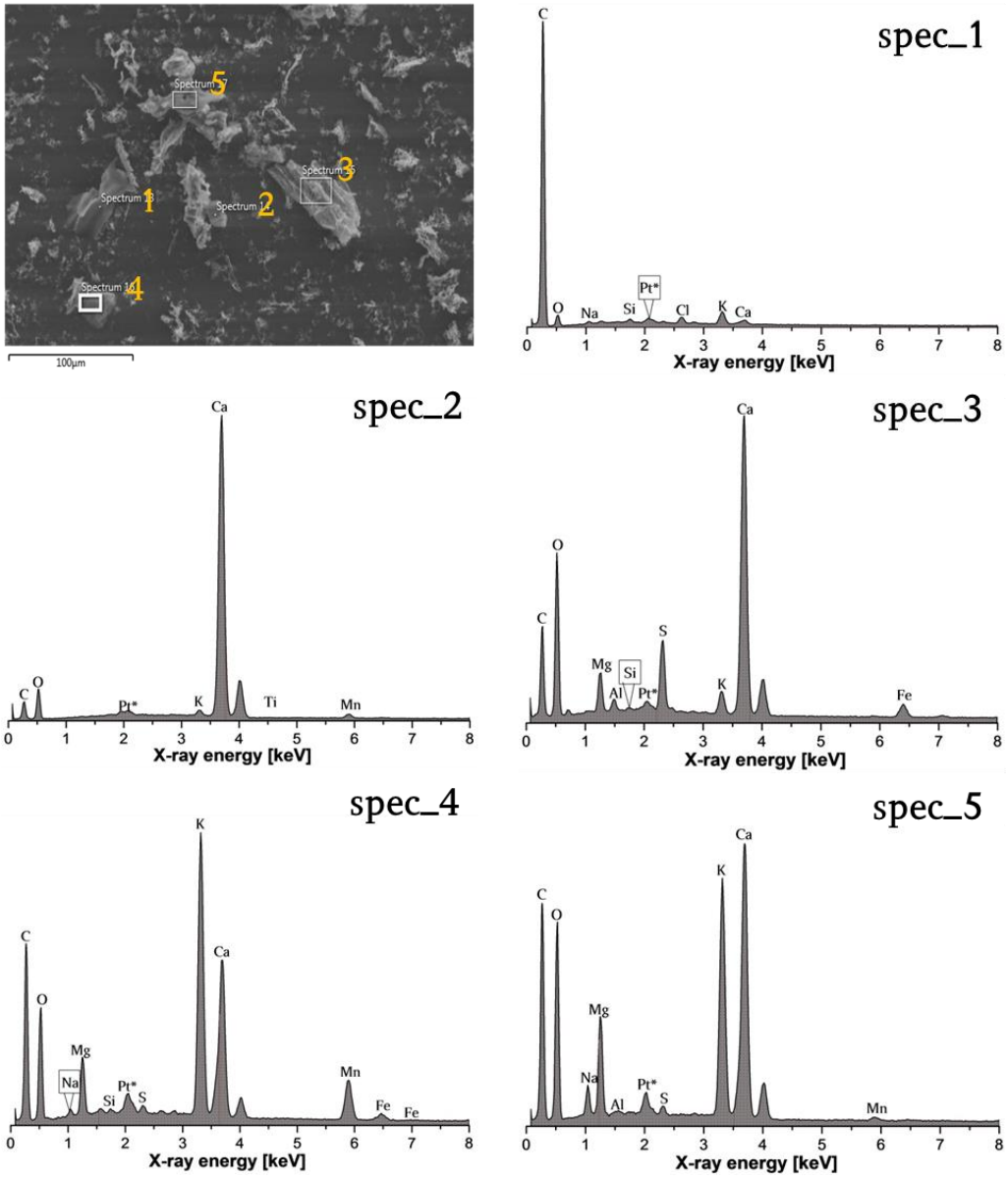

Figure 4.17: Elemental composition of wood bottom ash obtained from energy dispersive X-ray spectroscopy coupled to SEM. Platinum (Pt) was used to coat the ash particles before SEM/EDS was obtained; hence, it is asterisked in the spectra. The ordinate indicating count per second per energy unit (cps/eV) is not shown in the plots.

Interestingly, potassium was identified to have high counts but none of the minerals reported by the XRD method contained potassium. Potassium is frequently found in combustion particles coming from wood combustion (Jenkins et al., 1998), and may be part of the amorphous composition that was measured by XRD as 23.7%.

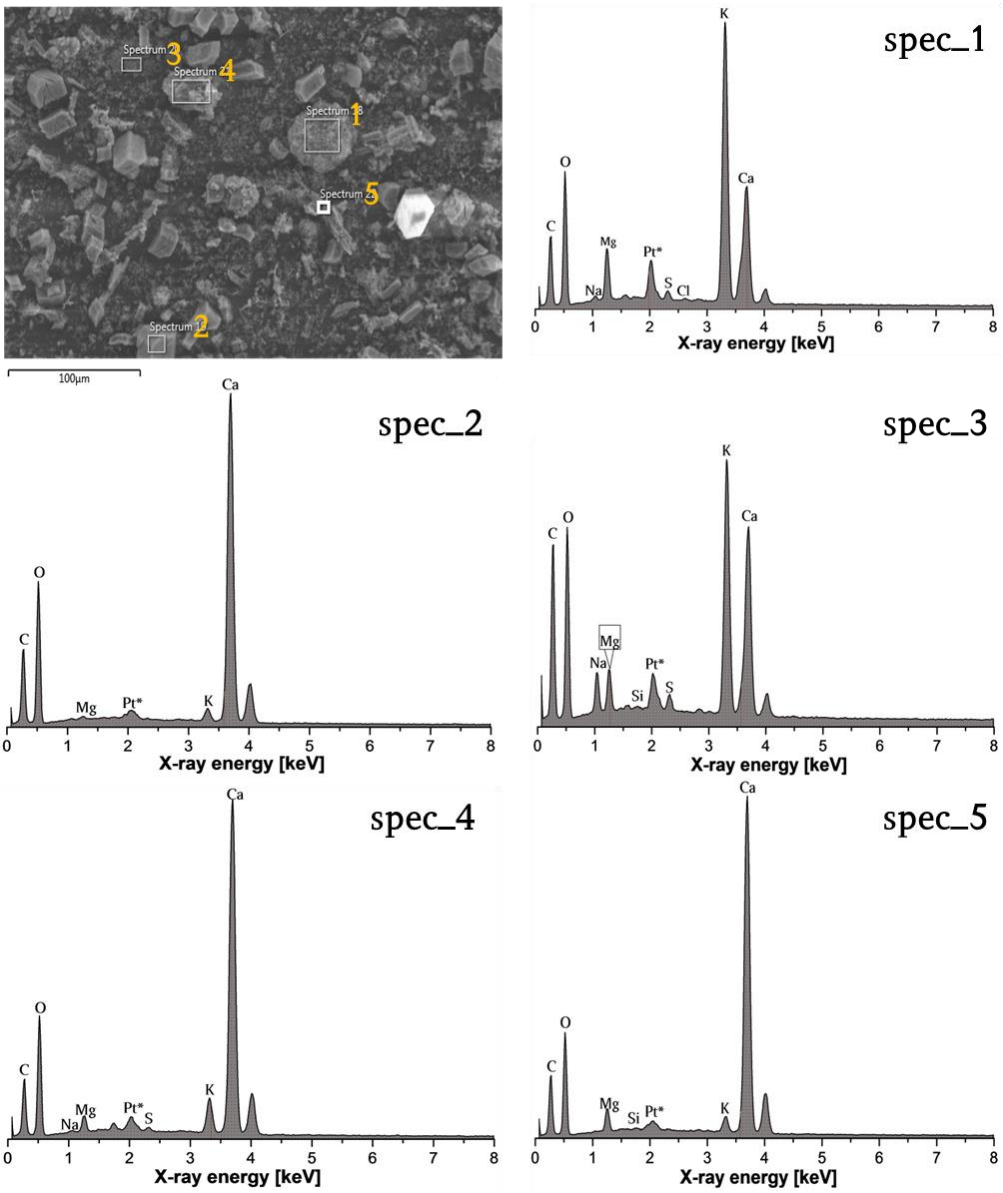

Figure 4.18: Elemental composition of domestic bottom ash obtained from energy dispersive X-ray spectroscopy coupled to SEM. Platinum (Pt) was used to coat the ashes before SEM/EDS was obtained; hence, it is asterisked in the spectra. The ordinate indicating count per second per energy unit (cps/eV) is not shown in the plots.

Coal bottom ash EDS spectra are shown in Figure 4.19. Again the elemental compositions identified in coal ash are: C, O, Ca, Si, Mn, Fe, Mg, S, Na, C, and K; with dominant ones as O, Si, Al, Ca, S, and Mg. The minerals found in larger proportion from the XRD analysis showed that these elements are the compositional elements of those minerals: SiO_2 (7.5%), $Al_6Si_2O_{13}$ (10.4%), FeS_2 (4.9%), and $CaCO_3$ / $CaSO_4$

(7.7%). The elemental compositions are similar to CFA elemental compositions, it will be sensible to establish that both ashes came from similar fuel source although they were generated differently. Sulphur (S) was also identified and this could be part of the pyrite (FeS_2) mineral reported. In the previous CFA, one would expect S to be completely removed at the combustion temperature reported which was high but in the case of the coal bottom ash some S contents of the solid fuel may still remain.

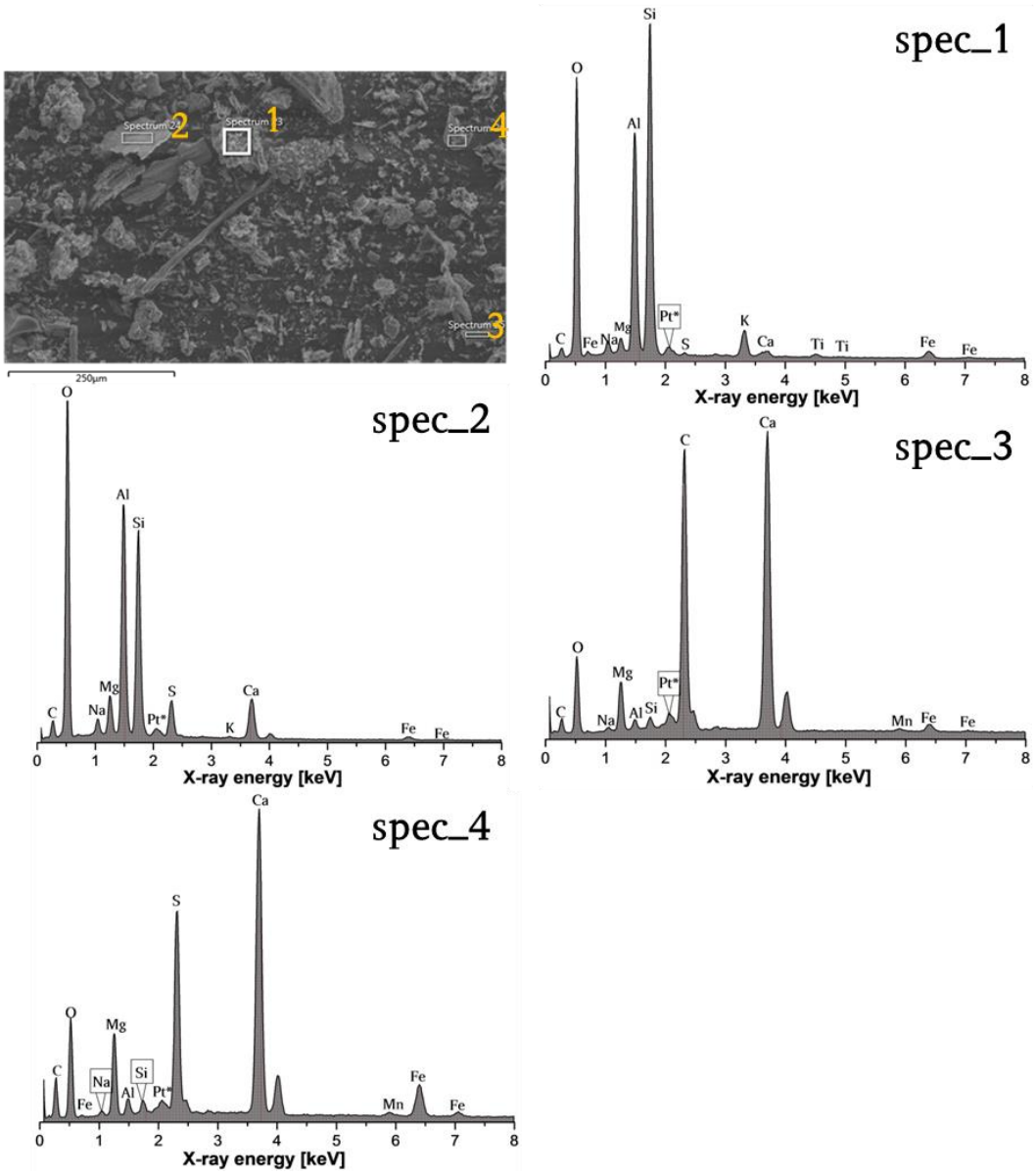

Figure 4.19: Elemental composition of coal bottom ash obtained from energy dispersive X-ray spectroscopy coupled to SEM. Platinum (Pt) was used to coat the ashes before SEM/EDS was obtained; hence, it is asterisked in the spectra. The ordinate indicating count per second per energy unit (cps/eV) is not shown in the plots.

4.4.4 Particle size analysis of combustion ashes – laser diffraction method and BET

The SEM images previously shown can be used to deduce the particle sizes of the combustion ashes; however, aside CFA, other ashes exhibited irregular shapes. This makes it challenging to use this method in estimating the particles sizes of these particles. Therefore, another method was adopted for particle size analysis: this was done by using a laser diffraction technique to look at the distribution of particle sizes. The advantage of this method is that, particles size analyses were carried out in the same medium as the freezing experiments; i.e. in aqueous suspension.

In laser diffraction method, as the name implies, a laser beam illuminates the sample, then the difference in the angular intensity of the diffracted light caused by the particles is measured. The instrument compares this information with the volume of a sphere that will give equivalent scattering. The instrument uses Mie light scattering theory in estimating the equivalent volume of the particles (Malvern, 2012; De Boer et al., 2002). For accurate measurements, the refractive index of the particles and the absorption factor need to be inputted.

For this analysis, a Malvern Mastersizer 2000E laser diffraction instrument was used. The instrument has a measuring potential of 0.02 μm to 2000 μm with an accuracy of about 1%, depending on the sample preparation. A refractive index of 1.62 and absorption value of 1.0 were used for CFA and coal bottom ash based on suggestions by Jewell and Rathbone (2009). In contrast, a refractive index of 1.65 and an absorption value of 0.1 were used for wood and domestic bottom ashes because of higher calcite content (> 10%) (Jewell and Rathbone, 2009). The particle size analysis results for CFA, wood, domestic, and coal bottom ashes are shown in Figure 4.20.

Two sets of measurements were made for each sample – ‘untreated’ and ‘stirred and agitated’. There was no prior dispersion of the ash sample before the ‘untreated’ measurement; in contrast, for the ‘stirred and agitated’, the ash sample was first made into suspension, put in an ultra-sonic bath for about 10 minutes and then left on a stirrer for at least 24 hours before measurements were taken. A similar approach had been previously adopted to break up aggregates of CFA particles (Brouwers and Eijk, 2003). Each plot was an average of three repeated measurements.

The two sets of measurements for CFA, with and without stirring for 24 hours overlapped indicating that the agitation process did not affect the particle sizes distribution or the mixing state. However, for wood, domestic, and coal bottom ashes, there was a shift in the distribution to smaller sizes that were similar, suggesting that the dispersion process assisted in breaking up ash aggregates in the suspension. The mode diameter measured for CFA was ~ 10 µm while that of the other ashes was ~ 8 µm.

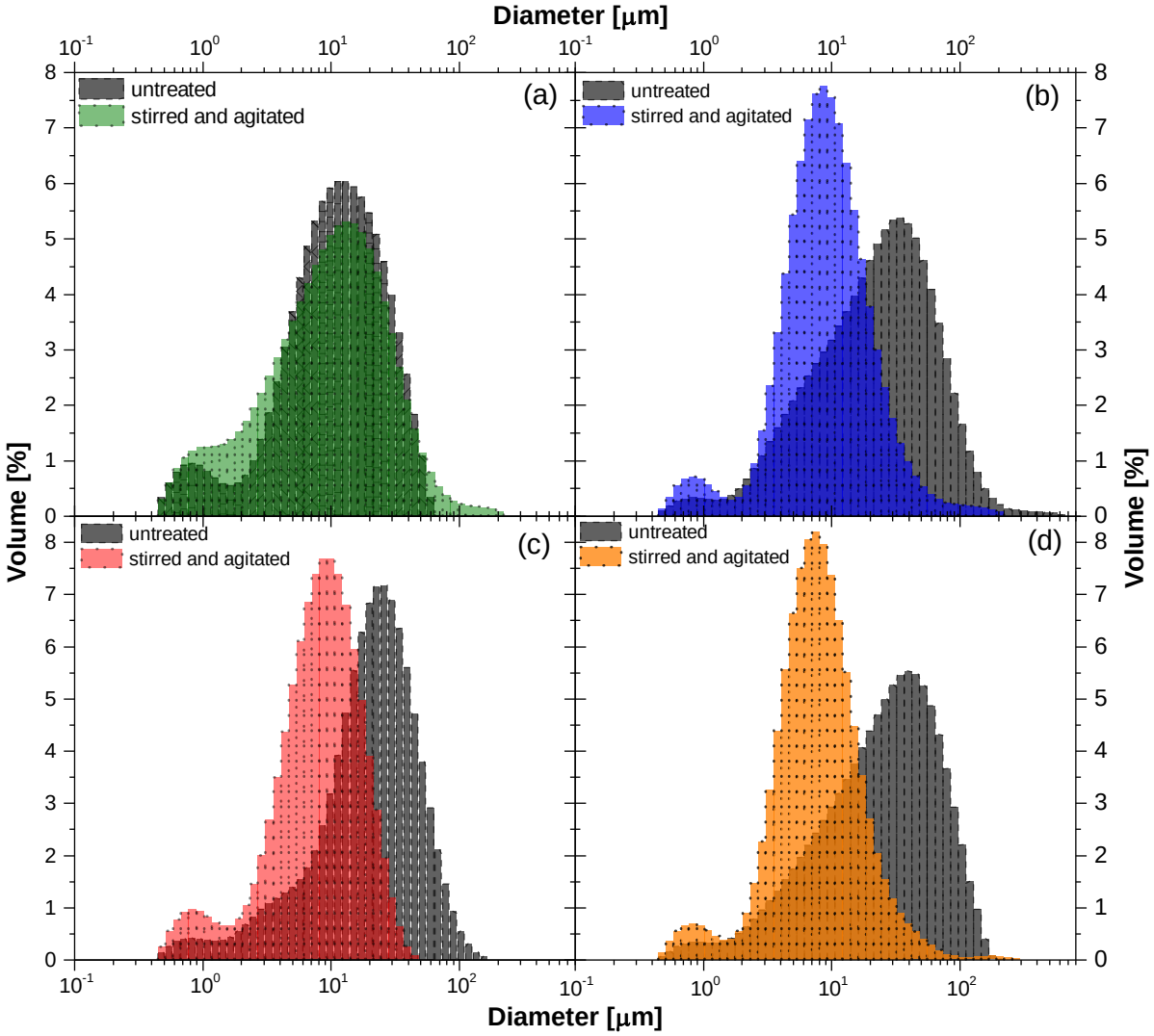

Figure 4.20: Particle size distribution of combustion ashes - coal fly ash, wood, domestic, and coal bottom ashes. The plot represented as 'untreated' indicates particle size distribution obtained without any prior dispersion measures such as mixing, mechanical or sonic agitation, stirring, while 'stirred and agitated' denotes particle size distribution of ash suspensions that were placed in an ultra-sonic bath for about 10 minutes and later stirred for 24 hours before laser diffraction measurements.

Laser diffraction technique has uncertainty associated with measuring larger particle (Eshel et al., 2004); errors could be introduced by particle swelling, agglomeration, air bubbles inclusions or variation in the refractive indices due to temperature variations

(BSI). Combustion ashes are reported to have swelling properties when suspended in water (Etiégni and Campbell, 1991; Phani Kumar and Sharma, 2004). This effect and particles agglomeration could contribute to the larger particle sizes observed for these ashes. This could have been tested with the use of the instrument's sample chamber equipped with an ultra-sonic probe but this test was not performed due to insufficient sample. The particle sizes of CFA estimated from the SEM images were < 20 µm and 90 % of the particles were smaller than 8 µm. Due to the nature of CFA particles, which forms cenospheres and plerospheres (Fenelonov et al., 2010), the laser diffraction could give a false sizing of the larger particle whereas the smaller particles were dominant by volume.

4.5 Effect of dispersant on particles size distribution of CFA

The effect of particles aggregation is one limitation in particle size analysis by laser diffraction method. This becomes worse when the material under investigation comprises some minerals with cementing properties such as alumino-siliceous minerals. In soil particle analyses, a dispersant is usually added to the suspension to disperse aggregates, and this has been shown to be very useful (Oorts et al., 2005).

From the mineralogy analyses, combustion ashes contain some minerals that could enhance coagulation. The particle size distribution plot in Figure 4.20 shows that some particles were above 40 µm, higher than the expected particle sizes because the ash sample was sieved with a 40 µm mesh before the laser diffraction analysis. To test the effect of aggregation, a common dispersant was used – sodium hexametaphosphate (SHMP) and sodium carbonate (SC). SHMP and SC solution was prepared by dissolving 3.3 g of SHMP and 0.7 g of SC (Tucker, 1988). Varied volumes (1.0 mL, 2.5 mL, 5.0 mL, and 10.0 mL) of the solution were added to 0.1 wt% CFA suspension, then placed in an ultra-sonic bath for about 10 minutes and shaken overnight (~ 26 hours) using a mechanical shaker (Stuart Orbital shaker SSL1 model).

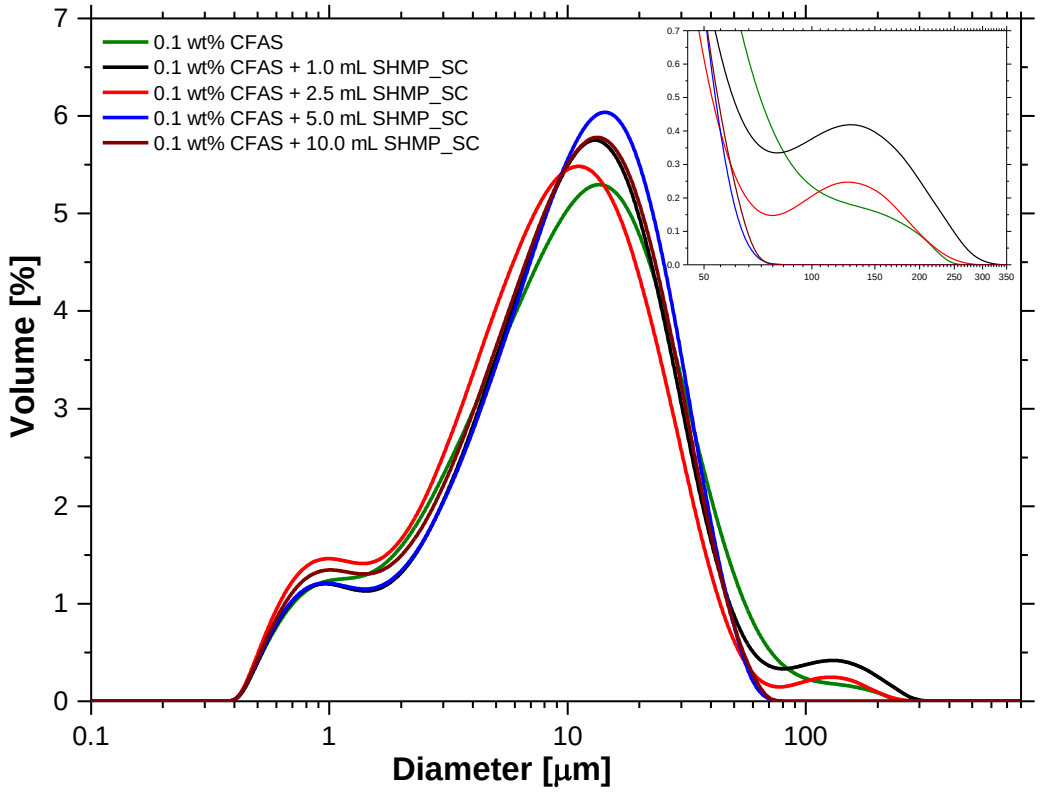

Figure 4.21: Effect of dispersant on the particle size distribution of coal fly ash (CFA). The dispersant used is standard sodium hexametaphosphate (SHMP) and sodium carbonate (SC) at varying volumes. Different colours on the plot show the different volume combinations of the dispersant (SHMP_SC) to the ash suspensions. Each plot is an average of three repeated runs ($\sigma < 0.01$) which means that the difference between the experiments were statistically insignificant.

The results of the particle size distribution of the different mixtures are shown in Figure 4.21. No significant changes were observed for mixtures of 0.1 wt% CFA and 1.0 mL or 2.5 mL solution of SHMP + SC. In contrast, 0.1 wt% CFA containing 5.0 and 10.0 mL of SHMP + SC showed no aggregation at around 70 – 350 µm diameter (see the Figure inserted in Figure 4.21). For all the volumes added, no observable effect was seen at the 0.4 µm – 1 µm diameter ranges for CFA, which is of more interest to this work, generally, due to the longer residence time of smaller particles or relative densities. This test showed that SHMP + SC solution was ineffective in dispersing the ash aggregates in the suspension.

4.6 Concentration of dissolved ions in ash suspensions

Combustion ashes were made into suspensions in order to carry out freezing experiments. This can cause some components of the ash to dissolve and the dissolved ions may modify the surface of the insoluble particles in the suspension. Obviously, from the mineralogy given in section 4.4.1, some components of the ashes may be

soluble in water, which served as a medium in preparing the suspensions. To measure the concentration of dissolved ions (both cations and anions) in the ash suspensions, a filtrate of ash suspensions containing 0.1 wt% CFA, wood, domestic, and coal bottom ashes were obtained by filtering it with a sterilised minisart 0.20 µm non-pyrogenic single-use filter unit (Satorius Stedim Biotech, UK). The filtrate was introduced to an ion chromatography instrument (DX-100 Ion Chromatograph, Dionex) to measure the dissolved cations and anions in it.

Ion chromatography (IC) method uses an ion-exchange principle to quantify the ion contents of an eluent. The eluent (filtrate) is passed through to the column with the aid of a pump and an injector system. The ion contents of the eluent is retained in the column and pass onto the detector which then estimate the amount of the ion based on a pre-recorded standards on the system (Mulik et al., 1976; Poole, 2004). The column can be cation-exchange or anion-exchange depending on ions of interest. However, before each analysis a blank of the sample is usually passed through the system to clean up the tubing; this process reduces the memory effect in sample measurements (Haddad and Jackson, 1990). In IC, retention times are used to identify individual ions present in the eluents.

The IC results for combustion ashes are shown in Table 4.4. Major cations measured across all ash filtrate solutions were: sodium ions (Na^+), calcium ions (Ca^{2+}), potassium ions (K^+), magnesium ions (Mg^{2+}), and lithium ions (Li^+) - which was only found in CFA filtrate. The anions measured were: acetate ($C_2H_3O_2^-$), nitrite (NO_2^-), nitrate (NO_3^-), chloride (Cl^-), and sulphate (SO_4^{2-}). Wood bottom ash and domestic bottom ash filtrate solutions had higher concentrations of K^+, 140.23 ppm and 116.21 ppm, respectively, whereas CFA and coal bottom ash showed lower concentrations. Potassium ions is a characteristic ion found in biomass combustion by-products (Murphy et al., 2007); therefore, it is not surprising that CFA and coal bottom ashes had lower K^+ concentrations in their filtrate. Both CFA and coal bottom ashes were generated from similar fuel. A positive correlation was observed for K^+ and Na^+, which indicates that both ions usually undergo similar chemistry; however, Na^+ was relatively low in CFA filtrate. Lithium ion was only found in CFA and in a smaller concentration; this may be associated with the coal fuel. Lithium has been detected in pulverised coal (Gilmour et al., 2004; Lipsky et al., 2004). All ashes had calcium ions in them in the order: wood ash<CFA<domestic ash<coal ash. Calcium ions showed strong positive correlations with $C_2H_3O_2^-$ and Mg^{2+} ions, R = 0.885 and R = 0.833, respectively (see

Appendix C1). Acetate ions can form a complex with Ca^{2+} (Hendershot et al., 2007) but the correlation with Mg^{2+} ions can be explained with similarities in the chemistry of both Ca^{2+} and Mg^{2+} ions.

Table 4.4: Concentrations (ppm) of dissolved ions (both cations and anions) in combustion ash solutions. The filtrate used for the ions analyses were obtained by passing 0.1 wt% suspensions of the CFA, wood (biomass), domestic, and coal ashes through a 0.20 µm sterilized non-pyrogenic filter. The results shown here were obtained after subtracting the ion concentrations of the blank solution (ultra-pure water – 18.2 MΩ.cm resistivity). The blank solution was also subjected through the same filtering process.

Ions	**Chemical formulae**	**Combustion ash samples/ concentrations (ppm)**			
Anions		CFA	wood bottom ash	domestic bottom ash	coal bottom ash
Acetate	$C_2H_3O_2^-$	-	1.13	-	76.26
Nitrite	NO_2^-	0.06	-	0.01	0.01
Nitrate	NO_3^-	0.70	0.84	-	0.78
Chloride	Cl^-	-	2.52	0.07	1.19
Sulfate	SO_4^{2-}	9.51	30.22	12.21	111.99
Cations					
Sodium	Na^+	0.13	12.32	4.94	7.71
Calcium	Ca^{2+}	4.46	3.55	14.49	26.75
Lithium	Li^+	0.37	-	-	-
Potassium	K^+	0.64	140.23	116.21	0.89
Magnesium	Mg^{2+}	0.23	0.28	1.22	0.83

For the anions, the concentration of SO_4^{2-} ions was highest in coal bottom ash and least in CFA. The same concentrations should be expected in both filtrates but in fact, they are different since both ashes were obtained at different combustion conditions. While CFA was generated in a high temperature combustion system, coal bottom ash was at lower temperatures as described in section 4.2.2. During CFA, the possibilities of losing the SO_2 components of the coal are higher due to other nucleation mechanisms going on in the emission process. Sulfate concentration values for wood and domestic ashes were comparable as would be expected as they were generated from similar fuel source and in a similar combustion condition. Interestingly, SO_4^{2-} ions showed a very strong correlation (R = 0.984) with ions $C_2H_3O_2^-$ ions, and both ions were measured in coal bottom ash but only SO_4^{2-} in CFA. Although, sulphate ions showed a strong relationship with Ca^{2+} ions that could be due to a reduction in the activation energy in forming compound with it, the correlation with $C_2H_3O_2^-$ is unclear. Nitrite and nitrate ions were relatively low across the filtrate of all combustion ashes investigated as well as Cl^- ions.

4.7 Variation in the pH of ash suspensions

The filtrates obtained from the ash suspensions as described in section 4.6 were tested to know their pH as a result of the dissolved ions in them. pH, which is the negative logarithm of the hydrogen ion concentration, for the ashes were: CFA (6.70), Wood bottom ash (9.27), domestic bottom ash (9.01), and coal bottom ash (8.57). CFA showed the lowest pH value; this could be due to the dissolution of some acidic gases such as CO_2 and SO_2 that are usually trapped in the cenospheres of CFA particles. In addition, the presence of these gases may contributed to this low pH but the correlation test showed a high negative R value (-0.988) for NO_2^- ions showing that the pH was not dependent on NO_2^- or NO_3^- ions. Sometimes, the low pH of CFA could be neutralised by the dissolution of basic oxides such as calcium oxides (Roy, 2011).

On the other hand, wood (biomass) bottom ash had the highest pH value. There were high concentrations of cations such as potassium ions (K^+) – 140.23 ppm, sodium ions (Na^+) - 12.32 ppm and calcium ions (Ca^{2+}) – 3.55 ppm present in it. These cations are commonly known to be associated with biomass combustion by-products (Ebert et al., 2011; Baustian et al., 2012; Pagels et al., 2013). The pH showed strong positive correlation with Na^+ ions (R = 0.851) and K^+ (R = 0.755); indicating that these ions could have influenced its high pH value. Domestic bottom ash suspensions (pH = 9.01) showed similar dissolved chemical components as wood bottom ash; however, with higher Ca^{2+} and Mg^{2+} ions concentrations, 14.49 ppm and 1.22 ppm, respectively. Coal bottom ash pH value is at the borderline of CFA and wood ash pH values. Uniquely, it has the highest sulphate ions (SO_4^{2-}) – 111.99 ppm; this could have served as a buffer to the high pH values common with the bottom ashes.

4.8 Chapter summary

Soot samples generated from eugenol and n-decane fuel were similar to soot obtained by different methods and from other fuel sources. Evidence of the fractal nature of soot particles and accretion phenomenon were observed from their morphologies. The Raman spectra for eugenol and n-decane soot particles were similar to other soot types reported in the literature, thereby, giving confidence that the material used for the ice nucleation studies were good representative of atmospheric soot. The chemical composition reported in previous studies (Wilson et al., 2013; Baeza-Romero et al., 2010) gave a clue of the EC/TC and PAHs compositions, which may give hints on the

small differences observed in the ice nucleation behaviours of eugenol and n-decane soot (Chapter 5).

All combustion ashes showed similar mineralogies. The mineral compositions of CFA particles did not show any significant difference for the sieved sample (≤ 40 μm) and the bulk sample. The EDS results were consistent with the XRD results indicating that irrespective of the method applied in the mineralogy assay, the crucial mineral components of the ashes were appropriately measured. The distribution of particle sizes showed a range of approximately 0.4 μm to 30 μm, which is similar to particle size range measured in the atmosphere. However, it should be stated here that there is greater uncertainty in the size measurements above 8 μm due to problems pose by ash aggregates. This was clearly observed in the laser diffraction measurements but the aggregation of particles was reduced when the suspensions were agitated (Figure 4.20). This did not pose a major problem as will be seen from the ice nucleation results in Chapter 6. The results obtained from the generation and characterisation of soot and combustion ashes aided in understanding the ice nucleation behaviour of these materials in mixed-phase clouds conditions.

Chapter 5

Ice nucleation by eugenol and n-decane soot

5.1 Freezing by eugenol and n-decane soot

The two soot types (enegenol and n-decane) were generated for use in this ice nucleation study as described in the chapter 4 of this thesis. This section describes the results obtained from the ice nucleation experiments of eugenol and n-decane soot particles in suspensions using the two experimental set-ups (µL- and nL-NIPI) described in chapter 3. All results are presented alongside the discussion in the following sub-sections.

5.1.1 Results from freezing experiments by eugenol and n-decane soot in the µL-NIPI

Before freezing experiments were carried out with eugenol and n-decane soot suspensions, a baseline was determined by freezing ultra-pure water (18.2 MΩ.cm resistivity) in the µL-NIPI. Detailed description of this instrument and the baseline experiments was previously described in the chapter 3. All suspensions of eugenol and n-decane soot used for these experiments were prepared by dispersing a known amount of eugenol or n-decane soot into a known volume of ultra-pure water, introduced to an ultra-sonic bath and stirred (details are described in chapter 3). Freezing results obtained for the various concentrations of soot suspensions using a µL-NIPI are shown in Figure 5.1.

From the results shown in Figure 5.1, it is clear that suspensions containing eugenol and n-decane froze heterogeneously in the immersion mode ice nucleation. Suspensions containing 0.1 wt%, 2.0 x 10^{-2} wt%, 2.0 x 10^{-3} wt%, and 2.0 x 10^{-4} wt% of eugenol soot (1st panel) showed varied freezing curves. Droplets of eugenol soot suspensions froze in the range of ~ -14 °C to ~ -24 °C. The gradient of the fraction of droplets frozen was relatively steep, i.e. with most freezing taking place within a few degrees, compared to fertile soil dust which the slope was less steep (O'Sullivan et al., 2014).

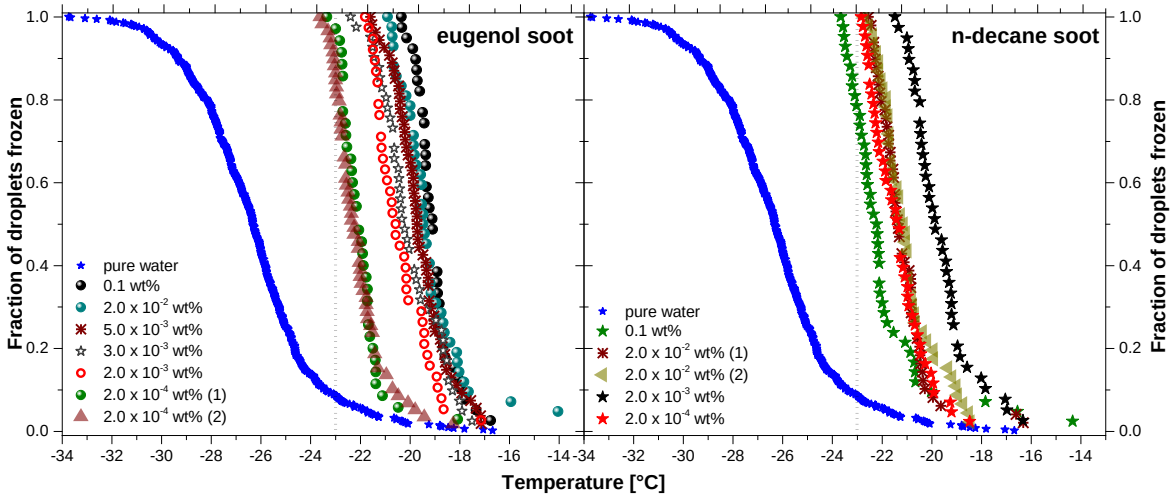

Figure 5.1: Freezing behaviour of eugenol soot particles from the µL-NIPI experiments. All droplets of soot suspension used were 1.00 ± 0.03 µL. The two panels represent fraction of droplets frozen for eugenol and n-decane soot. The blue data points on both panels represent the freezing of ultra-pure water (18.2 MΩ.cm resistivity), which was used to establish the baseline freezing for µL-NIPI experiments. The black dashed line indicates the cut-off for heterogeneous freezing on µL-NIPI while all other points shows varied concentrations of the soot suspensions used.

Evidently, from the fraction frozen plot, most of the droplets froze at temperatures above -23 °C. In general, the higher concentrations (0.1 wt% and 2.0 x 10^{-2} wt%) of the eugenol soot suspension froze at higher temperatures than the lower concentrations (2.0 x 10^{-3} wt% and 2.0 x 10^{-4} wt%). This was in line with what would be expected - that for the same droplet size, an increase in particle's concentration is found to trigger freezing at higher temperatures than the lower concentrations (Broadley et al., 2012). Freezing experiments with eugenol concentrations of 5.0 x 10^{-3} wt% and 3.0 x 10^{-3} wt%, obtained from a stepwise dilution of 2.0 x 10^{-2} wt% did not show any significant difference in the freezing temperatures from that of 2.0 x 10^{-2} wt% (Figure 5.1).

Freezing curves of n-decane soot as shown in the second panel on Figure 5.1 was slightly different from that of eugenol soot. No clear trend was observed between the fractions of droplets frozen for the various concentrations used in the study (0.1 wt%, 2.0 x 10^{-2} wt%, 2.0 x 10^{-3} wt%, and 2.0 x 10^{-4} wt%). In contrast to the observation that freezing temperatures increase with concentration of particles immersed in a droplet (Murray et al., 2011; Broadley et al., 2012), droplets containing 0.1 wt% n-decane froze at a lower temperature range than droplets of 2.0 x 10^{-4} wt%. This is different from what would be expected for a suspension with a higher concentration of particles, this could be due to instability of the particles in the suspension and it is discussed in more details in section 5.4. Generally, more than 90% of the droplets froze above -23 °C with a temperature range of ~ -16 °C to -23.3 °C.

The differences between the freezing signatures of the two soot types could be linked to their different chemical compositions, hygroscopicity, morphology, and particles stability in suspensions which are discussed further in subsequent sections. However, both eugenol and n-decane soot particles froze heterogeneously in the immersion mode.

5.1.2 Results from freezing experiments by eugenol and n-decane soot in the nL-NIPI

In nL-NIPI experiments, the baseline used was the homogeneous freezing of ultra-pure water droplets of similar size range to the soot-containing droplets. Droplets of ultra-pure water (18.2 MΩ.cm resistivity) in the diameter range of ~ 40 μm to ~ 400 μm froze within the homogeneous freezing temperatures (-36 °C to -38 °C), with an exception of the few droplets that froze heterogeneously at the beginning which was discussed in chapter 3. Similar soot-containing droplets sizes were used for the freezing experiments in nL-NIPI and the fractions of droplets frozen from nL-NIPI for both eugenol and n-decane soot suspensions are shown in Figure 5.2.

Two concentrations (2.0 x 10^{-3} wt% and 2.0 x 10^{-4} wt%) were used for these freezing experiments because in the higher concentrations (0.1 wt% and 2.0 x 10^{-2} wt%), soot particles were found to aggregate which could pose a problem as discussed in section 5.3. For both concentrations of eugenol soot, freezing of the droplets started at ~ -21 °C to ~ -27 °C whereas n-decane soot had a broader freezing range, from about -21 °C to ~ -36 °C, though a few droplets froze from ~ -29 °C to -36 °C. There is possibility that these few droplets observed here contained active sites that were not as high as the rest of the droplets. Interestingly, no marked difference was observed for the frozen fractions of both concentrations (2.0 x 10^{-3} wt% and 2.0 x 10^{-4} wt%) even though their concentrations were a factor of 10 difference. The freezing temperatures of n-decane soot were slightly lower than that of droplets containing eugenol soot.

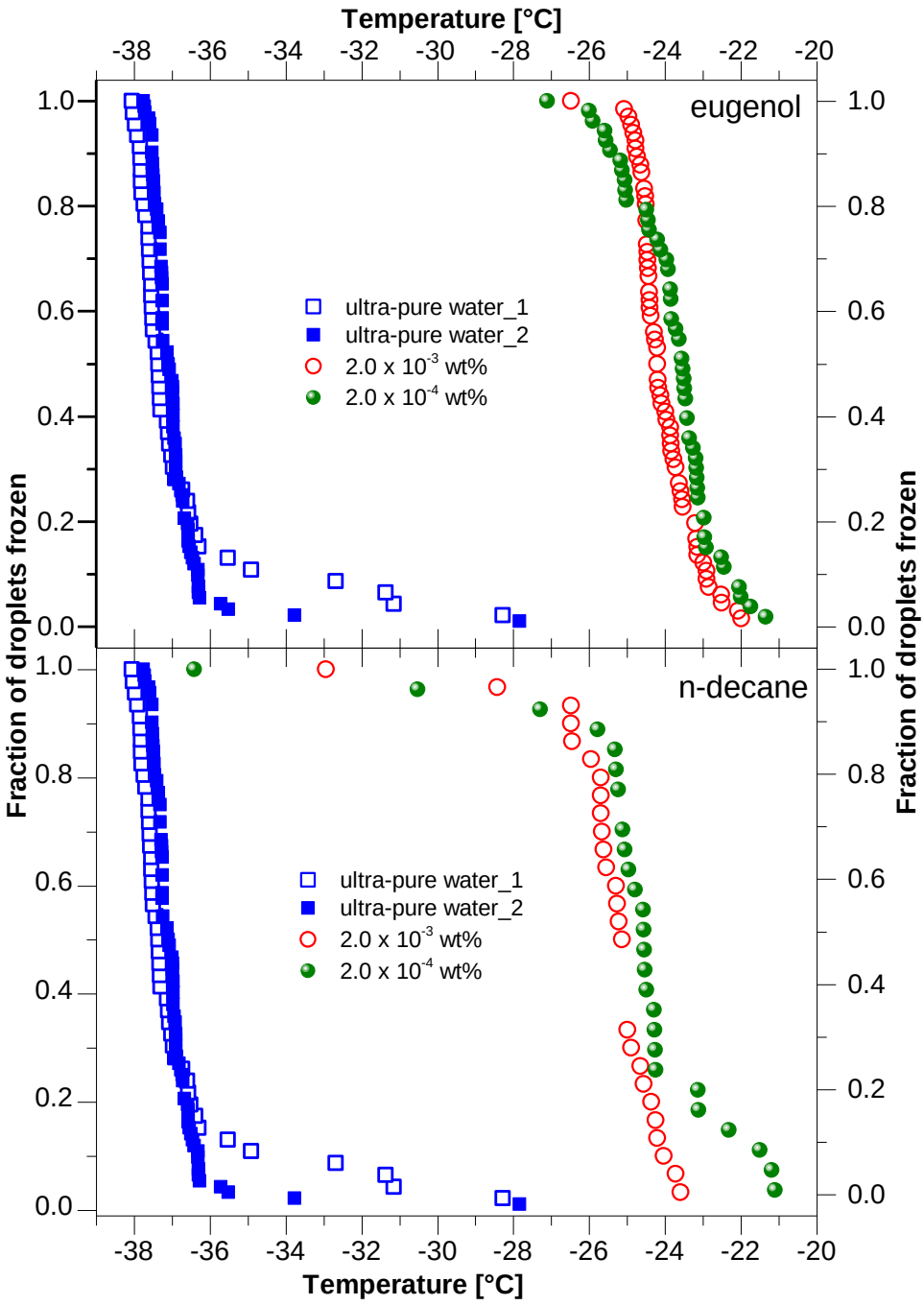

Figure 5.2: Fractions of droplets frozen for eugenol and n-decane soot obtained from the nL-NIPI set-up. The blue data points (open and filled cells) represent the freezing of ultra-pure water (18.2 MΩ.cm resistivity), which was used to establish the baseline freezing for the nL-NIPI experiments. The diameter sizes of droplets ranged from ~ 40 µm to ~ 400 µm.

5.2 Description of the ice nucleation efficiency of soot

In the past, many soot ice nucleation studies quantified their ice nucleation efficiency based on the freezing temperatures or the fraction of droplets activated to ice as a function of temperature e.g. Kireeva et al. (2009); DeMott (1990). The use of freezing temperatures to quantify ice nucleation abilities of particles does not only have a

setback of having discrepancies introduced by different experimental methods (or instruments) used, and cloud conditions at which the study is simulated - but, it also introduces difficulty in making a comparison between the ice nucleating efficiencies of other particle types in the atmosphere (Hoose and Möhler, 2012).

In this study, a singular model - which is time-independent, was adopted to describe the ice nucleation activity of eugenol and n-decane soot particles in the immersion mode. The reason for choosing this model over stochastic was earlier discussed in chapter 2. This model is used by many researchers in different studies to describe the efficiencies of IN, and detailed description of the model was given in chapter 2 of this thesis and in literature e.g. Broadley et al. (2012); Murray et al. (2012); Niedermeier et al. (2010); Hoose and Möhler (2012); Murray et al. (2011); Herbert et al. (2014). Briefly, the model estimates the cumulative number of active sites capable of nucleating ice per unit surface area of particles at a characteristic temperature. For this experiment, the unit surface area is per droplet. It is calculated with the following equation:

$$f_{ice}(T) = 1 - exp(-n_s(T)\sigma) \tag{5.1}$$

where f_{ice} is the fraction of frozen droplets at temperature (T), i.e. ice nucleation active fraction, n_s is the nucleation site density which is a function of temperature, meaning the number of nucleation sites per unit surface area of the particle, and σ is the surface area of the particles per drop.

The n_s here is defined as nucleation sites per surface area (SA) of the particles per drop which in this case, is that of eugenol and n-decane soot particles. The surface areas of eugenol and n-decane soot were measured by a Brunauer-Emmett-Teller (BET) nitrogen adsorption method as described in the previous chapter (see section 4.3.3). The SA for eugenol and n-decane soot was measured as 49.43 ± 0.89 m^2/g and 65.47 ± 0.81 m^2/g, respectively. The variation in the BET SA of eugenol and n-decane soot could be due to differences in the formation of soot particles, which can also be linked to the differences in soot source. It is established that the difference in soot types/properties may result from the differences in fuel sources, combustion conditions, and the fractal factor of a collection of soot spherules (Tesner and Shurupov, 1995; Wilson, 2011).

The use of n_s calculations to quantify the ice nucleation abilities of eugenol and n-decane soot will allow a direct comparison of their nucleation efficiencies to other soot types previously studied in similar conditions, and with other IN in the atmosphere. The nucleation site densities (n_s) of eugenol and n-decane soot are shown in Figure 5.3.

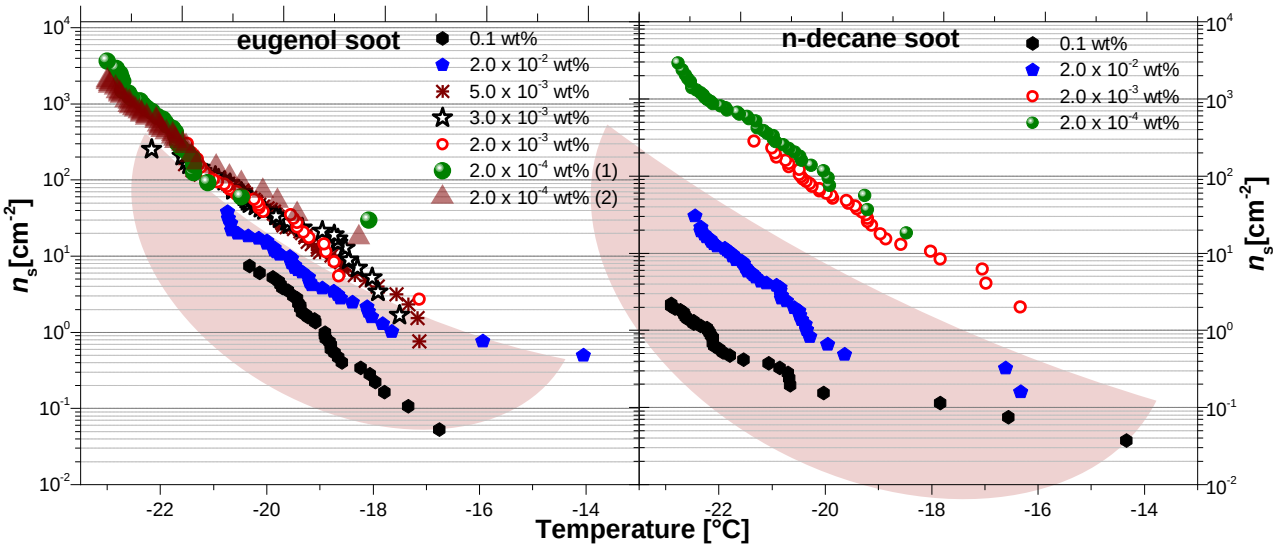

Figure 5.3: The cumulative number of ice nucleation active sites (n_s) for eugenol and n-decane soot particles reported at their characteristic temperatures. These datasets are from the µL-NIPI experiments. n_s values of lower concentrations (2.0 x 10^{-3} wt% and 2.0 x 10^{-4} wt%) of both eugenol and n-decane soot particles showed an agreement but higher concentrations (0.1 wt% and 2.0 x 10^{-2} wt%) indicated by the black and blue diamonds, respectively showed discrepancy as emphasized by the shaded region. This could be due to aggregation of soot particles in the higher wt%.

The n_s values of an IN would be expected to be independent of the concentration of the suspension (wt%) because it was normalized by the surface area of the particles. While this is true for the lower wt%, it is not true for higher concentrations of soot. From this singular or deterministic model, the upper range of ice nucleation active sites density (n_s) from the µL-NIPI for both eugenol and n-decane soot was calculated as ~ 10^3 cm^{-2} to ~ 10^4 cm^{-2} at -23 °C for 2.0 x 10^{-3} wt% and 2.0 x 10^{-4} wt % soot suspensions. For n-decane soot, the higher concentrations (0.1 wt% and 2.0 x 10^{-2} wt %) showed n_s values of about 2 to 3 orders of magnitude less than that of the lower concentrations. But for eugenol soot, n_s values of the higher concentrations were about 2 orders of magnitude less than that of the lower weight percent. Obviously, this indicates that both eugenol and n-decane soot types showed higher ice nucleating efficiency for the 2.0 x 10^{-3} wt% and 2.0 x 10^{-4} wt % soot suspensions than the 0.1 wt% suspension. In addition, droplets containing 2.0 x 10^{-3} wt% and 2.0 x 10^{-4} wt % of eugenol and n-decane soot particles showed a reasonable agreement in their n_s values, this was not the case with 0.1 wt % and 2.0 x 10^{-2} wt% soot-containing droplets.

The disparity between the n_s values of 0.1 wt % and 2.0 x 10^{-2} wt% suspensions of n-decane soot was higher than that observed for the eugenol soot. This difference may be attributed to the high tendency of aggregation or the dispersion instability of this soot type which is discussed in more details in the section 5.3. Given similar conditions of

temperature and pressure for different suspension concentrations, aggregation of particles is favoured when there is high concentration of particles because of an enhanced collision rate of particles (Maximova and Dahl, 2006). Therefore, higher concentrations (0.1 wt% and 0.02 wt%) of soot used here showed significant aggregation than the lower concentrations.

5.3 Evidence of aggregation of soot particles in suspensions

As earlier stated, in calculating the n_s used in describing the ice nucleation efficiency of eugenol and n-decane soot particles, the number of nucleation active sites was normalized to the surface area of the particles per droplet. Therefore, it would be expected that on a logarithmic scale there should be an agreement between the n_s values of the various concentrations of the soot particles; but this was not the case for 0.1 wt % and 2.0 x 10^{-2} wt% soot suspensions of eugenol and n-decane as depicted in Figure 5.3 (shaded regions). Soot is amorphous in nature (Sadezky et al., 2005), possesses a fractal-like structure when dispersed in air (Martin et al., 2013), and has a variable degree of hydrophobicity (Popovicheva et al., 2008b; Han et al., 2012a). These properties can contribute to the aggregation of soot particles in suspensions with higher mass of particles, thus, reducing the actual surface area available for ice nucleation.

From previous studies, it is shown that in high relative humidity, the fractal structure of soot can collapse into a more compacted structure and this can introduce bias in size measurements (Martin et al., 2013; Ma et al., 2013; Petters et al., 2009). This restructuring in soot is suggested to impact on the contact angle of the soot particles thereby influencing its ice nucleation properties (Persiantseva et al., 2004). However, the exact mechanism of this restructuring process is not well characterised, especially in a case where the soot particles are completely immersed in water. Also, Ma et al. (2013) proposed that soot restructuring is driven by capillary forces during an evaporation process and it is less likely to occur during a condensation process.

Soot restructuring can occur in suspension either in two forms: (1) the fractal soot spherules can be forced closer by van der Waals forces to make the particles more compact; or (2) soot particles can merge together or ‘collapse’ to form a bigger particle through a process of ‘accretion’ (Zelepouga et al., 2000; Prado et al., 1983). Both proposed mechanisms are illustrated in Figure 5.4. The behaviour of soot particles suspended in water is controlled by its hygroscopic properties and hence, no one mechanism can be easily predicted for their restructuring (Popovicheva et al., 2008b).

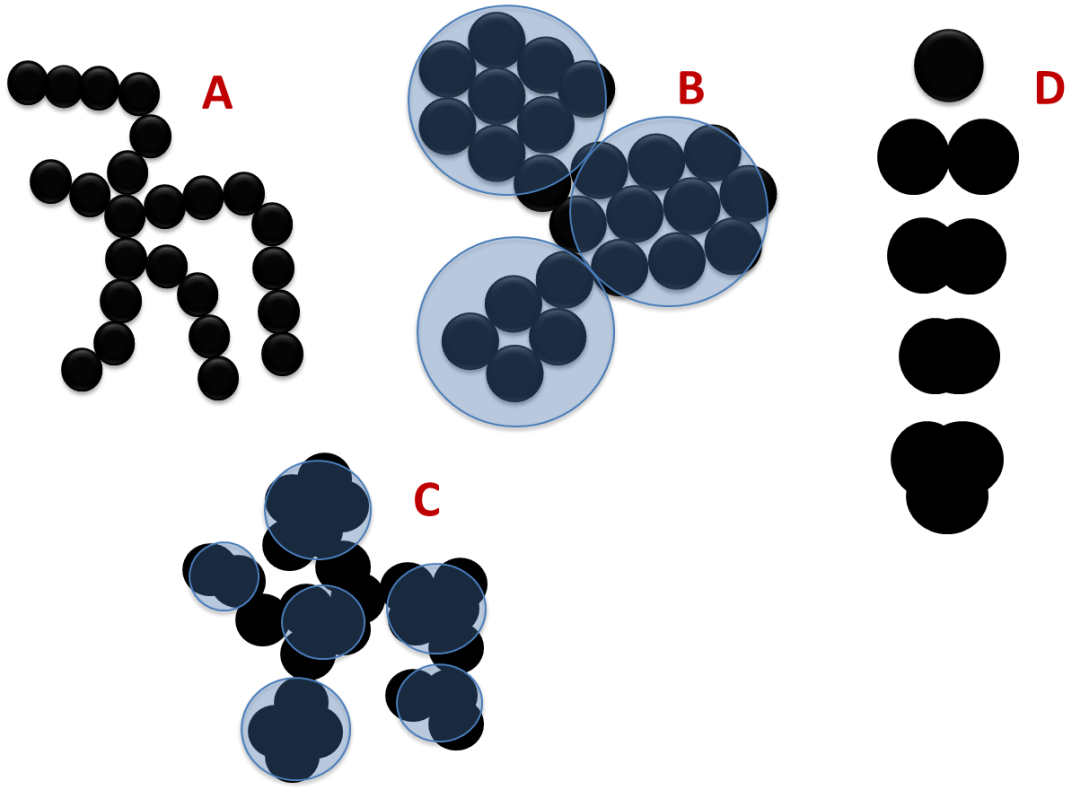

Figure 5.4: Possible forms that soot particles can restructure in water suspension. (**A**) shows a typical fractal arrangement of soot particles, while (**B**) represents a compact formation which can result from soot particles restructuring – here, it is mainly the re-arrangement of individual soot particles to make a more compact structure. As proposed, (**C**) shows a possible collapse of the soot particles into a bigger size particle which forms a material with a lower surface area compare to the cumulative surface area if individual particles were in isolation. (**D**) shows individual soot particles in its fractal-like structure and a few possible shapes/sizes that may result after the accretion process in water suspension.

In order to test the aggregation/accretion hypothesis, dynamic light scattering (DLS) measurements were carried out to probe the particle size distribution directly from soot suspensions. Various concentrations used for the freezing experiments were prepared for the DLS measurements. The particle size distribution of soot particles in suspensions was measured with a Malvern instrument (Zetasizer Nano series - Nano ZS, UK) using UV grade cuvettes; this instrument has a particle size measurement range of ~ 0.3 nm to 10 µm with an accuracy of ± 2%. The results showed that there was non-uniformity in their particle size distributions of 0.1 wt% (see Figure 5.5). The particle size distributions for the higher mass concentration (0.1 wt%) showed a bimodal distribution in contrast to what is observed for the lower concentrations (2.0×10^{-3} wt% and 2.0×10^{-4} wt%).

This method was used previously to characterise the size distribution of poly-dispersed fractal systems like soot (Kätzel et al., 2008b; Kätzel et al., 2008a). Kätzel et al. (2008b) indicated that the hydrodynamic radii determined by DLS had scaled with the mean

aggregate radius of gyration but that the influence of rotational diffusion has to be accounted for in the measurements; this relates to the soot restructuring mechanism discussed above.

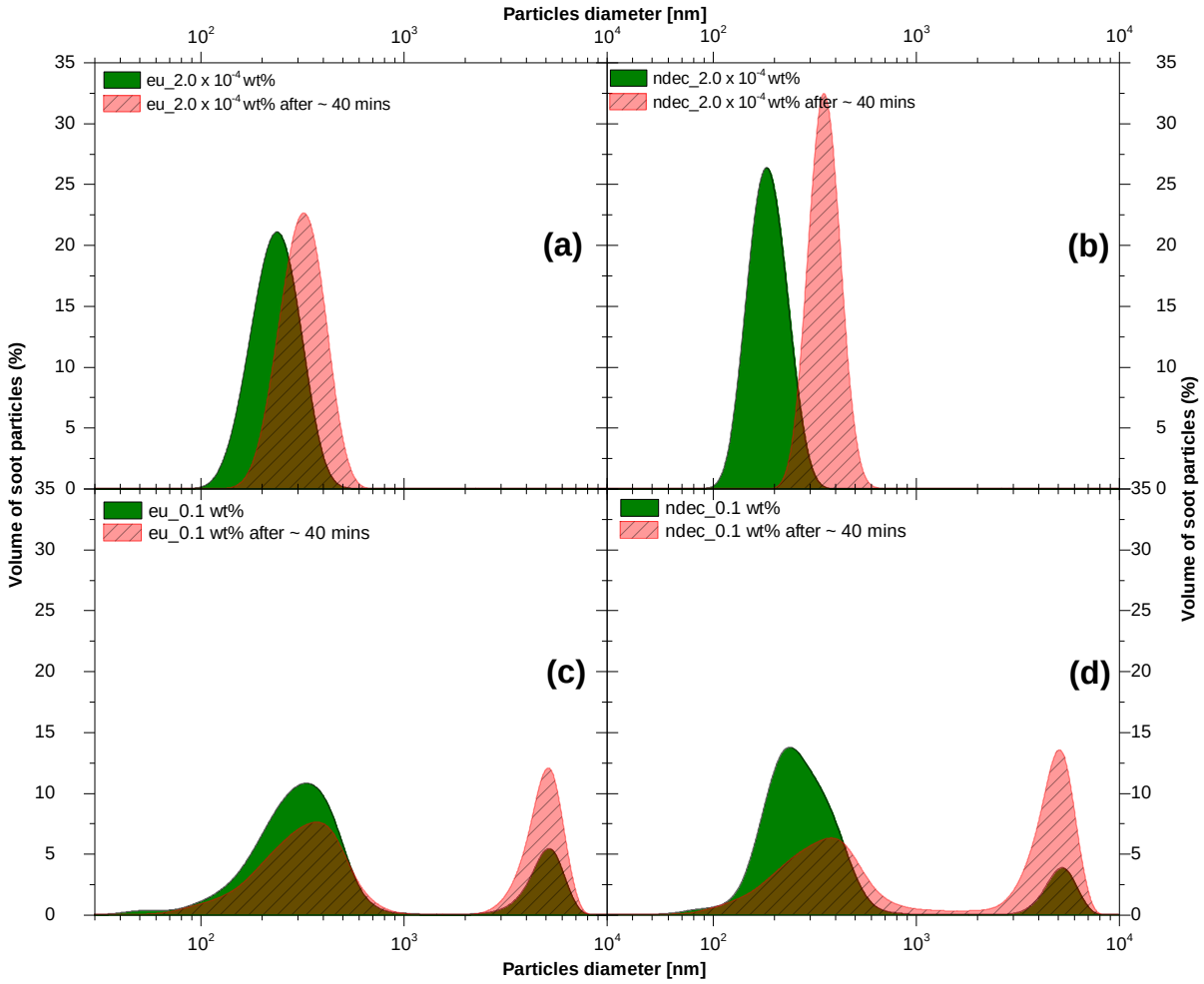

Figure 5.5: Particle size distribution obtained from a dynamic light scattering (DLS) instrument. Panels [**(a)** and **(c)**] are for eugenol soot suspensions and [**(b)** and **(d)**] are for n-decane soot suspensions. All red filled area plots represent size distribution for suspensions that were left standing for about 40 minutes while the black are measurements done immediately within the timescale of the DLS instrument.

It was clearly observed that the particle size distribution of 0.1 wt% suspensions for both eugenol and n-decane soot showed a bimodal size distribution whereas a single mode was seen for the 2.0 x 10^{-4} wt % concentration. When the suspension was left standing for about 40 minutes without stirring, an increase in the size of the second peak was observed suggesting that the number of aggregates formed depends on the duration that the suspension was left standing. This change in the second peak sizes was observed for 0.1 wt% suspensions of both eugenol and n-decane. In contrast, more diluted concentrations showed stability in the size distribution although the size range

tended towards a larger size but not up to an order of magnitude change (Figure 5.5). Relating these results to the observed disparity in the n_s values in this study, the lower mass concentrations showed higher n_s values; which mean there was more available surface per particle for nucleation to take place. This measurements suggests that soot surface area available for ice nucleation can be dramatically reduced when suspended in water; and this is consistent with observations by Ma et al. (2013). The degree to which the surface area is reduced depends on the concentration of the soot particles in the suspension.

5.4 Effect of soot-water interaction time on their ice nucleation activity

When soot particles are emitted into the atmosphere, its ultimate fate is its removal by various processes. The residence time of aerosol particles - that is, the approximate time taken for aerosol particles to be removed from the atmosphere from the time of emission - controls its fate. Soot particles have an average lifetime of 4 – 12 days in the atmosphere as reported by Cape et al. (2012). Removal of these particles from the atmosphere depends on some factors such as the prevailing meteorological factors e.g. convection, precipitation, which can also act as a scavenging route via wet deposition. Another factor is their ability to interact with water molecules over time in the atmosphere. It is known that water uptake by soot can depend on active sites or oxygenated functional groups present at the soot surface (Popovicheva et al., 2008c; Oubal et al., 2010), inter-particle porosity (Ferry et al., 2002) and this can be time-dependent too. Hygroscopic properties of soot is reported to modulate its ice nucleating ability in mixed-phase clouds (Yun et al., 2012).

Experiments were performed to quantify the influence of soot suspension ageing on its ice nucleating ability. This was studied by performing freezing experiments on a freshly prepared eugenol and n-decane soot suspensions (24 hours = 1 day), and then the soot suspension was left stirring for 6 days, and then 21 days. All freezing measurements were carried out in the µL_NIPI. The fractions of droplets frozen data for eugenol and n-decane soot are shown in Figures 5.6 and 5.7, respectively.

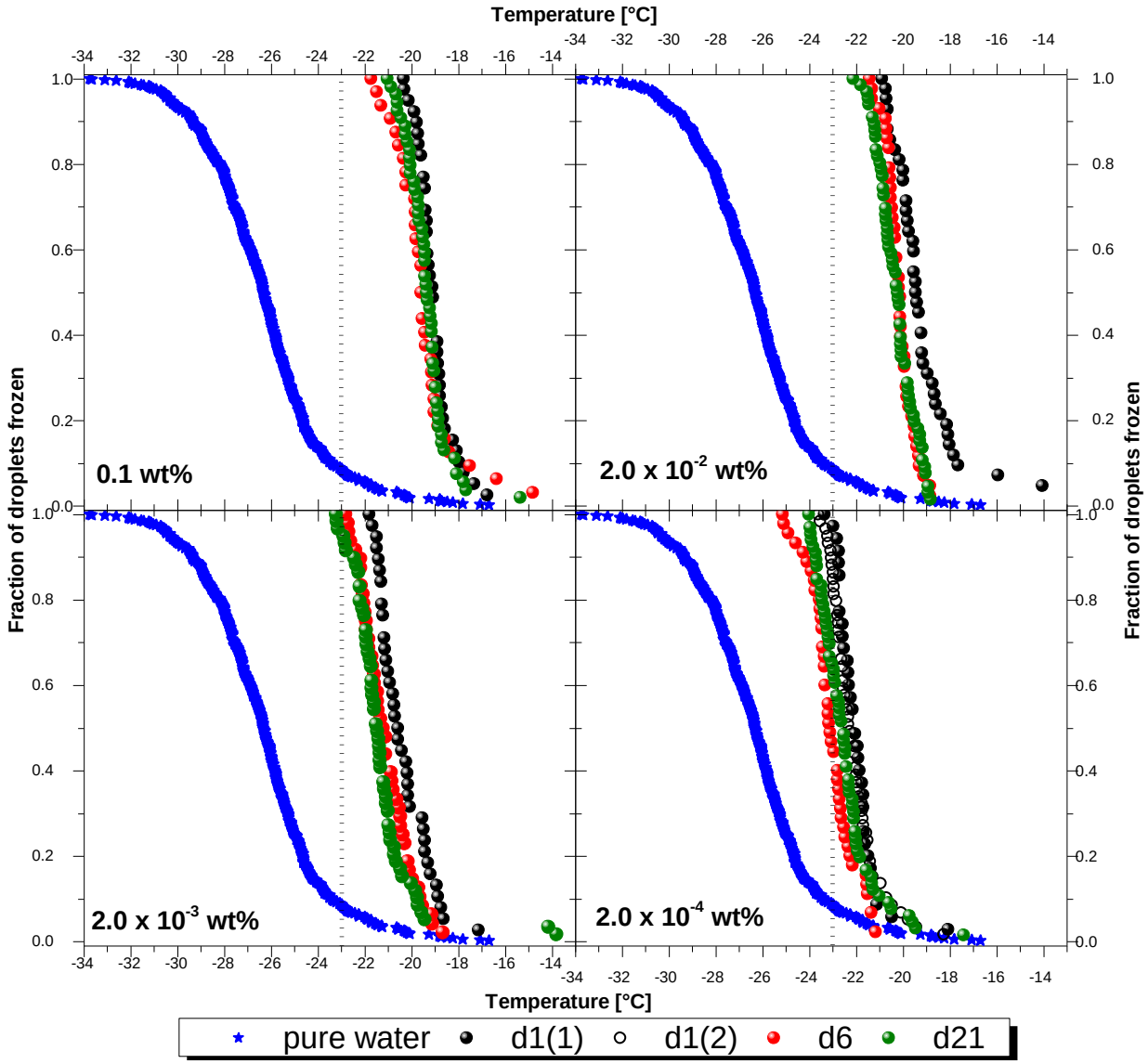

Figure 5.6: Freezing behaviour of eugenol soot particles in suspension over time from a µL-NIPI. All droplets of soot suspension were about 1.0 µL. The blue data points represent the freezing of ultra-pure water (18.2 MΩ.cm resistivity), which was used to establish the baseline freezing for µL-NIPI experiments. The dashed line indicates the cut-off for heterogeneous freezing on µL-NIPI while d1 (black), d6 (red) and d21 (green) are experiments performed with various concentration of eugenol soot suspensions were left standing for 24 hours (1 day), 144 hours (6 days) and 504 hours (21 days), respectively. Temperature uncertainty quoted for the experiments is ± 0.4 °C.

Three suspensions – 2.0 x 10^{-2} wt%, 2.0 x 10^{-3} wt%, and 2.0 x 10^{-4} wt% containing freshly prepared eugenol soot (1 day) were observed to freeze ~ 1 °C warmer than the same suspensions left for 6 and 21 days. But 0.1 wt% did not show any significant difference in the freezing temperatures for the time period studied. However, a steady decrease in the freezing temperatures was observed with suspension concentrations as would be expected (see section 5.1.1). Within the temperature uncertainty reported for the experiments (± 0.4 °C), there was no significant difference in the freezing curves of suspensions that were left for 6 days and 21 days (red and green data points).

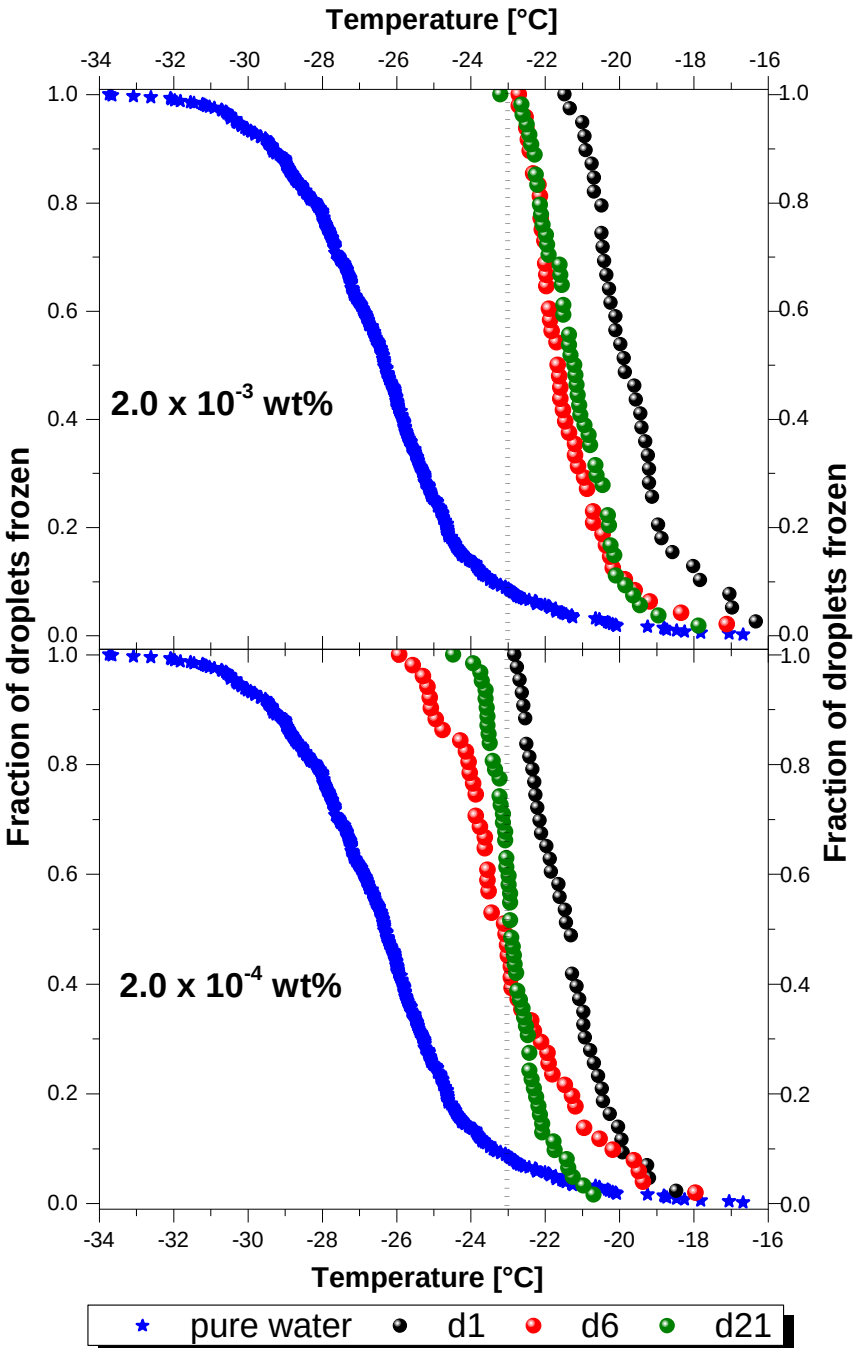

Figure 5.7: Freezing behaviour of n-decane soot particles in suspension over time from a µL-NIPI. All droplets of soot suspension used were about 1.0 µL. The blue data points represent the freezing of ultra-pure water (18.2 MΩ.cm resistivity), which was used to establish the baseline freezing for µL-NIPI experiments. The dashed line indicates the cut-off for heterogeneous freezing on µL-NIPI while d1 (black), d6 (red), and d21 (green) are experiments performed with various concentration of n-decane soot suspensions were left standing for 24 hours (1 day), 144 hours (6 days), and 504 hours (21 days), respectively. Temperature uncertainty quoted for the µL-NIPI experiments is ± 0.4 °C.

Freshly prepared (1 day) suspensions containing 2.0 x 10^{-3} wt% and 2.0 x 10^{-4} wt% n-decane soot froze at ~ 2 °C warmer than the suspensions that were stored for 6 days and 21 days. Suspensions containing 2.0 x 10^{-3} wt% of n-decane soot that were left for 6 days and 21 days did not show any significant changes in their freezing behaviour, but

for a 2.0 x 10^{-4} wt% n-decane suspensions, there was a change in the fraction of droplets frozen (Figure 5.7) for day 6 and day 21. However, it is not clear what could be responsible for this observation.

To clearly understand the effect of soot-water interaction time on the ice nucleation abilities of these particles, it is useful to calculate the n_s for the various timescale studied (d1, d6, and d21). This is because the fraction of droplets frozen is not normalized to the surface area available in each droplet for ice nucleation to occur. Therefore, it is useful to compare a normalized quantity to appreciate any existing differences. The n_s plots for both eugenol and n-decane soot are shown in Figures 5.8 and 5.9, respectively.

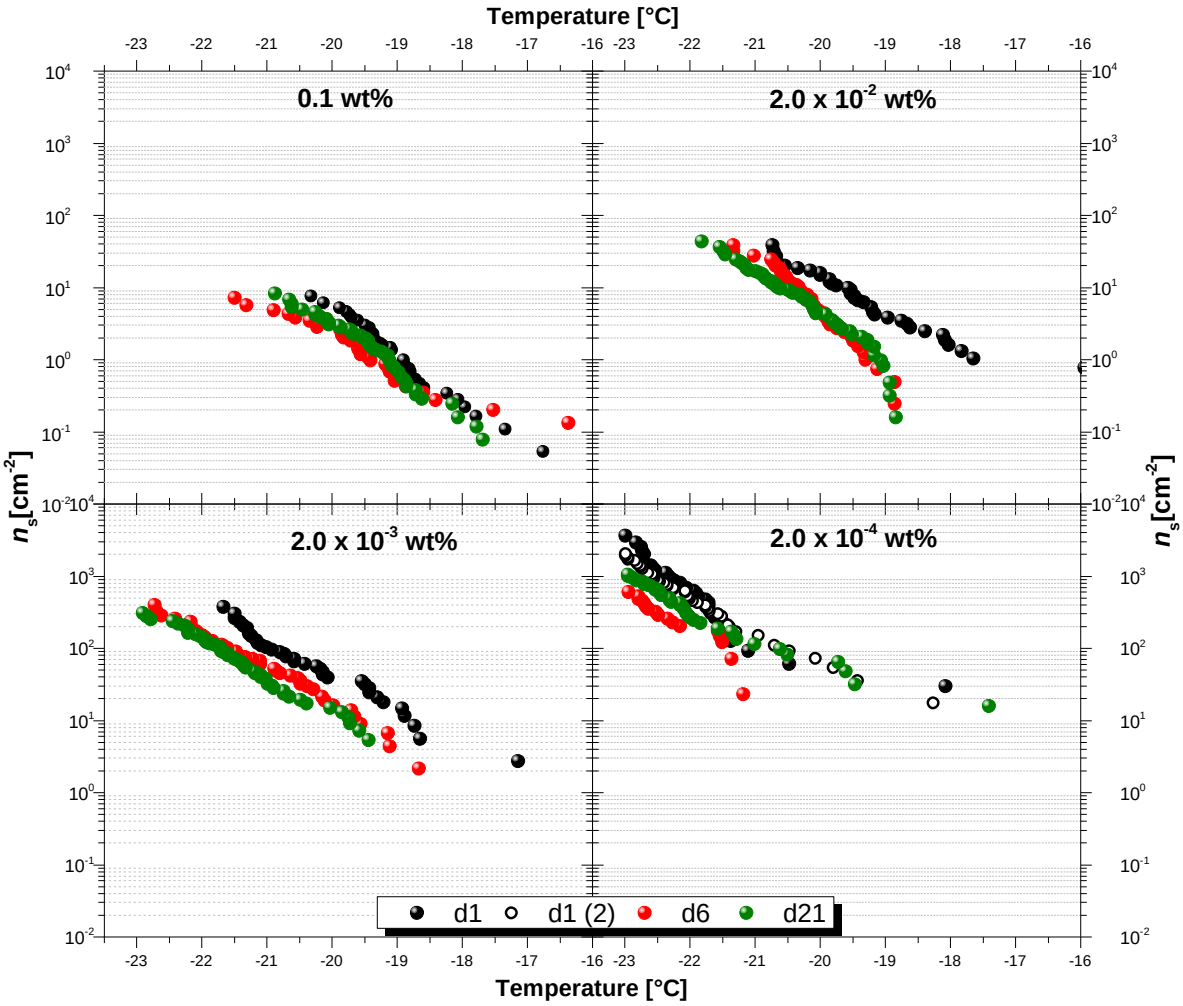

Figure 5.8: n_s plot of eugenol soot suspensions that were left stirring for 24 hours (d1), 144 hours (d6), and 504 hours (d21). The black, red, and green data points are for d1, d6, and d21, respectively. Each panel shows n_s plot for the different concentrations of eugenol - 0.1 wt%, 2.0 x 10^{-2} wt%, 2.0 x 10^{-3} wt%, and 2.0 x 10^{-4} wt%.

For eugenol soot, the n_s values of d1 suspensions were generally observed to be higher than d6 and d21 suspensions at a particular temperature. The ice nucleating abilities of d6, and d21 suspensions did not show any significant difference; however, for 0.1 wt%,

the n_s of d1, d6 and d21 were similar. For all timescales investigated, 2.0 x 10^{-4} wt% suspensions showed the highest n_s value.

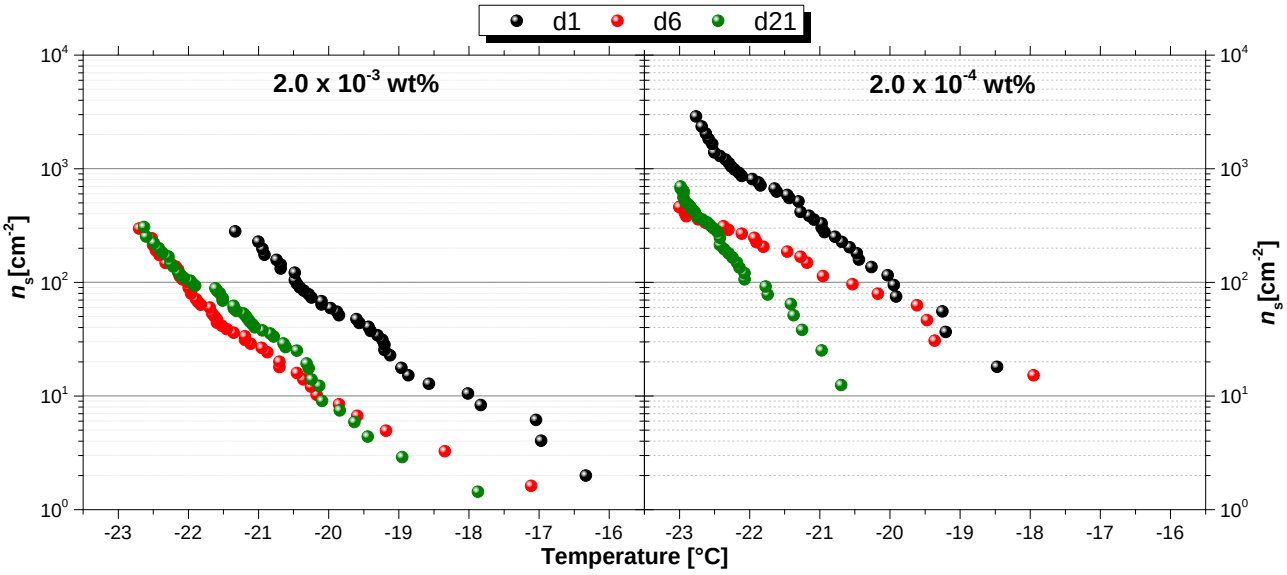

Figure 5.9: n_s plot of n-decane soot suspensions that were left stirring for 24 hours (d1), 144 hours (d6), and 504 hours (d21). The black, red, and green data points are for d1, d6, and d21, respectively. Each panel shows n_s plot for the two concentrations of n-decane - 2.0 x 10^{-3} wt% and 2.0 x 10^{-4} wt%.

Soot suspensions containing 2.0 x 10^{-3} wt% and 2.0 x 10^{-4} wt % of n-decane soot (1 day) showed a remarkable change, about an order of magnitude higher in n_s than the same concentrations that was left stirring for 6 days and 21 days (Figure 5.9). However, n-decane soot suspensions (2.0 x 10^{-3} and 2.0 x 10^{-4} wt %) left for 6 days and 21 days showed a good agreement in their n_s distribution except for suspension containing 2.0 x 10^{-4} wt % left for 6 days - which showed a distribution of ice active densities that cut-across the freshly prepared suspension (d1) and that of d6 and d21 soot suspensions (Figure 5.9). n-Decane showed a decrease in the n_s values up to about an order of magnitude from d1 to d6 and d21.

It can be observed that a general reduction in the ice nucleation activity of both eugenol and n-decane soot was observed for d6 and d21. The hygroscopic properties of soot can decrease with an increase in the interaction time of soot with water due to the dissolution of water soluble substances on the soot surface (Demirdjian et al., 2009); this phenomenon can impact on its surface properties (Persiantseva et al., 2004), which may be linked to the observed reduction in its ice nucleating ability.

Kireeva et al. (2009) studied the effect of a long-term contact of soot particles with water by freezing freshly prepared dispersions and stored dispersions. The study

showed that the highest increase in the freezing temperatures observed for acetylene soot was 2.9 °C. It was suggested that a high inter-particle porosity could be the major contributing factor to the increase in the freezing temperature of acetylene soot. This was in contrast to what was observed in the freezing behaviour of eugenol and n-decane soot in this study. In addition, Kireeva et al. (2009) study did not mention how long the suspensions were stored before the experiment. This study agrees with the theory that, the tendency of soot particles accreting is higher when they are left in a suspension for a longer time and this could generally reduce the surface area or sites available for ice nucleation to take place.

Generally, this investigation has atmospheric relevance for soot particle that are retained in clouds and humid atmospheric conditions for a long time (~ days to weeks). However for clouds that are short-lived such as some convective clouds it might have secondary importance as there is not enough time for any interactions to occur.

5.5 Comparison with other soot types studied in literature

A couple of studies have explored the understanding of ice nucleation by different soot types in the immersion mode; for example (DeMott, 1990; Diehl and Mitra, 1998; Kireeva et al., 2009; Popovicheva et al., 2008a; Wright et al., 2013). It has been suggested that, the heterogeneous ice nucleation behaviour of soot is generally unique to the nature of the soot type, which includes its structure, its hygroscopic properties, mixing state, and its chemical composition (Dymarska et al., 2006; Gorbunov et al., 2001; Crawford et al., 2011; Friedman et al., 2011). Other factors that may indirectly affect the nature of soot include the combustion conditions with which the soot was generated and the atmospheric processing (Mohler et al., 2005a; DeMott et al., 1999; Adachi and Buseck, 2008; Karcher et al., 2007; Friedman et al., 2011).

DeMott (1990) showed that soot obtained from an acetylene burner nucleates ice at temperatures from ~ -24 °C to -34 °C. Details of the experiment with acetylene soot (hereafter, referred to as ASD) were discussed in chapter 2. The study reported that the ASD particles generated appeared as aggregates, however, it did not state if isolated single soot particles were used for this study, given the diameters of the particles that were reported in that study. In addition, DeMott (1990) did not report nucleation sites density (n_s) of ASD. The n_s values were calculated and reported by Murray et al. (2012) from the fraction frozen data from the experiment. In the calculation, they assumed single particles per drop for the two diameters (0.08 µm and 0.12 µm), and a range of ~

10^6 cm^{-2} to 10^8 cm^{-2} at a temperature range of ~ -24 °C to -34 °C were obtained (Murray et al., 2012). Similar values were independently calculated and reported by Hoose and Möhler (2012). Both calculations were done by an assumption that soot particles were spherical in order to estimate the surface area of ASD particles. This type of assumption can introduce large discrepancy in the n_s values. For example, the n_s of mineral dusts with similar mineralogy were found to differ in about an order of magnitude when BET surface area and spherical estimation were used in estimating the n_s (Murray et al., 2012; Broadley et al., 2012; Niemand et al., 2012). The n_s values for the ASD described above and the two soot types (eugenol and n-decane soot) used in this study are presented in Figure 5.10. It could be seen that ASD is relatively about an order of magnitude higher than eugenol and n-decane soot possibly because the surface area was underestimated by using spherical estimation. However, there is a considerable agreement with both eugenol and n-decane soot in the lower temperature regime.

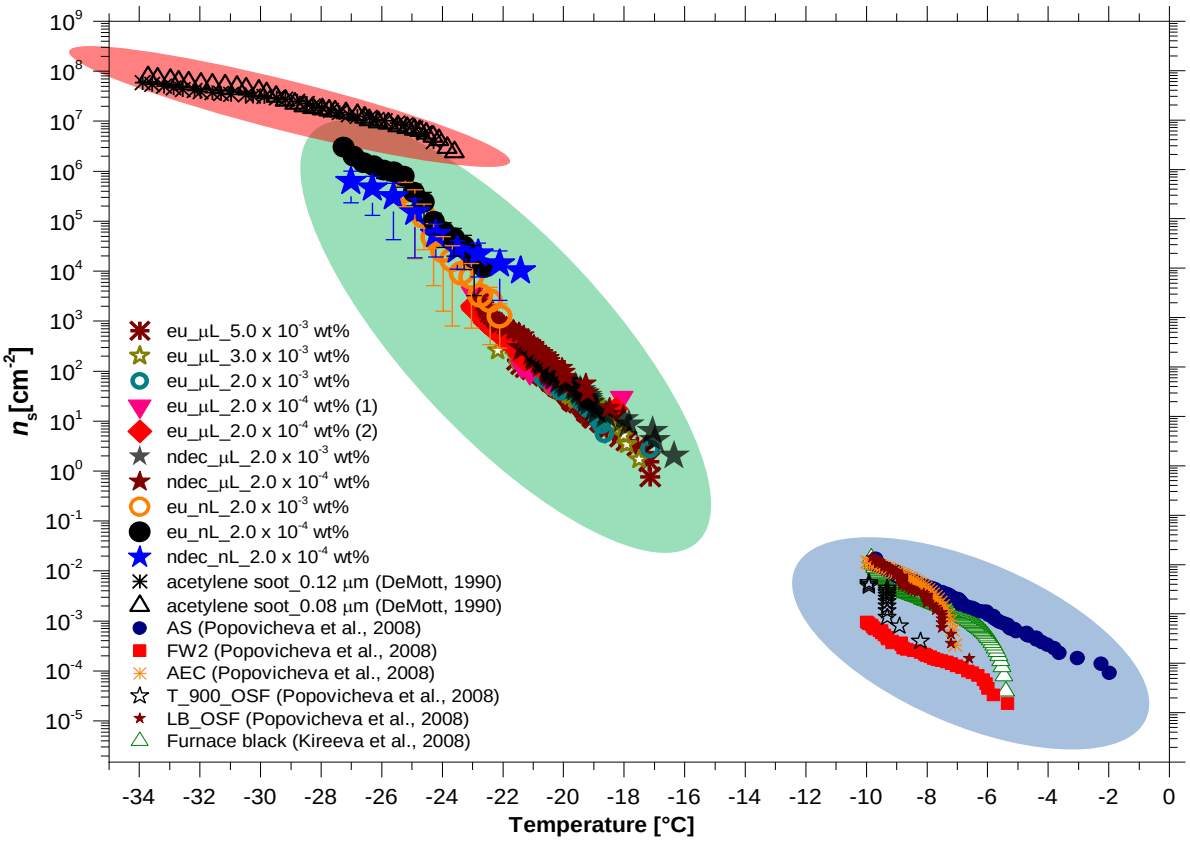

Figure 5.10: Nucleation sites density (n_s) for both eugenol and n-decane soot from both µL-NIPI and nL-NIPI experimental set-ups and other soot types studied in the literature. The legend shows the various concentrations of soot used in this study. All data obtained from this study has a green shade. The black triangle and the black asterisk data points (shaded red) represent data obtained from DeMott (1990) for the two soot sizes studied – 0.08 µm and 0.12 µm. The n_s distribution of soot types studied by Kireeva et al. (2009) and Popovicheva et al. (2008a) - Lamp Black (LB), Furnace Black (FB), FW2 (Channel Black), Acetylene (AS), Aircraft engine

combustor (AEC), and Thermal (T-900) are shaded with blue at the higher temperature regime of the plot.

Comparing the results of this present study to that of ASD, the n_s values for eugenol and n-decane soot showed a range of n_s values which covers about seven orders of magnitude and over a wider temperature range (~ -16 °C to -36 °C) whereas the n_s values of ASD soot was within an order of magnitude. Aside from the differences in the sources from which each soot type was obtained, the key difference in the two studies could be that while ASD was generated in an oxygen-deficient conditions, eugenol and n-decane soot were generated with an excess oxygen supply. These differences could account for the variability observed in their n_s values.

In another study, kerosene soot was used for an ice nucleation study, it was observed that soot particles triggered freezing at temperatures higher than -28 °C in the immersion mode (Diehl and Mitra, 1998). Aside from the influence that soot source can have on its ice nucleation properties (Karcher et al., 2007), another important factor that may be associated with differences in soot ice nucleating abilities is the presence of contaminants – this may be directly associated with the generated soot particles. As discussed in chapter 2, Diehl and Mitra (1998) reported that other 'pollutant' concentrations were measured alongside the soot particles from the kerosene aviation fuel. This sort of pollutants is also known to associate with soot from ship diesel engines (Popovicheva et al., 2012). In this case, it is unclear if the presence of these pollutants affected the freezing results obtained. In comparison, both eugenol and n-decane soot were obtained from a pure source with minimal or no risk of contamination (see section 4.2.2).

Diehl and Mitra (1998) study did not report the nucleation sites density (n_s) for the kerosene soot; however, Murray et al. (2012) attempted to calculate the n_s of the kerosene soot and showed that the n_s distribution of the kerosene soot was in agreement with the n_s values of ASD (Murray et al., 2012). This study only provided information on the number of particles per cm^3 as a function of the particle diameter, droplet sizes, and the fraction of the droplets for freezing temperatures between -18 °C and -28 °C. Using this information, the number of particles per drop was calculated by assuming the density of graphite (2.23 g cm^{-3}) for the soot particles. From this calculation it was observed that the resultant number of particles per droplet was << 1, which is unrealistic for the droplets sizes used in their investigation; hence, it was difficult to estimate the

ice nucleation sites density (n_s) by the kerosene soot. This was why the data is not included here.

The ice nucleation abilities of some other soot types such as Lamp Black (LB), Furnace Black (FB), FW2 (Channel Black), Acetylene soot (AS), Aircraft engine combustor (AEC), and Thermal (T-900), were studied by Kireeva et al. (2009) and Popovicheva et al. (2008a). The studies investigated the effect of soot in the immersion freezing of water and their efficiencies. They used an average droplet size of 0.13 cm that contained 2.5 wt% of soot particles. Higher freezing temperatures were reported compared to the study by Diehl and Mitra (1998); this can be explained by larger droplet size and the high particle concentrations. The median temperatures (T_{50}) reported for the various soot types were LB (-9.8 °C), FB (-8.2 °C), FW2 (-10.6 °C), AS (-10.0 °C), T-900 (-11.9 °C), and AEC (-11.1 °C). As other studies, e.g. DeMott (1990) and Diehl and Mitra (1998), the n_s values were not reported from these soot types; however, the fraction of droplets frozen were shown for FW2, AS, and the pure water that was used as the control. Comparing the freezing of the water pure shown to that of FW2 and AS, about 70 % of FW2 and 90 % of AS froze above the freezing temperatures of the pure water, given that about 10% of the droplets of pure water showed a sporadic freezing events which are usually associated with the freezing of pure water. These sporadic events are suggested to be caused by impurities in the water. Using the information reported in their study, n_s values for the various soot types were obtained as shown in Table 2.1 and plotted in Figure 5.10.

The n_s values of LB, FB, FW2, AS, T900 and AEC, showed a reasonable agreement with the eugenol and n-decane soot. This data provided a broad range of n_s values for higher temperatures. However, this data set was not used for the parameterization shown in Figure 5.11 because the degree of distribution of the freezing temperatures for four of the six soot types were best approximations given the available information provided, the actual degree of uncertainty could not be established.

Contact nucleation, which might be relevant to mixed-phase cloud (Bond et al., 2013) has been reported by soot at -25.6 °C (Fornea et al., 2009); however, the n_s could not be calculated because the surface area of contact by the soot particle and the water droplets is unknown. Hence, no direct comparison of its efficiency is reported here.

To generate a soot parameterisation for use in predicting the number of ice nuclei (section 5.6) and in a microphysics model, only data obtained from this experiment were used as shown in Figure 5.11.

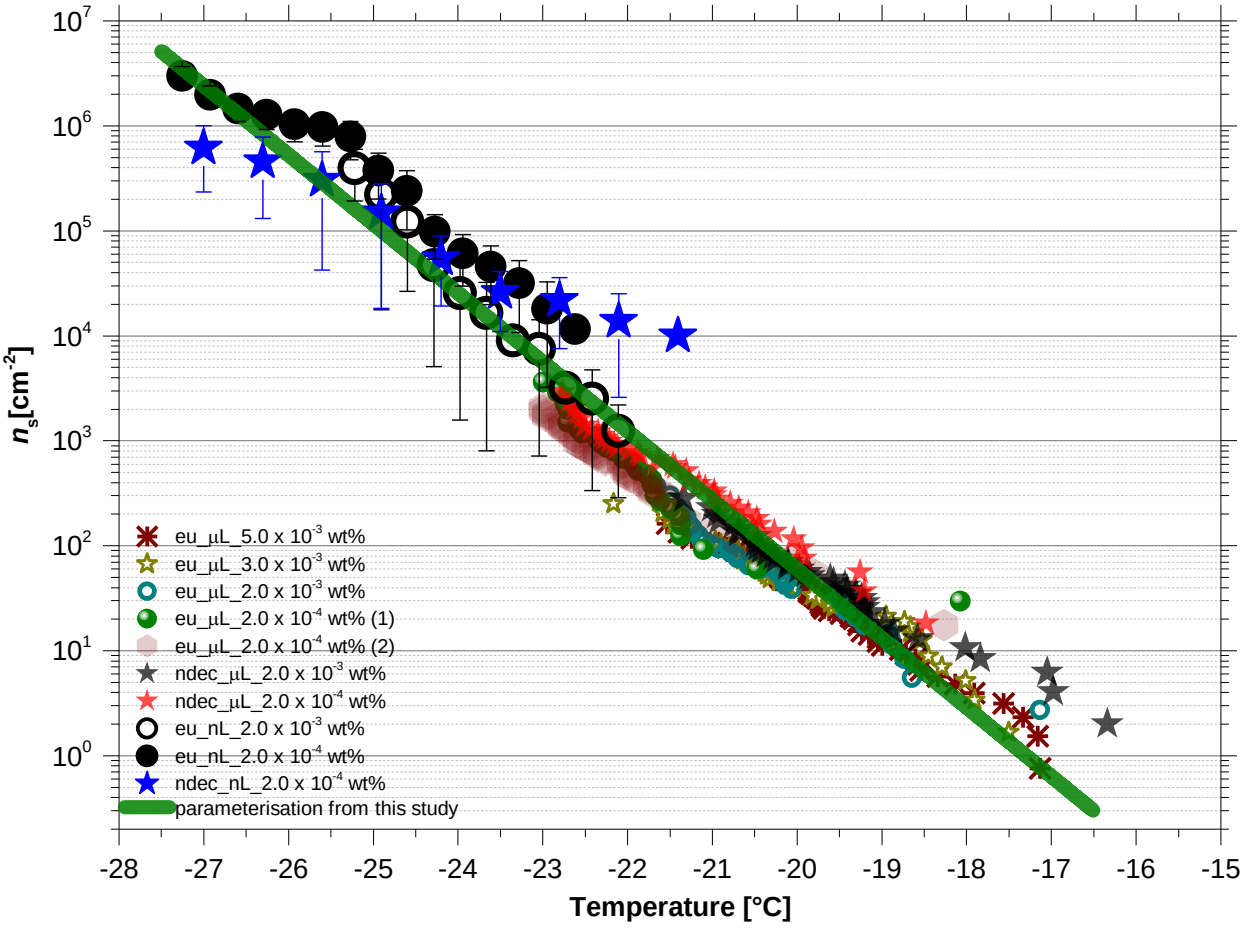

Figure 5.11: Nucleation sites density (n_s) plot for eugenol soot and n-decane soot used in this study. The parameterization (green line) [$\ln(n_s) = -1.5147T - 26.203$, $R^2 = 0.9338$] represents eugenol and n-decane soot data obtained from this study and it is valid from a temperature (T) range of -16.5 °C to -28 °C (± 0.2 °C). The errors in the n_s from the µL-NIPI experiments are not shown because they were too small; therefore, they were completely masked by the data points on this log scale.

Both eugenol and n-decane soot results from µL- and nL-NIPI experiments are represented in Figure 5.11. For the fit [$\ln(n_s) = -1.5147T - 26.203$, $R^2 = 0.9338$], T is valid from -16.5 °C to -28 °C (± 0.2 °C).

In summary, although the properties of different soot types may be influenced by some factors, these factors may not necessarily affect their ice nucleation abilities in isolation, it may be a combination of factors. Some major factors that may affect ice nucleation properties aside those listed in chapter 2 are:

(1) the *combustion temperature* - the type of soot produced could depend on the combustion temperature at which the soot was generated, as the higher the combustion temperature, the less oxygenated compounds are present (Fitzpatrick et al., 2007). The surface properties of soot is observed to differ with combustion temperature (Jones et al., 2005). Generally, higher temperature combustion produces more hydrophobic soot than lower temperatures combustion. Observational and model studies showed that the hygroscopicity of soot can modulate their ice nucleation ability (Yun et al., 2012; Popovicheva et al., 2008b). For example, the combustion temperature in an open fire is typically lower compared to combustion temperatures in jet engines and acetylene flames. ASD used by DeMott (1990) was produced from acetylene, which may be in a temperature regime of ~1000 °C or above, whereas eugenol and n-decane soot were generated at about 300 – 700 °C. However, these differences in their combustion temperatures did not show a significant difference in their ice nucleating ability (Figure 5.10). Rather the one order of magnitude difference with ASD can be attributed to the method with which the surface area of ASD was estimated and other experimental differences/uncertainties. Although there has been a report that high concentrations of ice particles have been measured in primary and secondary wakes of aircraft (Schumann et al., 2013), but it is not clear if this is connected to the high temperature soot from aircrafts.

(2) the *level of oxygen supply* during the combustion process could also affect the nature of soot obtained. In biomass combustion, which eugenol soot mimics, it was generated in an oxygen-rich environment, which could allow a formation of some oxygenated organic compounds with the soot. From mass spectrometer analyses, eugenol soot comprised more oxygenated compounds than n-decane soot (Baeza-Romero et al., 2010); in addition, non-oxygenated PAHs were also identified (Wilson et al., 2013). Again, this variation in the amount of oxygenated compounds present did not count in their general ice nucleation behaviour.

(3) *variation in soot particle sizes* has been proposed to introduce heterogeneity in estimating its nucleation activities (Koehler et al., 2009). Variability could be introduced in the estimation of ice nucleation efficiency due to the method adopted in surface area measurement or in particle sizing. In the immersion mode freezing studies, it will be more appropriate to use a hydrodynamic soot particle sizer but the problems associated with this method are: the influence of aggregation/accretion by soot particles, the timescale of the measurements, and the uncertainties in the refractive index and

absorbance values of soot. These limiting factors can introduce various size modes for a particular mass concentration. For example, using aerodynamic sizing can undermine the behaviour of soot in water. For instance, when soot is suspended in water, it has been reported that soot spherules in fractals (≥ 100 nm) can collapse into a more compact structure (Martin et al., 2013; Mikhailov et al., 2006) as discussed in section 5.3.

5.6 Estimation of ice nuclei from soot ice nucleation efficiency

Information provided by ice nucleation abilities of aerosols can be used in predicting its impact on clouds of interest. Specifically, the number of IN can be estimated based on the amount of such aerosol present in the atmosphere and the available surface area via the relationship in equation 5.2. This approach is used in predicting the number of IN of various aerosol particles in the atmosphere (Murray et al., 2012; Cziczo et al., 2013; Atkinson et al., 2013; O'Sullivan et al., 2014). A simple estimation of the ice number concentrations (N_{ice}) was calculated for the soot following the model below:

$$N_{\mathrm{ice}} = N_c(1 - \exp(-n_s\sigma)) \tag{5.2}$$

where N_c is the estimated soot particle number concentration in the atmosphere, n_s is the time-independent nucleation site density number of soot IN and σ is the surface area of soot in the atmosphere (N_c). The number density (Nc) of soot in the atmosphere was modelled as 0.1 cm^{-3} and 50 cm^{-3} for a lower limit and an upper limit, respectively (Hoose et al., 2010). The average size of soot particle was taken as ~ 50 nm. Each band takes into consideration the lower and the upper limits of the modelled number density of soot and is calculated from equation 5.2. The bands shows the The predicted IN that can result from soot due to its ice nucleation activity is shown in Figure 5.12 with the IN concentrations measured with a thermal diffusion chamber during field campaigns (DeMott et al., 2010). A Continuous Flow Diffusion Chamber (CFDC) was used for the field measurements; this limited the size of particles sampled to ≤ 1.6 µm. With this cut-off some particles greater than 1.6 µm were not taken into account which means some particles that may nucleate ice at higher temperatures (> -15 °C) were ignored. Aside from this limitation in the measurement, no sensitivity was reported for the IN distributions measured in the study; hence, the data should be treated with caution. This makes it difficult to access the whole range of IN in the atmosphere.

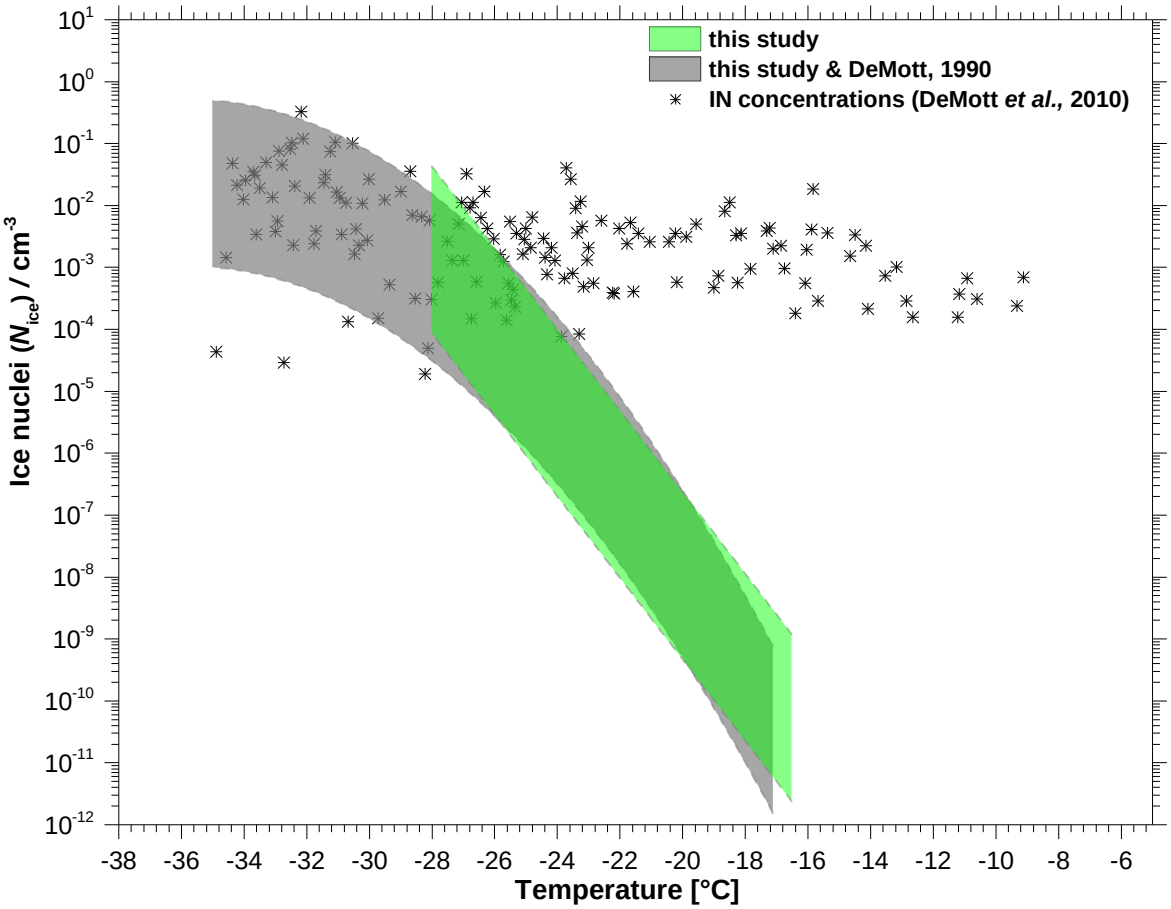

Figure 5.12: Estimation of IN from soot ice nucleation efficiency. The number of IN was estimated based on the upper limit and the lower limit of soot in the atmosphere as modelled by Hoose et al. (2010). The black star data points indicate IN concentrations as a function of temperature as reported in DeMott et al. (2010). The two bands represents two parameterizations (1) the green band is based on the ice nucleating abilities of eugenol and n-decane soot only whereas (2) the grey band shows the predicted number of IN based on the ice nucleation efficiency of eugenol, n-decane, and the acetylene soot studied by DeMott (1990).

The estimation shows that soot may be an important IN in the atmosphere especially within a temperature regime of ~ -22 °C to -36 °C. This estimate is approximately an order of magnitude lower than what was earlier reported by Murray et al. (2012) which was based on the review of experimental results by acetylene soot and kerosene soot. Also, the temperature range reported by Murray et al. (2012) remain the same, but soot does not show competiveness with IN such as mineral dust until about -24 °C to -25 °C. This means that in an area where mineral dust is not a dominant IN, soot can have an important impact on the formation of mixed-phase clouds in such regions.

With the knowledge of soot ice nucleating ability and the global distribution of soot in the atmosphere, the impacts or importance of soot can be quantified using sophisticated microphysical models such as a Global Model of Aerosol Processes (GLOMAP).

5.7 Atmospheric relevance of this study

The influence of soot on cloud properties has strong implications in the atmosphere and can ultimately affect the regional and global climate systems (Bond et al., 2013). From some previous ice nucleation studies by soot in the deposition mode, it has generally been thought that soot is not a good IN compared to other IN such as mineral dust, and therefore it is unimportant. However, in this study, it is shown that soot may be an important aerosol in assessing the total radiative budget of mixed-phase clouds due to its ice nucleating ability. Soot ice nucleation activity data is crucial in predicting and modelling these processes in aerosol-cloud microphysics models and global-climate models. The presence of more soot IN will result in higher ice content in mixed-phase clouds; this reduces the cloud's lifetime by triggering precipitation via the Bergeron-Findeisen process.

From these laboratory studies, it is shown that an aggregation of soot particles has an effect on its ice nucleation efficiency. This agrees with a past observation that a high ice freezing efficiency was observed for homogeneously or uniformly distributed soot particles (Popovicheva et al., 2008a; Kireeva et al., 2009). Therefore, this could imply that understanding the degree of soot particles dispersion in the troposphere may be important in quantifying its total impacts on climate. This would also suggest that factors such as the atmospheric dynamics at the time of soot particles emission may be more important in determining its role as IN than the nature of soot or combustion conditions such as temperature. Hence, it can be proposed that the ice nucleation efficiency of well-dispersed and stable soot particles in the atmosphere at water-saturated conditions may be higher than aggregated soot particles at similar conditions. This might be worth investigating using aerosol-cloud models in the future, as currently, large uncertainties is associated with climate models involving black carbon (soot) (Bond et al., 2013).

5.8 Conclusion

The main findings in this study are:

i. From the experimental results, it is clearly shown that water droplets containing eugenol soot and n-decane soot particles froze heterogeneously.

ii. It is also established that aggregation of soot particles in water droplets can influenced its ice nucleation efficiency. The agglomeration of soot particles

increases with the concentration of soot particles in a suspension and aging of soot. However, at lower concentrations the effect of soot particles aggregation is reduced to the minimum. The differences in the surface areas of eugenol and n-decane did not affect the ice nucleation abilities of both soot types instead the ice activity was controlled by the dispersion of the soot particles in the suspension.

iii. The potential IN number concentration was estimated based on a parameterisation from our experimental results, and compared with the atmospheric IN distribution measured by DeMott et al. (2010). Soot may contribute to the IN concentration from about -22 °C and may show competition with a more efficient IN such as mineral dust.

iv. It can also be concluded from this study that the impact of soot on mixed-phase clouds at a regional and global scale cannot be ignored due to its abundance in the atmosphere.

5.9 Chapter Summary

In this study, eugenol and n-decane soot were used as proxies for a biomass and hydrocarbon-derived atmospheric soot, respectively, to investigate the ice nucleation activity of soot particles immersed in water droplets at conditions relevant to the mixed-phase clouds. The study was carried out in the laboratory using two instrumental set-ups – µL- and nL-NIPI (i.e. drop freezing assay instruments). From this study, it is clearly shown that soot particles immersed in water droplets nucleate ice heterogeneously, and this may have an important impact on the mixed-phase cloud properties. The results from this study showed a reasonable agreement with two other soot studies in the past that were performed at different temperature regimes. Hence, a parameterisation covering a wider range of temperature can be generated for aerosol-cloud microphysics models.

Chapter 6

Combustion ashes as potential ice nuclei

6.1 Combustion ashes in the atmosphere

Combustion ashes are one of the major by-products that are released into the atmosphere from both natural and anthropogenic combustion processes (Block and Dams, 1976; Johansson et al., 2003). Combustion ashes can be classified into two groups – fly ash and bottom ashes (Van Loo and Koppejan, 2007). Bottom ashes are the non-combustible remains usually rich in minerals, whereas fly ashes refer to those ashes that are directly emitted into the atmosphere during a combustion process. Coal is a major source of fly ash while biomass burning, wild fires, and domestic combustion dominate the bottom ash emissions into the atmosphere.

6.2 Global emissions of combustion ashes

Annually, about 8000 Mt of coal are produced and utilized in coal-fired power plants to generate 41% of the world's electricity needs. And this quantity is on the increase due to the increasing population and energy demand for domestic and industrial consumption (Mahlaba et al., 2012; WCA, 2013). In a year, up to 600 Tg of fly ashes alongside flue gases, boiler slag, organic aerosols (Hu et al., 2013; WCA, 2013) and other materials are produced during power generation from coal power plants, which are distributed all over the globe.

The World Coal Association (WCA) reports that about 90% of these ashes are captured via different collection mechanisms such as electrostatic precipitators, fabric filters or bag houses, dust collectors and other hybrid engineering systems such as hot gas filtration systems (Bond et al., 2004; Wang et al., 2013; WCA, 2013). This is aimed at reducing the amount of particulates emitted into the atmosphere which can have negative impacts on health. On the other hand, the collected ashes are utilized in various construction activities, cement production and in agriculture (Basumajumdar et al., 2005; Adriano et al., 1980).

However, significant quantities of these fly ashes find their way into the atmosphere as a result of system failures, less efficient handling methods during transportation to disposal sites, less efficient installations/modes of operation by collectors (e.g. electrostatic precipitators), occasional malfunctioning of precipitators, accidents (WCA, 2013; Ruhl et al., 2010) and other processes. A summary of coal fly ash productions and emissions are shown in Figure 6.1. Data on the global production and emissions of bottom ashes from natural wild fires and biomass burnings are sparse or, worse still, lacking. Nevertheless, biomass burning has been noted as a major contributor to particles in the atmosphere including ashes (Williams et al., 2012).

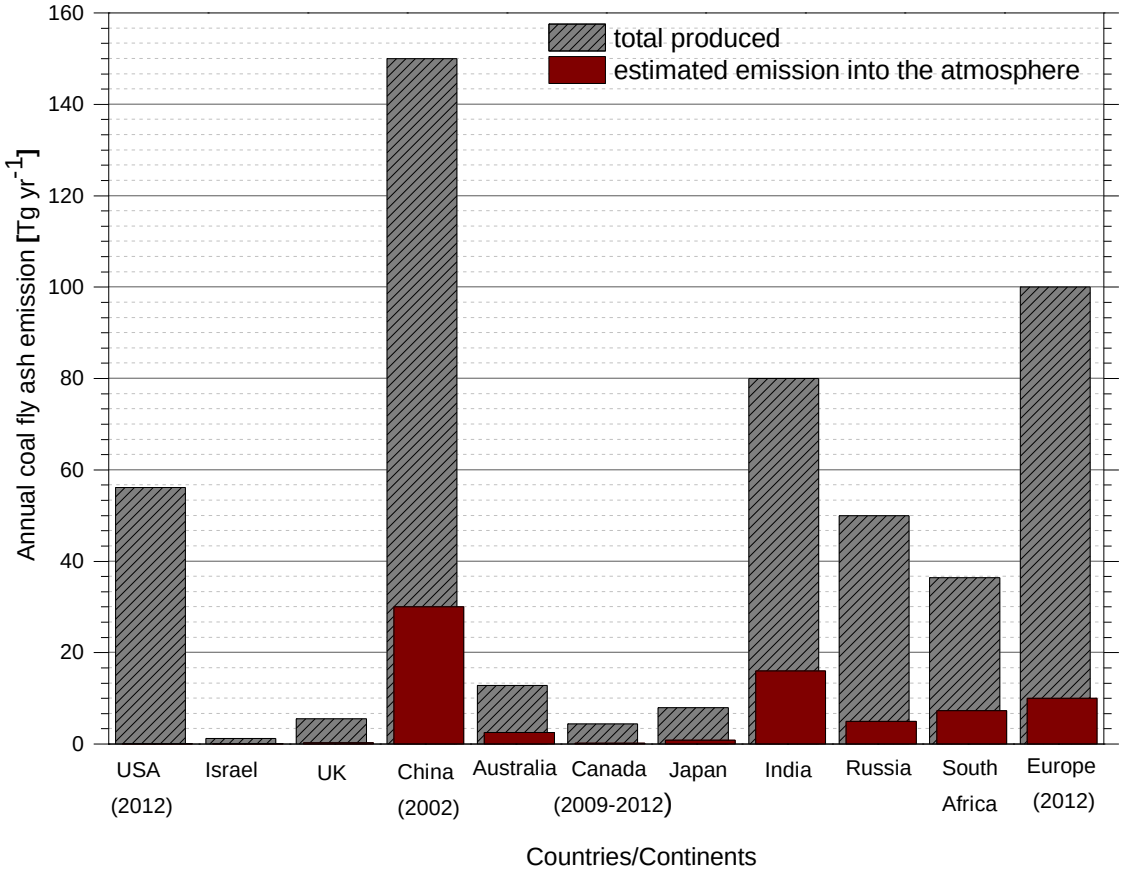

Figure 6.1: Annual emissions of coal fly ash (Tg) from different countries and continents. The estimated amount into the atmosphere is scaled to the handling efficiencies and available technology. The original data used here were collated from various sources - American Coal Association report, conference paper (Feuerborn, 2005), and a report from Enel Energy Group <www.enel.it> (Belz and Caramuscio, 2005).

6.3 Combustion ashes as aerosol particles and motivation for the study

While fly ashes make it directly into the atmosphere via some routes earlier highlighted, bottom ashes, which are the left over ashes after a combustion process (Vassilev et al., 2013) can be lofted into the atmosphere by light winds or by a convective system

sweeping through an area where these materials are left behind - similar to what is observed in dust storms (Goudie and Middleton, 2001). Eventually, these particles constitute part of the aerosol particles in the atmosphere. And generally, aerosols can have direct or indirect impacts on the climatic conditions of the Earth's atmosphere (Graf, 2004; Baker and Peter, 2008; Ramanathan et al., 2001; Pósfai and Buseck, 2010; Tao et al., 2012; Pöschl et al., 2010).

Some studies have highlighted the indirect impacts of soot, which is one of the combustion by-products, on cloud properties (DeMott, 1990; Dymarska et al., 2006; Popovicheva et al., 2008a), but data on the potential impacts of combustion ashes in modifying cloud properties are lacking. Yet, field studies have reported the presence of ash together with mineral dust in ice residues (Cziczo et al., 2013; Li and Shao, 2009; Richardson et al., 2007; DeMott et al., 2003), and also model studies have established a similarity between some elemental components of natural mineral dust (e.g AZTD) and fly ash in the atmosphere (Chen et al., 2012).

Also, in the past, different researchers have studied ice nucleation processes for various aerosols in different nucleation modes. Details of the ice nucleation modes are described in section 2.2. For example, ice nucleating properties of glassy aerosols was investigated in the deposition/condensation modes (Wilson et al., 2012; Murray et al., 2010b), freezing of mineral dust aerosol particles in the contact mode (Hoffmann et al., 2013; Ladino et al., 2011; Ladino Moreno et al., 2013), and in the immersion mode ice nucleation for mineral dusts and others (Murray et al., 2012) and references therein. The focus of this present study will be in the immersion mode ice nucleation because it has been noted that this is an important ice nucleation mechanism that may be dominant in mixed-phase clouds (Bond et al., 2013; Murray et al., 2012; Ansmann et al., 2009).

In this present work, a systematic investigation of ice nucleation activities of combustion ashes (coal fly ash (CFA), wood bottom ash, domestic bottom ash, and coal bottom ash) in the immersion mode at conditions relevant for mixed-phase clouds is reported. All the ashes used for this study were generated at controlled and well-defined conditions as described in section 4.2.2. An attempt is also made to estimate the amount of ash that is released into the atmosphere based on the available data, and to quantify the potential ice nuclei concentrations in mixed-phase clouds as a result of their ice nucleating activities.

6.4 Ice nucleation studies on ashes (literature)

In the literature, only a few studies are reported on the potential impact of combustion ash on ice formation (Schnell et al., 1976; Parungo et al., 1978; Langer et al., 1967). For example, Schnell and his co-workers investigated the ice activity of a plume from a coal-fired power plant, and this study was carried out in a diffusion chamber in the deposition and condensation modes. No investigation was carried out in the immersion mode to see if it nucleated ice.

Looking into available studies on ice nucleation by ashes, only a few reports are found: a study reported in 1976 by Schnell et al and a repeated work by Parungo et al in 1978. Schnell and co-workers (Schnell et al., 1976) conducted a study around the Four Corners power plants in the USA to measure the ice nucleating abilities of the particles in a plume from the coal-fired power plant. Their study showed that plume particles did not act as IN between -10 °C and -20 °C in the deposition or condensation mode, as no difference was observed between the background air and the plume as depicted in Figure 6.2. It was also concluded that the plume gases did not deactivate natural ice nuclei. In contrast, other fly ash source such as volcano has been proposed as a better IN than other combustion by-products such as soot (Fornea et al., 2009).

Conversely, a repeated study at a higher supersaturation showed an enhancement in the number of ice crystals, precisely twice as natural aerosols (Parungo et al., 1978). The study attributed the observed low ice activity to the presence of hygroscopic substances such as sulphuric acid and nitrates or hydrophilic coatings on the fly ash particles; which they suggested that the coatings could have caused a depression in the freezing point. In another experiment, Langer et al. (1967) showed that a heated sample of fly ash nucleated ice in an order of magnitude higher than an unheated sample of the fly ash; hence, they suggested that this could be due to volatilization of substances present on the surface of the fly ash particles (Langer et al., 1967). However, none of these studies measured the ice nucleating abilities of these particles in the immersion or contact freezing mode. Also, no specific examination of the particulates was reported although it was mentioned that the plume air was a mixture of fly ash particles and gases (Schnell et al., 1976). Interestingly, Parungo et al. (1978) did not rule out the possibility that fly ashes can have an important impact on the atmospheric ice nuclei budget.

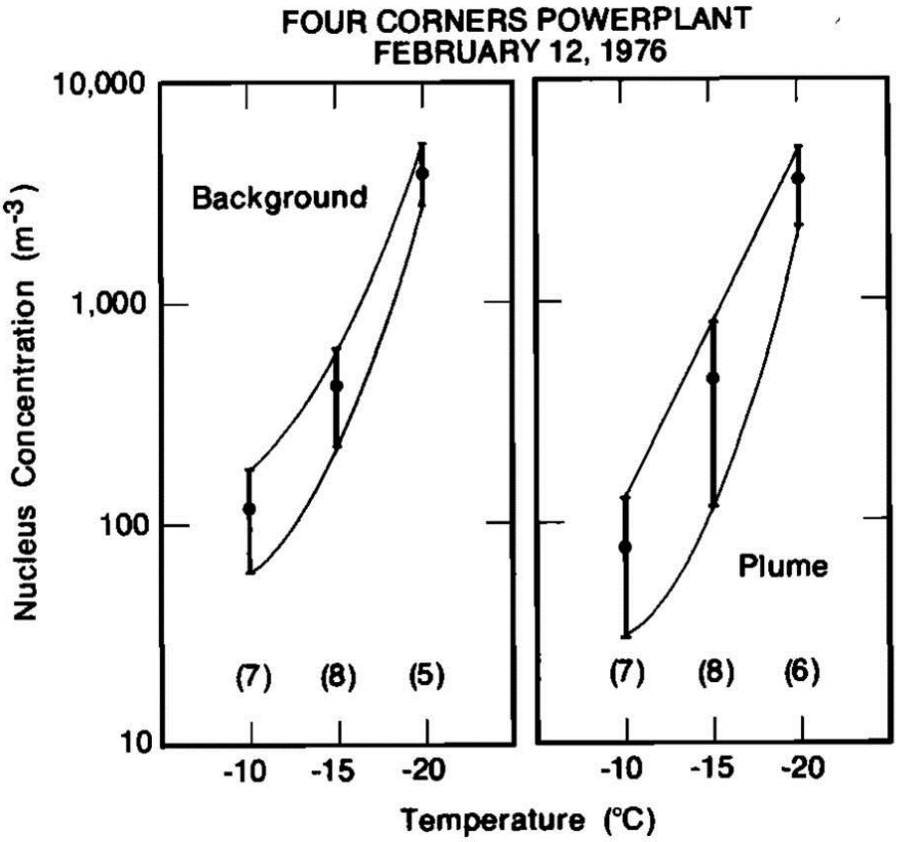

Figure 6.2: IN concentrations observed from Millipore filters exposed to a background air and a plume from a coal fired power plant. The activation temperatures were -10 °C, -15 °C, and -20 °C (Schnell et al., 1976).

Aside from these studies, no other investigation has been reported on the efficiency of combustion ashes as IN. Therefore, in an attempt to improve the understanding of the role of combustion ashes as IN, this present study, for the first time, investigated and reports the ice nucleating abilities of CFA and other combustion bottom ashes in the immersion mode.

6.5 Results and discussion

This section presents the results from the ice nucleation studies of CFA, wood, domestic and coal bottom ashes, and concurrently discusses them.

6.5.1 Freezing of ashes in the immersion mode – CFA, wood, domestic, and coal bottom ashes

Ash samples were generated and characterised as described in chapter 4. The ice nucleation experimental methods used in this study are described in sections 3.3.1 (µL-NIPI) and 3.3.3 (ρnL- and pL-NIPI), and references will be made to them.

Before any ice nucleation experiments with ash suspensions were conducted, an experiment with ultra-pure water (18.2 MΩ.cm resistivity) was carried out on the same set of instruments (µL-NIPI and nL-NIPI). The results obtained from these experiments served as a baseline for this study (see section 3.3.1 and 3.3.3.2), which are plotted as a background for each ash dataset shown. The fraction of droplets containing different concentrations (wt%) of CFA, wood, domestic, and coal bottom ashes are shown in Figures 6.3 and 6.4, and a plot of combined fraction of droplets frozen for 0.1 wt% ash suspensions is presented in Figure 6.5.

Ash suspensions (0.1 wt%) showed heterogeneous freezing in both set-ups - µL-NIPI and nL-NIPI experiments (Figures 6.3 and 6.4). In the µL-NIPI, fractions of droplets frozen for 0.1 wt% CFA suspension clearly froze above -23 °C (the threshold which < 9% of droplets freeze heterogeneously in the control experiments – see section 3.3.1), and the curves have steep gradients. This possibly indicates that CFA contained unique particles or sites on particles that trigger freezing within a 1 °C range (-16 °C to -17 °C). When the 0.1 wt% CFA suspension was diluted to 0.02 wt%, a similar steep curve was also observed but within 2 °C freezing temperature range. A factor of 15 dilution showed a less steep gradient, the droplets still froze above the set threshold (-23 °C) regardless of the dilution. A further 10-fold dilution from 2.0 x 10^{-3} wt% to 2.0 x 10^{-4} wt% showed a broader range of freezing temperatures even in the lower temperature regime of the baseline plot (blue data points). This indicates that some of the droplets may not have had ice active CFA particles in them due to large dilution.

In the nL-NIPI set-up, freezing of nanolitre droplets from CFA suspension was clearly above the homogeneous freezing threshold. Freezing events were observed from ~ -18 °C to -36 °C depending on the size distribution of the droplets. From the plots shown in Figure 6.4, CFA_1, 2, and 3 showed a steep gradient which indicates a more uniform droplets size distribution whereas a more broad freezing temperatures range as shown by CFA_A designates a more varied size distribution of CFA droplets used in the

experiment. When this was normalized to the surface area, there was a good agreement as will be shown in Figure 6.6.

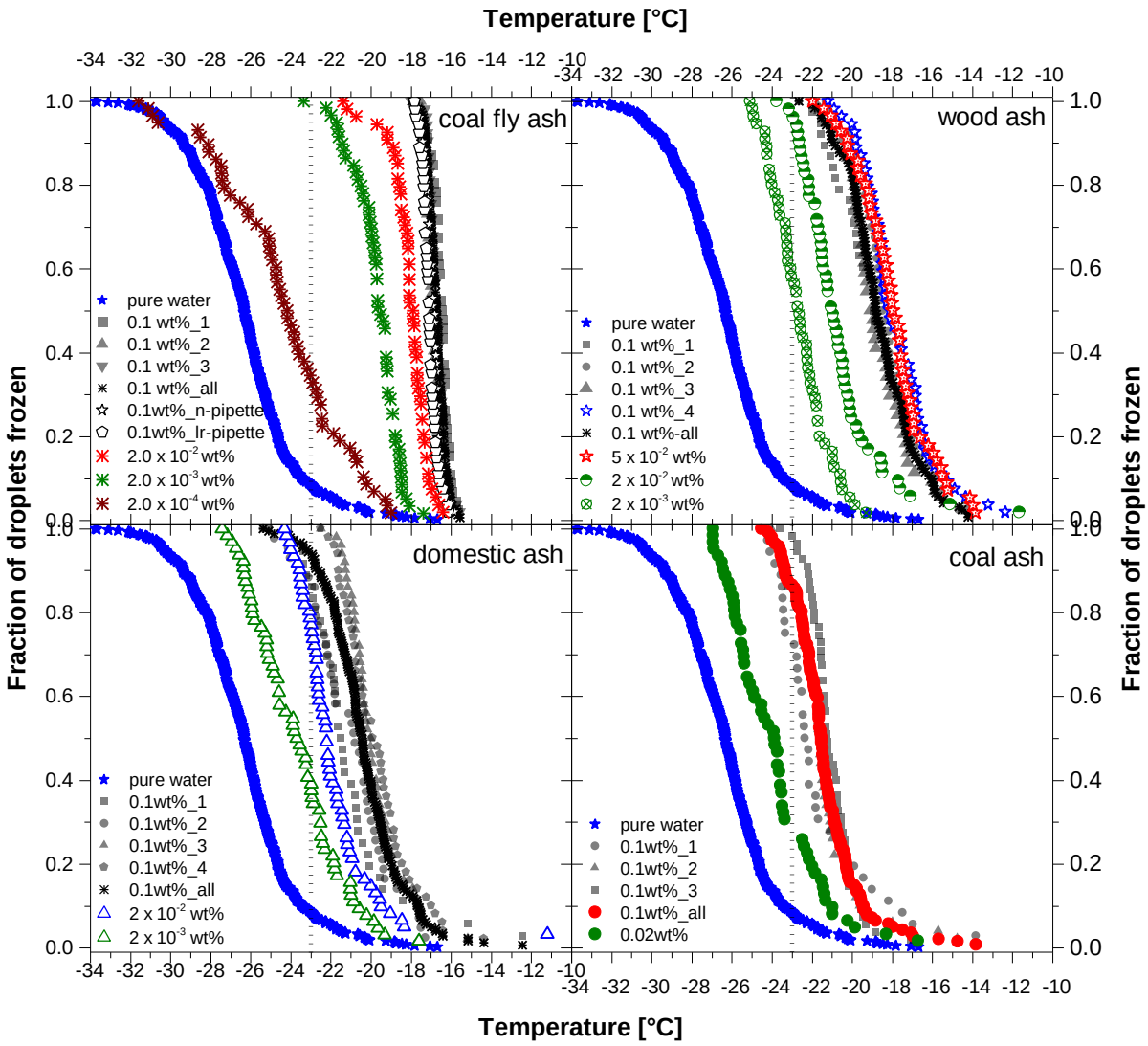

Figure 6.3: Fraction of droplets frozen from freezing experiments in the µL-NIPI. Each panel shows freezing curves of droplets made from a suspension containing known concentrations of coal fly ash (CFA), wood (biomass), domestic, and coal bottom ashes. For all the panels, the blue stars represent the freezing curve for ultra-pure water (18.2 MΩ.cm resistivity) and the dotted lines indicate a baseline or a threshold for homogeneous freezing taken as -23 °C. All plots of 0.1 wt%_all on every panel are cumulative fraction frozen obtained from several repeat experiments and are later showed in Figure 6.5.

The wood (biomass) bottom ash freezing pattern was different from CFA. For droplets containing 0.1 wt% of biomass bottom ash, freezing events were observed within 11 °C interval (~ -12 °C to -23 °C), which is broader than the equivalent concentration of CFA. A factor of 2 decrease in the suspension concentration did not show any significant decrease in the freezing temperatures. It is unclear why no shift to lower temperatures was observed for 5.0 x 10^{-2} wt% concentration. Freezing experiments with

varied droplet volumes (0.5 µL and 5.0 µL) showed similar freezing signatures as shown in Appendix D (D1 and D2). A further reduction in the wood ash concentration showed a decrease in freezing temperatures and a similar pattern was observed for 2.0 x 10^{-3} wt%. However, for wood ash, about 50% froze below the set baseline. The freezing trend of decreasing temperature as the concentration decreases had been observed in previous freezing experiments with mineral dust sample - kaolinite (Murray et al., 2011). Freezing temperatures of 0.1 wt% wood ash-containing droplets in the nL-NIPI system froze at ~ -24 °C down to the homogeneous limit (-36.5 °C) as shown in Figure 6.4.

For domestic ash suspensions, more than 90% of the 1.0 µL droplets froze above the baseline (-23 °C) within 5 °C interval. There was a decrease in the freezing temperatures for droplets that contained lesser amounts of domestic ash particles – i.e. up to 80% and 40% for droplets containing 2.0 x 10^{-2} wt% and 2.0 x 10^{-3} wt%, respectively, froze above -23 °C. For the nL-NIPI system, freezing of droplets was observed from ~ -18 °C to the homogeneous limit (-36.5 °C) as shown in Figure 6.4.

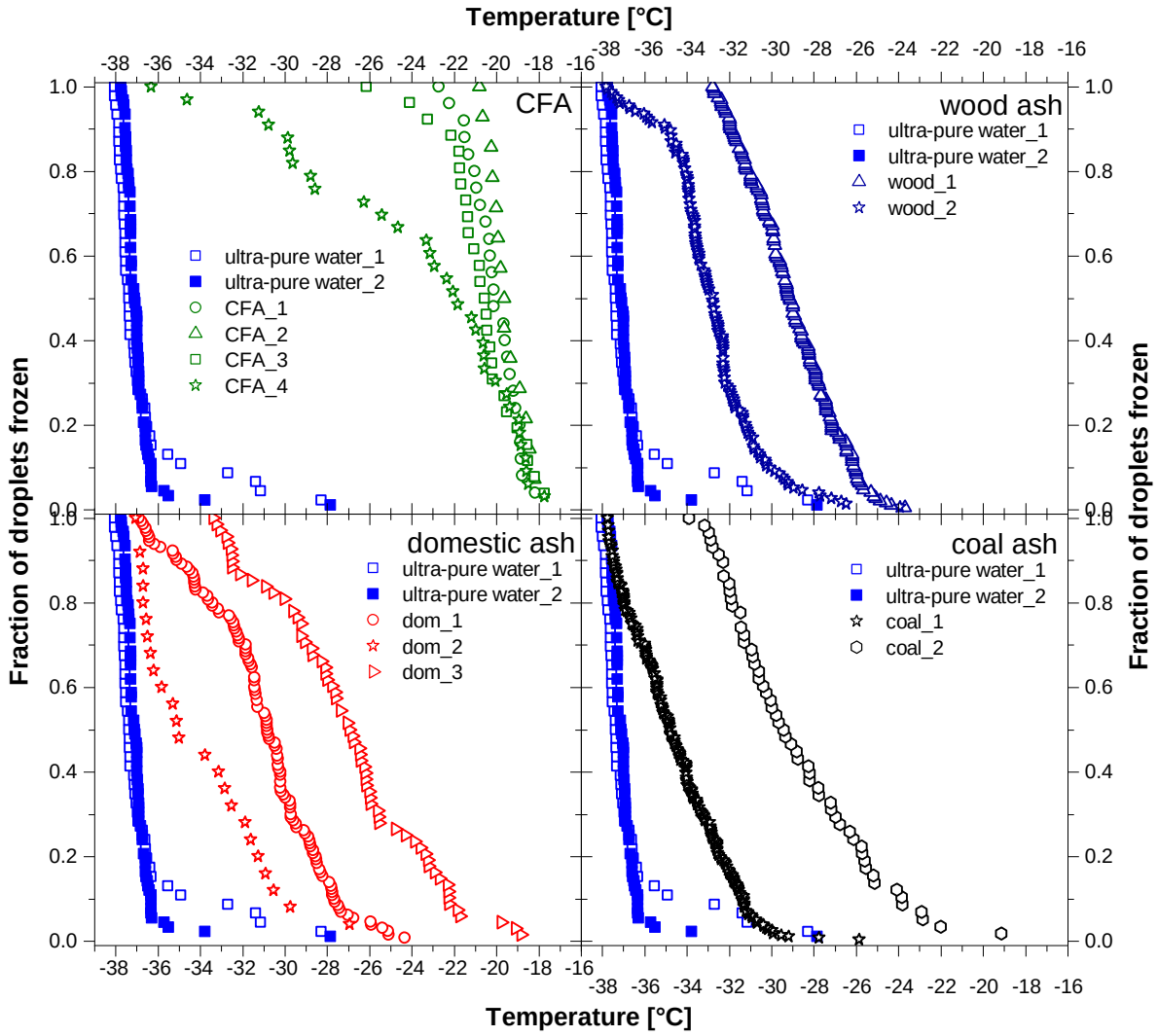

Figure 6.4: Fraction of droplets frozen from freezing experiment in the nL-NIPI. Each of the panels show freezing curves of droplets made from a suspension containing 0.1 wt% of coal fly ash (CFA), wood (biomass), domestic and coal bottom ashes. For all panels, the royal blue squares (filled and unfilled) represent the freezing curve for ultra-pure water (18.2 MΩ.cm resistivity). Uncertainty in the temperature measurements is quoted as ± 0.2 K. The size range of the droplets varied from ~10 µm to 140 µm radius, which volumes translate into picolitre (ρL) to nanolitre (nL) scales.

Droplets containing coal bottom ash showed the least freezing temperatures out of the four ash samples investigated; hence, only freezing results for 0.1 wt% and 0.02 wt% are reported as shown in Figures 6.3 and 6.4. The nL-NIPI freezing for nanolitre droplets from coal ash suspensions was observed from -19 °C to -36.5 °C (homogeneous limit). Generally, although coal bottom ash had lower freezing temperatures the freezing spanned up to 10 °C.

For repeated runs of the same concentration for each of the ashes in the µL-NIPI, a consistency was observed in the freezing temperatures for all repeated runs within the uncertainty in the temperature measurement for the µL-NIPI (± 0.4 °C) except for

domestic ash which the temperature variation was up to 1 °C which may be due to the aggregation of this particles in the suspension or surface effect of the substrate. By comparing the freezing curves for 1.0 µL droplets containing 0.1 wt% for all of the four ash types; CFA froze at a much higher temperature but with a steeper gradient than others. The freezing was in the following order: CFA>>wood bottom ash>domestic bottom ash>coal bottom ash as presented in Figure 6.5.

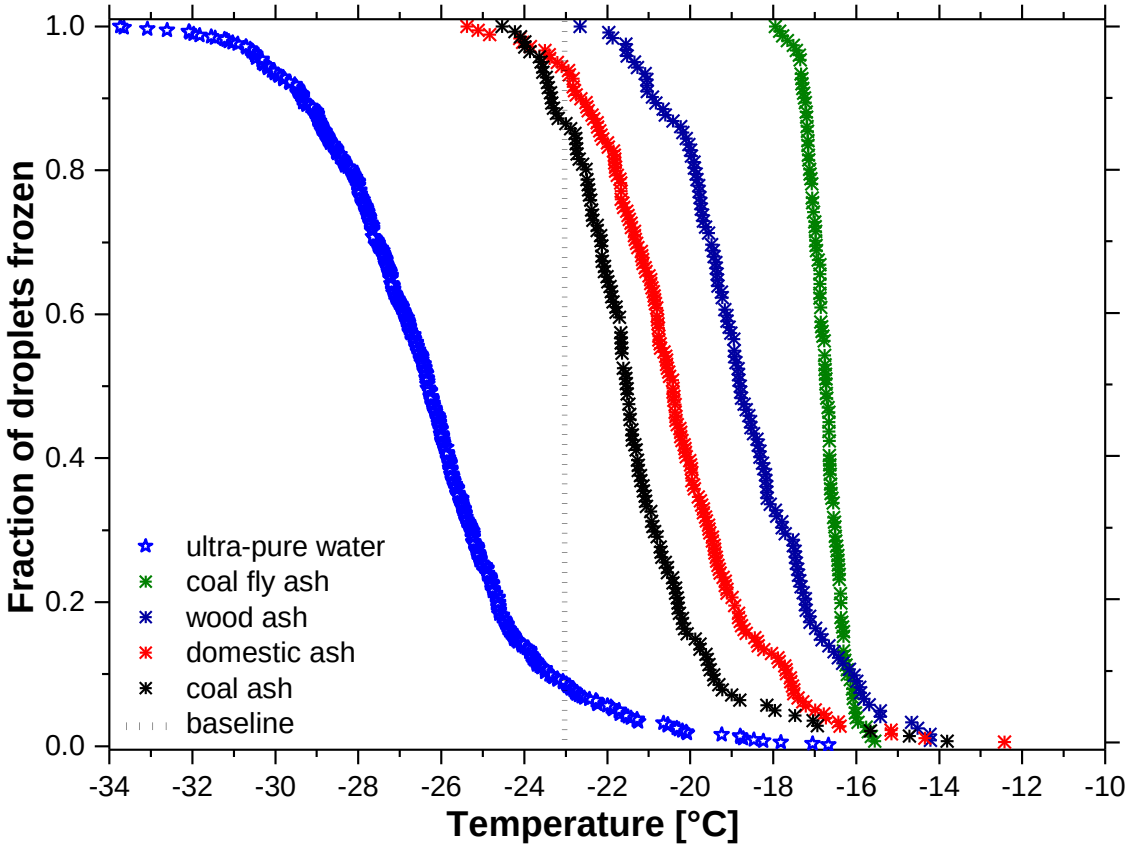

Figure 6.5: Fraction of droplets frozen for different freezing experiments of 0.1 wt% of CFA, coal, wood and domestic bottom ash suspensions using the µL-NIPI. The blue unfilled stars plot is data points from the freezing of ultra-pure water (18.2 MΩ.cm resistivity). The baseline for the µL-NIPI is taken as -23 °C for this experiment.

The freezing temperatures of domestic ash-containing droplets fell between that of wood and coal bottom ashes; this may be a reflection of its origin. It was obtained from burning a combination of biomass materials – hard and soft wood fuel; this inferably could impact a combined characteristic of both ashes on its freezing ability.

6.5.2 Distribution of ice nucleation sites of combustion ashes

In describing the ice nucleating abilities of the different combustion ashes studied, a singular model, which is time-independent, was adopted. Details of this approach were described in the previous chapters (sections 2.3 and 5.3).

In order to use this approximation to quantify the ice nucleating activities of CFA, wood, domestic, and coal bottom ashes, some parameters need to be determined independently of the freezing experiment. In this case, to determine the surface area per unit volume, a measurement of the specific surface area was carried out by BET method as reported in section 4.3.3 and Table 4.1. For the µL-NIPI, volume of the droplets used was measured directly from the electronic pipette used in the experiment; whereas in nL-NIPI experiment, the volume was determined by measuring the diameter of the droplets and using spherical cap volume calculation (section 3.5.2). All results showing the ice nucleation sites for each of the combustion ashes from both µL-NIPI and nL-NIPI, are presented in Figure 6.6. The ordinate is in a logarithm scale and the cumulative number of nucleation sites is quantified in cm^{-2} while the abscissa shows the characteristic temperature (°C), which covers the temperature range explored for both µL- and nL-NIPI experiments.

CFA has nucleation active sites in the range of ~ 10^{-2} to ~ 10^{6} cm^{-2} for the temperature range of -15 °C to -32 °C. The n_s values show that the CFA particles are very good IN; although, only a fraction of these particles are activated. This is an indication that some of the nucleation sites have less dependency on the amount of particles present as shown in Figure 6.6. The narrow temperature range with which the droplets froze also showed that some of CFA particles have unique active sites. Such trend of n_s had been observed for bacteria and biogenic components of soil (O'Sullivan et al., 2014; Murray et al., 2012). A levelling-off of the fraction frozen and nucleation sites have been seen for birch pollen and protein complexes which indicate a limited amount of active sites distribution in the droplets. They show a non-linear logarithm fit similar to what is observed for CFA (Augustin et al., 2013; Hartmann et al., 2013).

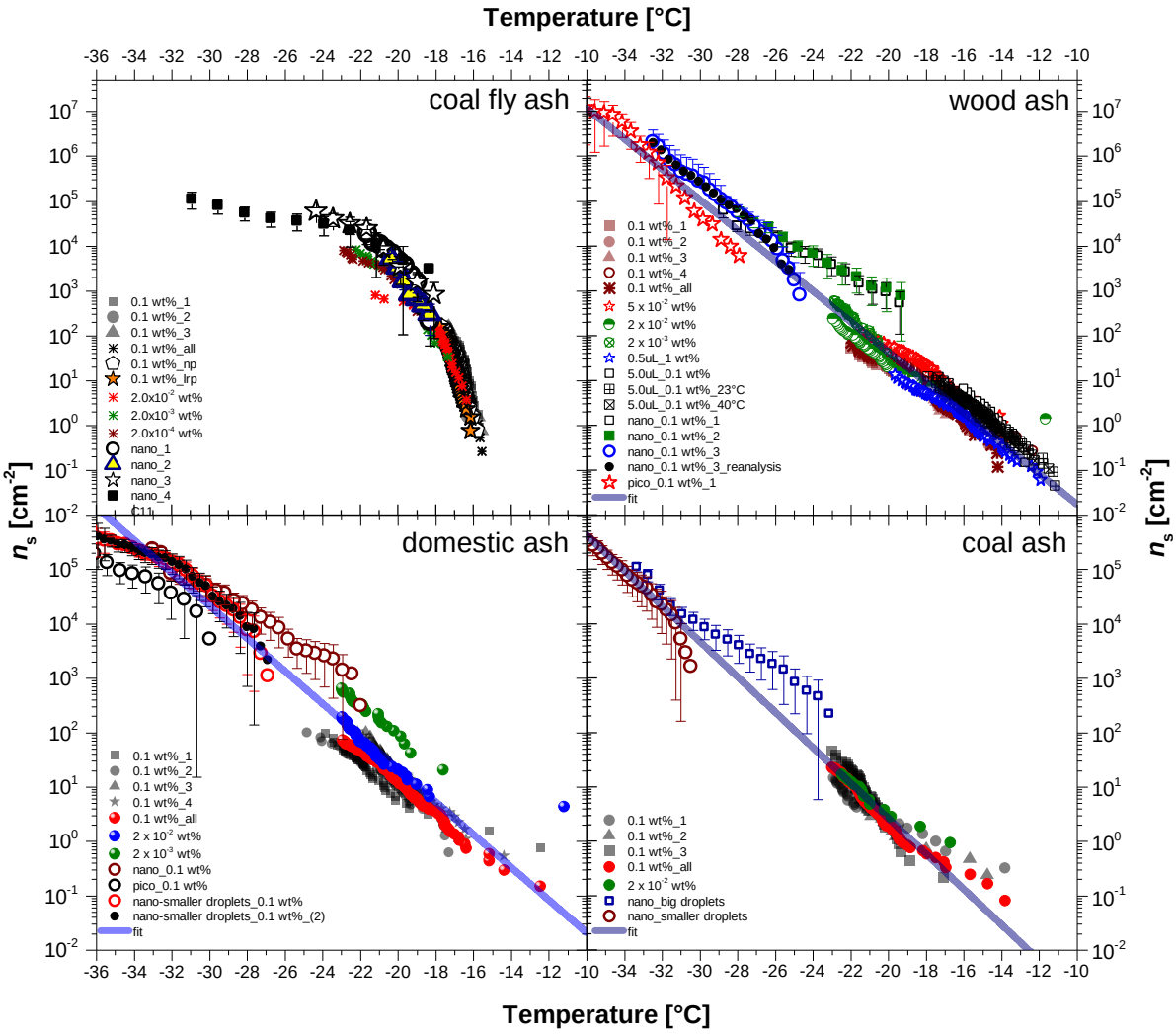

Figure 6.6: Ice nucleation active sites distribution for various weight percentages (wt%) of CFA, wood (biomass) bottom ash, domestic bottom ash, and coal bottom ash suspensions, obtained from freezing experiments in µL- and nL-NIPI. Each panel on the plot represents the cumulative number of active nucleation sites (n_s) on the ash particles calculated from ice nucleation singular model and it covers all the temperature range explored during the experiments.

In the contrast, wood, domestic and coal bottom ashes showed a good agreement between the n_s values from both NIPI set-ups similar to what have been observed for other IN such as kaolinite, feldspar, and soil dusts (Murray et al., 2011; Atkinson et al., 2013; O'Sullivan et al., 2014; Murray et al., 2012; Herbert et al., 2014). In comparing the activities of wood, domestic, and coal bottom ashes to that of CFA, while CFA exhibited a narrow freezing temperature range that is common to some active IN such as bacteria, pollen, snomax, and feldspar (Haga et al., 2013; Yankofsky et al., 1981; Atkinson et al., 2013), the latter group of the ashes (bottom ashes) had a broad range of freezing temperatures. CFA was made up of spherical particles, which some of them are cenospheres and plerospheres (Fenelonov et al., 2010) whereas wood, domestic, and

coal bottom ashes were irregular-shaped particles. In addition, they have a relatively lower surface area (2.5416 m^2/g) compared to the bottom ashes – wood, domestic, and coal ashes. Interestingly, CFA was also obtained from a high temperature combustion system, up to 1500 °C – 1900 °C that makes it different from other ashes studied here (see section 4.2.2).

However, it is still unclear what makes a good ice nucleus, although Pruppacher and Klett (2010) proposed particle's insolubility, size, the nature of chemical bonding and crystallography (lattice match). In terms of size, the particle sizes used for this study were between ~ 45 nm – 10 µm (Figure 4.20) and these are typical sizes of mineral dust found in the atmosphere (Maring et al., 2003; Li and Shao, 2009); and similar size range have been used in some ice nucleation studies (O'Sullivan et al., 2014; Lüönd et al., 2010). One thing to note here is that, the density of these particles varies from 1.60 - 2.45 g cm^{-3} (Fisher et al., 1978; Ghosal and Self, 1995), depending on their morphology i.e. a solid particle or a hollow particle. The properties of CFA which enabled it to form ice at relatively warmer temperatures and at a narrower temperature range than some dust particles, remain a subject for further investigation.

The distribution of ice active sites for the bottom ashes from wood (biomass), domestic, and coal fuel sources showed similar gradients of n_s values versus T. The n_s values for wood ash covering a temperature range of -11 °C to -36 °C were ~ 10^{-2} cm^{-2} to 10^{7} cm^{-2}. For the same temperature range, domestic ash n_s values range from ~ 10^{-1} cm^{-2} to 10^{6} cm^{-2}, which was about an order of magnitude lower than that of the wood ash. Coal bottom ash showed a similar range of n_s as that of domestic ash within -12 °C to -36 °C freezing temperatures.

The three bottom ash types exhibited similar surface morphologies as shown in Figures 4.12, 4.13 and 4.14, but they had different BET surface areas - wood ash (6.98 m^2/g), domestic ash (3.87 m^2/g), and coal ash (8.86 m^2/g). Although CFA and coal bottom ash were obtained from the same fuel source but their ash formation mechanisms were different (Williams et al., 2012), and this is reflected in their surface areas, particle size distributions, and morphologies. The surface area of CFA is about four times smaller than the surface area of coal bottom ash. The difference in their ice nucleation abilities can be attributed mainly to the difference in the formation mechanisms and temperature at which they were produced (section 4.2.2). While CFA was produced at a very high temperature, coal bottom ash was obtained at ~ 300 °C with sufficient oxygen supply.

These combustion conditions can affect the chemistry and composition of these particles (Misra et al., 1993).

The n_s values for all the ashes at the temperature range described in this study are in this order: CFA>>wood bottom ash>domestic bottom ash>coal bottom ash as shown in Figure 6.6.

6.6 Comparison of ice nucleation activities of combustion ashes to IN of varied mineralogies

There is a range of ice nucleation activities for various atmospheric particles which are described by n_s values (Murray et al., 2012; Hoose and Möhler, 2012). The variations in the ice nucleation activities of some of these particles may be linked to their mineralogies (Atkinson et al., 2013). Although, different aerosol particles may contain a percentage of a particular mineral such as quartz, the ice nucleation activity will be controlled by the most active of the components. Atkinson et al. (2013) showed that feldspar is the most ice active component of mineral dust, therefore, the ice nucleation activity of some dust particles may be scaled to the presence of this component (O'Sullivan et al., 2014). Based on these observations, it is important to compare the ice nucleation activity of the combustion ashes to the ice nucleation activities of other minerals reported in the literature.

The plot of the n_s values of CFA, wood, domestic and coal bottom ashes are plotted alongside the n_s values of pure minerals such as mica, montmorillonite, chlorite, feldspar (Na/Ca), calcite, Quartz, feldspar (K) (Atkinson et al., 2013), Kaolinite (KGa-1b) (Herbert et al., 2014), and kaolinite (Murray et al., 2011) as shown in Figure 6.7. From the plot, feldspar (K) is the most active at the temperature regime of -5 °C to -26 °C with n_s range of 10^{-1} cm^{-2} to ~ 10^{8} cm^{-2}, whereas mica showed the least ice nucleation activity at the margin of the homogeneous nucleation of pure water. The combustion ashes studied here has n_s values distributed from 10^{-2} cm^{-2} to 10^{7} cm^{-2} for the temperature range of -9 °C to -36 °C. The n_s values of the combustion ashes were higher than that of the kaolinite at the higher temperatures but showed agreement at the lower temperatures (-28 °C to -36.5 °C). Generally, they showed higher activity than montmorillonite, calcite, chlorite, and mica (see Figure 6.7). A parameterization for different dust types developed by Niemand et al. (2012) for immersion freezing of

desert dust particles for similar temperature range with which the combustion ashes were studied showed higher ice activity. A minor component of an ice-active mineral such as feldspar in these desert dusts (Israel dust, Canaries dust, Sahara dust, Asian dust) could be responsible for this higher activity as mentioned by Atkinson et al. (2013).

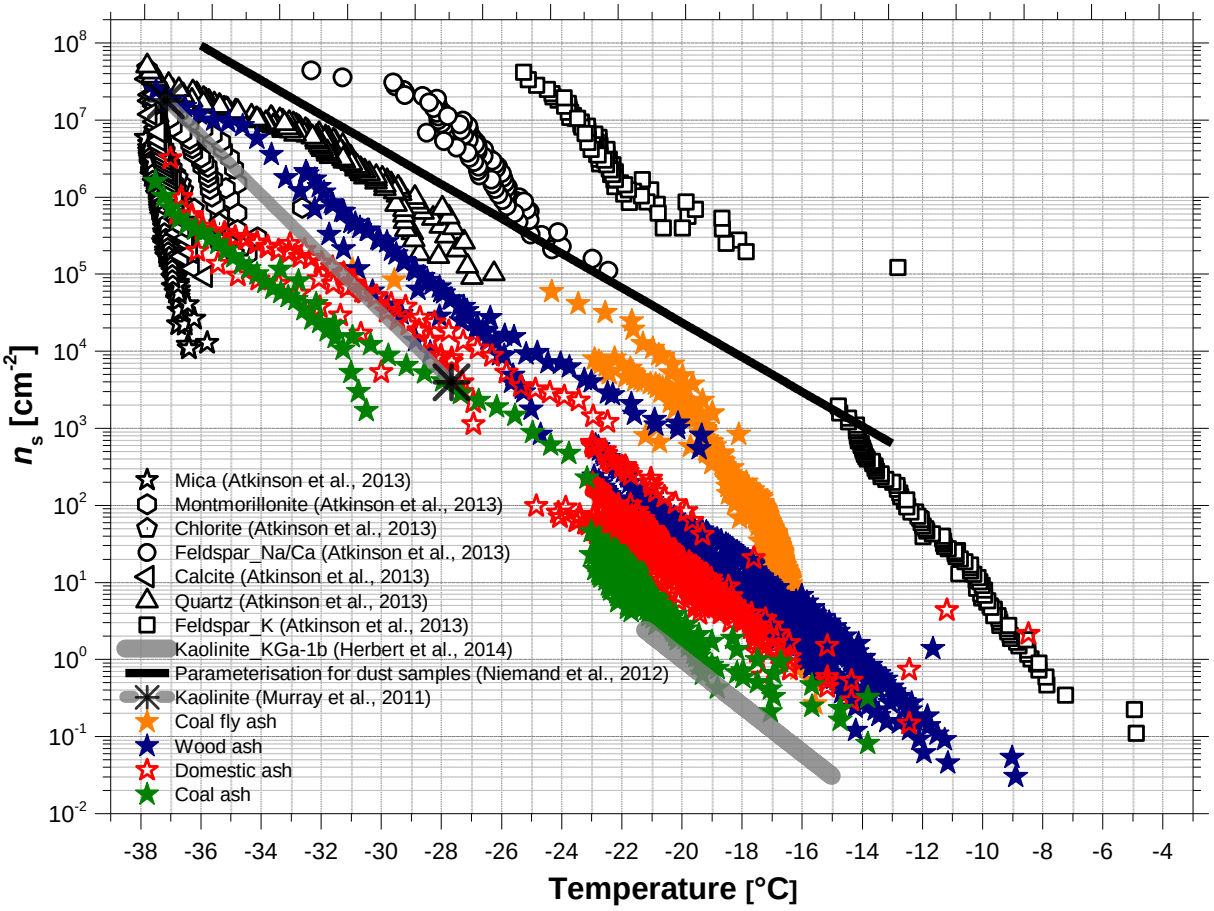

Figure 6.7: Comparison of ice nucleation sites distribution for combustion ashes and other mineral ice nuclei such as mica, montmorillonite, chlorite, feldspar (Na/Ca), calcite, quartz, feldspar (K) (Atkinson et al., 2013), kaolinite (KGa-1b) (Herbert et al., 2014), and kaolinite (Murray et al., 2011). The black line is the parameterisation for the immersion freezing of desert dusts (Niemand et al., 2012). All coloured data points are for combustion ashes.

The ice nucleation sites density reported for CFA, wood bottom ash, domestic bottom ash, and coal bottom ash in this present study fell within the range of most mineral dust IN studies compiled by Murray et al (2012). In general, combustion ashes have been reported to have some mineral/elemental compositions that are found in natural mineral dusts, volcanic ashes, shale, bottom ashes from power plants, rocks, flue gas desulfurization gypsum, volcanic dust, soil dusts, and others (EPRI, 2010).

Focusing on the CFA studied here, the mineral analyses (see section 4.4.1) showed that they are similar to the mineralogy results of CFAs from different sources and locations. The XRD signature for CFA in this study was found to have similar pattern as the one obtained from a coal fly ash from Sasol in South Africa (Nyambura et al., 2011) as shown in Appendix B6. Also, a study of five different CFAs from five separate power plants in the USA showed a similar mineral compositions (ACAA, 2012). Ashes from a domestic pellet-fired boiler that is mainly of biomass origin also showed similar composition (Fernandes and Costa, 2013) (see data in Appendices E1 and E2). It has been reported that over 90% of CFA contains silicon, aluminium, calcium, and iron based minerals (EPRI, 2009); this is consistent with the XRD and EDS results obtained for the CFA studied here, considering that the majority of the amorphous component is mainly silicates (see section 4.4.1). In general, fly ashes from large burning plants are not strongly varied; however, a slight difference could be observed for domestically emitted sources due to particle size variation (Block and Dams, 1976). Even though it has been noted that the ice nucleation activity of a particle may be dependent on a rare component of a particle (Ebert et al., 2011; Atkinson et al., 2013); an investigation to determine the distinct component that is controlling combustion ashes ice nucleation activity is a subject for future study.

Surface morphology have also been reported to impact on the ice nucleation efficiency of haematite particles in the immersion mode (Hiranuma et al., 2013). In this study, the surface morphology of the ashes reported in section 4.4.2 showed that CFA is made up of mainly spherical particles, whereas, other bottom ashes – wood, domestic and coal were dominantly irregular in shape and aggregated as shown in Figures 4.11, 4.12, 4.13 and 4.14 (details on the ashes morphology are discussed in section 4.4.2). Broadley et al (2012) has reported similar morphology for NX-illite particles. The surface morphology of particles does not affect the general composition of the ashes but it can influence the BET measurements, which value is used in calculating the ice nucleation sites density.

The n_s distributions for wood, domestic, and coal bottom ashes for both µL-NIPI and nL-NIPI were similar to that of feldspar (K) (Atkinson et al., 2013) but CFA showed a distribution akin to biological IN. However, most biological aerosol particles – pollen, bacteria, and fungi – have INAS densities from 10^{-1} to 10^{7} cm^{-2} at higher temperature range of ~ -1 to ~ -10 °C. This could be due to a different ice nucleation mechanism associated with these biological aerosol particles. Pollen IN n_s distributions occupied

temperatures of about -15 to -22 °C, which are very different from a core bacterial IN. Recent studies have shown that pollen ice nucleating activity may be attributed to the macromolecules released from the pollen (Augustin et al., 2013; Pummer et al., 2012), which might explain why they behave differently from other biological IN.

6.7 Study on the possible relationship between soluble ions concentration and pH on the ice nucleation activity of combustion ashes

Other factors could directly or indirectly influence ice nucleating abilities of some IN. It has been reported that the ice nucleating ability of some particles immersed in a droplet could depends on parameters such as pH (Attard et al., 2012), organic coatings (Hoose and Möhler, 2012), and ozone interactions with particles (Kanji et al., 2013; Wang and Knopf, 2011). In the laboratory investigation of ice nucleation in the immersion mode, potential IN particles are suspended in ultra-pure water, and mixed thoroughly before the freezing experiment are carried out. Majority of these particles are usually composite of other minerals, compounds or salts; some of these components can dissolve into solution, which could lead to other chemistries in the suspension or on the particles surface. An ion chromatography evaluation of the filtrate obtained from the combustion ash suspensions - CFA, wood, domestic, and coal bottom ashes did not show any correlation with the ice nucleation trend observed for these four ashes.

The pH of the filtrate had a direct relationship with the soluble components of the ashes. Again, the pH of the suspension filtrate did not show a clear trend in its correlation with the ice nucleation activities of the ashes. Looking at the pH of the suspensions, CFA (6.70), wood bottom ash (9.27), domestic bottom ash (9.01), and coal bottom ash (8.57). CFA had the lowest pH and showed the highest ice nucleating ability whereas coal bottom ash's ice nucleating ability was the lowest but its pH was intermediate between that of the CFA and wood or domestic ashes.

In the deposition mode ice nucleation, coating kaolinite particles with an acid (H_2SO_4) have been found to alter its ice nucleating ability (Eastwood et al., 2009). Similarly, sulphuric acid has been reported to alter ice nucleation by soot in the deposition mode (Mohler et al., 2005a). Treating Arizona Test Dust (ATD) with sulphuric acid was reported to decrease its ice nucleating activity (Sullivan et al., 2010), but it is unclear what sort of effect this might have on combustion particles immersed in an acidic

suspension. However, Parungo and co-workers suggested that removal of surface deposited compounds from fly ash could enhance its ice nucleating ability (Parungo et al., 1978); this can possibly be achieved by the particles existing in an acidic medium.

6.8 Study on the possible relationship between ice nucleation properties of ashes and dissolved chemical components

Some aerosol particles are made up of composite materials and sometimes, the main ice nucleating component is a minor constituent of the bulk particle (Atkinson et al., 2013), or even macromolecules that could be washed into the suspension. Macromolecules washed from pollen material have been found to act as ice nucleating agents in the immersion mode (Augustin et al., 2013). In another report, lead (Pb), which is usually a minor composition in nature have been found to enhance the ice nucleating ability of kaolinite in the deposition mode (Cziczo et al., 2009).

In this study, combustion ashes were made into a suspension of ultra-pure water that could result in the dissolution of some soluble constituents of the ashes or even ions. To check this, filtrates of the ash suspensions were tested using an ion chromatography instrument as described in section 4.6. All filtrates from the ash suspensions had high sulfate ions (SO_4^{2-}) concentrations with coal bottom ash having the highest concentration of about 111.99 ppm as shown in Table 4.4. Sulfate ions are usually associated with combustion processes and many times, this had been used as an indicator in tracking combustion emissions. Other ions seen in high levels include potassium ions (K^+), calcium ions (Ca^+), and sodium ions (Na^+). It is not surprising because these ions are often labelled as marker ions for most aerosol particles of combustion origin (Ebert et al., 2011; Murphy et al., 2007; Pagels et al., 2013) or anthropogenic emission (Svane et al., 2005). Although, some individual ions had a strong correlation with the pH of the filtrate and some other ions in the filtrate; no trend was observed between their dissolved ions concentrations and their ice nucleation activities.

6.9 Impacts of combustion ash aerosols on mixed-phase clouds

The relative importance of some IN in mixed-phase clouds have been previously assessed by estimating the ice nuclei concentration (cm^{-3}) that could result from such

particle. This is usually evaluated based on the ice nucleation activity of such IN and the amount of such IN present in the atmosphere (Cziczo et al., 2013; Murray et al., 2012; Atkinson et al., 2013; O'Sullivan et al., 2014). This sort of quantification gives an insight into the potential impact of IN to a specified cloud type at certain conditions. In making similar assessment for combustion ashes studied here, knowledge of the concentration of these materials in the troposphere is very crucial. Sometimes, this can be difficult to obtain, and many times, the available data has a considerable level of uncertainty due to some limiting factors.

Firstly, there is paucity of data because of lack or limited airborne and ground measurements of these aerosol particles (combustion ashes).

Secondly, most literature data that report aerosol particles concentration measurements in the atmosphere or ice residues usually grouped aerosol particles with similar mineral/elemental compositions together or named such aerosol particles as mineral dust. For example, in some ice residue measurements - natural mineral dusts, fly ashes, volcanic ashes, and others are often classed in a single category (Richardson et al., 2007; DeMott et al., 2003; Cziczo et al., 2013; Baustian et al., 2012; Kamphus et al., 2010; Friedman et al., 2013). Some studies, only used dust markers to class such aerosols as mineral dust e.g. (Pratt et al., 2009), and others indicated some groups of aerosols as mixed or industrial (Pratt et al., 2010). Similar observations have been made by Wang et al. (2013) about the incorrect apportionment of coal combustion particles in the atmosphere to biomass burning sources (Wang et al., 2013).

Thirdly, some available measurements do not specify the altitudes at which such measurements were made and this could lead to significant error in using such data for this type of assessment. However, despite these limitations, some rough estimation can be computed directly or indirectly based on some available data or better still; inferences could be drawn to depict something close to actual measurements, for example, a modelled dataset. For the purpose of this study, two approaches could be adopted in predicting the likely impact of combustion ashes as IN in mixed-phase clouds.

(1) The *first approach* is to make an assumption that the particle number concentrations reported for mineral dust could be attributed to the relative amount of combustion ashes in the atmosphere. This can come from ice residue measurements e.g. DeMott et al.

(2003), or any modelled dataset. However, this sort of attribution should be treated with caution. From this assumption, an attempt can be made to quantify the relative impact of combustion ashes as IN using the ice nucleation active sites (INAS) densities of combustion ashes reported in this present study.

(2) *Another approach* that could be applied to assess the potential impact of combustion ashes as IN is by using some available but sparse data about combustion ashes emissions into the atmosphere. This approach has a couple of shortcomings. For instance, most combustion ash emissions from domestic sources are not documented and very sparse data are available for any inference; also, this could lead to a more significant uncertainty in the assessment.

To avoid a higher level of uncertainty in this estimation, the first approach was adopted. The average particle number concentration of mineral dust for the troposphere at about 600 hpa as reported by Hoose et al. (2010) could range from 0.1 cm^{-3} to 50 cm^{-3} as a lower and a upper limits, respectively. Bearing the difficulty of clearly separating natural mineral dust from combustion ashes in mind, an assumption of 20% of the average particle number concentration of mineral dust is ascribed to have resulted directly from industrial sources. This is based on measurements by DeMott et al. (2003), which they reported that mineral dust or fly ash particles measured as ice residues from cirrus clouds, that about 20% are from industrial processes. The major industrial process that emits fly ash is mainly from power generating plants and metallurgical smelting processes. Ordinarily, these particles would be expected to interact in the lower troposphere before reaching the upper troposphere – which could lead to an increase in this number (20%). Notwithstanding, with this assumption and data on the ice nucleation abilities of the combustion ashes reported here, a simple estimation of potential IN concentration (N_{ice}) is calculated following the model below:

$$N_{\mathrm{ice}} = N_c(1 - \exp(-n_s(T)\sigma)) \tag{6.2}$$

Where N_{c} is the estimated particle number of combustion ashes scaled to that of mineral dust in the atmosphere and n_{s} (T) is the ice nucleation sites of combustion ash particles corresponding to their characteristic temperature and σ is the surface area of the total combustion particles available. For this approximation, the particle size assumed for all the combustion particles was 2 µm. The potential ice nuclei number concentration that

could result from combustion ashes at a temperature range of -10 °C to -36 °C is between 10^{-8} cm^{-3} to 1 cm^{-3} as shown in Figure 6.8.

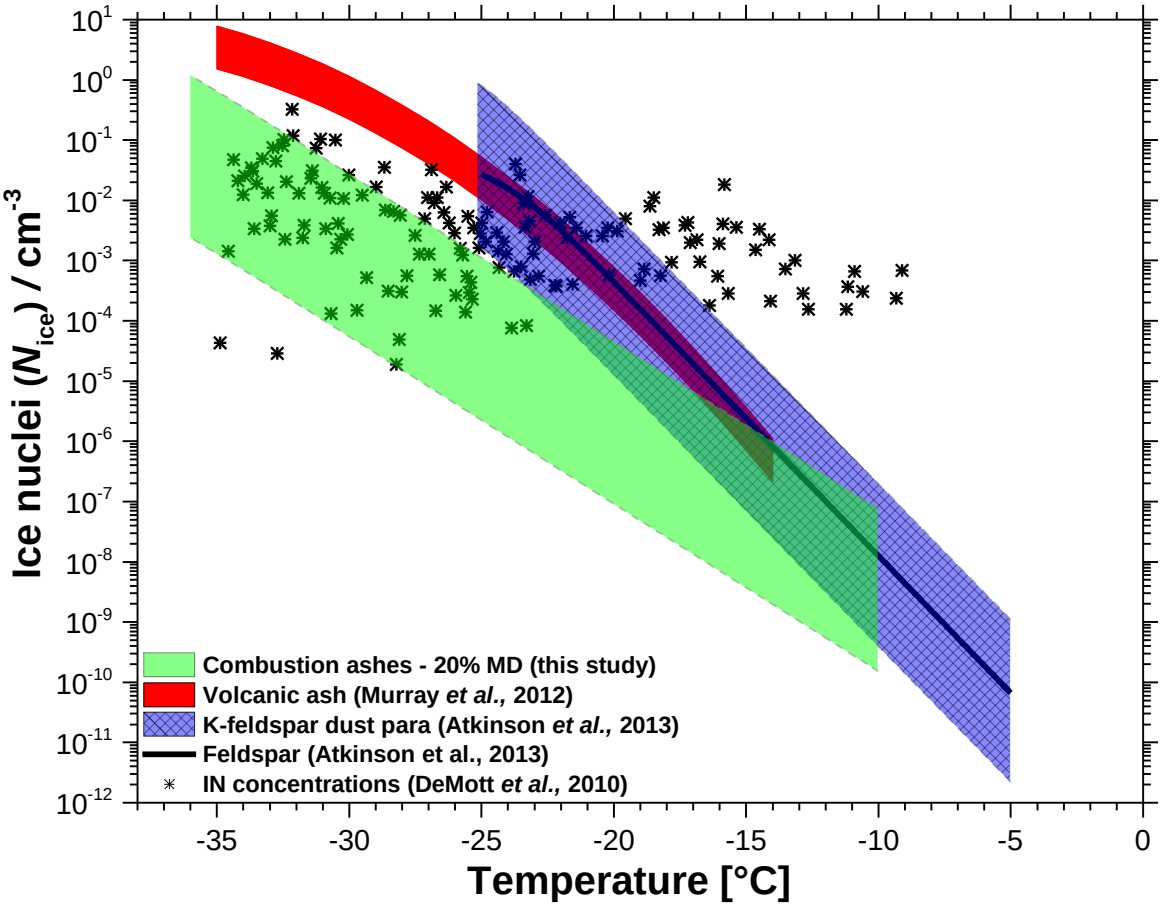

Figure 6.8: An estimation of ice nuclei number (N_{ice}) cm^{-3} that would result based on the ice nucleation activity of combustion ashes from this study. This estimation is based on assumption that 20% of mineral dust number concentration are from combustion ashes, for details about the assumption see section 6.9. The particle number concentration for dusts used here are modelled values from Hoose et al. (2010), while the star data points are IN observations from DeMott et al. (2010). IN parameterisations for volcanic ash and K-feldspar shown on the plot were taken from Murray et al. (2012) and Atkinson et al. (2013), respectively.

In order to make a relevant assessment, a set of data showing IN number obtained from a CFDC measurement (DeMott et al., 2010) is also plotted on Figure 6.8. From the plot, it can be observed that combustion ash particles could contribute significantly to the IN counts observed in the temperature regime of ~ -22 °C to -36 °C. For temperature range of -10 °C to ~ -22 °C, the estimated potential IN number does not agree with the field data. Partly, this could be due to uncertainty in field measurements or dust modelling. Such observations have been noted for predicted IN number due to K-feldspar by Koop and Mahowald (2013); this calls for an improved dust modelling or field measurements. With this assessment, the potential impact of combustion ashes can be compared to similar estimations made for soil dust (O'Sullivan et al., 2014), mineral dust (Atkinson

et al., 2013), volcanic ash, soot, bacteria, fungal spores, and birch pollen (Murray et al., 2012; Cziczo et al., 2013; Haga et al., 2013). Combustion ash potential IN number competes with that volcanic ash and that of mineral dusts; following this, it would be reasonable to suggest that combustion ashes could have a major influence on triggering primary ice formation in mixed-phase clouds. This is not just limited to cloud formation around the emissions sources but globally, largely because, these ashes are capable of long-range transportation due to their low densities.

This impact assessment is based on an assumption that 20% of mineral dust components of aerosols could come from combustion ashes. To ascertain the contribution of combustion ashes to tropospheric IN, a study is needed which will focus on quantifying the emission/abundance of this aerosol particle group in the atmosphere. For instance, during airborne measurements - a clear distinction should be made between mineral dust, fly ashes and volcanic ashes by using methods like magnetisation and coercive field factors (Flanders, 1999; Xie and Dearing, 1999). Coercive field factor gives an indication of the percentage of fly ash that is airborne in relation to the total amount of magnetic material that is airborne.

Other methods include isotopic labelling and back trajectories correction *(Personal communication with James B. McQuaid, University of Leeds)*. Isotopic labelling can be used during measurements by matching the spectra of the minerals in the atmosphere with the known isotopes characteristic of the possible sources of the measured particles. While back trajectory involves separating the emission sources of this combustion ash in comparison to the emission route for natural dusts. However, some of these methods need further development for meaningful measurements.

6.10 Conclusion

The ice nucleation efficiencies of combustion ashes – CFA, wood (biomass), domestic, and coal bottom ashes - were investigated in the immersion mode. The ice nucleation abilities of these materials are comparable with those of some mineral dusts reported in the literature. There are some limitations in assessing their potential impact in mixed-phase clouds: (1) Uncertainty in their atmospheric abundance (2) lack of data on their atmospheric distribution/variability, partly due their long-range transportation capability (3) being surrogates of other aerosol particles makes it difficult to clearly distinguish them from aerosol particles such as natural mineral dust and volcanic ashes. For

instance, the XRD characterisation of their mineral compositions has similar signature to that of a typical natural dust.

From this study, it has been clearly shown for the first time that;

- combustion ashes froze heterogeneously in the immersion mode with CFA showing a very steep gradient, which means that droplets containing CFA particles froze within a few degrees of temperature. This observation strongly suggests that the nucleation sites were present in every droplet investigated.

- For the ash samples studied here, it is clear that high temperature combustion ash particles (CFA) froze at higher temperatures than the lower temperature combustion ashes (bottom ashes of wood, domestic, and coal). More investigations are needed to make this generalisation for all high temperature combustion ashes as only one sample of high temperature combustion ash was studied here.

However, further studies should quantify the effect of atmospheric processing and its implications on their ice nucleation abilities. This can give information on the impact of freshly emitted combustion ash particles. Furthermore, additional airborne measurements are needed to constrain their abundance in the atmosphere considering the eminent problem of attributing minerals measured in the atmosphere to only natural mineral dust emissions or volcanic ashes source. The impact of these ashes on localized clouds in the region of emission may also be of interest for future assessment.

6.11 Chapter summary

Combustion ash particles are one of the major by-products released during the combustion process of most solid fuels. A significant amount of these ashes are injected into the atmosphere and this can influence cloud properties and impact climate. When these ashes are lofted into the atmosphere, they can interact with atmospheric water, which can trigger ice formation especially in mixed-phase cloud. For the first time, this study has reported laboratory measurements of ice nucleation activities of a set of combustion ashes (CFA, wood bottom ash, domestic bottom ash, and coal bottom ash) in the immersion mode at conditions relevant to mixed-phase clouds. The efficiency with which these ashes can form ice in the tropospheric atmosphere is quantified using a

simple ice nucleation singular model which describes ice nucleation sites density (INAS). For ash particles approximately ≤ 10 μm, the number of nucleation sites is between ~10^{-2} cm^{-2} and 10^{7} cm^{-2} at temperatures between -15 °C and -36 °C were in the following order CFA>>wood bottom ash >domestic bottom ash> coal bottom ash. From this particular study, the results show that ash emitted as a result of high-temperature combustion is relatively more active than low-temperature combustion bottom ashes. More data are needed for this hypothesis to be applied to all high-temperature combustion ash. Again based on this initial study, it can be proposed that combustion ashes may play an important role in the formation of primary ice in mixed-phase clouds, especially clouds that form near the emission source of these aerosol particles.

Chapter 7

Summary, conclusions, and future research directions

7.1 Summary of the major outcomes

This chapter highlights the major findings derived from this project. The study's overarching objective was to quantify the ice nucleation properties of soot and combustion ashes. The summary of each main finding is presented below:

(a) *Eugenol and n-decane soot particles in suspensions, prepared with water, froze heterogeneously and this can have an important impact on mixed-phase cloud properties.* The ice nucleation experiments clearly showed that eugenol and n-decane soot particles in suspensions prepared with ultra-pure water initiated ice nucleation in a temperature range of ~ -16 °C to ~ -28 °C in both instrumental set-ups used for the study – µL-NIPI and nL-NIPI. The estimated nucleation active sites density (n_s) for eugenol and n-decane soot particles increased from 1 cm^{-2} at -16 °C to 10^7 cm^{-2} at ~28 °C. Based on the n_s values obtained from this study and a model estimation of soot abundance in the atmosphere at 600 hPa (Hoose et al., 2010), soot was found as an important IN in mixed-phase clouds. Aside, showing a competition with mineral dust at about -25 °C; it can dominate primary ice formation in mixed-phase clouds from about -22 °C in regions where mineral dust or biological materials are not a dominant IN source.

(b) *Combustion ashes – coal fly ash, wood (biomass) bottom, domestic bottom, and coal bottom ashes – were found to nucleate ice heterogeneously in the immersion mode and they can impact mixed-phase cloud properties.* Coal fly ash particles were found as the most active IN of the four ashes investigated and uniquely, the only ash that was produced from a high-temperature system. The order of ice nucleation activity were CFA >> wood (biomass) bottom ash > domestic bottom ash > coal bottom ash. The n_s values ranged from ~10^{-2} cm^{-2} and 10^7 cm^{-2} at a temperature range of -15 °C to ~ -36 °C. An estimation of the potential ice number that could result from the ice-nucleating efficiency of

combustion ashes was up to 1 cm^{-3}. This estimation was done based on the assumption that about 20% of the measured mineral components of ice residues from mixed-phase clouds could be from combustion ashes (DeMott et al., 2003).

(c) *Characterization of combustion aerosols showed that: fly ash particles are distinguished from bottom ash particles, and this variability may be linked to their ice nucleation abilities.* Fly ash particles showed well-defined spherical shapes, whereas the bottom ashes were irregular in shape and tend to aggregate. The mineralogies of the ashes were similar, and any observed variability in the mineral composition could be interconnected to the source of the biofuel or fossil fuel that the ash was generated from. For example, it is not uncommon for ashes from biofuel obtained from iron-rich soils to have high iron contents. This means that their mineralogies could be associated with the accumulation of these minerals over time from the source of the fuel

7.2 Major conclusions

The following conclusions can be drawn from the results obtained in this study:

(a) From this work, it is shown that soot particles from both biomass and hydrocarbon sources nucleated ice in the immersion mode. This was quantified in a temperature range and conditions relevant to mixed phase clouds; in addition, a parameterisation was developed from the results obtained in this study for use in aerosol-cloud microphysics models. Importantly, this work has clearly shown that there is no significant difference between the ice nucleation activity of n-decane and eugenol soot types in the immersion mode[1]. Also, based on the results from this study, it has been shown that the contribution of soot particles to the ice nucleating particles number in mixed-phase clouds is important and should not be neglected as a source of IN especially in areas that soot particles are dominant aerosol components.

(b) For the first time, it is shown from a systematic study that combustion ashes act as IN in mixed-phase cloud conditions, and are quite active compared to soot particles. Coal fly ash particles that come from a high-temperature combustion

[1] This may not be the case in the deposition mechanism ice nucleation. Because if a substance such as sulphuric acid is present on the soot surface, it may influence its hygroscopicity which is crucial in the deposition mode; hence this may affect the ice nucleation activity of such soot particles.

source showed a higher activity compared to bottom ashes from a low-temperature combustion system. Their ice nucleation activities may have some correlations with their physical and chemical properties. The higher ice nucleation activity of CFA particles could be attributed to the unique shapes and some of its chemical compositions (pyrite (FeS_2) and mullite ($Al_6Si_2O_{13}$)). Although the ice nucleation activity of coal bottom ash was in the range of other bottom ashes (wood and domestic), it comprises pyrite and mullite but with irregular shapes. From this study, it can be hypothesized that for the combustion ash particles studied here, that the spherical shapes of CFA particles was the differentiating property from the bottom ashes. Further studies are needed to establish this hypothesis.

7.3 Recommendations for future research

To further the understanding of combustion aerosol particles contributions to cloud adjustments, the following recommendations are proposed for future investigations:

(a) Aging of soot and combustion ashes by atmospheric species such as ozone (O_3), sulfuric acid, NO_x and SOAs *could* influence their ice nucleation properties in the immersion mode. The surface of these particles can be altered by these species due to chemical oxidation or dissolution of the components or structures at the surface (Zuberi et al., 2005). Once the surface properties of these particles are changed, it can affect the water-particle surface interaction which may influence their ice nucleation activities (Gorbunov et al., 2001). Therefore, to constrain the impact of these atmospheric species on the ice- and cloud-forming properties of combustion aerosols, a systematic study to investigate the influence of aging by the species mentioned above at atmospherically relevant concentrations and conditions would be highly recommended.

(b) Recently, it has been shown from modelling studies that the ice nucleating abilities of carbon surfaces such as soot correlate with the layering of water on the carbon surface rather than the surface properties such as the chemical groups on the surface of the carbon material (Lupi et al., 2014; Lupi and Molinero, 2014). It is strongly recommended that the actual mechanism of ice nucleation on soot surfaces be probed in the laboratory by using analogues of carbon surface with known surface properties such as graphene and modified graphene.

This will help in the understanding of what controls ice nucleation of carbon surfaces in the immersion mode.

(c) Understanding the ice nucleation properties of fly ashes from biomass combustion and specifically, other combustion by-products such as tar balls will be useful in quantifying the total impact of combustion by-products in mixed-phase clouds. Fly ashes emitted during wild fires are injected directly into the atmosphere: therefore, they could contribute to the total combustion aerosol particles loading in the atmosphere.

(d) Presently, there is no clear distinction between fly ash and mineral dusts in reports of components of ice residues e.g. Cziczo et al. (2013) and others; except a study by DeMott et al. (2003) that an attempt was made to distinguish these particles – more of this type of study is needed. This non-distinction can pose difficulty in quantifying the contribution of each aerosol category to ice formation in clouds. Therefore, it would be useful to develop an atmospheric measurement method to clearly distinguish these aerosol groups, especially in aerosol particles measurements, and in ice residue characterisation. Secondly, it is difficult to report the impact of combustion ashes from the domestic sources alone because of limited data on the quantities of combustion ashes emitted from domestic sources. From the experience gained from this study, it is strongly recommended that an assessment of combustion ashes emission be carried out to track different loading sources of this group of aerosol particles into the atmosphere.

Appendix

Appendix A: Pictures from the laboratory

Appendix A1: A picture of EF600 Asymptote Stirling Engine used for µL-NIPI experiments. The full description of the instrument is given in section 3.3.1.

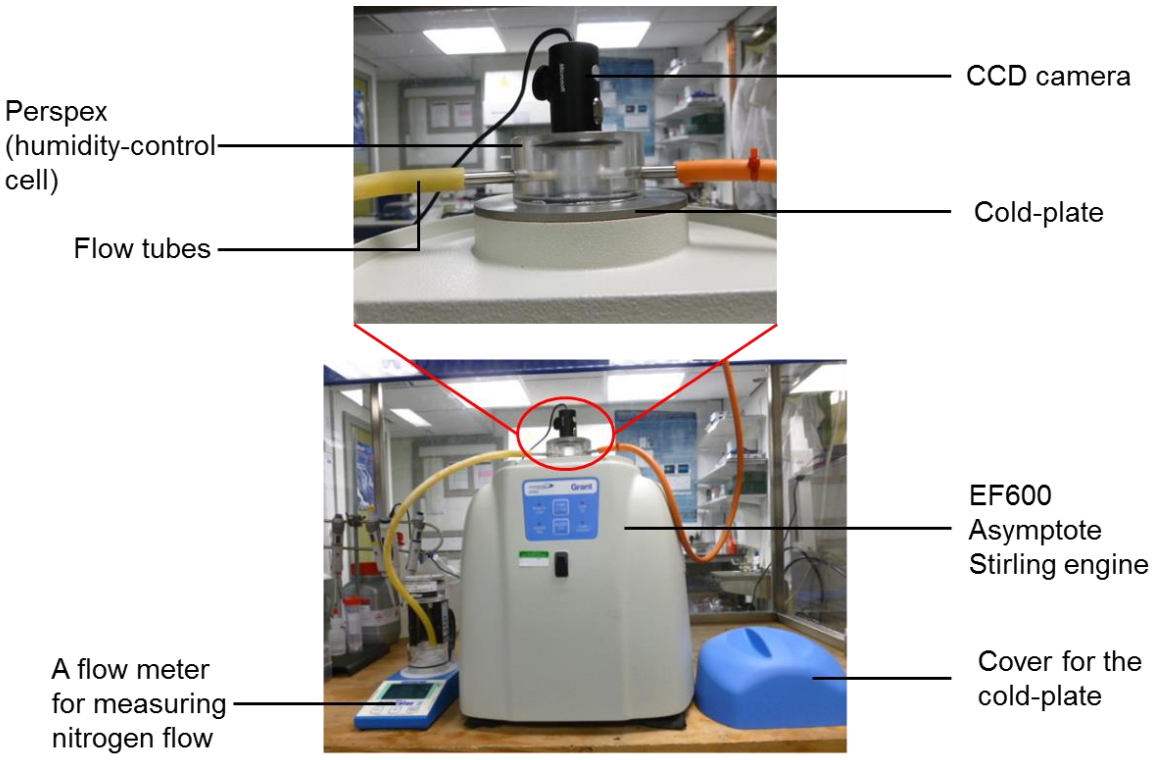

Appendix A2: Pictures of soot/soot suspensions used in this study: (**A**) shows soot particles as obtained from the combustion process in the laboratory, and (**B**) shows soot suspensions prepared by adding soot to ultra-pure water, placed in an ultra-sonic bath and stirred.

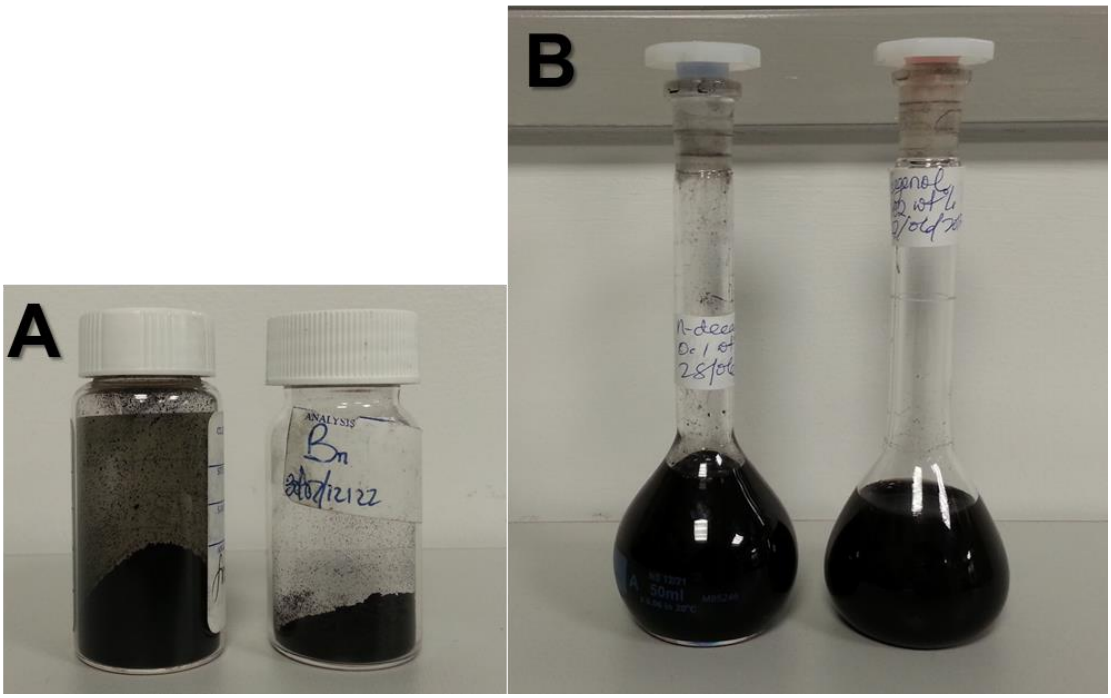

Appendix A3: Pictures of combustion ashes. Various ashes generated from combustion processes (**A**) and ash suspensions prepared by adding ash particles to ultra-water, placed in an ultra-sonic bath and stirred (**B**).

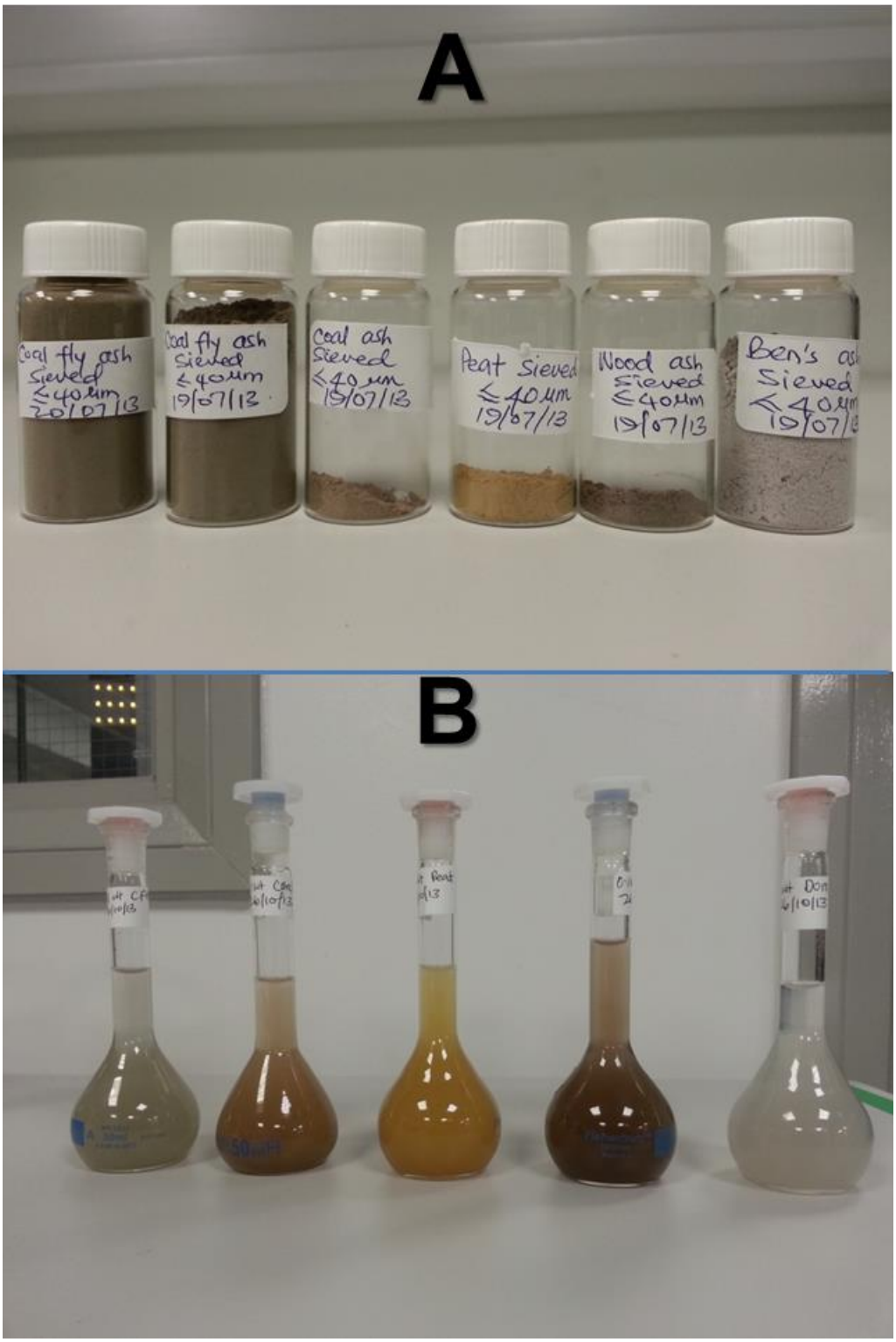

Appendix B: X-ray diffraction patterns

Appendix B1: X-ray diffraction pattern of bulk coal fly ash (CFA) for the qualitative and quantitative analyses of its composition. The letters on the plot are: mullite (M), quartz (Q), magnetite (Me), haematite (H), and pyrite (Py).

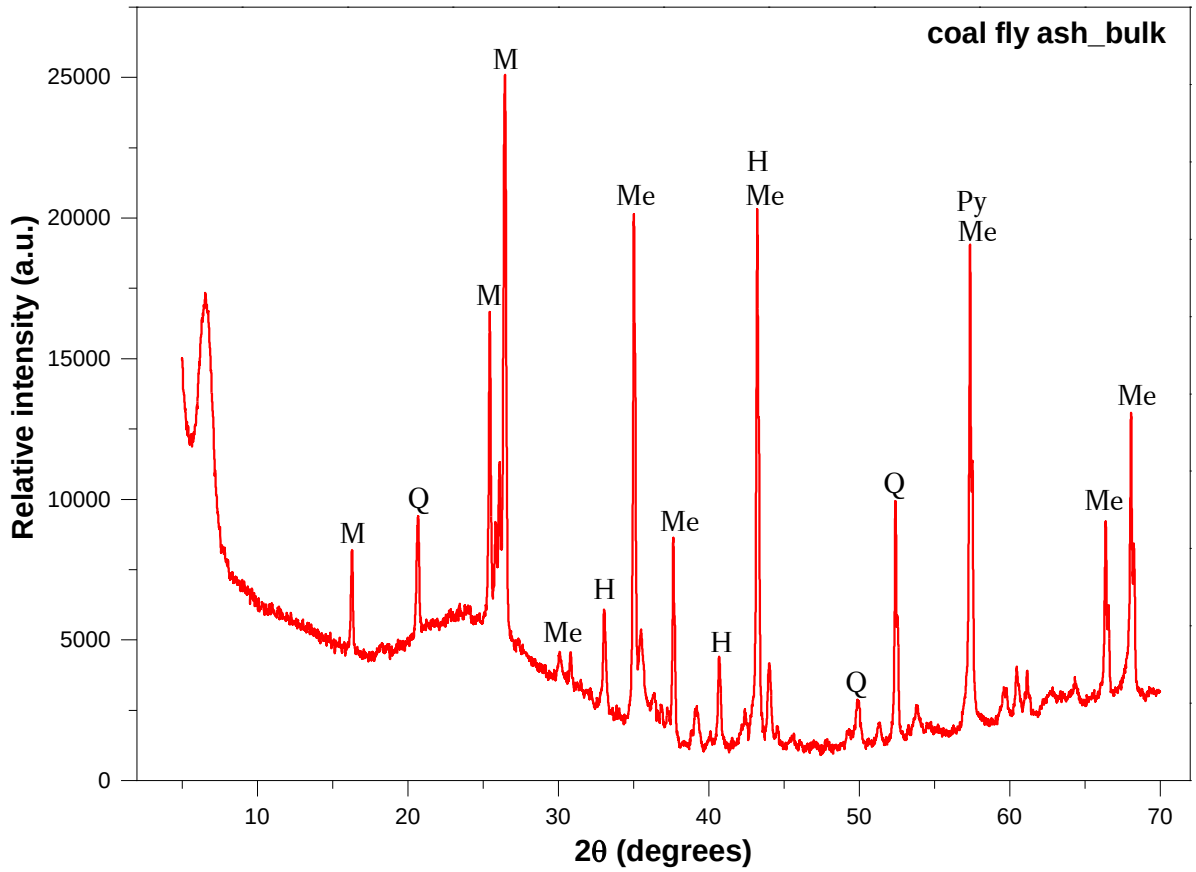

Appendix B2: X-ray diffraction pattern of sieved CFA (sieved to 40 μm) for the qualitative and quantitative analyses of its composition. The letters on the plot are: mullite (M), quartz (Q), magnetite (Me), haematite (H), and pyrite (Py).

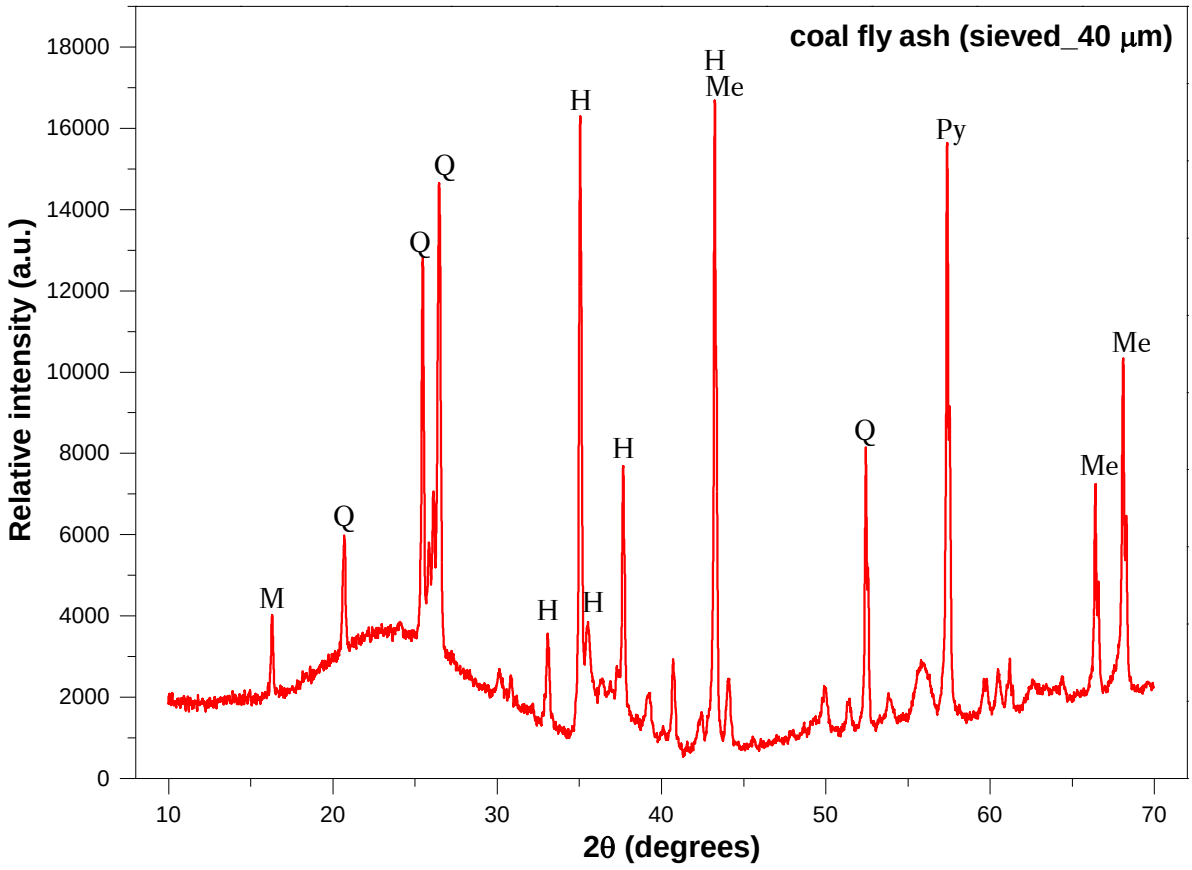

Appendix B3: X-ray diffraction pattern of wood (biomass) bottom ash sieved to 40 µm for the qualitative and quantitative analyses of its composition. The letters on the plot are: quartz (Q), haematite (H), dolomite or gypsum (D), and calcite (Ct).

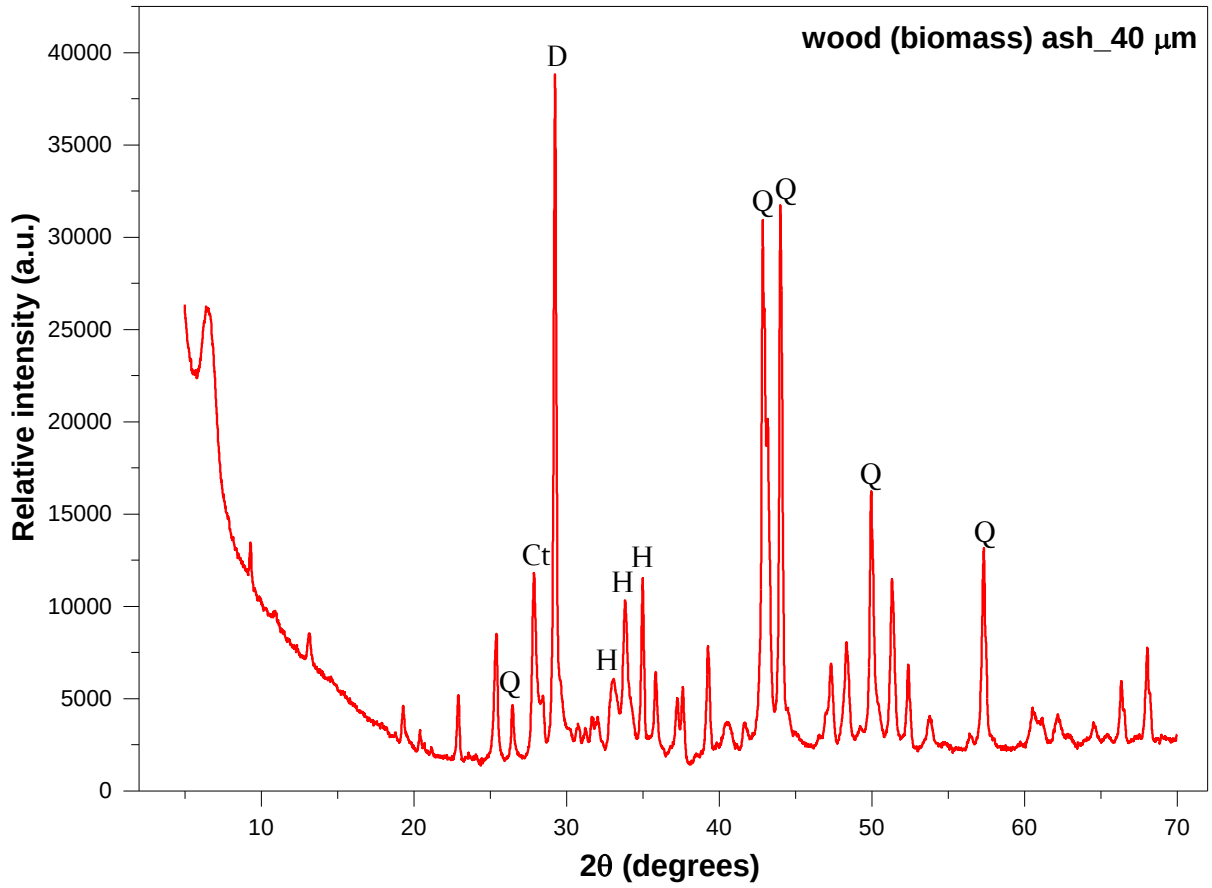

Appendix B4: X-ray diffraction pattern of domestic bottom ash sieved to 40 µm for the qualitative and quantitative analyses of its composition. The letters on the plot are: quartz (Q), haematite (H), and calcite (Ct).

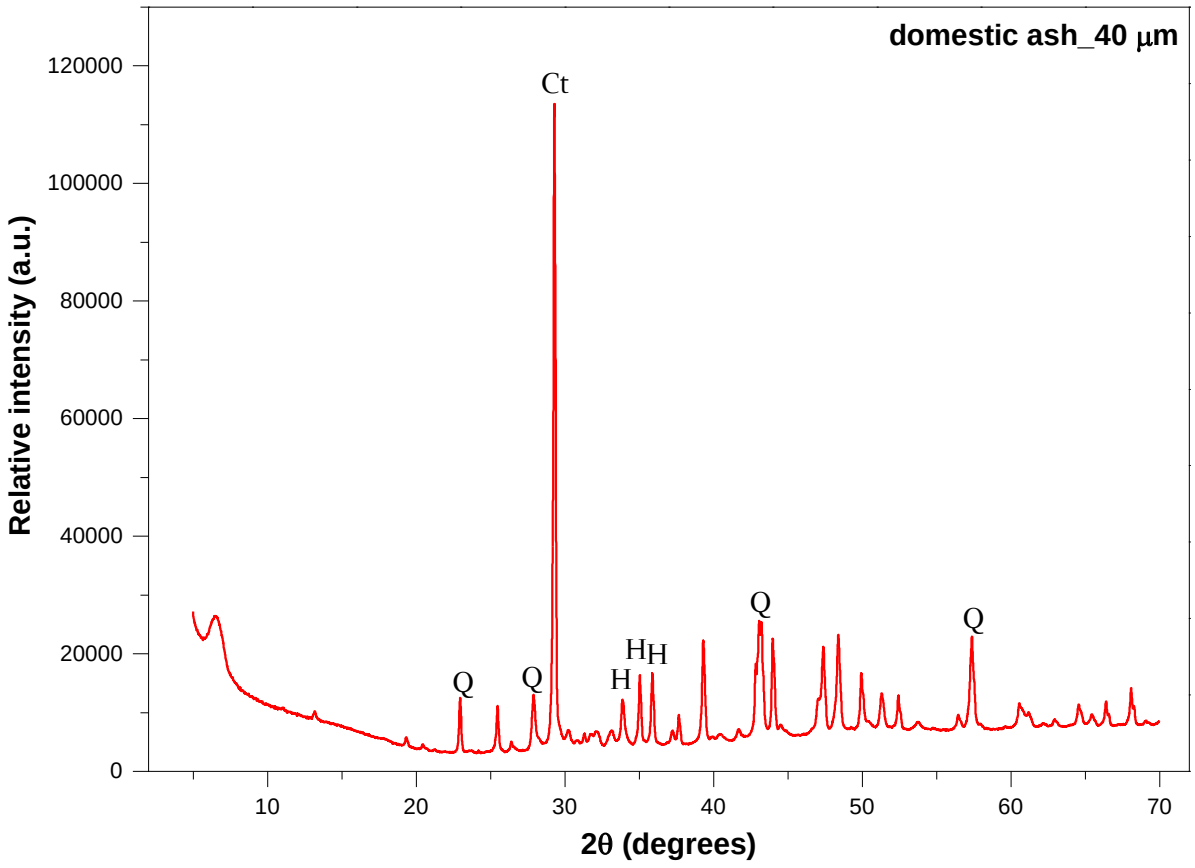

Appendix B5: X-ray diffraction pattern of coal bottom ash sieved to 40 µm for the qualitative and quantitative analyses of its composition. The letters on the plot are: mullite (M), quartz (Q), magnetite (Me), haematite (H), calcite (Ct), dolomite or gypsum (D), and pyrite (Py).

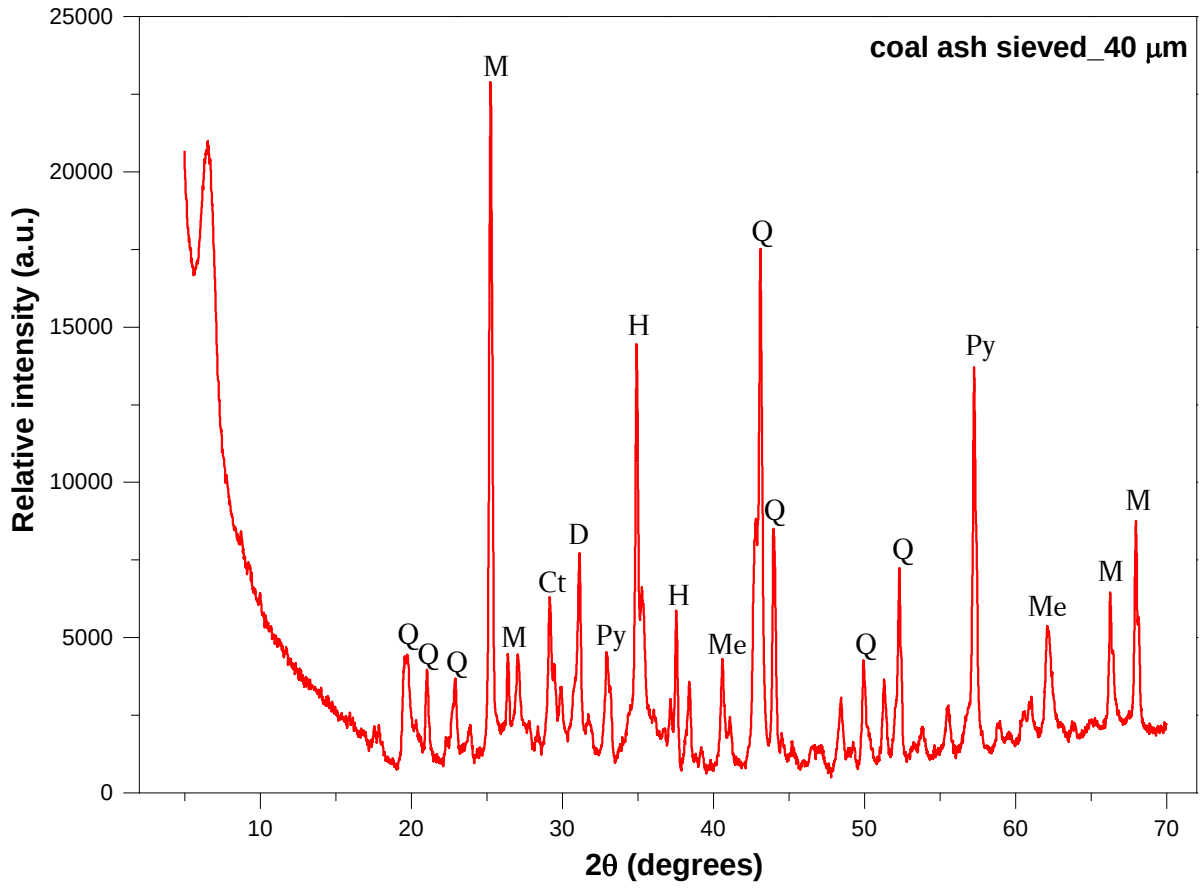

Appendix B6: X-ray diffraction pattern showing the mineralogy of coal fly ash obtained from Coal burning power plants in the Mpumalanga province of South Africa as reported by Nyambura et al. (2011). M (mullite), Q (quartz), C (calcite), A (anhydrite), P (plagioclase), B (bassanite), and Mt (magnetite).

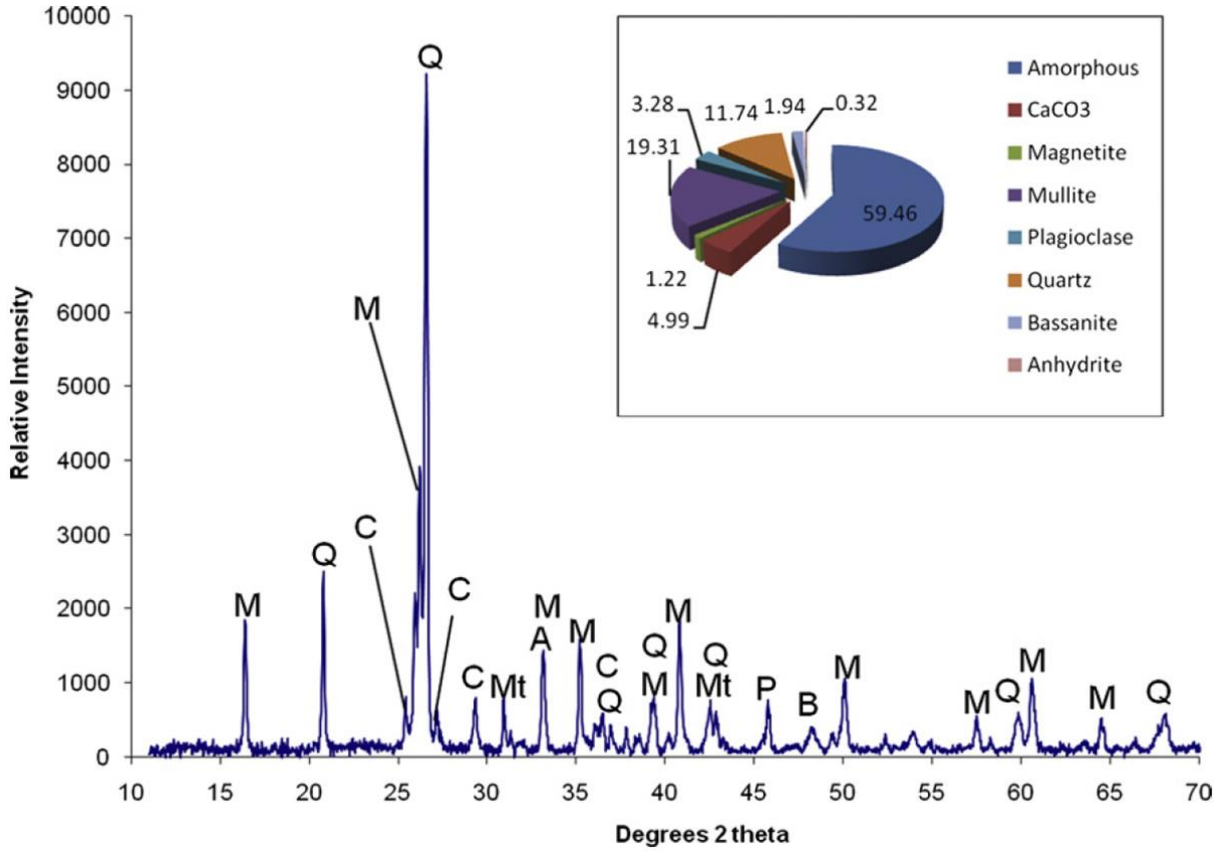

Appendix C: Ion chromatography correlation result

Appendix C1: Pearson correlation values for dissolved ions present in filtrate solutions of combustion ashes suspensions – CFA, wood bottom ash, domestic bottom ash, and coal bottom ash. Green = negative correlation, Red = Positive correlation

	$C_2H_3O_2^-$	NO_2^-	NO_3^-	Cl^-	SO_4^{2-}	Na^+	Ca^{2+}	Li^+	K^+	Mg^{2+}	pH
$C_2H_3O_2^-$	1										
NO_2^-	-0.2547	1									
NO_3^-	0.3494	0.1071	1								
Cl^-	0.1519	-0.6555	0.6145	1							
SO_4^{2-}	0.9842	-0.3742	0.4300	0.3235	1						
Na^+	0.2001	-0.8868	0.3167	0.9300	0.3638	1					
Ca^{2+}	0.8853	-0.3468	-0.1257	-0.1236	0.8326	0.0790	1				
Li^+	-0.3399	0.9847	0.2047	-0.5325	-0.4351	-0.8027	-0.4835	1			
K^+	-0.5638	-0.6549	-0.3525	0.4508	-0.4479	0.6070	-0.4014	-0.5734	1		
Mg^{2+}	0.2617	-0.4401	-0.7960	-0.3818	0.1986	-0.0219	0.6762	-0.5783	0.1598	1	
pH	0.1128	-0.9877	-0.2185	0.6027	0.2301	0.8511	0.2521	-0.9686	0.7545	0.4675	1

182

Appendix D: Droplet freezing data for ultra-pure water from µL-NIPI

Appendix D1: Freezing experiments with 0.5 µL droplets of ultra-pure water used as a quality control for µL-NIPI tests with the same droplet sizes. The temperature uncertainty is ± 0.4 °C for all fraction frozen curves as plotted for the ultra-pure water.

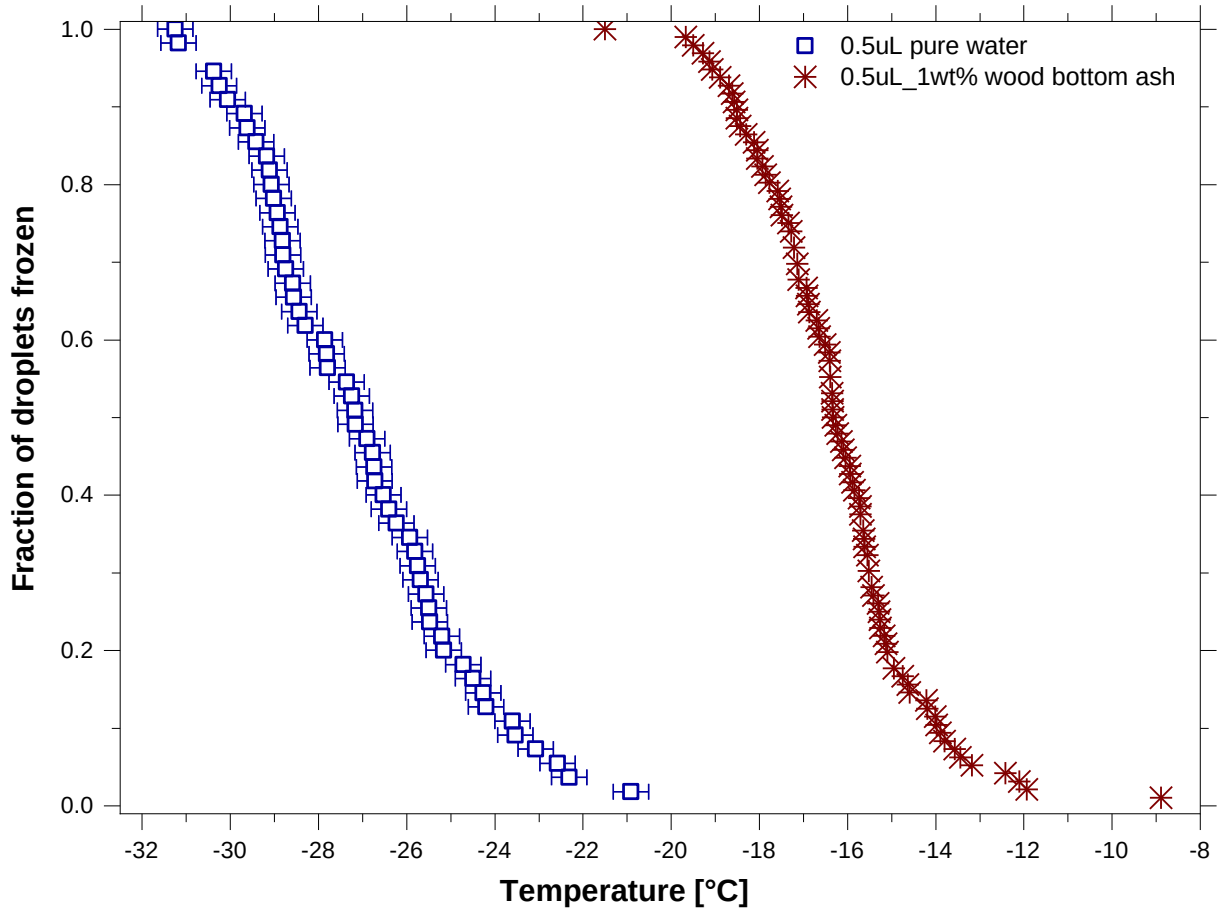

Appendix D2: Fraction of droplets frozen for 5.0 µL droplets for ultra-pure water used as a quality control for µL-NIPI tests with similar droplet sizes. The 5.0 µL_0.1 wt%_normal denotes experiments where the droplets were at room temperature while 5.0 µL_0.1 wt%_23 °C and 5.0 µL_0.1 wt%_40 °C indicate freezing experiments that the suspensions were 23 °C and 40 °C, respectively, before the start of the experiments. The temperature uncertainty is ± 0.4 °C for all fraction frozen curves as plotted for the pure water.

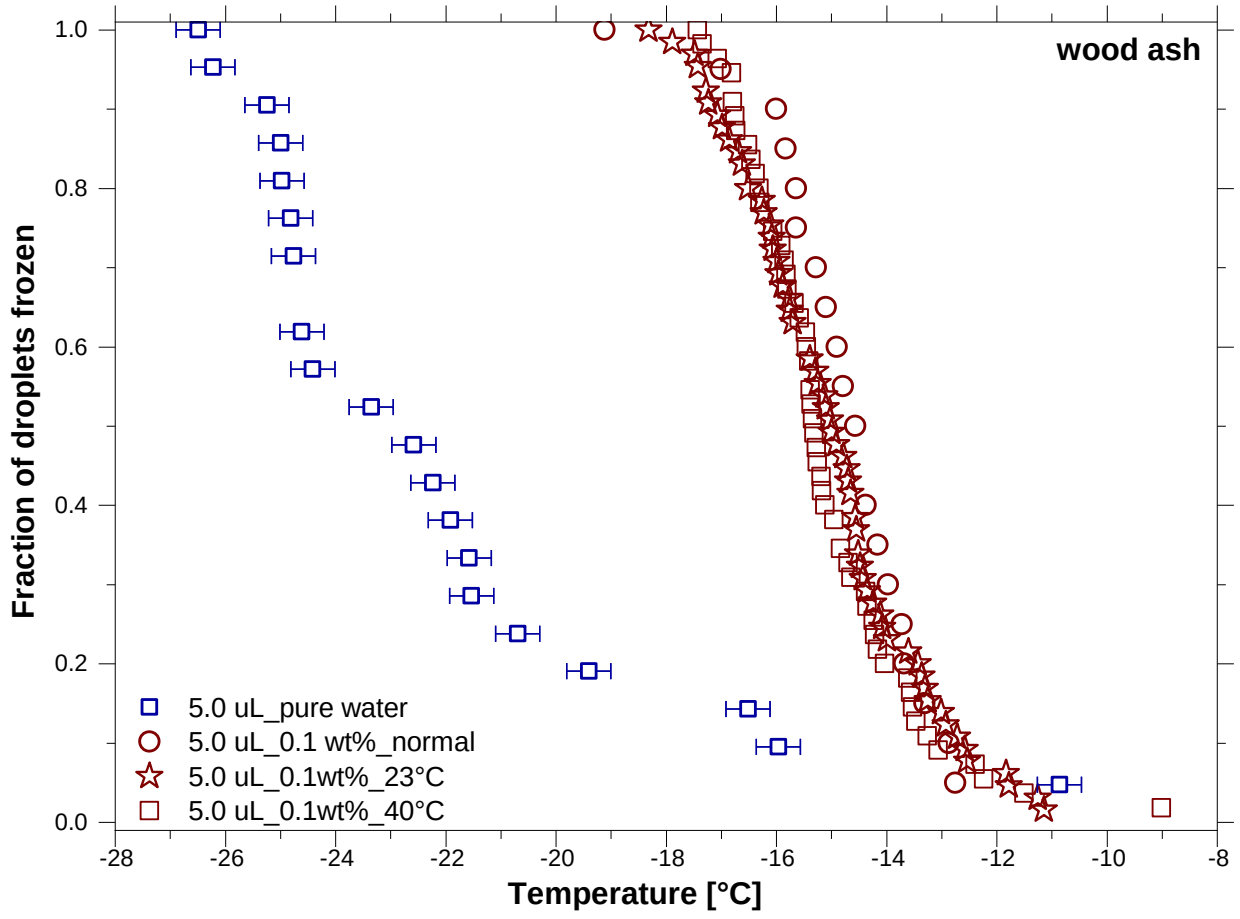

Appendix E: Mineral composition of coal fly ash

Appendix E1: Major and minor elemental compositions of CCPS evaluated from five power plants in the United States of America (ACAA, 2012).

State	Alaska	Indiana	New Mexico		Ohio		Wyoming	
Material	Fly/Bottom Ash	Fly Ash	Flya Ash (Product)	Bottom Ash	Fly Ash	Bottom Ash	Fly Ash	Bottom Ash
USGS Table No. (a)	14	18	24	20	30	28	36	34
Major and Minor Elements	Mean (Average) Percent							
SiO_2	45.3	41.1	62.8	64.8	41.7	40	29	43.3
Al_2O_3	19.3	21.5	26	24.1	18.2	17.6	15.6	20
CaO	19.9	1.46	2.62	2.95	2.32	2.32	26.3	16.3
MgO	3.37	0.79	0.821	0.735	0.631	0.594	3.34	3.81
Na_2O	0.262	0.384	1.31	1.04	1.75	0.317	0.543	0.266
K_2O	1.21	2.13	0.89	0.871	1.47	1.29	0.398	0.423
Fe_2O_3	7.72	25.7	3.57	4.36	26.9	29.9	3.32	9.75
TiO_2	0.787	1.09	0.938	0.821	0.959	0.895	1.14	1.51
P_2O_5	0.181	0.181	0.183	0.123	0.218	0.169	0.462	0.446
SO_3	0.491	0.491	0.07	0.122	2.46	0.197	19.2	0.503
Total mean Percent	99.093	94.826	99.202	99.922	96.608	93.282	99.303	96.308
Remainder	0.927	5.174	0.798	0.078	3.392	6.718	0.697	3.692

Notes:

(a) – Data from USGS. 2011. Geochemical Database of Feed Coal and Coal Combustion Products (CCPs) from Five Power plants in the United States. Data Series 635.

Available at: http://pubs.usgs.gov/ds/635/

185

Appendix E2: Minerals/elemental analyses of ash from biomass pellets (Fernandes and Costa, 2013).

Major and minor elements	**Percentages**
SiO_2	20.9
Al_2O_3	6.2
Fe_2O_3	21.6
CaO	26.2
SO_3	0.3
MgO	4.3
P_2O_5	4.2
K_2O	11.5
Na_2O	2.5
ZnO	1.0
Cl	0.04
other oxides	1.3

References

Acaa 2012. Coal ash material safety - a health risk-based evaluation of usgs coal ash data from five us power plants. Chelmsford, MA: American Coal Ash Association.

Acca 2013. Coal combustion products production & use statistics by american coal ash association. *Advancing the Management & Use of Coal Combustion Products.*

Adachi, K. and Buseck, P. R. 2008. Internally mixed soot, sulfates, and organic matter in aerosol particles from mexico city. *Atmos. Chem. Phys.,* 8**,** 6469-6481.

Adachi, K. and Buseck, P. R. 2013. Changes of ns-soot mixing states and shapes in an urban area during calnex. *Journal of Geophysical Research: Atmospheres,* 118**,** 3723-3730.

Adriano, D. C., Page, A. L., Elseewi, A. A., Chang, A. C. and Straughan, I. 1980. Utilization and disposal of fly ash and other coal residues in terrestrial ecosystems: A review1. *J. Environ. Qual.,* 9**,** 333-344.

Andreae, M. O. and Gelencsér, A. 2006. Black carbon or brown carbon? The nature of light-absorbing carbonaceous aerosols. *Atmos. Chem. Phys.,* 6**,** 3131-3148.

Anenberg, S. C., Talgo, K., Arunachalam, S., Dolwick, P., Jang, C. and West, J. J. 2011. Impacts of global, regional, and sectoral black carbon emission reductions on surface air quality and human mortality. *Atmos. Chem. Phys.,* 11**,** 7253-7267.

Ansmann, A., Tesche, M., Seifert, P., Althausen, D., Engelmann, R., Fruntke, J., Wandinger, U., Mattis, I. and Müller, D. 2009. Evolution of the ice phase in tropical altocumulus: Samum lidar observations over cape verde. *Journal of Geophysical Research: Atmospheres,* 114**,** D17208.

Atkinson, J. D. 2013. *Freezing of droplets under mixed-phase cloud conditions.* PhD, University of Leeds.

Atkinson, J. D., Murray, B. J., Woodhouse, M. T., Whale, T. F., Baustian, K. J., Carslaw, K. S., Dobbie, S., O/'Sullivan, D. and Malkin, T. L. 2013. The importance of feldspar for ice nucleation by mineral dust in mixed-phase clouds. *Nature,* 498**,** 355-358.

Attard, E., Yang, H., Delort, A. M., Amato, P., Pöschl, U., Glaux, C., Koop, T. and Morris, C. E. 2012. Effects of atmospheric conditions on ice nucleation activity of pseudomonas. *Atmos. Chem. Phys.,* 12**,** 10667-10677.

Augustin, S., Wex, H., Niedermeier, D., Pummer, B., Grothe, H., Hartmann, S., Tomsche, L., Clauss, T., Voigtländer, J., Ignatius, K., et al. 2013. Immersion freezing of birch pollen washing water. *Atmos. Chem. Phys.,* 13**,** 10989-11003.

Baeza-Romero, M. T., Wilson, J. M., Fitzpatrick, E. M., Jones, J. M. and Williams, A. 2010. In situ study of soot from the combustion of a biomass pyrolysis intermediate-eugenol-and n-decane using aerosol time of flight mass spectrometry. *Energy & Fuels,* 24**,** 439-445.

Baker, M. B. and Peter, T. 2008. Small-scale cloud processes and climate. *Nature,* 451**,** 299-300.

Banús, E. D., Milt, V. G., Miró, E. E. and Ulla, M. A. 2009. Structured catalyst for the catalytic combustion of soot: Co,ba,k/zro2 supported on al2o3 foam. *Applied Catalysis A: General,* 362**,** 129-138.

Banwell, C. N. and Mccash, E. M. 1994. *Fundamentals of molecular spectroscopy*, McGraw-Hill London.

Barry, R. G. and Chorley, R. J. 2009. *Atmosphere, weather and climate*, Routledge.

Basumajumdar, A., Das, A. K., Bandyopadhyay, N. and Maitra, S. 2005. Some studies on the reaction between fly ash and lime. *Bulletin of Materials Science,* 28**,** 131-136.

Baustian, K. J., Cziczo, D. J., Wise, M. E., Pratt, K. A., Kulkarni, G., Hallar, A. G. and Tolbert, M. A. 2012. Importance of aerosol composition, mixing state, and morphology for heterogeneous ice nucleation: A combined field and laboratory approach. *Journal of Geophysical Research: Atmospheres,* 117**,** D06217.

Belz, G. and Caramuscio, P. 2005. Production of high value coal fly ash. ENEL Produzione Ricerca - Italy.

Benz, S., Megahed, K., Mohler, O., Saathoff, H., Wagner, R. and Schurath, U. 2005. T-dependent rate measurements of homogeneous ice nucleation in cloud droplets using a large atmospheric simulation chamber. *Journal of Photochemistry and Photobiology a-Chemistry,* 176**,** 208-217.

Block, C. and Dams, R. 1976. Study of fly ash emission during combustion of coal. *Environmental Science & Technology,* 10**,** 1011-1017.

Bond, T. C., Doherty, S. J., Fahey, D. W., Forster, P. M., Berntsen, T., Deangelo, B. J., Flanner, M. G., Ghan, S., Kärcher, B., Koch, D., et al. 2013. Bounding the role of black carbon in the climate system: A scientific assessment. *Journal of Geophysical Research: Atmospheres,* 118**,** 5380-5552.

Bond, T. C., Streets, D. G., Yarber, K. F., Nelson, S. M., Woo, J. H. and Klimont, Z. 2004. A technology-based global inventory of black and organic carbon emissions from combustion. *Journal of Geophysical Research-Atmospheres,* 109.

Boucher, O., D. Randall, P. Artaxo, C. Bretherton, G. Feingold, P. Forster, V.-M. Kerminen, Y. Kondo, H. Liao, U. Lohmann, P. Rasch, S.K. Satheesh, S. Sherwood, B. Stevens, and X.Y. Zhang, 2013. Clouds and aerosols. *Climate Change 2013: The Physical Science Basis. Contribution of Working Group I to the Fifth Assessment Report of the Intergovernmental Panel on Climate Change [Stocker, T.F., D. Qin, G.-K. Plattner, M. Tignor, S.K. Allen, J. Boschung, A. Nauels, Y. Xia, V. Bex and P.M. Midgley (eds.)]*. Cambridge University Press, Cambridge, United Kingdom and New York, NY, USA.

Brereton, R. G. 2003. *Chemometrics: Data analysis for the laboratory and chemical plant*, John Wiley & Sons.

Broadley, S. L., Murray, B. J., Herbert, R. J., Atkinson, J. D., Dobbie, S., Malkin, T. L., Condliffe, E. and Neve, L. 2012. Immersion mode heterogeneous ice nucleation by an illite rich powder representative of atmospheric mineral dust. *Atmos. Chem. Phys.,* 12**,** 287-307.

Brouwers, H. and Eijk, V. R. Chemical reaction of fly ash. 11th International Congress on the Chemistry of Cement (ICCC), 2003 Durban, South Africa.

Browse, J., Carslaw, K. S., Arnold, S. R., Pringle, K. and Boucher, O. 2012. The scavenging processes controlling the seasonal cycle in arctic sulphate and black carbon aerosol. *Atmos. Chem. Phys.,* 12**,** 6775-6798.

Brunauer, S., Emmett, P. H. and Teller, E. 1938. Adsorption of gases in multimolecular layers. *Journal of the American Chemical Society,* 60**,** 309-319.

Bsi 1999. Iso, bs - 13320-1: 1999 particle size analysis-laser diffraction methods. Part 1: General principles. London: British Standards Institution.

Buseck, P. R., Adachi, K., Gelencsér, A., Tompa, É. and Pósfai, M. 2012. Are black carbon and soot the same? *Atmos. Chem. Phys. Discuss.,* 12**,** 24821-24846.

Buseck, P. R., Adachi, K., Gelencsér, A., Tompa, É. and Pósfai, M. 2014. Ns-soot: A material-based term for strongly light-absorbing carbonaceous particles. *Aerosol Science and Technology,* 48**,** 777-788.

Cai, J., Lu, N. and Sorensen, C. M. 1993. Comparison of size and morphology of soot aggregates as determined by light scattering and electron microscope analysis. *Langmuir,* 9**,** 2861-2867.

Cao, J. J., Zhu, C. S., Tie, X. X., Geng, F. H., Xu, H. M., Ho, S. S. H., Wang, G. H., Han, Y. M. and Ho, K. F. 2013. Characteristics and sources of carbonaceous aerosols from shanghai, china. *Atmos. Chem. Phys.,* 13**,** 803-817.

Cape, J. N., Coyle, M. and Dumitrean, P. 2012. The atmospheric lifetime of black carbon. *Atmospheric Environment,* 59**,** 256-263.

Carslaw, K. S., Boucher, O., Spracklen, D. V., Mann, G. W., Rae, J. G. L., Woodward, S. and Kulmala, M. 2010. A review of natural aerosol interactions and feedbacks within the earth system. *Atmos. Chem. Phys.,* 10**,** 1701-1737.

Catelani, T., Pratesi, G. and Zoppi, M. 2013. Raman characterization of ambient airborne soot and associated mineral phases. *Aerosol Science and Technology,* 48**,** 13-21.

Charlson, R. J. and Heintzenberg, J. 1995. *Aerosol forcing of climate,* New York, John Wiley & Sons.

Chen, H., Laskin, A., Baltrusaitis, J., Gorski, C. A., Scherer, M. M. and Grassian, V. H. 2012. Coal fly ash as a source of iron in atmospheric dust. *Environmental Science & Technology,* 46**,** 2112-2120.

Chen, Y., Shah, N., Huggins, F. E. and Huffman, G. P. 2005. Transmission electron microscopy investigation of ultrafine coal fly ash particles. *Environmental Science & Technology,* 39**,** 1144-1151.

Chen, Y. L., Kreidenweis, S. M., Mcinnes, L. M., Rogers, D. C. and Demott, P. J. 1998. Single particle analyses of ice nucleating aerosols in the upper troposphere and lower stratosphere. *Geophysical Research Letters,* 25**,** 1391-1394.

Cheng, J., Zhou, J., Liu, J., Zhou, Z., Huang, Z., Cao, X., Zhao, X. and Cen, K. 2003. Sulfur removal at high temperature during coal combustion in furnaces: A review. *Progress in Energy and Combustion Science,* 29**,** 381-405.

Chou, C., Kanji, Z. A., Stetzer, O., Tritscher, T., Chirico, R., Heringa, M. F., Weingartner, E., Prévôt, A. S. H., Baltensperger, U. and Lohmann, U. 2013.

Effect of photochemical ageing on the ice nucleation properties of diesel and wood burning particles. *Atmos. Chem. Phys.,* 13**,** 761-772.

Claeys, M., Wang, W., Ion, A. C., Kourtchev, I., Gelencsér, A. and Maenhaut, W. 2004. Formation of secondary organic aerosols from isoprene and its gas-phase oxidation products through reaction with hydrogen peroxide. *Atmospheric Environment,* 38**,** 4093-4098.

Corbin, J. C., Rehbein, P. J. G., Evans, G. J. and Abbatt, J. P. D. 2012. Combustion particles as ice nuclei in an urban environment: Evidence from single-particle mass spectrometry. *Atmospheric Environment,* 51**,** 286-292.

Cozic, J., Mertes, S., Verheggen, B., Cziczo, D. J., Gallavardin, S. J., Walter, S., Baltensperger, U. and Weingartner, E. 2008. Black carbon enrichment in atmospheric ice particle residuals observed in lower tropospheric mixed phase clouds. *Journal of Geophysical Research: Atmospheres,* 113**,** D15209.

Crawford, I., Möhler, O., Schnaiter, M., Saathoff, H., Liu, D., Mcmeeking, G., Linke, C., Flynn, M., Bower, K. N., Connolly, P. J., et al. 2011. Studies of propane flame soot acting as heterogeneous ice nuclei in conjunction with single particle soot photometer measurements. *Atmos. Chem. Phys.,* 11**,** 9549-9561.

Cui, Z., Davies, S., Carslaw, K. S. and Blyth, A. M. 2011. The response of precipitation to aerosol through riming and melting in deep convective clouds. *Atmos. Chem. Phys.,* 11**,** 3495-3510.

Cziczo, D. J., Froyd, K. D., Hoose, C., Jensen, E. J., Diao, M., Zondlo, M. A., Smith, J. B., Twohy, C. H. and Murphy, D. M. 2013. Clarifying the dominant sources and mechanisms of cirrus cloud formation. *Science,* 340**,** 1320-1324.

Cziczo, D. J., Stetzer, O., Worringen, A., Ebert, M., Weinbruch, S., Kamphus, M., Gallavardin, S. J., Curtius, J., Borrmann, S., Froyd, K. D., et al. 2009. Inadvertent climate modification due to anthropogenic lead. *Nature Geoscience,* 2**,** 333-336.

Davies, D., Kumar, S. and Descloitres, J. 2004. Global fire monitoring using modis near-real-time satellite data. *GIM International,* 18**,** 41 - 43.

De Boer, A., Gjaltema, D., Hagedoorn, P. and Frijlink, H. 2002. Characterization of inhalation aerosols: A critical evaluation of cascade impactor analysis and laser diffraction technique. *International journal of pharmaceutics,* 249**,** 219-231.

Del Monte, M. and Sabbioni, C. 1984. Morphology and mineralogy of fly ash from a coal-fueled power plant. *Archives for meteorology, geophysics, and bioclimatology, Series B,* 35**,** 93-104.

Demirdjian, B., Ferry, D., Suzanne, J., Popovicheva, O. B., Persiantseva, N. M., Kamaev, A. V., Shonija, N. K. and Zubareva, N. A. 2009. Freezing of water adsorbed on hydrophobic and activated soot particles. *Chemical Physics Letters,* 480**,** 247-252.

Demott, P. J. 1990. An exploratory-study of ice nucleation by soot aerosols. *Journal of Applied Meteorology,* 29**,** 1072-1079.

Demott, P. J., Chen, Y., Kreidenweis, S. M., Rogers, D. C. and Sherman, D. E. 1999. Ice formation by black carbon particles. *Geophysical Research Letters,* 26**,** 2429-2432.

Demott, P. J., Cziczo, D. J., Prenni, A. J., Murphy, D. M., Kreidenweis, S. M., Thomson, D. S., Borys, R. and Rogers, D. C. 2003. Measurements of the

concentration and composition of nuclei for cirrus formation. *Proceedings of the National Academy of Sciences of the United States of America,* 100**,** 14655-14660.

Demott, P. J., Petters, M. D., Prenni, A. J., Carrico, C. M., Kreidenweis, S. M., Collett, J. L. and Moosmuller, H. 2009. Ice nucleation behavior of biomass combustion particles at cirrus temperatures. *Journal of Geophysical Research-Atmospheres,* 114.

Demott, P. J., Prenni, A. J., Liu, X., Kreidenweis, S. M., Petters, M. D., Twohy, C. H., Richardson, M. S., Eidhammer, T. and Rogers, D. C. 2010. Predicting global atmospheric ice nuclei distributions and their impacts on climate. *Proceedings of the National Academy of Sciences*.

Demott, P. J., Prenni, A. J., Mcmeeking, G. R., Sullivan, R. C., Petters, M. D., Tobo, Y., Niemand, M., Möhler, O., Snider, J. R., Wang, Z., et al. 2014. Integrating laboratory and field data to quantify the immersion freezing ice nucleation activity of mineral dust particles. *Atmos. Chem. Phys. Discuss.,* 14**,** 17359-17400.

Diehl, K. and Mitra, S. K. 1998. A laboratory study of the effects of a kerosene-burner exhaust on ice nucleation and the evaporation rate of ice crystals. *Atmospheric Environment,* 32**,** 3145-3151.

Dimitrov, A. S., Miwa, T. and Nagayama, K. 1999. A comparison between the optical properties of amorphous and crystalline monolayers of silica particles†. *Langmuir,* 15**,** 5257-5264.

Ding, A. J., Fu, C. B., Yang, X. Q., Sun, J. N., Petäjä, T., Kerminen, V. M., Wang, T., Xie, Y., Herrmann, E., Zheng, L. F., et al. 2013. Intense atmospheric pollution modifies weather: A case of mixed biomass burning with fossil fuel combustion pollution in eastern china. *Atmos. Chem. Phys.,* 13**,** 10545-10554.

Dinnebier, R. E. and Billinge, S. J. 2008. *Powder diffraction: Theory and practice*, Royal Society of Chemistry.

Disselkamp, R. S., Carpenter, M. A., Cowin, J. P., Berkowitz, C. M., Chapman, E. G., Zaveri, R. A. and Laulainen, N. S. 2000. Ozone loss in soot aerosols. *Journal of Geophysical Research: Atmospheres,* 105**,** 9767-9771.

Duckett, S. and Gilbert, B. 2000. *Foundations of spectroscopy*, Oxford University Press New York.

Dymarska, M., Murray, B. J., Sun, L. M., Eastwood, M. L., Knopf, D. A. and Bertram, A. K. 2006. Deposition ice nucleation on soot at temperatures relevant for the lower troposphere. *Journal of Geophysical Research-Atmospheres,* 111.

Eastwood, M. L., Cremel, S., Wheeler, M., Murray, B. J., Girard, E. and Bertram, A. K. 2009. Effects of sulfuric acid and ammonium sulfate coatings on the ice nucleation properties of kaolinite particles. *Geophys. Res. Lett.,* 36**,** L02811.

Ebert, M., Worringen, A., Benker, N., Mertes, S., Weingartner, E. and Weinbruch, S. 2011. Chemical composition and mixing-state of ice residuals sampled within mixed phase clouds. *Atmos. Chem. Phys.,* 11**,** 2805-2816.

Engelhart, G. J., Hennigan, C. J., Miracolo, M. A., Robinson, A. L. and Pandis, S. N. 2012. Cloud condensation nuclei activity of fresh primary and aged biomass burning aerosol. *Atmos. Chem. Phys.,* 12**,** 7285-7293.

Epri 2009. Is coal ash toxic? : Electric Power Research Institute.

Epri 2010. Comparison of coal combustion products to other common materials: Chemical characteristics. Electric Power Research Institute

Ervens, B. and Feingold, G. 2013. Sensitivities of immersion freezing: Reconciling classical nucleation theory and deterministic expressions. *Geophysical Research Letters,* 40**,** 3320-3324.

Eshel, G., Levy, G., Mingelgrin, U. and Singer, M. 2004. Critical evaluation of the use of laser diffraction for particle-size distribution analysis. *Soil Science Society of America Journal,* 68**,** 736-743.

Etiégni, L. and Campbell, A. G. 1991. Physical and chemical characteristics of wood ash. *Bioresource Technology,* 37**,** 173-178.

Fenelonov, V. B., Mel'gunov, M. S. and Parmon, V. N. 2010. The properties of cenospheres and the mechanism of their formation during high-temperature coal combustion at thermal power plans. *KONA Powder and Particle Journal*.

Ferge, T., Karg, E., Schröppel, A., Coffee, K. R., Tobias, H. J., Frank, M., Gard, E. E. and Zimmermann, R. 2006. Fast determination of the relative elemental and organic carbon content of aerosol samples by on-line single-particle aerosol time-of-flight mass spectrometry. *Environmental Science & Technology,* 40**,** 3327-3335.

Fernandes, U. and Costa, M. 2013. Formation of fine particulate matter in a domestic pellet-fired boiler. *Energy & Fuels,* 27**,** 1081-1092.

Ferry, D., Suzanne, J., Nitsche, S., Popovitcheva, O. B. and Shonija, N. K. 2002. Water adsorption and dynamics on kerosene soot under atmospheric conditions. *Journal of Geophysical Research: Atmospheres,* 107**,** 4734.

Feuerborn, H.-J. 2005. Coal ash utilisation over the world and in europe. *Workshop on Environmental and Health Aspects of Coal Ash Utilization.* Tel-Aviv, Israel

Fisher, G. L., Chang, D. P. Y. and Brummer, M. 1976. Fly ash collected from electrostatic precipitators: Microcrystalline structures and the mystery of the spheres. *Science,* 192**,** 553-555.

Fisher, G. L., Prentice, B. A., Silberman, D., Ondov, J. M., Biermann, A. H., Ragaini, R. C. and Mcfarland, A. R. 1978. Physical and morphological studies of size-classified coal fly ash. *Environmental Science & Technology,* 12**,** 447-451.

Fitzpatrick, E. M., Jones, J. M., Pourkashanian, M., Ross, A. B., Williams, A. and Bartle, K. D. 2008. Mechanistic aspects of soot formation from the combustion of pine wood. *Energy & Fuels,* 22**,** 3771-3778.

Fitzpatrick, E. M., Ross, A. B., Bates, J., Andrews, G., Jones, J. M., Phylaktou, H., Pourkashanian, M. and Williams, A. 2007. Emission of oxygenated species from the combustion of pine wood and its relation to soot formation. *Process Safety and Environmental Protection,* 85**,** 430-440.

Flanders, P. J. 1999. Identifying fly ash at a distance from fossil fuel power stations. *Environmental Science & Technology,* 33**,** 528-532.

Fornea, A. P., Brooks, S. D., Dooley, J. B. and Saha, A. 2009. Heterogeneous freezing of ice on atmospheric aerosols containing ash, soot, and soil. *Journal of Geophysical Research: Atmospheres,* 114**,** D13201.

Forster, P., V. Ramaswamy, P. Artaxo, T. Berntsen, R. Betts, D.W. Fahey, J. Haywood, J. Lean, D.C. Lowe, G. Myhre, J. Nganga, R. Prinn, G. Raga, M. Schulz and R.

Van Dorland 2007. Changes in atmospheric constituents and in radiative forcing. *In:* SOLOMON, S., D. QIN, M. MANNING, Z. CHEN, M. MARQUIS, K.B. AVERYT, M.TIGNOR AND H.L. MILLER (ed.) *Climate Change 2007: The Physical Science Basis. Contribution of Working Group I to the Fourth Assessment Report of the Intergovernmental Panel on Climate Change.* Cambridge, United Kingdom.

Frenklach, M. 2002. Reaction mechanism of soot formation in flames. *Physical Chemistry Chemical Physics,* 4**,** 2028-2037.

Friedman, B., Kulkarni, G., Beránek, J., Zelenyuk, A., Thornton, J. A. and Cziczo, D. J. 2011. Ice nucleation and droplet formation by bare and coated soot particles. *J. Geophys. Res.,* 116**,** D17203.

Friedman, B., Zelenyuk, A., Beranek, J., Kulkarni, G., Pekour, M., Gannet Hallar, A., Mccubbin, I. B., Thornton, J. A. and Cziczo, D. J. 2013. Aerosol measurements at a high-elevation site: Composition, size, and cloud condensation nuclei activity. *Atmos. Chem. Phys.,* 13**,** 11839-11851.

Fultz, B. and Howe, J. M. 2012. *Transmission electron microscopy and diffractometry of materials,* Springer.

Gettelman, A., Morrison, H., Terai, C. R. and Wood, R. 2013. Microphysical process rates and global aerosol–cloud interactions. *Atmos. Chem. Phys.,* 13**,** 9855-9867.

Ghazi, R. and Olfert, J. S. 2012. Coating mass dependence of soot aggregate restructuring due to coatings of oleic acid and dioctyl sebacate. *Aerosol Science and Technology,* 47**,** 192-200.

Ghosal, S. and Self, S. A. 1995. Particle size-density relation and cenosphere content of coal fly ash. *Fuel,* 74**,** 522-529.

Gibbs, J. 1948. *The collected works. Vol. 1. Thermodynamics,* Yale University Press.

Giglio, L., Descloitres, J., Justice, C. O. and Kaufman, Y. J. 2003. An enhanced contextual fire detection algorithm for modis. *Remote Sensing of Environment,* 87**,** 273-282.

Gill, A. E. 1982. *Atmosphere-ocean dynamics,* Academic press.

Gilmour, M. I., O'connor, S., Dick, C. a. J., Miller, C. A. and Linak, W. P. 2004. Differential pulmonary inflammation and in vitro cytotoxicity of size-fractionated fly ash particles from pulverized coal combustion. *Journal of the Air & Waste Management Association,* 54**,** 286-295.

Goldstein, J. I., Newbury, D. E., Echlin, P., Joy, D., Romig, A., Lyman, C., Fiori, C. and Lifshin, E. 1997. Scanning electron microscopy and x-ray microanalysis. Kluwer Academia. Plenium Publishers, 3rd Edition, (USA, 2003).

Gorbunov, B., Baklanov, A., Kakutkina, N., Windsor, H. L. and Toumi, R. 2001. Ice nucleation on soot particles. *Journal of Aerosol Science,* 32**,** 199-215.

Goudie, A. S. and Middleton, N. J. 2001. Saharan dust storms: Nature and consequences. *Earth-Science Reviews,* 56**,** 179-204.

Graf, H.-F. 2004. The complex interaction of aerosols and clouds. *Science,* 303**,** 1309-1311.

Haddad, P. R. and Jackson, P. E. 1990. *Ion chromatography: Principles and applications,* Elsevier Amsterdam.

Haga, D. I., Iannone, R., Wheeler, M. J., Mason, R., Polishchuk, E. A., Fetch, T., Van Der Kamp, B. J., Mckendry, I. G. and Bertram, A. K. 2013. Ice nucleation properties of rust and bunt fungal spores and their transport to high altitudes, where they can cause heterogeneous freezing. *Journal of Geophysical Research: Atmospheres,* 118**,** 7260-7272.

Han, C., Liu, Y., Liu, C., Ma, J. and He, H. 2012a. Influence of combustion conditions on hydrophilic properties and microstructure of flame soot. *The Journal of Physical Chemistry A,* 116**,** 4129-4136.

Han, C., Liu, Y., Ma, J. and He, H. 2012b. Key role of organic carbon in the sunlight-enhanced atmospheric aging of soot by o2. *Proceedings of the National Academy of Sciences,* 109**,** 21250-21255.

Hansen, J., Sato, M. and Ruedy, R. 1997. Radiative forcing and climate response. *Journal of Geophysical Research: Atmospheres (1984–2012),* 102**,** 6831-6864.

Harris, J. W. and Stöcker, H. 1998. *Handbook of mathematics and computational science,* Springer.

Hartmann, S., Augustin, S., Clauss, T., Wex, H., Šantl-Temkiv, T., Voigtländer, J., Niedermeier, D. and Stratmann, F. 2013. Immersion freezing of ice nucleation active protein complexes. *Atmos. Chem. Phys.,* 13**,** 5751-5766.

Hendershot, W., Lalande, H. and Duquette, M. 2007. Ion exchange and exchangeable cations. *Soil sampling and methods of analysis***,** 167-176.

Herbert, R. J., Murray, B. J., Whale, T. F., Dobbie, S. J. and Atkinson, J. D. 2014. Representing time-dependent freezing behaviour in immersion mode ice nucleation. *Atmos. Chem. Phys. Discuss.,* 14**,** 1399-1442.

Hill, A. A. and Dobbie, S. 2008. The impact of aerosols on non-precipitating marine stratocumulus. Ii: The semi-direct effect. *Quarterly Journal of the Royal Meteorological Society,* 134**,** 1155-1165.

Hiranuma, N., Hoffmann, N., Kiselev, A., Dreyer, A., Zhang, K., Kulkarni, G., Koop, T. and Möhler, O. 2013. Influence of surface morphology on the immersion mode ice nucleation efficiency of hematite particles. *Atmos. Chem. Phys. Discuss.,* 13**,** 23757-23780.

Hiranuma, N., Hoffmann, N., Kiselev, A., Dreyer, A., Zhang, K., Kulkarni, G., Koop, T. and Möhler, O. 2014. Influence of surface morphology on the immersion mode ice nucleation efficiency of hematite particles. *Atmos. Chem. Phys.,* 14**,** 2315-2324.

Hoffmann, N., Duft, D., Kiselev, A. and Leisner, T. 2013. Contact freezing efficiency of mineral dust aerosols studied in an electrodynamic balance: Quantitative size and temperature dependence for illite particles. *Faraday Discussions,* 165**,** 383-390.

Hoose, C., Kristjánsson, J. E., Chen, J.-P. and Hazra, A. 2010. A classical-theory-based parameterization of heterogeneous ice nucleation by mineral dust, soot, and biological particles in a global climate model. *Journal of the Atmospheric Sciences,* 67**,** 2483-2503.

Hoose, C. and Möhler, O. 2012. Heterogeneous ice nucleation on atmospheric aerosols: A review of results from laboratory experiments. *Atmos. Chem. Phys.,* 12**,** 9817-9854.

Hu, W. W., Hu, M., Yuan, B., Jimenez, J. L., Tang, Q., Peng, J. F., Hu, W., Shao, M., Wang, M., Zeng, L. M., et al. 2013. Insights on organic aerosol aging and the influence of coal combustion at a regional receptor site of central eastern china. *Atmos. Chem. Phys.*, 13**,** 10095-10112.

Ipcc 2013. Summary for policymakers. *Climate Change 2013: The Physical Science Basis. Contribution of Working Group I to the Fifth Assessment Report of the Intergovernmental Panel on Climate Change [Stocker, T.F., D. Qin, G.-K. Plattner, M. Tignor, S.K. Allen, J. Boschung, A. Nauels, Y. Xia, V. Bex and P.M. Midgley (eds.)]*. Cambridge, United Kingdom and New York, NY, USA.

Jacobson, M. Z. 2001. Strong radiative heating due to the mixing state of black carbon in atmospheric aerosols. *Nature,* 409**,** 695-697.

Jacobson, M. Z. 2012. Investigating cloud absorption effects: Global absorption properties of black carbon, tar balls, and soil dust in clouds and aerosols. *Journal of Geophysical Research: Atmospheres,* 117**,** D06205.

Jenkins, B. M., Baxter, L. L., Miles Jr, T. R. and Miles, T. R. 1998. Combustion properties of biomass. *Fuel Processing Technology,* 54**,** 17-46.

Jewell, R. B. and Rathbone, R. F. 2009. Optical properties of coal combustion byproducts for particle-size analysis by laser diffraction. *Coal Combustion and Gasification Products,* 1**,** 1-7.

Johansson, L. S., Tullin, C., Leckner, B. and Sjövall, P. 2003. Particle emissions from biomass combustion in small combustors. *Biomass and Bioenergy,* 25**,** 435-446.

Johnson, K. S., Zuberi, B., Molina, L. T., Molina, M. J., Iedema, M. J., Cowin, J. P., Gaspar, D. J., Wang, C. and Laskin, A. 2005. Processing of soot in an urban environment: Case study from the mexico city metropolitan area. *Atmospheric Chemistry and Physics,* 5**,** 3033-3043.

Jones, J. M., Ross, A. B. and Williams, A. 2005. Atmospheric chemistry implications of the emission of biomass smoke. *Journal of the Energy Institute,* 78**,** 199-200.

Kadarohman, A., Hernani, Khoerunisa, F. and Astuti, R. M. 2010. A potential study on clove oil, eugenol and eugenyl acetate as diesel fuel bio-additives and their performance on one cylinder engine. *Transport,* 25**,** 66-76.

Kamphus, M., Ettner-Mahl, M., Klimach, T., Drewnick, F., Keller, L., Cziczo, D. J., Mertes, S., Borrmann, S. and Curtius, J. 2010. Chemical composition of ambient aerosol, ice residues and cloud droplet residues in mixed-phase clouds: Single particle analysis during the cloud and aerosol characterization experiment (clace 6). *Atmos. Chem. Phys.*, 10**,** 8077-8095.

Kanji, Z. A. and Abbatt, J. P. D. 2006. Laboratory studies of ice formation via deposition mode nucleation onto mineral dust and n-hexane soot samples. *Journal of Geophysical Research-Atmospheres,* 111.

Kanji, Z. A., Demott, P. J., Möhler, O. and Abbatt, J. P. D. 2011. Results from the university of toronto continuous flow diffusion chamber at icis 2007: Instrument intercomparison and ice onsets for different aerosol types. *Atmos. Chem. Phys.,* 11**,** 31-41.

Kanji, Z. A., Welti, A., Chou, C., Stetzer, O. and Lohmann, U. 2013. Laboratory studies of immersion and deposition mode ice nucleation of ozone aged mineral dust particles. *Atmos. Chem. Phys.*, 13**,** 9097-9118.

Karcher, B., Mohler, O., Demott, P. J., Pechtl, S. and Yu, F. 2007. Insights into the role of soot aerosols in cirrus cloud formation. *Atmospheric Chemistry and Physics,* 7**,** 4203-4227.

Kätzel, U., Bedrich, R., Stintz, M., Ketzmerick, R., Gottschalk-Gaudig, T. and Barthel, H. 2008a. Dynamic light scattering for the characterization of polydisperse fractal systems: I. Simulation of the diffusional behavior. *Particle & Particle Systems Characterization,* 25**,** 9-18.

Kätzel, U., Vorbau, M., Stintz, M., Gottschalk-Gaudig, T. and Barthel, H. 2008b. Dynamic light scattering for the characterization of polydisperse fractal systems: Ii. Relation between structure and dls results. *Particle & Particle Systems Characterization,* 25**,** 19-30.

Kireeva, E. D., Popovicheva, O. B., Persiantseva, N. M., Khokhlova, T. D. and Shonija, N. K. 2009. Effect of black carbon particles on the efficiency of water droplet freezing. *Colloid Journal,* 71**,** 353-359.

Knauer, M., Schuster, M. E., Su, D., SchlöGl, R., Niessner, R. and Ivleva, N. P. 2009. Soot structure and reactivity analysis by raman microspectroscopy, temperature-programmed oxidation, and high-resolution transmission electron microscopy. *The Journal of Physical Chemistry A,* 113**,** 13871-13880.

Koehler, K. A., Demott, P. J., Kreidenweis, S. M., Popovicheva, O. B., Petters, M. D., Carrico, C. M., Kireeva, E. D., Khokhlova, T. D. and Shonija, N. K. 2009. Cloud condensation nuclei and ice nucleation activity of hydrophobic and hydrophilic soot particles. *Physical Chemistry Chemical Physics,* 11**,** 7906-7920.

Koop, T. and Mahowald, N. 2013. Atmospheric science: The seeds of ice in clouds. *Nature,* 498**,** 302-303.

Köylü, Ü. Ö., Faeth, G. M., Farias, T. L. and Carvalho, M. G. 1995. Fractal and projected structure properties of soot aggregates. *Combustion and Flame,* 100**,** 621-633.

Ladino, L., Stetzer, O., Lüönd, F., Welti, A. and Lohmann, U. 2011. Contact freezing experiments of kaolinite particles with cloud droplets. *J. Geophys. Res.,* 116**,** D22202.

Ladino Moreno, L. A., Stetzer, O. and Lohmann, U. 2013. Contact freezing: A review of experimental studies. *Atmos. Chem. Phys.,* 13**,** 9745-9769.

Langer, G., Rosinski, J. and Edwards, C. P. 1967. A continuous ice nucleus counter and its application to tracking in the troposphere. *Journal of Applied Meteorology,* 6**,** 114-125.

Li, W. and Shao, L. 2009. Transmission electron microscopy study of aerosol particles from the brown hazes in northern china. *Journal of Geophysical Research: Atmospheres,* 114**,** D09302.

Lin-Vien, D., Colthup, N. B., Fateley, W. G. and Grasselli, J. G. 1991. *The handbook of infrared and raman characteristic frequencies of organic molecules,* Academic Press.

Lipsky, E. M., Pekney, N. J., Walbert, G. F., O'dowd, W. J., Freeman, M. C. and Robinson, A. 2004. Effects of dilution sampling on fine particle emissions from pulverized coal combustion. *Aerosol Science and Technology,* 38**,** 574-587.

Liu, D., Allan, J., Whitehead, J., Young, D., Flynn, M., Coe, H., Mcfiggans, G., Fleming, Z. L. and Bandy, B. 2013. Ambient black carbon particle hygroscopic properties controlled by mixing state and composition. *Atmos. Chem. Phys.,* 13**,** 2015-2029.

Liu, Y., Liu, C., Ma, J., Ma, Q. and He, H. 2010. Structural and hygroscopic changes of soot during heterogeneous reaction with o3. *Physical Chemistry Chemical Physics,* 12**,** 10896-10903.

Lohmann, U. 2002. A glaciation indirect aerosol effect caused by soot aerosols. *Geophysical Research Letters,* 29.

Lohmann, U. and Diehl, K. 2006. Sensitivity studies of the importance of dust ice nuclei for the indirect aerosol effect on stratiform mixed-phase clouds. *Journal of the Atmospheric Sciences,* 63**,** 968-982.

Lohmann, U. and Feichter, J. 2005. Global indirect aerosol effects: A review. *Atmospheric Chemistry and Physics,* 5**,** 715-737.

Lu, Z. and Sokolik, I. N. 2013. The effect of smoke emission amount on changes in cloud properties and precipitation: A case study of canadian boreal wildfires of 2007. *Journal of Geophysical Research: Atmospheres***,** 2013JD019860.

Lüönd, F., Stetzer, O., Welti, A. and Lohmann, U. 2010. Experimental study on the ice nucleation ability of size-selected kaolinite particles in the immersion mode. *Journal of Geophysical Research: Atmospheres,* 115**,** D14201.

Lupi, L., Hudait, A. and Molinero, V. 2014. Heterogeneous nucleation of ice on carbon surfaces. *Journal of the American Chemical Society,* 136**,** 3156-3164.

Lupi, L. and Molinero, V. 2014. Does hydrophilicity of carbon particles improve their ice nucleation ability? *The Journal of Physical Chemistry A.*

Ma, X., Zangmeister, C. D., Gigault, J., Mulholland, G. W. and Zachariah, M. R. 2013. Soot aggregate restructuring during water processing. *Journal of Aerosol Science,* 66**,** 209-219.

Mahlaba, J. S., Kearsley, E. P. and Kruger, R. A. 2012. Microstructural and mineralogical transformation of hydraulically disposed fly ash—implications to the environment.

Malvern 2012. A basic guide to particle characterization. Worcestershire, UK: Malvern Instruments Limited.

Mandrioli, P., Negrini, M. G., Cesari, G. and Morgan, G. 1984. Evidence for long range transport of biological and anthropogenic aerosol particles in the atmosphere. *Grana,* 23**,** 43-53.

Marcolli, C., Gedamke, S., Peter, T. and Zobrist, B. 2007. Efficiency of immersion mode ice nucleation on surrogates of mineral dust. *Atmospheric Chemistry and Physics,* 7**,** 5081-5091.

Maring, H., Savoie, D. L., Izaguirre, M. A., Custals, L. and Reid, J. S. 2003. Mineral dust aerosol size distribution change during atmospheric transport. *Journal of Geophysical Research: Atmospheres,* 108**,** 8592.

Martin, M., Tritscher, T., Jurányi, Z., Heringa, M. F., Sierau, B., Weingartner, E., Chirico, R., Gysel, M., Prévôt, A. S. H., Baltensperger, U., et al. 2013. Hygroscopic properties of fresh and aged wood burning particles. *Journal of Aerosol Science,* 56**,** 15-29.

Mason, B. J. 1962. *Clouds, rain, and rainmaking*, Cambridge University Press.

Maximova, N. and Dahl, O. 2006. Environmental implications of aggregation phenomena: Current understanding. *Current Opinion in Colloid & Interface Science,* 11**,** 246-266.

Mcmeeking, G. R., Good, N., Petters, M. D., Mcfiggans, G. and Coe, H. 2011a. Influences on the fraction of hydrophobic and hydrophilic black carbon in the atmosphere. *Atmospheric Chemistry and Physics,* 11**,** 5099-5112.

Mcmeeking, G. R., Morgan, W. T., Flynn, M., Highwood, E. J., Turnbull, K., Haywood, J. and Coe, H. 2011b. Black carbon aerosol mixing state, organic aerosols and aerosol optical properties over the united kingdom. *Atmos. Chem. Phys.,* 11**,** 9037-9052.

Mikhailov, E. F., Vlasenko, S. S., Podgorny, I. A., Ramanathan, V. and Corrigan, C. E. 2006. Optical properties of soot–water drop agglomerates: An experimental study. *Journal of Geophysical Research: Atmospheres,* 111**,** n/a-n/a.

Misra, M. K., Ragland, K. W. and Baker, A. J. 1993. Wood ash composition as a function of furnace temperature. *Biomass and Bioenergy,* 4**,** 103-116.

Mohler, O., Buttner, S., Linke, C., Schnaiter, M., Saathoff, H., Stetzer, O., Wagner, R., Kramer, M., Mangold, A., Ebert, V., et al. 2005a. Effect of sulfuric acid coating on heterogeneous ice nucleation by soot aerosol particles. *Journal of Geophysical Research-Atmospheres,* 110.

Mohler, O., Linke, C., Saathoff, H., Schnaiter, M., Wagner, R., Mangold, A., Kramer, M. and Schurath, U. 2005b. Ice nucleation on flame soot aerosol of different organic carbon content. *Meteorologische Zeitschrift,* 14**,** 477-484.

Monteith, J. and Unsworth, M. 2013. *Principles of environmental physics: Plants, animals, and the atmosphere*, Academic Press.

Mossop, S. C. 1985. The origin and concentration of ice crystals in clouds. *Bulletin of the American Meteorological Society,* 66**,** 264-273.

Mulik, J., Puckett, R., Williams, D. and Sawicki, E. 1976. Ion chromatographic analysis of sulfate and nitrate in ambient aerosols. *Analytical Letters,* 9**,** 653-663.

Mullin, J. W. 2001. *Crystallization*, Butterworth-Heinemann.

Murphy, D. M., Hudson, P. K., Cziczo, D. J., Gallavardin, S., Froyd, K. D., Johnston, M. V., Middlebrook, A. M., Reinard, M. S., Thomson, D. S., Thornberry, T., et al. 2007. Distribution of lead in single atmospheric particles. *Atmospheric Chemistry and Physics,* 7**,** 3195-3210.

Murphy, D. M. and Koop, T. 2005. Review of the vapour pressures of ice and supercooled water for atmospheric applications. *Quarterly Journal of the Royal Meteorological Society,* 131**,** 1539-1565.

Murray, B. J., Broadley, S. L., Wilson, T. W., Atkinson, J. D. and Wills, R. H. 2011. Heterogeneous freezing of water droplets containing kaolinite particles. *Atmospheric Chemistry and Physics,* 11**,** 4191-4207.

Murray, B. J., Broadley, S. L., Wilson, T. W., Bull, S. J., Wills, R. H., Christenson, H. K. and Murray, E. J. 2010a. Kinetics of the homogeneous freezing of water. *Phys Chem Chem Phys,* 12**,** 10380-7.

Murray, B. J., O'sullivan, D., Atkinson, J. D. and Webb, M. E. 2012. Ice nucleation by particles immersed in supercooled cloud droplets. *Chemical Society Reviews,* 41**,** 6519-6554.

Murray, B. J., Wilson, T. W., Dobbie, S., Cui, Z. Q., Al-Jumur, S., Mohler, O., Schnaiter, M., Wagner, R., Benz, S., Niemand, M., et al. 2010b. Heterogeneous nucleation of ice particles on glassy aerosols under cirrus conditions. *Nature Geoscience,* 3**,** 233-237.

Nakamoto, K. 1978. *Infrared and raman spectra of inorganic and coordination compounds*, Wiley Online Library.

Newbury, D. E., Joy, D. C., Echlin, P., Fiori, C. E. and Goldstein, J. I. 1987. Advanced scanning electron microscopy and x-ray microanalysis. *New York.: Plenum Press. Review by WMS in J. Microsc,* 146**,** 109.

Niedermeier, D., Hartmann, S., Shaw, R. A., Covert, D., Mentel, T. F., Schneider, J., Poulain, L., Reitz, P., Spindler, C., Clauss, T., et al. 2010. Heterogeneous freezing of droplets with immersed mineral dust particles – measurements and parameterization. *Atmos. Chem. Phys.,* 10**,** 3601-3614.

Niedermeier, D., Shaw, R. A., Hartmann, S., Wex, H., Clauss, T., Voigtländer, J. and Stratmann, F. 2011. Heterogeneous ice nucleation: Exploring the transition from stochastic to singular freezing behavior. *Atmos. Chem. Phys.,* 11**,** 8767-8775.

Niemand, M., Möhler, O., Vogel, B., Vogel, H., Hoose, C., Connolly, P., Klein, H., Bingemer, H., Demott, P., Skrotzki, J., et al. 2012. A particle-surface-area-based parameterization of immersion freezing on desert dust particles. *Journal of the Atmospheric Sciences,* 69**,** 3077-3092.

Nussbaumer, T. 2003. Combustion and co-combustion of biomass: Fundamentals, technologies, and primary measures for emission reduction†. *Energy & Fuels,* 17**,** 1510-1521.

Nyambura, M. G., Mugera, G. W., Felicia, P. L. and Gathura, N. P. 2011. Carbonation of brine impacted fractionated coal fly ash: Implications for co2 sequestration. *Journal of Environmental Management,* 92**,** 655-664.

O'sullivan, D., Murray, B. J., Malkin, T. L., Whale, T., Umo, N. S., Atkinson, J. D., Price, H. C., Baustian, K. J., Browse, J. and Webb, M. E. 2013. Ice nucleation by soil dusts: Relative importance of mineral dust and biogenic components. *Atmos. Chem. Phys. Discuss.,* 13**,** 20275-20317.

O'sullivan, D., Murray, B. J., Malkin, T. L., Whale, T. F., Umo, N. S., Atkinson, J. D., Price, H. C., Baustian, K. J., Browse, J. and Webb, M. E. 2014. Ice nucleation by fertile soil dusts: Relative importance of mineral and biogenic components. *Atmos. Chem. Phys.,* 14**,** 1853-1867.

Oorts, K., Vanlauwe, B., Recous, S. and Merckx, R. 2005. Redistribution of particulate organic matter during ultrasonic dispersion of highly weathered soils. *European Journal of Soil Science,* 56**,** 77-91.

Oubal, M., Picaud, S., Rayez, M.-T. and Rayez, J.-C. 2010. Water adsorption on oxidized single atomic vacancies present at the surface of small carbonaceous nanoparticles modeling soot. *Chemphyschem,* 11**,** 4088-4096.

Pagels, J., Dutcher, D. D., Stolzenburg, M. R., Mcmurry, P. H., Gälli, M. E. and Gross, D. S. 2013. Fine-particle emissions from solid biofuel combustion studied with single-particle mass spectrometry: Identification of markers for organics, soot,

and ash components. *Journal of Geophysical Research: Atmospheres,* 118**,** 859-870.

Pant, A., Parsons, M. T. and Bertram, A. K. 2006. Crystallization of aqueous ammonium sulfate particles internally mixed with soot and kaolinite: Crystallization relative humidities and nucleation rates. *The Journal of Physical Chemistry A,* 110**,** 8701-8709.

Parungo, F., Ackerman, E., Proulx, H. and Pueschel, R. 1978. Nucleation properties of fly ash in a coal-fired power-plant plume. *Atmospheric Environment (1967),* 12**,** 929-935.

Perry, K. D., Cahill, T. A., Schnell, R. C. and Harris, J. M. 1999. Long-range transport of anthropogenic aerosols to the national oceanic and atmospheric administration baseline station at mauna loa observatory, hawaii. *Journal of Geophysical Research: Atmospheres,* 104**,** 18521-18533.

Persiantseva, N. M., Popovicheva, O. B. and Shonija, N. K. 2004. Wetting and hydration of insoluble soot particles in the upper troposphere. *Journal of Environmental Monitoring,* 6**,** 939-945.

Petters, M. D., Parsons, M. T., Prenni, A. J., Demott, P. J., Kreidenweis, S. M., Carrico, C. M., Sullivan, A. P., Mcmeeking, G. R., Levin, E., Wold, C. E., et al. 2009. Ice nuclei emissions from biomass burning. *Journal of Geophysical Research-Atmospheres,* 114.

Petzold, A., Ogren, J. A., Fiebig, M., Laj, P., Li, S. M., Baltensperger, U., Holzer-Popp, T., Kinne, S., Pappalardo, G., Sugimoto, N., et al. 2013. Recommendations for reporting "black carbon" measurements. *Atmos. Chem. Phys.,* 13**,** 8365-8379.

Phani Kumar, B. and Sharma, R. 2004. Effect of fly ash on engineering properties of expansive soils. *Journal of Geotechnical and Geoenvironmental Engineering,* 130**,** 764-767.

Phillips, V. T. J., Choularton, T. W., Illingworth, A. J., Hogan, R. J. and Field, P. R. 2003. Simulations of the glaciation of a frontal mixed-phase cloud with the explicit microphysics model. *Quarterly Journal of the Royal Meteorological Society,* 129**,** 1351-1371.

Phillips, V. T. J., Demott, P. J. and Andronache, C. 2008. An empirical parameterization of heterogeneous ice nucleation for multiple chemical species of aerosol. *Journal of the Atmospheric Sciences,* 65**,** 2757-2783.

Phillips, V. T. J., Demott, P. J., Andronache, C., Pratt, K. A., Prather, K. A., Subramanian, R. and Twohy, C. 2012. Improvements to an empirical parameterization of heterogeneous ice nucleation and its comparison with observations. *Journal of the Atmospheric Sciences,* 70**,** 378-409.

Platt, C. M. R. 1977. Lidar observation of a mixed-phase altostratus cloud. *Journal of Applied Meteorology,* 16**,** 339-345.

Poole, C. F. 2004. Chromatographic and spectroscopic methods for the determination of solvent properties of room temperature ionic liquids. *Journal of Chromatography a,* 1037**,** 49-82.

Popovicheva, O., Kireeva, E., Persiantseva, N., Khokhlova, T., Shonija, N., Tishkova, V. and Demirdjian, B. 2008a. Effect of soot on immersion freezing of water and possible atmospheric implications. *Atmospheric Research,* 90**,** 326-337.

Popovicheva, O., Kireeva, E., Persiantseva, N., Timofeev, M., Bladt, H., Ivleva, N. P., Niessner, R. and Moldanova, J. 2012. Microscopic characterization of individual particles from multicomponent ship exhaust. *Journal of Environmental Monitoring,* 14**,** 3101-3110.

Popovicheva, O., Persiantseva, N. M., Shonija, N. K., Demott, P., Koehler, K., Petters, M., Kreidenweis, S., Tishkova, V., Demirdjian, B. and Suzanne, J. 2008b. Water interaction with hydrophobic and hydrophilic soot particles. *Physical Chemistry Chemical Physics,* 10**,** 2332-2344.

Popovicheva, O. B., Persiantseva, N. M., Lukhovitskaya, E. E., Shonija, N. K., Zubareva, N. A., Demirdjian, B., Ferry, D. and Suzanne, J. 2004. Aircraft engine soot as contrail nuclei. *Geophysical Research Letters,* 31**,** L11104.

Popovicheva, O. B., Persiantseva, N. M., Tishkova, V., Shonija, N. K. and Zubareva, N. A. 2008c. Quantification of water uptake by soot particles. *Environmental Research Letters,* 3**,** 025009.

Pöschl, U., Martin, S. T., Sinha, B., Chen, Q., Gunthe, S. S., Huffman, J. A., Borrmann, S., Farmer, D. K., Garland, R. M., Helas, G., et al. 2010. Rainforest aerosols as biogenic nuclei of clouds and precipitation in the amazon. *Science,* 329**,** 1513-1516.

Pósfai, M. and Buseck, P. R. 2010. Nature and climate effects of individual tropospheric aerosol particles. *Annual Review of Earth and Planetary Sciences,* 38**,** 17-43.

Posfai, M., Gelencser, A., Simonics, R., Arato, K., Li, J., Hobbs, P. V. and Buseck, P. R. 2004. Atmospheric tar balls: Particles from biomass and biofuel burning. *Journal of Geophysical Research-Atmospheres,* 109.

Prado, G., Lahaye, J. and Haynes, B. 1983. Soot particle nucleation and agglomeration. *In:* LAHAYE, J. & PRADO, G. (eds.) *Soot in combustion systems and its toxic properties.* Springer US.

Pratt, K. A., Demott, P. J., French, J. R., Wang, Z., Westphal, D. L., Heymsfield, A. J., Twohy, C. H., Prenni, A. J. and Prather, K. A. 2009. In situ detection of biological particles in cloud ice-crystals. *Nature Geosci,* 2**,** 398-401.

Pratt, K. A., Heymsfield, A. J., Twohy, C. H., Murphy, S. M., Demott, P. J., Hudson, J. G., Subramanian, R., Wang, Z., Seinfeld, J. H. and Prather, K. A. 2010. In situ chemical characterization of aged biomass-burning aerosols impacting cold wave clouds. *Journal of the Atmospheric Sciences,* 67**,** 2451-2468.

Price, H. C., Murray, B. J., Mattsson, J., O'sullivan, D., Wilson, T. W., Baustian, K. J. and Benning, L. G. 2014. Quantifying water diffusion in high-viscosity and glassy aqueous solutions using a raman isotope tracer method. *Atmos. Chem. Phys.,* 14**,** 3817-3830.

Pruppacher, H. R. 1995. A new look at homogeneous ice nucleation in supercooled water drops. *Journal of the Atmospheric Sciences,* 52**,** 1924-1933.

Pruppacher, H. R. and Klett, J. D. 2010. *Microphysics of clouds and precipitation,* Netherlands, Springer

Pummer, B. G., Bauer, H., Bernardi, J., Bleicher, S. and Grothe, H. 2012. Suspendable macromolecules are responsible for ice nucleation activity of birch and conifer pollen. *Atmos. Chem. Phys.,* 12**,** 2541-2550.

Ramanathan, V. and Carmichael, G. 2008. Global and regional climate changes due to black carbon. *Nature Geosci,* 1**,** 221-227.

Ramanathan, V., Crutzen, P. J., Kiehl, J. T. and Rosenfeld, D. 2001. Aerosols, climate, and the hydrological cycle. *Science,* 294**,** 2119-2124.

Ramanathan, V., Li, F., Ramana, M. V., Praveen, P. S., Kim, D., Corrigan, C. E., Nguyen, H., Stone, E. A., Schauer, J. J., Carmichael, G. R., et al. 2007. Atmospheric brown clouds: Hemispherical and regional variations in long-range transport, absorption, and radiative forcing. *Journal of Geophysical Research: Atmospheres,* 112**,** D22S21.

Richardson, M. S., Demott, P. J., Kreidenweis, S. M., Cziczo, D. J., Dunlea, E. J., Jimenez, J. L., Thomson, D. S., Ashbaugh, L. L., Borys, R. D., Westphal, D. L., et al. 2007. Measurements of heterogeneous ice nuclei in the western united states in springtime and their relation to aerosol characteristics. *Journal of Geophysical Research-Atmospheres,* 112.

Riechers, B., Wittbracht, F., Hutten, A. and Koop, T. 2013. The homogeneous ice nucleation rate of water droplets produced in a microfluidic device and the role of temperature uncertainty. *Physical Chemistry Chemical Physics,* 15**,** 5873-5887.

Rigg, Y. J., Alpert, P. A. and Knopf, D. A. 2013. Immersion freezing of water and aqueous ammonium sulfate droplets initiated by humic-like substances as a function of water activity. *Atmos. Chem. Phys.,* 13**,** 6603-6622.

Rissler, J., Messing, M. E., Malik, A. I., Nilsson, P. T., Nordin, E. Z., Bohgard, M., Sanati, M. and Pagels, J. H. 2013. Effective density characterization of soot agglomerates from various sources and comparison to aggregation theory. *Aerosol Science and Technology,* 47**,** 792-805.

Rosenfeld, D. and Woodley, W. L. 2000. Deep convective clouds with sustained supercooled liquid water down to -37.5 °c. *Nature,* 405**,** 440-442.

Rosenfeld, D., Yu, X., Liu, G., Xu, X., Zhu, Y., Yue, Z., Dai, J., Dong, Z., Dong, Y. and Peng, Y. 2011. Glaciation temperatures of convective clouds ingesting desert dust, air pollution and smoke from forest fires. *Geophysical Research Letters,* 38**,** L21804.

Roy, W. R., Berger, P. M., 2011. Geochemical controls of coal fly ash leacheate ph. *Coal Combustion and Gasification Products***,** 63 - 66.

Ruhl, L., Vengosh, A., Dwyer, G. S., Hsu-Kim, H. and Deonarine, A. 2010. Environmental impacts of the coal ash spill in kingston, tennessee: An 18-month survey. *Environmental Science & Technology,* 44**,** 9272-9278.

Ruuskanen, J., Tuch, T., Ten Brink, H., Peters, A., Khlystov, A., Mirme, A., Kos, G. P. A., Brunekreef, B., Wichmann, H. E., Buzorius, G., et al. 2001. Concentrations of ultrafine, fine and pm2.5 particles in three european cities. *Atmospheric Environment,* 35**,** 3729-3738.

Sadezky, A., Muckenhuber, H., Grothe, H., Niessner, R. and Pöschl, U. 2005. Raman microspectroscopy of soot and related carbonaceous materials: Spectral analysis and structural information. *Carbon,* 43**,** 1731-1742.

Sakaeda, N., Wood, R. and Rasch, P. J. 2011. Direct and semidirect aerosol effects of southern african biomass burning aerosol. *Journal of Geophysical Research-Atmospheres,* 116.

Saleh, R., Hennigan, C. J., Mcmeeking, G. R., Chuang, W. K., Robinson, E. S., Coe, H., Donahue, N. M. and Robinson, A. L. 2013. Absorptivity of brown carbon in

fresh and photo-chemically aged biomass-burning emissions. *Atmos. Chem. Phys.,* 13**,** 7683-7693.

Salzmann, C. G., Chu, B. T. T., Tobias, G., Llewellyn, S. A. and Green, M. L. H. 2007. Quantitative assessment of carbon nanotube dispersions by raman spectroscopy. *Carbon,* 45**,** 907-912.

Samson, R. J., Mulholland, G. W. and Gentry, J. W. 1987. Structural analysis of soot agglomerates. *Langmuir,* 3**,** 272-281.

Sassen, K., Demott, P. J., Prospero, J. M. and Poellot, M. R. 2003. Saharan dust storms and indirect aerosol effects on clouds: Crystal-face results. *Geophysical Research Letters,* 30.

Schauer, J. J., Kleeman, M. J., Cass, G. R. and Simoneit, B. R. T. 2001. Measurement of emissions from air pollution sources. 3. C1−c29 organic compounds from fireplace combustion of wood. *Environmental Science & Technology,* 35**,** 1716-1728.

Schnell, R. C., Van Valin, C. C. and Pueschel, R. F. 1976. Atmospheric ice nuclei: No detectable effects from a coal-fired powerplant plume. *Geophysical Research Letters,* 3**,** 657-660.

Schumann, U., Jeßberger, P. and Voigt, C. 2013. Contrail ice particles in aircraft wakes and their climatic importance. *Geophysical Research Letters,* 40**,** 2867-2872.

Seinfeld, J. H. and Pandis, S. N. 2006. *Atmospheric chemistry and physics : From air pollution to climate change / john h. Seinfeld and spyros n. Pandis,* Hoboken, N.J. : Chichester :, Wiley ; John Wiley [distributor].

Simoneit, B. R. T. 2002. Biomass burning — a review of organic tracers for smoke from incomplete combustion. *Applied Geochemistry,* 17**,** 129-162.

Sing, K. and Gregg, S. 1982. Adsorption, surface area and porosity. *Adsorption, Surface Area and Porosity*.

Singh, T., Khillare, P. S., Shridhar, V. and Agarwal, T. 2008. Visibility impairing aerosols in the urban atmosphere of delhi. *Environmental Monitoring and Assessment,* 141**,** 67-77.

Slowik, J. G., Cross, E. S., Han, J. H., Davidovits, P., Onasch, T. B., Jayne, J. T., Williams, L. R., Canagaratna, M. R., Worsnop, D. R., Chakrabarty, R. K., et al. 2007. An inter-comparison of instruments measuring black carbon content of soot particles. *Aerosol Science and Technology,* 41**,** 295-314.

Smekens, A., Godoi, R., Berghmans, P. and Grieken, R. 2005. Characterisation of soot emitted by domestic heating, aircraft and cars using diesel or biodiesel. *Journal of Atmospheric Chemistry,* 52**,** 45-62.

Spracklen, D. V., Carslaw, K. S., Pöschl, U., Rap, A. and Forster, P. M. 2011. Global cloud condensation nuclei influenced by carbonaceous combustion aerosol. *Atmos. Chem. Phys.,* 11**,** 9067-9087.

Starik, A., Popovicheva, O., Savel'ev, A., Titova, N. and Reyn, O. 2006. On the effects of processes inside the engine and in the exhaust plume on the ccn activation of combustion particles. *Chem. Eng. Trans,* 10**,** 541-546.

Stith, J. L., Twohy, C. H., Demott, P. J., Baumgardner, D., Campos, T., Gao, R. and Anderson, J. 2011. Observations of ice nuclei and heterogeneous freezing in a western pacific extratropical storm. *Atmos. Chem. Phys.,* 11**,** 6229-6243.

Sullivan, R. C., Petters, M. D., Demott, P. J., Kreidenweis, S. M., Wex, H., Niedermeier, D., Hartmann, S., Clauss, T., Stratmann, F., Reitz, P., et al. 2010. Irreversible loss of ice nucleation active sites in mineral dust particles caused by sulphuric acid condensation. *Atmos. Chem. Phys.*, 10**,** 11471-11487.

Suzanne, J., Ferry, D., Popovitcheva, O. and Shonija, N. K. 2003. Ice nucleation by kerosene soot under upper tropospheric conditions. *Canadian Journal of Physics,* 81**,** 423-429.

Svane, M., Janhäll, S., Hagström, M., Hallquist, M. and Pettersson, J. B. C. 2005. On-line alkali analysis of individual aerosol particles in urban air. *Atmospheric Environment,* 39**,** 6919-6930.

Tao, W.-K., Chen, J.-P., Li, Z., Wang, C. and Zhang, C. 2012. Impact of aerosols on convective clouds and precipitation. *Reviews of Geophysics,* 50**,** RG2001.

Tegen, I. and Fung, I. 1995. Contribution to the atmospheric mineral aerosol load from land surface modification. *Journal of Geophysical Research: Atmospheres,* 100**,** 18707-18726.

Tesner, P. A. and Shurupov, S. V. 1995. Some physico-chemieal parameters of soot formation during pyrolysis of hydrocarbons. *Combustion Science and Technology,* 105**,** 147-161.

Tishkova, V., Demirdjian, B., Ferry, D. and Johnson, M. 2011. Neutron diffraction study of water freezing on aircraft engine combustor soot. *Physical Chemistry Chemical Physics,* 13**,** 20729-20735.

Tucker, M. E. 1988. *Techniques in sedimentology*, Blackwell Science.

Tumolva, L., Park, J.-Y., Kim, J.-S., Miller, A. L., Chow, J. C., Watson, J. G. and Park, K. 2010. Morphological and elemental classification of freshly emitted soot particles and atmospheric ultrafine particles using the tem/eds. *Aerosol Science and Technology,* 44**,** 202-215.

Twohy, C. H., Demott, P. J., Pratt, K. A., Subramanian, R., Kok, G. L., Murphy, S. M., Lersch, T., Heymsfield, A. J., Wang, Z. E., Prather, K. A., et al. 2010. Relationships of biomass-burning aerosols to ice in orographic wave clouds. *Journal of the Atmospheric Sciences,* 67**,** 2437-2450.

Vali, G. 1971. Quantitative evaluation of experimental results an the heterogeneous freezing nucleation of supercooled liquids. *Journal of the Atmospheric Sciences,* 28**,** 402-409.

Vali, G. 1985. Nucleation terminology. *Journal of Aerosol Science,* 16**,** 575-576.

Vali, G. 1994. Freezing rate due to heterogeneous nucleation (vol 51, pg 1885, 1994). *Journal of the Atmospheric Sciences,* 51**,** 2683-2683.

Vali, G. 1999. *Ice nucleation - theory. A tutorial* [Online]. Available: http://www-das.uwyo.edu/~vali/nucl_th.pdf [Accessed 24th June 2010].

Vali, G. 2008. Repeatability and randomness in heterogeneous freezing nucleation. *Atmos. Chem. Phys.*, 8**,** 5017-5031.

Vali, G. and Stansbury, E. 1966. Time-dependent characteristics of heterogeneous nucleation of ice. *Canadian Journal of Physics,* 44**,** 477-&.

Van Loo, S. and Koppejan, J. 2007. *The handbook of biomass combustion and co-firing*, Earthscan.

Vassilev, S. V., Baxter, D., Andersen, L. K. and Vassileva, C. G. 2013. An overview of the composition and application of biomass ash. Part 1. Phase–mineral and chemical composition and classification. *Fuel,* 105**,** 40-76.

Wallace, J. M. and Hobbs, P. V. 2006. *Atmospheric science: An introductory survey*, Academic press.

Wang, B. and Knopf, D. A. 2011. Heterogeneous ice nucleation on particles composed of humic-like substances impacted by o3. *Journal of Geophysical Research: Atmospheres,* 116**,** D03205.

Wang, X., Williams, B. J., Wang, X., Tang, Y., Huang, Y., Kong, L., Yang, X. and Biswas, P. 2013. Characterization of organic aerosol produced during pulverized coal combustion in a drop tube furnace. *Atmos. Chem. Phys.,* 13**,** 10919-10932.

Warner, J. and Twomey, S. 1967. The production of cloud nuclei by cane fires and the effect on cloud droplet concentration. *Journal of the Atmospheric Sciences,* 24**,** 704-706.

Wca 2013. Coal combustion products report. World Coal Association.

Weingartner, E., Burtscher, H. and Baltensperger, U. 1997. Hygroscopic properties of carbon and diesel soot particles. *Atmospheric Environment,* 31**,** 2311-2327.

Williams, A., Jones, J. M., Ma, L. and Pourkashanian, M. 2012. Pollutants from the combustion of solid biomass fuels. *Progress in Energy and Combustion Science,* 38**,** 113-137.

Williams, D. B., Carter, C. B. and Veyssiere, P. 1998. Transmission electron microscopy: A textbook for materials science. *MRS Bulletin-Materials Research Society,* 23**,** 47.

Williams, D. H. and Fleming, I. 1980. *Spectroscopic methods in organic chemistry*, McGraw-Hill London.

Wilson, J. M. 2011. *Characterisation of soot produced on combustion of biomass and fossil fuel proxy compounds.* PhD, University of Leeds.

Wilson, J. M., Baeza-Romero, M. T., Jones, J. M., Pourkashanian, M., Williams, A., Lea-Langton, A. R., Ross, A. B. and Bartle, K. D. 2013. Soot formation from the combustion of biomass pyrolysis products and a hydrocarbon fuel, n-decane: An aerosol time of flight mass spectrometer (atofms) study. *Energy & Fuels*.

Wilson, T. W., Murray, B. J., Wagner, R., Möhler, O., Saathoff, H., Schnaiter, M., Skrotzki, J., Price, H. C., Malkin, T. L., Dobbie, S., et al. 2012. Glassy aerosols with a range of compositions nucleate ice heterogeneously at cirrus temperatures. *Atmos. Chem. Phys.,* 12**,** 8611-8632.

Wright, T. P. and Petters, M. D. 2013. The role of time in heterogeneous freezing nucleation. *Journal of Geophysical Research: Atmospheres,* 118**,** 3731-3743.

Wright, T. P., Petters, M. D., Hader, J. D., Morton, T. and Holder, A. L. 2013. Minimal cooling rate dependence of ice nuclei activity in the immersion mode. *Journal of Geophysical Research: Atmospheres,* 118**,** 10,535-10,543.

Xie, S. and Dearing, J. A. 1999. Comment on "identifying fly ash at a distance from fossil fuel power stations". *Environmental Science & Technology,* 33**,** 4140-4140.

Yankofsky, S. A., Levin, Z., Bertold, T. and Sandlerman, N. 1981. Some basic characteristics of bacterial freezing nuclei. *Journal of Applied Meteorology,* 20**,** 1013-1019.

Young, K. C. 1993. *Microphysical processes in clouds,* Oxford, UK, Oxford University Press.

Yu, H., Kaufman, Y. J., Chin, M., Feingold, G., Remer, L. A., Anderson, T. L., Balkanski, Y., Bellouin, N., Boucher, O., Christopher, S., et al. 2006. A review of measurement-based assessments of the aerosol direct radiative effect and forcing. *Atmospheric Chemistry and Physics,* 6**,** 613-666.

Yun, Y., Penner, J. E. and Popovicheva, O. 2012. The effects of hygroscopicity of fossil fuel combustion aerosols on mixed-phase clouds. *Atmos. Chem. Phys. Discuss.,* 12**,** 19987-20006.

Zaveri, R. A., Shaw, W. J., Cziczo, D. J., Schmid, B., Ferrare, R. A., Alexander, M. L., Alexandrov, M., Alvarez, R. J., Arnott, W. P., Atkinson, D. B., et al. 2012. Overview of the 2010 carbonaceous aerosols and radiative effects study (cares). *Atmos. Chem. Phys.,* 12**,** 7647-7687.

Zelepouga, S. A., Saveliev, A. V., Kennedy, L. A. and Fridman, A. A. 2000. Relative effect of acetylene and pahs addition on soot formation in laminar diffusion flames of methane with oxygen and oxygen-enriched air. *Combustion and Flame,* 122**,** 76-89.

Zhao, Y., Wang, S., Duan, L., Lei, Y., Cao, P. and Hao, J. 2008. Primary air pollutant emissions of coal-fired power plants in china: Current status and future prediction. *Atmospheric Environment,* 42**,** 8442-8452.

Zheng, M., Hagler, G. S. W., Ke, L., Bergin, M. H., Wang, F., Louie, P. K. K., Salmon, L., Sin, D. W. M., Yu, J. Z. and Schauer, J. J. 2006. Composition and sources of carbonaceous aerosols at three contrasting sites in hong kong. *Journal of Geophysical Research: Atmospheres,* 111**,** D20313.

Zuberi, B., Johnson, K. S., Aleks, G. K., Molina, L. T., Molina, M. J. and Laskin, A. 2005. Hydrophilic properties of aged soot. *Geophysical Research Letters,* 32**,** L01807.